Universitá degli Studi di Palermo

Dipartimento di Matematica e Informatica

PhD course in Mathematics and Computer Science
XXXV cycle

Pattern formation in hyperbolic reaction-transport systems and applications to dryland ecology

Advisor
Prof. Giancarlo CONSOLO
Co-advisor
Prof. Carmela CURRÓ

Candidate
Gabriele GRIFÓ

Coordinator
Prof. Maria Carmela LOMBARDO

A.A. 2021-2022

Contents

Acknowledgements

Before starting the full immersion into the wonderful world of patterns, I would like to thank all those who have supported me during this journey by dedicating a lot of their precious time and effort.

First of all, I would like to give my deepest gratitude to the "Fantastic Three" group, without whom my Ph.D. experience could never have been the same. In particular, special thanks to Prof. Giancarlo Consolo for introducing me to the beautiful world of pattern formation and for dedicating most of his time to me. He has guided and supported me each day. I also wish to thank Prof. Carmela Curró, without whom my Ph.D. journey would never have started. I will never stop being grateful to her for introducing me in this very special team in which I found not only excellent researchers but also fantastic people. Last but not least, special thanks to Prof. Giovanna Valenti who supported me a lot from both research and emotional sides. They gave a huge contribution to my research and personal growth through a lot of stimulating discussions, emerging criticism, and giving always powerful suggestions, also in everyday life.

I am grateful also to Prof. Frits Veerman, who welcomed me at Leiden University during my permanence in the Netherlands and introduced me to the fascinating world of geometric singular perturbation theory. Thanks also to Annalisa Iuorio for her huge patience in our meetings and her company during our dutch lunches. I strongly hope this leads to fruitful collaborations.

I want to thank all my university colleagues for having created a pleasant working atmosphere and stimulating discussions during chocolate breaks.

Finally, I would like to express my deep gratitude to my whole family, especially to my brother Gianmarco, my mother Ornella, my father Giancarlo, and my girlfriend Roberta. They have been the most important people in this journey, and my life, whom supported me every time and everywhere. They helped me in staying up during the difficulties and in staying grounded in my good times. I will be infinitely grateful to them and no word able to translate my feelings for them exists.

Abstract

Pattern formation and modulation is an active branch of mathematics, not only from the perspective of fundamental theory but also for its huge applications in many fields of physics, ecology, chemistry, biology, and other sciences. In this thesis, the occurrence of Turing and wave instabilities, giving rise to stationary and oscillatory patterns, respectively, is theoretically investigated by means of two-compartment reaction-transport hyperbolic systems. The goal is to elucidate the role of inertial times, which are introduced in hyperbolic models to account for the finite-time propagation of disturbances, in stationary and transient dynamics, in supercritical and subcritical regimes.

In particular, starting from a quite general framework of reaction-transport model, three particular cases are derived. In detail, in the first case, the occurrence of stationary patterns is investigated in one-dimensional domains by looking for the inertial dependence of the main features that characterize the formation and stability process of the emerging patterns. In particular, the phenomenon of Eckhaus instability, in both supercritical and subcritical regimes, is studied by adopting linear and multiple-scale weakly-nonlinear analysis and the role played by inertia during the transient regime, where an unstable patterned state evolves towards a more favorable stable configuration through sequences of phase-slips, is elucidated.

Then, in the second topic, the focus is moved to oscillatory periodic patterns generated by wave (or oscillatory Turing) instability. This phenomenon is studied by considering 1D two-compartment hyperbolic reaction-transport systems where different transport mechanisms of the species here involved are taken into account. In these cases, by using linear and weakly nonlinear stability analysis techniques, the dependence of the non-stationary patterns on hyperbolicity is underlined at and close to the criticality. In particular, it is proven that inertial effects play a role, not only during transient regimes from the spatially-homogeneous steady state toward the patterned state but also in altering the amplitude, the wavelength, the migration speed, and even the stability of the travelling waves.

Finally, in the last case, the formation and stability of stationary patterns are investigated in bi-dimensional domains. To this aim, a general class of two-species hyperbolic reaction-transport systems is deduced following the guidelines of Extended Thermodynamics theory. To characterize the emerging Turing patterns, linear and weakly nonlinear stability analysis on the uniform steady states are addressed for rhombic and hexagonal planform solutions.

In order to gain some insight into the above-mentioned dynamics, the previous

theoretical predictions are corroborated by numerical simulations carried out in the context of dryland ecology. In this context, patterns become a relevant tool to identify early warning signals toward desertification and to provide a measure of resilience of ecosystems under climate change. Such ecological implications are discussed in the context of the Klausmeier model, one of the easiest two-compartment (vegetation biomass and water) models able to describe the formation of patterns in semi-arid environments. Therefore, it will be also here discussed how the experimentally-observed inertia of vegetation affects the formation and stability of stationary and oscillatory periodic vegetation patterns.

List of Abbreviations

CCGL	**C**ubic **C**omplex **G**inzburg-**L**andau
CQRGL	**C**ubic **Q**uintic **R**eal **G**inzburg-**L**andau
CRGL	**C**ubic **R**eal **G**inzburg-**L**andau
EI	**E**ckhaus **I**nstability
ET	**E**xtended **T**hermodynamics
GL	**G**inzburg-**L**andau
LSA	**L**inear **S**tability **A**nalysis
ODE	**O**rdinary **D**ifferential **E**quation
PDE	**P**artial **D**ifferential **E**quation
RAD	**R**eaction **A**dvection **D**iffusion
RD	**R**eaction **D**iffusion
RT	**R**eaction **T**ransport
SL	**S**tuart-**L**andau
WNA	**W**eakly-**N**onlinear **A**nalysis

Chapter 1

Introduction

Self-organized patterns are quite ubiquitous in nature and the study of the associated nonlinear spatial processes has become nowadays a sub-area of complexity science. Due to the huge amount of field applications, i.e. physics, ecology, chemistry, biology, epidemiology, and others [1–7], in the last century a lot of effort has been spent to propose different approaches that are able to describe these complex phenomena. The difficulties in replying nature phenomena under laboratory conditions, and/or the long time scale in which they occur, brought scientists to dedicate their efforts in developing different mathematical tools apt to predict and replicate the observed dynamics. These led mathematicians to play an active role in describing the pattern formation process and, in particular, in improving their own tools to achieve always a deeper description of them.

The aim of this chapter is to briefly introduce the subject of this thesis from a mathematical perspective but using a simple formalism in order to be understandable to a general audience.

1.1 Patterns as a natural fascinating phenomenon

All of us have already seen a pattern, some in a conscious way while others not. They represent amazing products of nature and their presence in everyday life is really common, from animals to beaches, by the way of cooking and beautiful landscapes. The first time that you're gonna open a book that handles patterns, even a mathematical one, you may be amazed in finding a lot of strange pictures, such as tigers, fingerprints, ripples in sandy deserts, or hexagons on a frying pan, but the question that easily arises is: "What are patterns?"

The word "pattern" has a very general connotation that encloses a lot of different phenomena. In the most general context, it can be associated with a regular spatial structure or spatiotemporal scheme that is periodic in space, at least locally. In the one-dimensional case, it refers to only stripes or bands, whereas in the two-dimensional one many shapes can be achieved, such as squares, spots, gaps, hexagons, spirals, and many others. In a wrong way, they are usually associated with something that assumes a symmetric behaviour, but, on the contrary, they may break the global symmetry maintaining the local one.

Patterned dynamics can be observed in huge quantities of different phenomena that are very far from each other, but which share the same formation mechanism. For example, let us consider the stripes on a zebra coat and the desert sand ripples, they represent events completely different from the physical viewpoint but show the same phenomenon in which two stripes merge into one or one splits into two of them. Once having realized what a pattern is and how it looks like, one may ask: "How do they arise?"

In the last century, a lot of effort has been made in extracting information about patterns, understanding their nature and characterizing them. Firstly, motivated by experiments, scientists focused their attention on patterns resulting from the convective phenomenon [8]: a fluid that is heated from below creates a movement of mass that gives rise to the so-called convection rolls. Then, stimulated by observations in the context of chemical reactions (such as the Belousov-Zhabotinsky ones [9]), they understood that spatial dispersal of species may play an important and decisive role in the pattern formation process. In particular, following Alan Turing's idea of morphogenesis [10], it was realized that spatial instabilities at the macroscale emerge as a consequence of competition between two concurrent mechanisms operating at different spatial scales: a short-range activation and a long-range inhibition. These observations conducted mathematicians to take into account tools able to mimic these spatial behaviours through reaction-diffusion (RD) systems. Indeed, RD models are considered the most simple evolutionary processes able to exhibit complex spatial patterns [4, 11]. A form of the N-component RD systems for the field $\mathbf{W} = (W_1, \ldots, W_N) \in \mathbb{R}^N$ is given by

$$\mathbf{W}_t = \mathrm{D}\Delta\mathbf{W} + \mathbf{F}(\mathbf{W}, B) \tag{1.1}$$

where $\mathbf{W}(\mathbf{x}, t)$ acts on $(\mathbf{x}, t) \in [\Omega, \mathbb{R}^+]$ with $\Omega \subseteq \mathbb{R}^n$ $(n = 1, 2, 3)$, $W_1, \ldots, W_N$ represent the state variables, D represents the diffusion squared matrix of order N, Δ is the Laplacian operator, and $\mathbf{F}(\mathbf{W}, B)$ is the kinetic vector depending also on the control parameter $B \in \mathbb{R}$.

To obtain a more detailed description of the natural phenomena, mathematicians started to focus on different approaches to study RD models that can provide more details on these complex phenomena [3, 4, 6, 7, 12, 13]. In particular, the mechanism of pattern formation proposed by Alan Turing in 1952 arises from the coupling of diffusion and reaction kinetics and is based on the destabilization of a spatially uniform steady state due to a perturbation of a given wavenumber. In the case where only two agents interact with each other $\mathbf{U} = (U_1, U_2)$, they give rise to Turing instability only if one of the following scenarios take place: (i) U_1 is an activator for both U_2 and itself whereas U_2 is always an inhibitor; (ii) U_1 is a self-activator and an inhibitor for U_2, whereas U_2 is a self-inhibitor and an activator for U_1. Note that, in both cases, the inhibitor U_2 has to diffuse faster than the activator U_1 [4].

Turing's instability has been hugely proposed in so many fields and was able to fill a lot of gaps of knowledge on the pattern formation mechanism. For sake of completeness, it should be mentioned that other mechanisms, different from Turing's one, have been proposed to explain the origin of such structures. They are mostly based on the concept of "prepatterning" but this is beyond the scope of the present thesis [3, 4].

1.2 Towards the hyperbolic framework

Standard RD systems of parabolic type are usually employed to study the formation and the stability of self-organized patterns in many research areas [1–7]. They have been studied extensively over the last decades and they provide a good description of the dynamics in many applications. There exist, however, some contexts where such parabolic models provide a non-entirely satisfactory description, mainly due to the fact that simple diffusive transport admits the flux of a species to follow the gradient of the species "adiabatically", i.e. instantaneously, with no time delay [14]. This occurs when the dissipative fluxes obey gradient-like laws, as in the case of Fourier law in thermodynamics, Fick's law for concentration of species or particles, and Darcy's law for porous media. From a mathematical viewpoint, parabolic models suffer from the unrealistic propagation of local disturbances through the system with infinite speed. This issue can be overcome by rebuilding the governing equations in terms of hyperbolic reaction-transport (RT) systems where the finite-time propagation of disturbances, i.e. the inertia of the involved species, is explicitly taken into account.

In particular, from a mesoscopic viewpoint, RD systems describe an uncorrelated random-walk of particles, referred to as Brownian motion. In this framework, localized disturbances are allowed to spread infinitely fast, although heavily attenuated, through the system. In addition, in this case, the motion of particles became unpredictable even on small time scales. These phenomena are not observed in nature. Brownian motion, and therefore RD systems, fail to well describe the dispersion of species in those cases where particles or individuals take a well-defined velocity. On the other hand, it still works as a good approximation where the inertia is negligible, i.e. the velocity does not take a relevant role and the position is determined by different independent effects, such as in liquids.

In order to avoid the above-mentioned unphysical problem, one should take hyperbolic RT systems into account, as they account for finite speed of propagation and a predictable motion in small time intervals. Therefore, hyperbolic RT models constitute a step forward in the mathematical modelling of natural phenomena giving a better description for those in which persistence, i.e. inertial, effects are not negligible on macroscopic scales, such as dilute gases, turbulent diffusion, motion of animals, and vegetation dynamics. Moreover, they also appear more suitable to describe transient phenomena characterized by waves evolving in space over a finite time, especially those involving long-time scales. Moreover, from a mathematical viewpoint, the inertial times constitute additional degrees of freedom that may be used to better mimic experimental observations and, at the same time, offer a richer scenario of dynamics [15–27].

The most commonly used approaches that rely on hyperbolic evolution equations and that have a physical foundation are in the form of reaction-telegraph, reaction correlated random walk, or reaction-Cattaneo systems [14–16, 21, 22, 28–37]. The approach here followed falls into the latter category and is based upon Extended Thermodynamics (ET) theory [38]. According to ET theory, the dissipative fluxes are considered as additional state variables that obey some thermodynamically-consistent balance laws and that reduce to the gradient-based constitutive law in parabolic models and in the stationary case.

1.3 Vegetation patterns in dryland ecology

Now more than ever, the world is changing very quickly. By comparing nowadays data with those dating back to the 1880s, the increase in the global temperature of 1°C, the raise in the sea level of 10 centimeters, and the decrease of the 12% in the Arctic sea ice show how climate change is going to perform unrecoverable damages [39]. A lot of long-term effects have been observed in all geographic scales, such as the widespread changes in precipitations, ocean salinity, wind strength, and aspects of extreme weather including droughts, heavy precipitation, heat waves, and tropical cyclones. More intense and longer droughts have been observed over wider areas since the 1970s. As it stands, the World Meteorological Organization (WMO) in the next future expects an increase in global temperature of 0.2°C per decade, such as in the amount of precipitation in high latitudes. A rainfall decrease is forecasted in subtropical regions. Hot extremes, heat waves, and heavy precipitation will be more frequent. Land degradation will increase due to droughts and soil erosion. The expectations on water availability are an increase of 10-40% at high latitudes and a decrease of 10-30% over dry regions. Dryland areas will undergo an increase in extension [40].

To prevent this catastrophic scenario, several multidisciplinary approaches, enclosing mathematical modelling of complex phenomena, have been proposed to predict future behaviors of ecosystems as well as to identify ecological indicators of climate change, land degradation, and ecosystem resilience. Unfortunately, from a mathematical viewpoint, modelling the complex processes occurring at physical, biological, ecological, and socio-economical levels, makes the study of desertification very hard to study. However, thanks to simplifying assumptions, many features of this phenomenon have been captured and understood. In particular, it has already been proven that pattern formation acquires a very important role to address the study of desertification mechanisms and dynamics, to detect as it may be representative of early warning signals of imminent transition toward desertification. At the same time, the use of mathematical tools may help in finding some restoration strategies for degraded areas [7].

Mathematically speaking, the desertification process is often viewed as a sudden global transition from a stable (uniformly or not) vegetated state, i.e. a vegetated area, to an unproductive alternative stable state, i.e. the soil bare ground, dictated by a variation of a control parameter (such as the decrease in rainfall or increase of plant loss). It can be associated, for instance, to the occurrence of subcritical bifurcation that admits a sudden transition toward the desert state when main control parameter values go beyond the turning point, so that the productive state no longer exists. This simplified view of the desertification mechanism may provide warning signals for the occurrence of imminent desertification that can be extracted from a bifurcation analysis. Of course, real ecological dynamics are much more complex than this simplistic view. Indeed some recent satellite observations, combined with mathematical modelling, suggest that ecosystems may "evade" the tipping points through pattern formation, so that patterns may be a signature of ecosystem resilience instead of marking a sharp transition toward desertification. Also, spatial disturbances are often limited in space, so leading to a *local* rather than *global* transition toward

an alternative stable state.

During the last decades, many mathematical models have been proposed to describe the mechanism of pattern formation and stability in the context of dryland ecology [41–62]. Among these, one of the easiest two-compartment models able to provide a sufficiently adequate description of the vegetation patterned dynamics in semi-arid environments is the Klausmeier model [41]. It is based on the water redistribution hypothesis under which spatial instability at the macro-scale arises from the local biomass-water positive feedback at the micro-scale. In particular, in its original formulation, it captures the dynamics of vegetation biomass $u(x,t)$ and surface water $w(x,t)$ and accounts for the isotropic diffusion of vegetation and the anisotropic transport of water along the hillslope. In dimensionless form, it reads:

$$\begin{cases} u_t - \Delta u = u^2 w - Bu \\ w_t - \nu w_x = A - u^2 w - w \end{cases} \tag{1.2}$$

where subscripts denote the partial derivatives with respect to the indicated variable and Δ is the Laplacian operator. Furthermore, the model encloses a per-capita rate of water uptake proportional to plant biomass, the plant growth rate proportional to water uptake, a linear dependence of plant loss with strength B, a mean annual rainfall represented by the parameter A, and the last term in the balance equation for water is representative of losses by evaporation. Note that, previous investigations suggest that realistic values of plant loss and rainfall rate belong to the ranges $B \in (0,2)$ and $A \in (0,3)$, respectively [41, 63, 64]. From an ecological viewpoint, the original version of the Klausmeier model (1.2) is able to predict the formation of vegetated patterns along sloped terrains only.

Later, some variants or extensions of it have been proposed in order to depict different scenarios and to acquire additional information about vegetation dynamics. In detail, Refs. [53, 65, 66] modified the water equation by removing the advection term, which models the downhill run-off of surface water and substituting it with a diffusion term. In this case, the most suitable ecological interpretation is that $w(x,t)$ is now representative of soil water and vegetated dynamics occurring over flat terrains may be better mimicked. Then, the model (1.2) has been further extended to account also for the diffusion of water [46]. Here, the diffusion term has been added in order to better capture the movement of surface water induced by spatial differences in infiltration rate. It should be noticed that, this latter model is more general and encloses the previous ones as limit cases: when the diffusion coefficient is set to zero, we retrieve the original model for sloped terrains, when the advective one is set to zero, we deal with the modified version for flat areas. Finally, a further generalization was introduced in Ref. [67] to better account for another ecological phenomenon, i.e. the secondary seed dispersal. Indeed, all previous models ignore the possibility of the seed to be transported downhill by an overland flow. To mimic this behaviour, an advective term has to be considered in the vegetation equation.

Therefore, the Klausmeier model, in all its variants, is able to qualitatively capture the uphill or stationary migration of vegetation bands in both sloped and flat environments, which are believed to be observed experimentally [27, 68–70]. However, the parabolic nature of the above model prevents the possibility of taking into account

those inertial effects which are observed in the vegetation response, in particular for the woody component [18, 20, 24, 26, 27]. It was indeed emphasized that inertia of existing plant populations, namely the tendency to continue residing in a given location when the environmental conditions become unfavorable, takes an active role in response to climate change and presence of pollutants. To this aim, as well as to provide a proper description of long transient pattern dynamics [71–74], hyperbolic generalizations of the above models have been proposed in [75–80]. Literature on this topic has indeed emphasized that inertia plays a non-trivial role, as it can be more than just a time lag in response to an ongoing stressor (global climate change, pollutants, etc.). Indeed, it can mask future deterioration in ecosystem conditions and can even lead a species to change toward an alternative state even after a stressor is removed [18, 27].

1.4 Models and goals

The main aim of this thesis is to extend the literature of two-compartment hyperbolic RT systems in order to provide a deeper understanding on the pattern formation and stability mechanisms there involved.

By reviewing the literature on hyperbolic RT systems, it is possible to face with 1D RT systems where pattern formation is addressed via linear stability analysis (LSA) and/or weakly nonlinear analysis (WNA). In detail, wave instability in systems where one species diffuses and the other one undergoes advection is performed by adopting LSA only [75], Turing and wave instabilities in the presence of cross-diffusion, with no advection, is considered by adopting LSA and WNA in limited domains [81] or LSA only [32, 82], Turing instability in the absence of advection is taken into account by using LSA and WNA in extended domains with constant [15, 16, 76] and non-constant [77] inertial times, and travelling fronts are studied in models with advection [14, 31] or in its absence considering self-diffusion [29] and cross-diffusion [83]. On the contrary, investigation in the bi-dimensional hyperbolic RT case are performed through LSA tools and numerical simulations only [15, 16, 32–35].

With this in mind, here the study of both stationary and oscillatory patterns in the one- and bi-dimensional case will be tackled by means of LSA and WNA in both limited and infinite domains. Moreover, to emphasize the role played by inertial effects in the context of dryland ecology, the corresponding hyperbolic generalizations of the Klausmeier model will be taken into account as illustrative examples.

Our analysis starts from the following, general, two-compartment bidimensional parabolic reaction-advection-diffusion (RAD) system that in dimensionless form reads:

$$\mathbf{W}_t = \mathrm{D}\Delta\mathbf{W} + \mathrm{M}\mathbf{W}_x + \mathbf{F}\left(\mathbf{W}, B\right) \tag{1.3}$$

where the subscripts denote partial derivatives and Δ is the Laplacian operator in $\mathbb{R}^2$. The column vector enclosing the dependent field variables $\mathbf{W}$, the diffusion matrix D, the advective one M, and the reaction kinetics $\mathbf{F}(\mathbf{W}, B)$ are defined as follows

$$\mathbf{W} = \begin{bmatrix} u \\ w \end{bmatrix}, \ \mathrm{D} = \begin{bmatrix} 1 & 0 \\ 0 & d \end{bmatrix}, \ \mathrm{M} = \begin{bmatrix} \psi & 0 \\ 0 & \nu \end{bmatrix}, \ \mathbf{F}\left(\mathbf{W}, B\right) = \begin{bmatrix} f(u, w, B) \\ g(u, w, B) \end{bmatrix}, \tag{1.4}$$

where B is the control parameter, $d \gg 1$ denotes the w-by-u diffusion ratio while ψ and ν are the advection speeds of species u and w, respectively, along the privileged direction x. In the applicative example of Klausmeier dynamics, the kinetic terms $f(u,w)$ and $g(u,w)$ take the form reported in (1.2).

Then, in order to account for inertial effects, it is possible to build up a hyperbolic generalization via the ET theory. It takes the form:

$$\mathbf{U}_t + \mathrm{M}^{(1)}(\mathbf{U})\mathbf{U}_x + \mathrm{M}^{(2)}(\mathbf{U})\mathbf{U}_y = \mathbf{N}(\mathbf{U}, B) \tag{1.5}$$

being the vector of field variables now defined as $\mathbf{U} = \left[u\,, w\,, J_1^u, J_2^u, J_1^w, J_2^w\right]^T$ with (J_1^u, J_2^u) and (J_1^w, J_2^w) the vectors of the planar fluxes associated to the species u and w, respectively, whereas the 6×6 matrices $\mathrm{M}^{(1)}$ and $\mathrm{M}^{(2)}$ are expressed as:

$$\mathrm{M}^{(1)} = \begin{bmatrix} -\psi & 0 & 1 & 0 & 0 & 0 \\ 0 & -\nu & 0 & 0 & 1 & 0 \\ \frac{1}{\tau^u} & 0 & 0 & 0 & 0 & 0 \\ 0 & 0 & 0 & 0 & 0 & 0 \\ 0 & \frac{d}{\tau^w} & 0 & 0 & 0 & 0 \\ 0 & 0 & 0 & 0 & 0 & 0 \end{bmatrix}, \quad \mathrm{M}^{(2)} = \begin{bmatrix} 0 & 0 & 0 & 1 & 0 & 0 \\ 0 & 0 & 0 & 0 & 0 & 1 \\ 0 & 0 & 0 & 0 & 0 & 0 \\ \frac{1}{\tau^u} & 0 & 0 & 0 & 0 & 0 \\ 0 & 0 & 0 & 0 & 0 & 0 \\ 0 & \frac{d}{\tau^w} & 0 & 0 & 0 & 0 \end{bmatrix} \tag{1.6}$$

and the vector of kinetic terms is given by:

$$\mathbf{N}\left(\mathbf{U}, B\right) = \left[f(u,w,B),\, g(u,w,B),\, -J_1^u/\tau^u, -J_2^u/\tau^u,\, -J_1^w/\tau^w,\, -J_2^w/\tau^w\right]^T. \tag{1.7}$$

In (1.6), $\tau^u > 0$ and $\tau^w > 0$ are the inertial times related to the species u and w, respectively. For the sake of simplicity, the inertial times are hereafter treated as constants. In the 1D case, the above system reduces to:

$$\mathbf{U}_t + \mathrm{M}\mathbf{U}_x = \mathbf{N}(\mathbf{U}, B) \tag{1.8}$$

being

$$\mathbf{U} = \begin{bmatrix} u \\ w \\ J^u \\ J^w \end{bmatrix}, \quad \mathrm{M} = \begin{bmatrix} -\psi & 0 & 1 & 0 \\ 0 & -\nu & 0 & 1 \\ \frac{1}{\tau^u} & 0 & 0 & 0 \\ 0 & \frac{d}{\tau^w} & 0 & 0 \end{bmatrix}, \quad \mathbf{N} = \begin{bmatrix} f(u,w,B) \\ g(u,w,B) \\ -\frac{1}{\tau^u} J^u \\ -\frac{1}{\tau^w} J^w \end{bmatrix}. \tag{1.9}$$

Details on the derivation of 2D hyperbolic RT model (1.5)-(1.7) are given in Appendix A, while those related to the 1D model (1.8)-(1.9) can be found in Ref. [31]. It should be noticed that, in the limiting case $\tau^u \to 0$ and $\tau^w \to 0$, the hyperbolic models reduce to the classical parabolic ones and the constitutive Fick's law of dispersion is retrieved.

Before investigating pattern formation, it will be necessary to preliminarily address the LSA of the spatially-homogeneous steady-states admitted by these models. As known, such states are obtained by setting the reaction terms to zero, i.e.

$\mathbf{N}(\mathbf{U}, B) = 0$. In the case of Klausmeier dynamics, the number of steady states depends upon the relative value of plant loss B and rainfall A. In particular, if $A \leq 2B$, the model admits only a spatially-homogeneous steady state of desert-type:

$$\mathbf{U}_D^* = (0, A, \mathbf{0}), \tag{1.10}$$

while, if $A \geq 2B$, it also admits two states representative of spatially-homogeneous vegetated regions:

$$\begin{aligned} \mathbf{U}_L^* &= (u_L, w_L, \mathbf{0}), \\ \mathbf{U}_S^* &= (u_S, w_S, \mathbf{0}), \end{aligned} \tag{1.11}$$

where $u_L = \left(A - \sqrt{A^2 - 4B^2}\right)/(2B)$, $u_S = \left(A + \sqrt{A^2 - 4B^2}\right)/(2B)$, $w_L = B/u_L$, $w_S = B/u_S$, with $u_L < 1 < u_S$. Notice that the steady states are always associated to null fluxes of the involved species.

Here, the study of the pattern formation arising from the destabilization of the above equilibria will be addressed in three different frameworks which constitute subsets of the general class presented in (1.5)-(1.7). In detail, this thesis can be subdivided into the following chapters.

In Chapter 2, the focus is given on the pattern mechanisms by looking for stationary periodic patterns in two-compartment 1D hyperbolic RT systems (1.8)-(1.9) where both species undergo self-diffusion ($\psi = \nu = 0$). In the context of dryland ecology, it is representative of pattern dynamics taking place over a flat terrain. The species $u(x,t)$ and $w(x,t)$ denote vegetation biomass and soil water, respectively, both undergo a primary dispersal and no passive transport phenomena are here included. Here, a detailed investigation is performed by means of LSA and WNA in a large finite domain in order to establish the inertial dependence of the main features that characterize the emerging patterns. Then, the focus is moved to the re-stabilization pattern mechanism known as Eckhaus instability (EI) in both supercritical and subcritical dynamics. Here, the cubic real (CRGL) and cubic-quintic (CQRGL) Ginzburg-Landau equations are deduced to characterize the pattern amplitude evolution near the onset of criticality and the stability behaviour of each primary and secondary patterned branch. Numerical simulations in the framework of vegetation dynamics are performed to confirm and validate the theoretical prediction. Results achieved in this chapter are published in Ref. [79].

In Chapter 3, the study of oscillatory periodic patterns in two-compartment 1D hyperbolic RT systems (1.8)-(1.9) is, in turn, addressed considering two different frameworks. The first considered model accounts for the self-diffusion of both species and the advection of only one of them ($\psi = 0$) whereas the second one encloses the advection of both species and the self-diffusion to only one of them ($d = 0$). In the context of dryland ecology, these models are representative of pattern dynamics taking place over a hillside of a semiarid environment, with the variable ν measuring the slope of the terrain and in turn the water advection speed. The species $u(x,t)$ and $w(x,t)$ here denote vegetation biomass and surface water, respectively. In the first model, both species undergo a primary dispersal and no passive transport of seeds is considered. In the second model, water dispersal is neglected as the

unidirection downhill flow is taken as the dominant contribution, whereas both primary and secondary dispersals of seeds are taken into account. In both frameworks, the LSA and WNA tools are used to gain some insight into the pattern evolution with particular emphasis on the dependence of the migration speed on hyperbolicity. Additional information is given in the framework of the illustrative example of the Klausmeier model where it is proved how inertia significantly modifies the features associated with the vegetation patterns. Moreover, further details will be provided by a comparison with experimental data. Results here achieved are published in Refs. [78, 80]

In Chapter 4, the bi-dimensional dynamics occurring in two-compartment hyperbolic RT systems (1.5)-(1.7) are considered in the presence of a diffusive character only ($\psi = \nu = 0$). In this case, the ecological scenario is again the one discussed in Chapter 2, where isotropic primary dispersal acts over flat terrains and advective fluxes are consequently neglected. In this context, particular focus will be given to the formation of rhombic and hexagonal Turing patterns. First, the 2D hyperbolic RT model is derived by means of ET theory and, then, LSA and WNA are applied to characterize the near criticality evolution of patterns that are different from stripes. Qualitative results are compared with those achieved in 1D dynamics. Results here achieved are contained in a publication which is currently under review.

Chapter 2

Stationary patterns in 1D hyperbolic RT systems

Turing-driven stationary periodic patterns, in the one-dimensional case, are variously referred to as bands, rolls, or stripes. It is known that, in a large domain, the equation ruling the spatio-temporal evolution of pattern amplitude close to onset is in the form of GL equation [84–87]. This equation also allows to inspect the dependence of the stability of the resulting periodic states on wavelength. Indeed, patterns may undergo different destabilization mechanisms associated with changes in wavelength and amplitude, one of which is the EI [5, 88–91]. EI acts on the roll phase to compress or dilate pattern wavelength and takes place when a given roll wavelength cannot be accommodated by the environment so that some of them are eventually created or eliminated. The process leading the system to be rearranged in a more favorable configuration is referred to as phase-slip [5, 88, 90].

A large body of literature has successfully addressed the bifurcation analysis of EI in both infinite and finite spatial domains and has also addressed the study of complex intriguing dynamics, such as those associated to quasi-periodic solutions and homoclinic snaking bifurcation structures [5, 88–90, 92–98]. However, none of those works has inspected the EI of stationary and quantized Turing patterns in the context of hyperbolic models. As widely reported in literature [15, 28, 30, 32, 75–79, 81], despite the mathematical convergence of parabolic and hyperbolic models is expected in the long-time limit due to the stationary nature of the excited patterns, the coupling between hyperbolicity and nonlinearity may generate richer transient dynamics.

In particular, this chapter addresses the analysis of one-dimensional stationary patterns emerging in the subclass of two-compartments hyperbolic RT models (1.8)-(1.9) where both species undergo self-diffusion ($\psi = \nu = 0$), defined on a large finite domain. Here, the aim is focused at addressing the stability and quantization of spatially-periodic patterns, in both supercritical and subcritical regimes.

With this in mind, it is deduced, first, the equation governing the evolution of pattern amplitude close to the onset of supercritical and subcritical bifurcation. To this aim, a multiple-scale weakly nonlinear expansion, pushed up to the fifth perturbative order, is applied. Depending on the perturbative order at which the expansion is truncated, this procedure allows to build a CRGL or CQRGL equation. Moreover,

taking into account the quantization of modes due to the spatial confinement, a bifurcation analysis of the EI is addressed, to accurately describe the existence and stability thresholds of all periodic branches [89]. This investigation is finalized at inspecting the qualitatively different dynamical features captured by the above GL equations.

Theoretical predictions here developed are then validated through a comparison with numerical simulations. To this aim, the EI in the context of dryland ecology is investigated by considering the hyperbolic generalization of the modified Klausmeier model [41, 53, 65, 66, 76, 77].

The comparison between analytical and numerical results made it possible to address several issues: (i) to validate theoretical predictions on bifurcation analysis developed in the frameworks of CRGL and CQRGL equations, in both supercritical and subcritical regimes; (ii) to investigate how hyperbolicity affects not only transient regime dynamics between different patterned states but also the occurrence of phase-slips observed during an Eckhaus-driven restabilizing process; (iii) the feasibility to control, independently of each other, the time and the spatial location at which such phase-slips occur.

This chapter is organized as follows. In Section 2.1, LSA and WNA are performed. Then, in Section 2.2, the bifurcation analysis of the EI is addressed. In detail, a brief review of the most relevant results associated with the supercritical regime in the framework of the CRGL equation is summarized, whereas the subcritical regime is inspected via both CRGL and CQRGL equations. Finally, in Section 2.3, a validation of the theoretical predictions is developed by means of a comparison with numerical simulations carried out on the hyperbolic modified Klausmeier model. Numerical investigations are addressed to inspect the spatio-temporal dependence of phase-slip and to emphasize the role played by inertial times. Concluding remarks are given in the last section.

2.1 LSA and WNA

The considered class of 1D hyperbolic RT models (1.8)-(1.9), where both species $u(x,t)$ and $w(x,t)$ undergo self-diffusion ($\psi = \nu = 0$) is given by

$$\mathbf{U}_t + \mathrm{M}\mathbf{U}_x = \mathbf{N}(\mathbf{U}, B) \tag{2.1}$$

being

$$\mathbf{U} = \begin{bmatrix} u \\ w \\ J^u \\ J^w \end{bmatrix}, \quad \mathrm{M} = \begin{bmatrix} 0 & 0 & 1 & 0 \\ 0 & 0 & 0 & 1 \\ \frac{1}{\tau^u} & 0 & 0 & 0 \\ 0 & \frac{d}{\tau^w} & 0 & 0 \end{bmatrix}, \quad \mathbf{N} = \begin{bmatrix} f(u,w,B) \\ g(u,w,B) \\ -\frac{1}{\tau^u} J^u \\ -\frac{1}{\tau^w} J^w \end{bmatrix}. \tag{2.2}$$

In the literature, the hyperbolic structure (2.1),(2.2) has been successfully employed in different contexts, such as plant ecology [76], epidemiology [99], air pollution [100] and chemistry [15].

Before entering the details of the analysis, let us briefly recall the conditions for the onset of Turing instability [3, 4]. Turing instability is the phenomenon that breaks the spatial symmetry of a system. It arises when a steady state $\mathbf{U}^*$ is stable against spatially-uniform ($k = 0$) perturbations but loses stability under non-homogeneous ($k \neq 0$) ones. As known [4], this is equivalent to suppose that, after introducing a perturbation in the form $e^{(\omega t+ikx)}$, the characteristic polynomial admits a null eigenvalue ($\omega = 0$) for a non-null value of k, named critical wavenumber k_c. Also, the transition from stability to unstability has to occur via a maximum, that is $(\partial\omega/\partial k|_{k=k_c} = 0)$. By considering B as a control parameter and the above perturbation, the following characteristic polynomial is obtained:

$$\omega^4 + A_1\omega^3 + A_2\omega^2 + A_3\omega + A_4 = 0 \tag{2.3}$$

where

$$\begin{aligned}
A_1 &= \tfrac{1}{\tau^u} + \tfrac{1}{\tau^w} - (f_u^* + g_w^*)\,,\\
A_2 &= \left(\tfrac{1}{\tau^u} + \tfrac{d}{\tau^w}\right) k^2 + \tau^u\tau^w - (f_u^* + g_w^*)\left(\tfrac{1}{\tau^u} + \tfrac{1}{\tau^w}\right) + f_u^* g_w^* - f_w^* g_u^*,\\
A_3 &= \left[(d+1)\,\tau^u\tau^w - f_u^*\tfrac{d}{\tau^w} - g_w^*\tfrac{1}{\tau^u}\right] k^2 + (f_u^* g_w^* - f_w^* g_u^*)\left(\tfrac{1}{\tau^u} + \tfrac{1}{\tau^w}\right) - (f_u^* + g_w^*)\,\tau^u\tau^w,\\
A_4 &= \tfrac{d}{\tau^u\tau^w}\left[k^4 - \left(f_u^* + \tfrac{g_w^*}{d}\right) k^2 + \tfrac{f_u^* g_w^* - f_w^* g_u^*}{d}\right],
\end{aligned}$$

Then, by requiring that $\mathbf{U}^*$ is stable against spatially-uniform perturbations but unstable with respect to non-homogeneous ones, we get the following restrictions:

$$\begin{cases}
f_u^* + g_w^* < 0\\
f_u^* g_w^* - f_w^* g_u^* > 0\\
d f_u^* + g_w^* > 0\\
(d f_u^* + g_w^*)^2 - 4d\,(f_u^* g_w^* - f_w^* g_u^*) > 0
\end{cases} \tag{2.4}$$

where the asterisk denotes that the function is evaluated at $\mathbf{U}^*$.

From (2.4), it can be easily deduced that the critical values of control parameter B_c and wavenumber k_c at the onset of Turing instability are obtained by solving:

$$d^2 f_u^* + 2d\,(2 f_w^* g_u^* - f_u^* g_w^*) + {g_w^*}^2 = 0, \tag{2.5}$$

$$k_c^2 = \sqrt{\frac{f_u^* g_w^* - f_w^* g_u^*}{d}}. \tag{2.6}$$

Note that, since we deal with the formation of stationary patterns, the hyperbolic structure of system (2.1),(2.2) does not affect the expression of the critical parameters at onset, so that the occurrence of Turing instability is ruled by the same conditions found in classical parabolic models [4].

To describe the spatio-temporal evolution of pattern amplitude close to Turing threshold (2.5),(2.6), multiple-scale WNA is now addressed [5, 58, 88, 92, 101]. To this

aim, we consider a small dimensionless parameter ϵ, expand the control parameter B around B_c and the field $\overline{\mathbf{U}} = \mathbf{U} - \mathbf{U}^*$ as

$$\begin{aligned} B &= B_c + \epsilon^2 B_2 + \epsilon^4 B_4 + O(\epsilon^6), \\ \overline{\mathbf{U}} &= \epsilon\overline{\mathbf{U}}_1 + \epsilon^2\overline{\mathbf{U}}_2 + \epsilon^3\overline{\mathbf{U}}_3 + \epsilon^4\overline{\mathbf{U}}_4 + \epsilon^5\overline{\mathbf{U}}_5 + O(\epsilon^6) \end{aligned} \tag{2.7}$$

and introduce different time and spatial scales as follows:

$$\begin{aligned} \frac{\partial}{\partial t} &\to \epsilon^2 \frac{\partial}{\partial T_2} + \epsilon^4 \frac{\partial}{\partial T_4}, \\ \frac{\partial}{\partial x} &\to \frac{\partial}{\partial x} + \epsilon \frac{\partial}{\partial X}. \end{aligned} \tag{2.8}$$

After substituting the above expansions into the governing system (2.1),(2.2), applying zero-flux boundary conditions over the physical domain $x \in [0, \mathcal{D}]$ and collecting terms of the same orders of ϵ, a set of linear equations for the $\overline{\mathbf{U}}_i$ is obtained:

$$\begin{aligned} &\text{at order 1} && \frac{\partial\overline{\mathbf{U}}_1}{\partial x} - K_c^*\overline{\mathbf{U}}_1 = \mathbf{0} \\ &\text{at order 2} && \frac{\partial\overline{\mathbf{U}}_2}{\partial x} - K_c^*\overline{\mathbf{U}}_2 = \mathrm{M}^{-1}\,\widetilde{\mathbf{F}}_2 \\ &\text{at order 3} && \frac{\partial\overline{\mathbf{U}}_3}{\partial x} - K_c^*\overline{\mathbf{U}}_3 = \mathrm{M}^{-1}\,\widetilde{\mathbf{F}}_3 \\ &\text{at order 4} && \frac{\partial\overline{\mathbf{U}}_4}{\partial x} - K_c^*\overline{\mathbf{U}}_4 = \mathrm{M}^{-1}\,\widetilde{\mathbf{F}}_4 \\ &\text{at order 5} && \frac{\partial\overline{\mathbf{U}}_5}{\partial x} - K_c^*\overline{\mathbf{U}}_5 = \mathrm{M}^{-1}\,\widetilde{\mathbf{F}}_5 \end{aligned} \tag{2.9}$$

where the vectors $\widetilde{\mathbf{F}}_j$ $(j = 2, ..., 5)$ are given by

$$\begin{aligned} \widetilde{\mathbf{F}}_2 = {} & \tfrac{1}{2}\left[\left(\overline{\mathbf{U}}_1\cdot\nabla\right)^{(2)}\mathbf{N}\right]_{B_c}^{*} - \mathrm{M}\tfrac{\partial\overline{\mathbf{U}}_1}{\partial X}, \\ \widetilde{\mathbf{F}}_3 = {} & \left[\left(\overline{\mathbf{U}}_1\cdot\nabla\right)\left(\left(\overline{\mathbf{U}}_2\cdot\nabla\right)\mathbf{N}\right) + \tfrac{1}{6}\left(\overline{\mathbf{U}}_1\cdot\nabla\right)^{(3)}\mathbf{N}\right]_{B_c}^{*} - \mathrm{M}\tfrac{\partial\overline{\mathbf{U}}_2}{\partial X} - \tfrac{\partial\overline{\mathbf{U}}_1}{\partial T_2} + \mathcal{L}\overline{\mathbf{U}}_1, \\ \widetilde{\mathbf{F}}_4 = {} & \left[\left(\overline{\mathbf{U}}_1\cdot\nabla\right)\left(\left(\overline{\mathbf{U}}_3\cdot\nabla\right)\mathbf{N}\right) + \tfrac{1}{2}\left(\overline{\mathbf{U}}_2\cdot\nabla\right)^{(2)}\mathbf{N} + \tfrac{1}{2}\left(\overline{\mathbf{U}}_1\cdot\nabla\right)^{(2)}\left(\left(\overline{\mathbf{U}}_2\cdot\nabla\right)\mathbf{N}\right) + \right. \\ & \left. + \tfrac{1}{24}\left(\overline{\mathbf{U}}_1\cdot\nabla\right)^{(4)}\mathbf{N}\right]_{B_c}^{*} + \tfrac{B_2}{2}\left[\frac{\mathrm{d}\left[\left(\overline{\mathbf{U}}_1\cdot\nabla\right)^{(2)}\mathbf{N}\right]^{*}}{\mathrm{d}B}\right]_{B_c} - \mathrm{M}\tfrac{\partial\overline{\mathbf{U}}_3}{\partial X} - \tfrac{\partial\overline{\mathbf{U}}_2}{\partial T_2} + \mathcal{L}\overline{\mathbf{U}}_2, \\ \widetilde{\mathbf{F}}_5 = {} & \left[\left(\overline{\mathbf{U}}_1\cdot\nabla\right)\left(\left(\overline{\mathbf{U}}_4\cdot\nabla\right)\mathbf{N}\right) + \tfrac{1}{2}\left(\overline{\mathbf{U}}_1\cdot\nabla\right)^{(2)}\left(\left(\overline{\mathbf{U}}_3\cdot\nabla\right)\mathbf{N}\right) + \left(\overline{\mathbf{U}}_2\cdot\nabla\right)\left(\left(\overline{\mathbf{U}}_3\cdot\nabla\right)\mathbf{N}\right) + \right. \\ & \left. + \tfrac{1}{2}\left(\overline{\mathbf{U}}_2\cdot\nabla\right)^{(2)}\left(\left(\overline{\mathbf{U}}_1\cdot\nabla\right)\mathbf{N}\right) + \tfrac{1}{120}\left(\overline{\mathbf{U}}_1\cdot\nabla\right)^{(5)}\mathbf{N} + \tfrac{1}{6}\left(\overline{\mathbf{U}}_1\cdot\nabla\right)^{(3)}\left(\left(\overline{\mathbf{U}}_2\cdot\nabla\right)\mathbf{N}\right)\right]_{B_c}^{*} + \\ & + \tfrac{B_2}{6}\left[\frac{\mathrm{d}\left[\left(\overline{\mathbf{U}}_1\cdot\nabla\right)^{(3)}\mathbf{N} + 3\left(\overline{\mathbf{U}}_1\cdot\nabla\right)\left(\left(\overline{\mathbf{U}}_2\cdot\nabla\right)\mathbf{N}\right)\right]^{*}}{\mathrm{d}B}\right]_{B_c} - \mathrm{M}\tfrac{\partial\overline{\mathbf{U}}_4}{\partial X} - \tfrac{\partial\overline{\mathbf{U}}_3}{\partial T_2} - \tfrac{\partial\overline{\mathbf{U}}_1}{\partial T_4} + \mathcal{L}\overline{\mathbf{U}}_3 + \widetilde{\mathcal{L}}\overline{\mathbf{U}}_1, \end{aligned} \tag{2.10}$$

being $\nabla = \partial/\partial\mathbf{U}$, together with

$$K_c^* = \begin{bmatrix} 0 & 0 & -1 & 0 \\ 0 & 0 & 0 & -\frac{1}{d} \\ f_u^* & f_w^* & 0 & 0 \\ g_u^* & g_w^* & 0 & 0 \end{bmatrix}, \tag{2.11}$$

$$\mathcal{L} = B_2 \left[\frac{\mathrm{d}(\nabla\mathbf{N})^*}{\mathrm{d}B}\right]_{B_c}, \quad \widetilde{\mathcal{L}} = B_4 \left[\frac{\mathrm{d}(\nabla\mathbf{N})^*}{\mathrm{d}B}\right]_{B_c} + \frac{B_2^2}{2}\left[\frac{\mathrm{d}^2(\nabla\mathbf{N})^*}{\mathrm{d}B^2}\right]_{B_c}.$$

Moreover, for a generic vector $\mathbf{H}$, the expression $(\mathbf{H}\cdot\nabla)^{(j)}$ stands for the operator

$$\mathbf{H}\cdot\nabla = H_1\frac{\partial}{\partial u} + H_2\frac{\partial}{\partial w} + H_3\frac{\partial}{\partial J^u} + H_4\frac{\partial}{\partial J^w} \tag{2.12}$$

applied j times.

The set of equations (2.9)-(2.11) has to be solved sequentially, as sketched in the Appendix B. The removal of secular terms at $O(\epsilon^3)$ leads to an envelope equation ruling the spatio-temporal evolution of the pattern complex amplitude $\Omega(X, T_2, T_4)$ that takes the form of a CRGL equation:

$$\frac{\partial\Omega}{\partial T_2} = \sigma\Omega - L|\Omega|^2\Omega + \nu\frac{\partial^2\Omega}{\partial X^2}, \tag{2.13}$$

which preserves the structure found in classical parabolic models [5, 87–89]. It is worth noticing that the real coefficients σ, L and ν inherit the dependence on the inertial times as follows:

$$\begin{aligned} \sigma(\tau^u, \tau^w) &= \frac{\Pi}{d - 1 + k_c^2 d(\tau^w - \tau^u)}, \\ L(\tau^u, \tau^w) &= \frac{\Gamma}{d - 1 + k_c^2 d(\tau^w - \tau^u)}, \\ \nu(\tau^u, \tau^w) &= \frac{\Psi}{d - 1 + k_c^2 d(\tau^w - \tau^u)}, \end{aligned} \tag{2.14}$$

where the functions Π, Γ and Ψ depend upon the w-by-u diffusion ratio d and the kinetic terms, together with their partial derivatives, but are independent of the inertial times. The explicit expressions of these functions are given in the Appendix B for the case of vegetation dynamics illustrated by the hyperbolic modified Klausmeier model. Therefore, the hyperbolic structure of the system may affect the spatio-temporal evolution of pattern amplitude. In particular, the growth rate σ and coefficient ν, that in the pattern forming region are always positive, play a significant role during transient regime. On the other hand, the sign of the Landau coefficient L determines the nature of the dynamical regime: $L > 0$ corresponds to the supercritical regime, whereas $L < 0$ to the subcritical one [76].

From the removal of secular terms at $O(\epsilon^4)$, the following compatibility condition for the spatially evolution of the pattern amplitude is obtained [93]:

$$k_1\Omega_{XXX} + k_2|\Omega|^2\Omega_X + k_3\Omega_X = 0. \tag{2.15}$$

Therefore, to investigate subcritical dynamics, we push weakly nonlinear analysis up to the fifth perturbative order where the removal of secular terms leads to the following envelope equation for the pattern amplitude:

$$\frac{\partial \Omega}{\partial T} = \overline{\sigma}\Omega - \overline{L}|\Omega|^2\Omega + \overline{R}|\Omega|^4\Omega + \overline{\nu}\frac{\partial^2 \Omega}{\partial X^2}, \tag{2.16}$$

which is in the form of a CQRGL equation. In (2.16), $\partial/\partial T = \partial/\partial T_2 + \epsilon^2 \partial/\partial T_4$, the coefficients here appearing are real and represent second-order corrections of the coefficient involved in CRGL equation (2.13), namely $\overline{\sigma} = \sigma + \epsilon^2\widetilde{\sigma}$, $\overline{L} = L + \epsilon^2\widetilde{L}$, $\overline{\nu} = \nu + \epsilon^2\widetilde{\nu}$ and $\overline{R} = \epsilon^2\widetilde{R}$. Moreover, each of these coefficients encloses a non trivial dependence on the inertial times which, acting as additional degrees of freedom, may offer a richer scenario of spatio-temporal dynamics with respect to the parabolic counterpart. This statement holds true despite hyperbolic and parabolic models share the same structure of weakly inverted bifurcations to a stationary spatially-periodic state [94–97, 102, 103]. However, due to the cumbersome expressions here involved, conclusions can be only given through numerical simulations. For this reason, as well as to keep the length of this thesis within reasonable limits, the full expressions of all the real coefficients involved in eqs.(2.13)-(2.16) will be explicitly given in the Appendix B for the hyperbolic generalization of the modified Klausmeier model.

2.2 Bifurcation analysis of the EI

The analysis carried out in this section focuses on the formation and stability of *stationary* 1D Turing patterns originating in the hyperbolic RT system (2.1),(2.2) over a large finite domain ($\mathcal{D} \propto 1/\epsilon$). In detail, the occurrence of the phenomenon of EI will be analytically investigated in both supercritical and subcritical regime, with the main aim of quantifying some key dynamical features: stationary amplitude of patterns, existence and stability thresholds of each periodic bifurcating branch and linear growth rate. To address how a non-favorable wavelength may lead to pattern instability, the standard procedure adopted in the literature by Tuckermann and Barkley is followed [5, 89], which is briefly reviewed in the next subsection.

2.2.1 Supercritical regime (a brief review)

To describe the spatio-temporal evolution of pattern amplitude close to onset of Turing instability in the supercritical regime, it suffices to push WNA up to the third perturbative order, where the CRGL equation (2.13) is retrieved. We remind that the coefficients σ and ν are always positive whereas the Landau coefficient L is positive in the supercritical regime only. To reduce the number of coefficients here involved, let us apply the following rescaling:

$$\tilde{x} = \frac{\pi}{\mathcal{D}}x = \frac{\pi}{\epsilon\mathcal{D}}X, \quad \tilde{t} = \frac{\pi^2\nu}{\mathcal{D}^2}t = \frac{\pi^2\nu}{\epsilon^2\mathcal{D}^2}T_2, \quad \tilde{\Omega} = \frac{\epsilon\mathcal{D}\sqrt{L}}{\pi\sqrt{\nu}}\Omega, \quad \zeta = \frac{\epsilon^2\mathcal{D}^2}{\pi^2\nu}\sigma, \quad Q = \frac{\mathcal{D}}{\pi}k, \tag{2.17}$$

that allows to recast eq.(2.13) as:

$$\frac{\partial \tilde{\Omega}}{\partial \tilde{t}} = \zeta\tilde{\Omega} - \tilde{\Omega}|\tilde{\Omega}|^2 + \frac{\partial^2 \tilde{\Omega}}{\partial \tilde{x}^2}. \tag{2.18}$$

For simplicity, let us drop the tilde notation and assume that rolls take the structure:

$$\Omega = \Xi e^{iQx} e^{i\theta}, \tag{2.19}$$

where Ξ and Q describe, respectively, the amplitude and the phase of the envelope, whereas θ is an arbitrary constant to be determined according to boundary conditions. Substituting (2.19) into (2.18) gives, apart from the null solution $\Xi = 0$, the stationary amplitude:

$$\Xi = \sqrt{\zeta - Q^2}. \tag{2.20}$$

Patterned solution (2.19),(2.20) exists for $\zeta > Q^2$ and is referred in the literature to as *pure* mode [89]. It has to be distinguished from the trivial solution $\Omega = 0$ which is termed *conductive* mode.

Note that, according to (2.17),(2.19) and the structure of $\overline{\mathbf{U}}_1$ (see (B.12) in the Appendix B), the field has total wavenumber $(Q + Q_c)$. The finite domain, however, implies quantization of modes, i.e. not all wavenumbers are admitted but only those integer ones satisfying $(Q_n + Q_c) \in \mathbb{Z}, n \in \mathbb{N}_0$. Let us call

$$\Xi_n = \sqrt{\zeta - Q_n^2} \tag{2.21}$$

the quantized amplitude of the n-th mode, that exists for $\zeta > Q_n^2 := \zeta_{e,n}$. Zero-flux boundary conditions, together with quantization of modes, restrict the possible values of θ to 0 and π only. For simplicity, we set $\theta = 0$. To address linear stability of patterns, let us apply small perturbations in amplitude and phase of rolls as follows:

$$\Omega = \Xi_n (1 + \xi) e^{i(Q_n x + \phi)}, \tag{2.22}$$

where $|\xi|, |\phi| \ll 1$. Substituting (2.22) into (2.18), keeping the linear terms in ξ and ϕ and taking real and imaginary parts, the system ruling the evolution of perturbations results:

$$\begin{cases} \frac{\partial \phi}{\partial t} = 2Q_n \frac{\partial \xi}{\partial x} + \frac{\partial^2 \phi}{\partial x^2} \\ \frac{\partial \xi}{\partial t} = -2\Xi_n^2 \xi + \frac{\partial^2 \xi}{\partial x^2} - 2Q_n \frac{\partial \phi}{\partial x} \end{cases} \tag{2.23}$$

Then, by assuming:

$$\begin{cases} \phi = \hat{\phi} e^{\lambda t + i\tilde{k}x} \\ \xi = \hat{\xi} e^{\lambda t + i\tilde{k}x} \end{cases} \tag{2.24}$$

being $\hat{\phi}$ and $\hat{\xi}$ arbitrary constants and the dimensionless wavenumber $\tilde{k} \neq 0$, the following quadratic equation for the linear growth rate λ is obtained:

$$\lambda^2 + 2\left(\tilde{k}^2 + \Xi_n^2\right)\lambda + \tilde{k}^2\left(2\Xi_n^2 + \tilde{k}^2 - 4Q_n^2\right) = 0, \tag{2.25}$$

whose roots are:

$$\lambda_n^{(1,2)} = -\Xi_n^2 - \tilde{k}^2 \pm \sqrt{\Xi_n^4 + 4Q_n^2\tilde{k}^2}. \tag{2.26}$$

Since the eigenvalue $\lambda_n^{(2)}$ is always negative, the stability of the associated mode depends on $\lambda_n^{(1)}$ which, taking into account (2.21), can be expressed as:

$$\lambda_n^{(1)} = Q_n^2 - \tilde{k}^2 - \zeta + \sqrt{\left(\zeta - Q_n^2\right)^2 + 4Q_n^2\tilde{k}^2}. \tag{2.27}$$

Stationary amplitude of pure modes	$n \geq 0$	$\Xi_n = \sqrt{\zeta - Q_n^2}$
Existence threshold	$n \geq 0$	$\zeta_{e,n} = Q_n^2$
(Unstable) bifurcation points	$1 < \tilde{k} \leq n$	$\zeta_{n,\tilde{k}} = 3Q_n^2 - \frac{1}{2}\tilde{k}^2$
(Restabilizing) Eckhaus threshold	$n \geq 1$	$\zeta_{E,n} = \zeta_{n,1} = 3Q_n^2 - \frac{1}{2}$
Range of existence	$n \geq 0$	$\zeta \geq \zeta_{e,n}$
Range of stability	$n = 0$	$\zeta \geq \zeta_{e,0}$
	$n \geq 1$	$\zeta \geq \zeta_{E,n} > \zeta_{e,n}$

Table 2.1: Dynamical features predicted by CRGL equation (2.18) in the supercritical regime.

Consequently, stable roll solutions in a finite domain satisfy:

$$\zeta > \sup_{k \in \mathbb{N}} \{3Q_n^2 - \frac{1}{2}\tilde{k}^2\} = 3Q_n^2 - \frac{1}{2} := \zeta_{E,n}, \tag{2.28}$$

the last equality of which identifies the well-known Eckhaus parabola in the (Q, ζ) plane [5, 89].

By means of this approach, a well-known result is retrived: the primary branch Ω_0 is always stable at onset ($\zeta \geq \zeta_{e,0}$) while all the other branches Ω_n (with $n \geq 1$) have always n unstable directions at onset and undergo n secondary bifurcations (of pitchfork type) in order to become stable. The final, restabilizing, bifurcation corresponds to the Eckhaus threshold [89]. The analysis developed in the supercritical regime, where pattern amplitude obeys CRGL equation (2.18) can be thus summarized in tabular form, see Table 2.1.

Moreover, taking into account (2.14) and (2.17), we can conclude that the stationary amplitude of each pure mode Ξ_n, the existence thresholds $\zeta_{e,n}$ and the Eckhaus thresholds $\zeta_{E,n}$ are unaffected by hyperbolicity, being the ratio σ/ν independent of inertial times. This result is compatible with the stationary nature of the emerging spatially-periodic patterns.

2.2.2 Subcritical regime

In this section we aim to describe the pattern amplitude close to onset of a subcritical bifurcation via a CRGL equation or CQRGL equation. Although it is known that these amplitude equations may capture different dynamical features, the goal of the subsequent analyses is to detect and emphasize such differences keeping in mind that the Landau coefficient L is negative in this regime.

Stationary amplitude of pure modes	$n \geq 0$	$\Xi_n = \sqrt{Q_n^2 - \zeta}$
Existence threshold	$n \geq 0$	$\zeta_{e,n} = Q_n^2$
(Restabilizing) Eckhaus threshold	$n = 0$	$\zeta_{E,0} = 3Q_0^2 - \frac{1}{2}$
Range of existence	$n \geq 0$	$\zeta \leq \zeta_{e,n}$
Range of stability	$n = 0$	$\zeta_{E,0} \leq \zeta \leq \zeta_{e,0}$

Table 2.2: Dynamical features predicted by CRGL equation (2.30) in the subcritical regime.

2.2.2.1 Description via CRGL equation

Starting from CRGL equation (2.13), let us rescale the variables as in (2.17) except for the amplitude:

$$\tilde{\Omega} = \frac{\epsilon \mathcal{D}\sqrt{-L}}{\pi\sqrt{\nu}}\Omega. \tag{2.29}$$

This allows to recast the CRGL equation as follows:

$$\frac{\partial \tilde{\Omega}}{\partial \tilde{t}} = \zeta\tilde{\Omega} + \tilde{\Omega}|\tilde{\Omega}|^2 + \frac{\partial^2 \tilde{\Omega}}{\partial \tilde{x}^2}. \tag{2.30}$$

Removing tilde notation and adopting similar arguments as those addressed in the previous subsection, the quantized pure modes can be expressed as:

$$\Omega_n = \sqrt{Q_n^2 - \zeta}e^{iQ_n x} \tag{2.31}$$

and exist for

$$\zeta < Q_n^2 := \zeta_{e,n}. \tag{2.32}$$

For each Q_n, the previous expression is representative of two periodic branches that originate from the conductive state through a subcritical pitchfork bifurcation. It is easy to verify that the expression of the eigenvalue determining stability of each bifurcating branch $\lambda_n^{(1)}$ (given in (2.27)) as well as the condition on pattern stability (given in (2.28)) are formally unchanged with respect to those found in the supercritical case. However, a key point has to be stressed according to the analysis here carried out: the existence (2.32) and stability (2.28) conditions are simultaneously fulfilled in the subcritical regime for $n = 0$ only. Results are summarized in Table 2.2. Therefore, if the pattern amplitude obeyed CRGL equation (2.30) close to the onset of a subcritical bifurcation, the sole primary branch Ω_0 would undergo Eckhaus instability [104]. This marks a notably difference with respect to the behavior outlined in the supercritical regime.

2.2.2.2 Description via CQRGL equation

Let us now inspect whether the CQRGL equation (2.16), obtained by pushing WNA expansion up to fifth order, may provide a qualitatively different description of subcritical dynamics. The signs of the coefficients are assumed to be $\overline{\sigma} > 0$, $\overline{L} < 0$, $\overline{\nu} > 0$

and $\widetilde{R} < 0$ in order to guarantee that the the primary branch exhibits a weakly inverted bifurcation at onset (i.e., it shows hysteresis) and that such a bifurcation saturates to quintic order [94]. By using the following rescaling of variables:

$$\begin{gathered}\tilde{x} = \frac{\pi}{\epsilon\mathcal{D}}X, \quad \tilde{t_2} = \frac{\pi^2\overline{\nu}}{\epsilon^2\mathcal{D}^2}T_2, \quad \tilde{t_4} = \frac{\pi^2\overline{\nu}}{\epsilon^2\mathcal{D}^2}T_4, \quad \tilde{\Omega} = \frac{\epsilon\mathcal{D}\sqrt{-\overline{\overline{L}}}}{\pi\sqrt{\overline{\nu}}}\Omega, \\ \zeta = \frac{\epsilon^2\mathcal{D}^2}{\pi^2\overline{\nu}}\overline{\sigma}, \quad Q = \frac{\mathcal{D}}{\pi}k, \quad \rho = -\frac{\pi^2\overline{\nu}}{\mathcal{D}^2\overline{L}^2}\widetilde{R},\end{gathered} \tag{2.33}$$

the CQRGL equation (2.16) may be recast as:

$$\frac{\partial\tilde{\Omega}}{\partial\tilde{t}} = \zeta\tilde{\Omega} + \tilde{\Omega}|\tilde{\Omega}|^2 - \rho\tilde{\Omega}|\tilde{\Omega}|^4 + \frac{\partial^2\tilde{\Omega}}{\partial\tilde{x}^2}, \tag{2.34}$$

being $\partial/\partial\tilde{t} = \partial/\partial\tilde{t_2} + \epsilon^2\left(\partial/\partial\tilde{t_4}\right)$. Notice that the coefficients ζ and ρ are real and positive.

Dropping tilde notation, considering "perfect" rolls structure as in (2.19) and using similar arguments as those addressed in the previous subsections, the quantized pure modes originating from the turning point can be expressed as $\Omega_n = \Xi_n e^{iQ_n x}$ with:

$$\Xi_n = \sqrt{\frac{1 \pm \sqrt{1 + 4\rho\left(\zeta - Q_n^2\right)}}{2\rho}}. \tag{2.35}$$

The large amplitude branch exists for

$$\zeta > Q_n^2 - \frac{1}{4\rho} := \zeta_{e,n}, \tag{2.36}$$

whereas the small amplitude one exists for

$$\zeta_{e,n} < \zeta < Q_n^2. \tag{2.37}$$

Considering (2.22),(2.24) and (2.34), the eigenvalue $\lambda_n^{(1)}$ determining stability of pure modes is given by

$$\lambda_n^{(1)} = \Xi_n^2 - \tilde{k}^2 - 2\rho\Xi_n^4 + \sqrt{4\rho^2\Xi_n^8 - 4\rho\Xi_n^6 + \Xi_n^4 + 4Q_n^2\tilde{k}^2}, \tag{2.38}$$

that, using (2.35), allows to deduce the following stability condition for the large amplitude branch:

$$\begin{aligned}\zeta > \sup_{\tilde{k}\in\mathbb{N}}\left\{2Q_n^2 - \frac{1}{4}\tilde{k}^2 - \frac{1}{8\rho}\left[1 - \sqrt{1 - 4\rho\left(\tilde{k}^2 - 4Q_n^2\right)}\right]\right\} = \\ = 2Q_n^2 - \frac{1}{4} - \frac{1}{8\rho}\left[1 - \sqrt{1 - 4\rho\left(1 - 4Q_n^2\right)}\right] := \zeta_{E,n},\end{aligned} \tag{2.39}$$

the last equality of which defines the Eckhaus threshold predicted by CQRGL equation. From the comparison between existence (2.36) and Eckhaus thresholds (2.39), it is possible to identify which bifurcating branch may undergo EI as:

$$\zeta_{e,n} \leq \zeta_{E,n} \quad \Leftrightarrow \quad -8\rho\left(Q_n^2 - \frac{1}{4}\right) - 1 \leq \sqrt{1 - 4\rho\left(1 - 4Q_n^2\right)}. \tag{2.40}$$

Inequality (2.40) points out that the restabilizing mechanism depends on the order of the bifurcating branch. Indeed, for $n = 0$, since quantization of modes implies $\left(Q_0^2 - 1/4\right) \leq 0$, the necessary and sufficient condition for the restabilization of the primary branch becomes:

$$2\left(1 - 4Q_0^2\right)\rho \leq 1, \tag{2.41}$$

that represents a restriction on the allowed values of the coefficient ρ. On the other hand, for $n \geq 1$, since $\left(Q_n^2 - 1/4\right) > 0$, the inequality (2.40) is fulfilled for any $\rho > 0$, so implying that all the secondary branches exhibit restabilizing Eckhaus bifurcations.

According to this analysis, the existence and consequently the amount of secondary bifurcations originating from periodic branches requires:

$$\tilde{k} \leq 2|Q_n|\sqrt{1 + \frac{1}{8\rho Q_n^2}} := \tilde{k}_n^*, \tag{2.42}$$

with $\tilde{k} \in \mathbb{N}$. Since $\rho > 0$, the radicand is always greater than 1, so that $\tilde{k}_n^* \geq 2|Q_n|$.

Notice that, fulfillment of conditions (2.40) and (2.41), as well as the numerical estimation of the quantity $\tilde{k}_n^*$ in (2.42), depends on the value of the coefficient ρ and thus, it has to be checked numerically for the specific model under consideration. This issue will be addressed in next sections.

Therefore, the CQRGL equation predicts at least four key differences with respect to the cubic counterpart: (i) the range of existence of patterns is bounded from below $\zeta \geq \zeta_{e,n} := Q_n^2 - 1/(4\rho)$; (ii) such an existence threshold is smaller than the bifurcation point ($\zeta_n = Q_n^2$) at which periodic branches originate from the conductive state; (iii) the primary branch may undergo EI provided that condition (2.41) is satisfied whereas (iv) all the secondary branches undergo EI and the number of restabilizing bifurcations depends on value of ρ through condition (2.42).

Results contained in this subsection, that represent one of the novelties, are summarized in Table 2.3.

In the literature [94], Brand and Deissler tackled a similar study on Eckhaus instability and deduced the analog of the Benjamin-Feir-Newell instability criterion for a weakly inverted bifurcation. However, some differences with respect to the present work should be pointed out. Indeed, those authors addressed the analysis on infinite domains only, so that quantization of modes was not investigated. Furthermore, the stability domain for finite-amplitude plane-wave solutions of CQRGL equation that are stable against the EI was provided in terms of wavenumber instead of control parameter.

2.2.3 Spatio-temporal dependence of phase-slip

The analysis carried out so far has revealed that the transition from an Eckhaus unstable state towards a more favorable, stable, patterned configuration may occur under different dynamical regimes. This process involves a sequence of transient states during which the wavelength of patterns is adjusted via the formation of amplitude defects and the appearance of *phase-slips*. Phases-slips are defined as solutions of

Stationary amplitude of pure modes	$n \geq 0$	$\Xi_n = \sqrt{\left[1 + \sqrt{1 + 4\rho\left(\zeta - Q_n^2\right)}\right]/(2\rho)}$
Existence threshold	$n \geq 0$	$\zeta_{e,n} = Q_n^2 - \frac{1}{4\rho}$
(Unstable) bifurcation points	$1 < \tilde{k} \leq \tilde{k}_n^*$	$\zeta_{n,k} = 2Q_n^2 - \frac{1}{4}\tilde{k}^2 - \frac{1}{8\rho}\left[1 - \sqrt{1 - 4\rho\left(\tilde{k}^2 - 4Q_n^2\right)}\right]$
(Restabilizing) Eckhaus threshold	$n \geq 0$	$\zeta_{E,n} = 2Q_n^2 - \frac{1}{4} - \frac{1}{8\rho}\left[1 - \sqrt{1 - 4\rho\left(1 - 4Q_n^2\right)}\right]$
Range of existence	$n \geq 0$	$\zeta \geq \zeta_{e,n}$
Range of stability	$n = 0$	$\zeta \geq \zeta_{E,0} > \zeta_{e,0} \quad \Leftrightarrow \quad 2\left(1 - 4Q_0^2\right)\rho \leq 1$
	$n \geq 1$	$\zeta \geq \zeta_{E,n} > \zeta_{e,n}$ always

Table 2.3: Dynamical features predicted by CQRGL equation (2.34) in the subcritical regime.

the real GL equation whose number of zeros varies as a function of time. In other words, assuming the pattern amplitude $\Omega = \Xi(x,t)\mathrm{e}^{i\psi(x,t)}$, a wavelength can only be created or destroyed where the local spatial phase $\psi(x,t)$ is undefined, namely at time instants (t') and locations (x') where $\mathrm{Re}(\Omega(x',t')) = \mathrm{Im}(\Omega(x',t')) = 0$ [90, 105, 106].

Unfortunately, the global evolution of a given perturbation cannot be correctly described by a local analysis around a steady state, as the one performed in the previous sections, so that the occurrence in time and the location in space of phase slips is hard to be predicted. To the best of our knowledge, some good approximations of these quantities have been obtained by means of *local* theories under the assumption that phase slip occurs 'just' after an *ad-hoc* choice of initial data [90, 106], but no explicit expressions have been provided in the general, *global*, case. Moreover, some works pointed out the possibility to control and vary the time to phase slip only if some 'free' model parameters, not involved in the spectrum of the linearized problem, are available [96, 104, 107]. At the same time, those works inspected the dependence of the time to phase slip on the linear growth rate but no mention was given on the functional dependence of the spatial location at which phase slip occurs. Therefore, the issue of controlling, independently of each other, time and space at which phase slip takes place appears to be still unaddressed. This issue will be investigated numerically in the next section.

2.3 An illustrative example: the hyperbolic modified Klausmeier model

In order to validate the theoretical predictions carried out in the previous sections, let us now investigate, as an illustrative example, the occurrence of EI in the context of dryland ecology. To this aim, let us take into account the Klausmeier model.

It has been proposed in the literature both in parabolic (1.2) [41] and hyperbolic (1.8)-(1.9) [75–77] versions. This latter has been introduced to account for inertial effects [18, 20, 24, 26, 27] and long transient regimes [71–74]. In line with the analysis carried out previously, plant mortality B is taken as the main control parameter as it encloses variability due to natural, human, and herbivory effects. To evaluate the spatio-temporal evolution of pattern dynamics, the governing system is integrated numerically over a finite domain of length $\mathcal{D}$ by means of COMSOL Multiphysics [108]. Moreover, the MATLAB package PDE2PATH [109] is used to build up the bifurcation diagrams in both supercritical and subcritical regimes.

In Appendix B all the expressions of the quantities arising from LSA and WNA for the hyperbolic generalization of the modified Klausmeier model are reported.

2.3.1 Supercritical regime

In the supercritical regime, the following model parameters are chosen: water-to-plant diffusion ratio $d = 10^3$ and rainfall $A = 2.8$. According to (2.5),(2.6),(2.14), the considered setup gives rise to a critical value of plant loss $B_c = 3529 \times 10^{-4}$, critical wavenumber $k_c = 0.3814$ and Landau coefficient $L = +113 \times 10^{-5} > 0$. The governing system is integrated over a spatial domain of length $\mathcal{D} = 200$. For the computation of spatio-temporal dynamics the overall time window here considered is $t \in [0, 1.5 \times 10^4]$.

The bifurcation diagram obtained in the supercritical regime is depicted in Fig.2.1, where solid red (dashed black) lines are representative of stable (unstable) branches. In agreement with theoretical predictions (see Table 2.1), it consists of a primary branch ($n = 0$) and several secondary branches (the cases $n = 1, 2, 3$ are here shown). The primary branch bifurcates supercritically at $B_{e,0}$ giving rise to two stable branches for $B > B_{e,0}$. The secondary branches originate from the conductive state at $B_{e,n}$ and, for $n > 1$, undergo $(n-1)$ unstable (pitchfork) bifurcations, namely $B_{n,i}$ $\forall i = 1, \ldots, n-1$, until they re-stabilize at the Eckhaus threshold $B_{E,n}$. The bifurcation diagram is computed for different values of inertial times achieving the same result, as expected from the theoretical analysis.

The numerically-computed values of the existence and Eckhaus thresholds are summarized in Table 2.4 and compared to the theoretical ones given in Table 2.1. As it can be noticed, the resulting agreement between them is satisfying for all the investigated branches. The agreement gets slightly worse for higher-order branches, as the dimensionless distance from the Turing threshold ϵ^2 increases, as expected from weakly nonlinear approximation. It should be also remarked that the following inequalities on existence and Eckhaus thresholds, $B_{e,n} > B_{e,n-1}$ and $B_{E,n+1} > B_{E,n}$, hold for any $n \geq 1$.

In order to check the validity of the bifurcation diagram and, in turn, to confirm the theoretical predictions carried out, let us now integrate numerically the governing systems by varying the control parameter B. In all simulations, the initial condition is assumed to take the form given by $(2.7)_2$ and (B.12), where the pattern amplitude is taken as a small perturbation of the stationary value for each considered branch $\Omega_n = \sqrt{\zeta - Q_n^2} e^{iQ_n x}$, in line with eqs.(2.19),(2.21). Results are shown in Fig.2.2.

Zero-flux boundary conditions impose that only integer values of the wavenumber

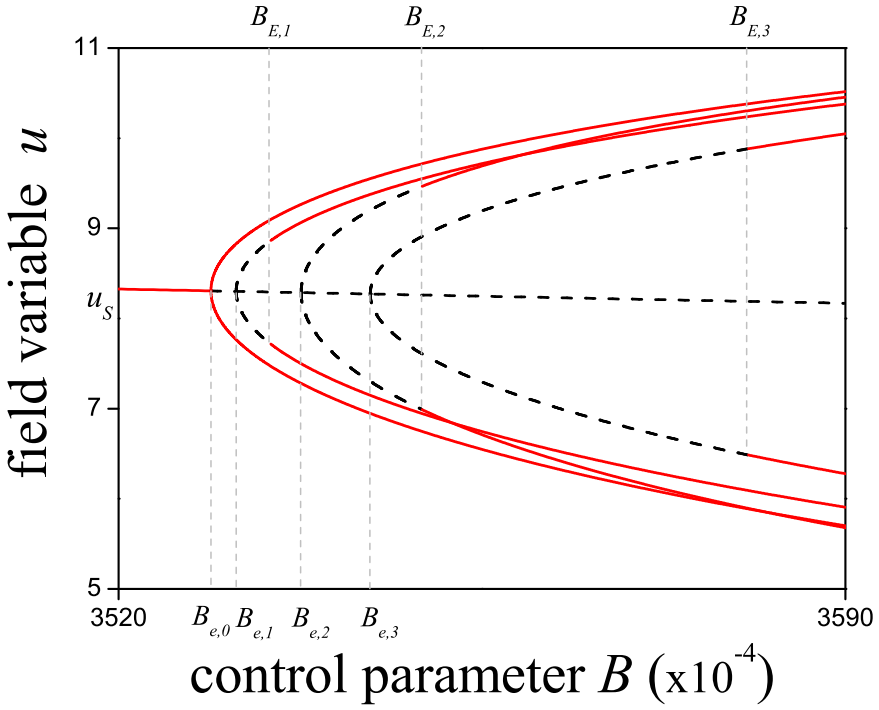

Figure 2.1: Bifurcation diagram in the supercritical regime. Solid red (dashed black) lines represent stable (unstable) stationary branches. Existence $B_{e,n}$ and Eckhaus $B_{E,n}$ thresholds are indicated in the bottom and in the top part of the figure, respectively.

Branch	$\tilde{k}$	***BP***	***theoretical*** $\times 10^{-4}$	***numerical*** $\times 10^{-4}$	ϵ^2
Ω_0		$B_{e,0}$	3529	3529	$1,1 \times 10^{-4}$
Ω_1		$B_{e,1}$	3531	3531	$7,1 \times 10^{-4}$
	1	$B_{E,1}$	3534	3535	$1,8 \times 10^{-3}$
Ω_2		$B_{e,2}$	3537	3538	$2,7 \times 10^{-3}$
	2	$B_{2,2}$	3544	3543	$4,1 \times 10^{-3}$
	1	$B_{E,2}$	3553	3550	$6,1 \times 10^{-3}$
Ω_3		$B_{e,3}$	3545	3544	$4,4 \times 10^{-3}$
	3	$B_{3,3}$	3552	3554	$7,2 \times 10^{-3}$
	2	$B_{3,2}$	3566	3570	$1,2 \times 10^{-2}$
	1	$B_{E,3}$	3574	3580	$1,5 \times 10^{-2}$

Table 2.4: Comparison between theoretically-estimated and numerically-computed bifurcation points for the first four periodic branches characterizing the supercritical regime. The quantity ϵ^2 represents the dimensionless distance from Turing threshold.

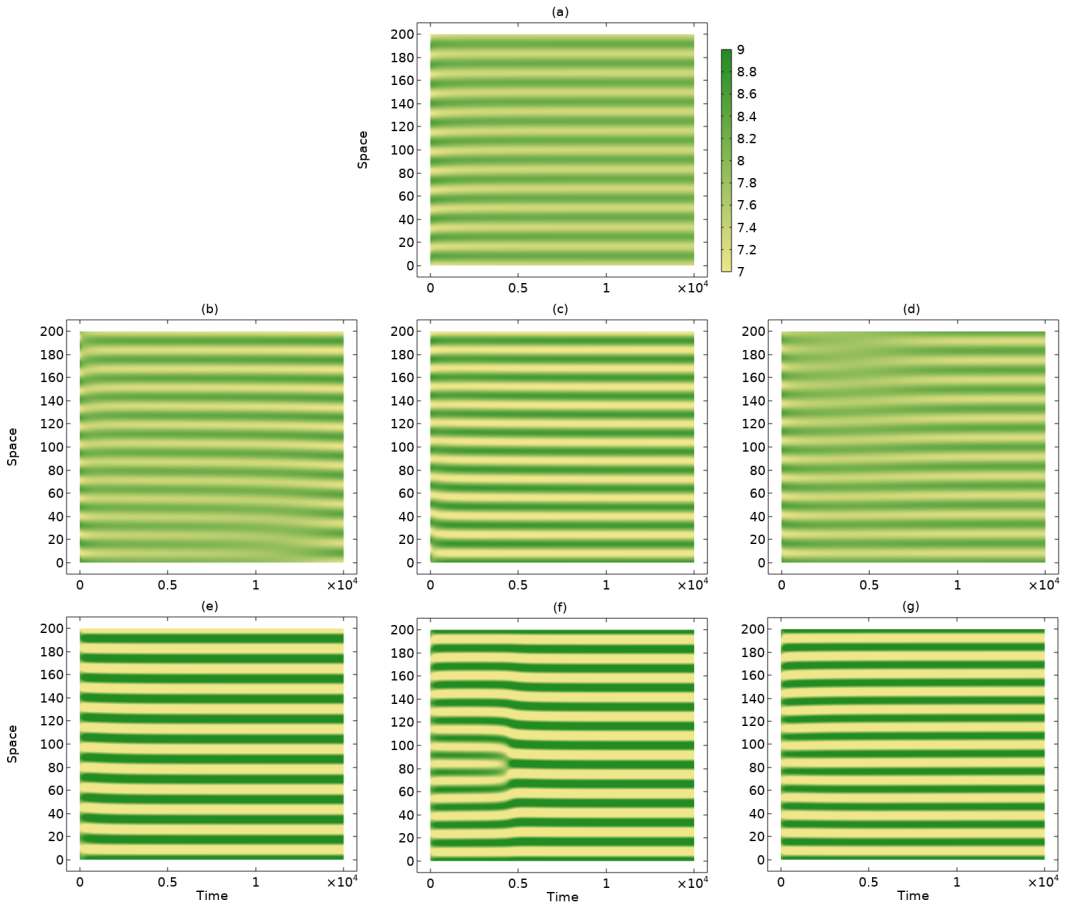

Figure 2.2: Spatio-temporal evolution of supercritical pattern dynamics obtained integrating numerically the hyperbolic modified Klausmeier model with the following parameter set: $\mathcal{D} = 200$, $A = 2.8$, $d = 10^3$, $\tau^u = \tau^w = 10^{-2}$. In the figures, the control parameter B is varied as follows: (a) $B > B_{e,0}$, (b) $B_{e,1} < B < B_{E,1}$, (c) $B > B_{E,1}$, (d) $B_{e,2} < B < B_{E,2}$, (e) $B > B_{E,2}$, (f) $B_{e,3} < B < B_{E,3}$ and (g) $B > B_{E,3}$. The different initial conditions here used are specified in the main text.

are allowed. Therefore, the system will only support periodic patterns whose overall wavenumber $Q_c + Q_n$ are integer. Since $k_c = 0.3814$, according to (2.17), the rescaled value of wavenumber becomes $Q_c = 24.28$ and the closest integer is 24, so that the finite geometry shall select a primary mode with wavenumber $Q_c + Q_0 = 24$. Considering that $\pi(Q_c + Q_0)/\mathcal{D} = 2\pi/\Lambda$, with Λ the pattern wavelength, the whole computational domain $\mathcal{D}$ shall thus accommodate 12Λ. Indeed, by choosing a value $B > B_{e,0}$, starting from a small perturbation of the branch Ω_0, the confirmation of the stability of the primary branch is achieved, as can be seen from Fig.2.2(a). Analogously, starting from $B_{e,1} < B < B_{E,1}$ and setting as initial condition a small perturbation of the branch Ω_1, the system undergoes a phase slip, during which the number of wavelengths is reduced, and finally it converges towards the stable Ω_0 branch (Fig.2.2(b)). On the contrary, by leaving the previous initial condition

unchanged, if the control parameter is set just above the Eckhaus threshold, i.e. $B > B_{E,1}$, the system now stabilizes along the stable branch Ω_1. In this latter case, in fact, the next closest integer is 25, so the finite geometry shall select a mode with wavenumber $Q_c + Q_1 = 25$ that corresponds to $\mathcal{D} = 12.5\Lambda$ (see Fig.2.2(c)). Similar conclusions can be drawn for higher-order branches. In detail, Fig.2.2(d) represents the evolution from a small perturbation of the branch Ω_2 (characterized by $Q_c + Q_2 = 23$ and $\mathcal{D} = 11.5\Lambda$) by using $B_{e,2} < B < B_{E,2}$. Indeed, in this range of the control parameter, the initial branch is unstable, so the system converges to the stable branch Ω_0 and a phase slip at the boundary of the domain occurs. Instead, if the value of the control parameter is slightly increased to overcome Eckhaus threshold, $B > B_{E,2}$, the branch Ω_2 now stabilizes (see Fig.2.2(e)). Finally, the last two figures correspond to simulations where the initial conditions are set as small perturbations of branch Ω_3 with control parameter slightly smaller ($B_{e,3} < B < B_{E,3}$, Fig.2.2(f)) or larger ($B > B_{E,3}$, Fig.2.2(g)) than the Eckhaus threshold of the corresponding branch. As can be seen, in the former case, the initial branch is unstable and system experiences a transition towards the stable Ω_0 branch whereas, in the latter case, the system stabilizes along the branch Ω_3, consistently with theoretical predictions.

2.3.2 Subcritical regime

Numerical investigations carried out in the subcritical regime make use of the following parameters: water-to-plant diffusion ratio $d = 10^3$ and rainfall $A = 0.02$. These parameters provide a critical value of plant loss $B_c = 9.378 \times 10^{-3}$, critical wavenumber $k_c = 5.62 \times 10^{-2}$ and Landau coefficient $L = -5.69 \times 10^{-5} < 0$. As can be noticed, the much smaller value of critical wavenumber suggests that the excited wavelengths are much larger than those observed in the supercritical regime, consistently with previous results [76]. For this reason, the computational domain has been enlarged to $\mathcal{D} = 10^3$. Moreover, since subcritical pattern dynamics are expected to occur over much longer timescales, the spatio-temporal evolution is observed over a wider time window $t \in [0, 2 \times 10^5]$.

Two main considerations can be drawn from the bifurcation diagram obtained in the subcritical regime, shown in Fig.2.3. First, the primary branch undergoes a subcritical bifurcation at B_0 (corresponding to $\zeta = Q_0^2$) where two unstable periodic branches originate from the conductive states, become stable at the Eckhaus threshold $B_{E,0} < B_0$ and still survive for $B > B_0$ ($\zeta > Q_0^2$). Second, the secondary branches ($n \geq 1$) undergo a restabilizing bifurcation for $B_{E,n} > B_n$ ($\zeta_{E,n} > \zeta_n$).

Therefore, two striking features appear markedly in contrast with the analysis developed in the framework of CRGL equation: the existence of periodic solutions beyond the predicted threshold and the occurrence of restabilizing bifurcations for higher order branches too. Evidently, WNA previosly developed fails to describe this phenomenon as it is based on the assumption that pattern amplitude behaves as $O(\epsilon)$ close to onset. The approach based on CRGL equation appears to be, thus, not suitable to predict the occurrence of restabilizing bifurcations at large amplitudes, whose description requires WNA nonlinear expansion to be pushed forward to higher orders.

The features exhibited by the bifurcation diagram in Fig.2.3 are, indeed, fully

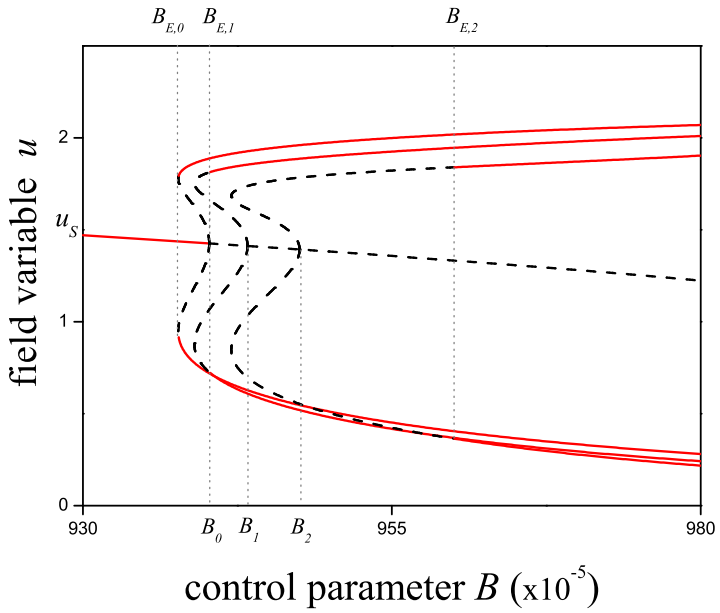

Figure 2.3: Diagram of the first three subcritical bifurcating branches. The bifurcation points of the conductive branch B_n are indicated in the bottom part of the figure, whereas the Eckhaus thresholds $B_{E,n}$ are shown in the top part.

compatible with results obtained in the framework of CQRGL equation (summarized in Table 2.3). Several considerations may be addressed on this point. First of all, the occurrence of EI on the primary branch at $\zeta_{E,0} < Q_0^2$ confirms that the numerically-computed value of the coefficient $\widetilde{R}$ is negative and fulfills the restriction (2.41). Moreover, the secondary branches originating from the unstable conductive state do exhibit Eckhaus restabilizing bifurcations for values of the control parameter larger than existence threshold, i.e. $B_{E,n} > B_{e,n}$. Furthermore, each n-th order branch undergoes exactly $(n-1)$ secondary unstable bifurcations (as in the supercritical regime), in agreement with the numerical values of the coefficient $\tilde{k}_n^*$ that always fall in the range $n < \tilde{k}_n^* < n+1$.

Let us finally comment that the bifurcation diagram drawn in Fig.2.3 has been computed for different inertial times (by varying them over different order of magnitudes) obtaining identical results, so verifying the independence of existence and Eckhaus thresholds on inertial effects. The theoretical values of Eckhaus threshold of the first three branches originating from the conductive state arising from cubic and quintic analysis are reported in Table 2.5. The previous theoretical values are then compared to the numerical ones, obtaining a satisfying agreement in all cases. Of course, theoretical values deviate away from numerical ones as far as the dimensionless distance from the threshold is increased, as expected from WNA. It should be finally noticed that, in relation to both Figs. 2.1 and 2.3, the fact that the bifurcation points are so close from each other is strictly related to the range of validity of WNA, i.e. not so far from threshold.

Branch	$\tilde{k}_n^*$	***BP***	***theoretical (cubic)*** $\times 10^{-5}$	***theoretical (quintic)*** $\times 10^{-5}$	***numerical*** $\times 10^{-5}$
Ω_0	0.8	$B_{e,0}$	939	938	938
		$B_{E,0}$	938	938	938
		B_0	939	939	940
Ω_1	1.9	$B_{e,1}$	942	939	939
		B_1	942	942	943
		$B_{E,1}$	–	940	940
Ω_2	2.4	$B_{e,2}$	945	941	942
		B_2	945	945	947
		$B_{2,2}$	–	948	957
		$B_{E,2}$	–	949	960

Table 2.5: Comparison between theoretically-estimated and numerically-computed bifurcation points for the first three periodic branches characterizing the subcritical regime.

Let us now inspect the spatio-temporal evolution of patterns resulting from variation of the control parameter B along the different branches characterizing the bifurcation diagram of Fig.2.3. To achieve this goal, the governing system is integrated numerically by using the same boundary and initial conditions as the ones adopted in the supercritical regime. Results of this analysis are shown in Fig.2.4. According to the previous values of critical parameters together with the scaling of variables (2.33), the dimensionless value of critical wavenumber becomes $Q_c = 17.89$. Therefore, the finite geometry shall select a primary mode with wavenumber $Q_c + Q_0 = 18$, i.e. the computational domain shall accommodate $\mathcal{D} = 9\Lambda$. Indeed, by choosing a value $B_{E,0} < B < B_0$, starting from a small perturbation of the branch Ω_0, the primary branch results to be stable even for values of the control parameter smaller than the primary bifurcation threshold, so confirming the subcritical character (see Fig.2.4(a)). Let us now set the initial condition as a small perturbation of the branch Ω_1, which is characterized by $Q_c + Q_1 = 17$ and $\mathcal{D} = 8.5\Lambda$, and choose a control parameter which falls into the range $B_1 < B < B_{E,1}$ or $B_{E,1} < B < B_2$, i.e. respectively slightly below or above the Eckhaus threshold of the first secondary branch (predicted by quintic GL equation). Results reveal that, in the former case, the system undergoes a phase slip and finally converges towards the stable Ω_0 branch (see Fig.2.4(b)). In the latter case, the system remains on the stable Ω_1 branch, proving the occurrence of a restabilizing bifurcation (see Fig.2.4(c)). The instability of the last secondary branch for values smaller than Eckhaus threshold can be proved by setting the initial condition as a small perturbation of Ω_2 ($Q_c + Q_2 = 19$ and $\mathcal{D} = 9.5\Lambda$) and choosing $B_2 < B < B_{E,2}$. As shown in Fig.2.4(d), the system selects a different wavelength and stabilizes along the stable Ω_0 branch. On the contrary, if the control parameter is chosen in such a way that $B > B_{E,2}$, no phase slips occurs and the system stabilizes on the Ω_2 branch, as depicted in Fig.2.4(e). In all cases, results agree with theoretical predictions developed in previous sections.

Let us finally comment that all the simulations reported in this section have been obtained by integrating numerically the hyperbolic model by using $\tau^w = 10^{-2}$ and $\tau^u = 0.9$, that represent a good approximation of the behavior close to the parabolic limit in the subcritical regime. In the next section, the behavior far away from the parabolic limit is explored in more detail.

2.3.3 Spatio-temporal dependence of phase slip

Let us characterize more deeply the phenomenon of phase slip taking place during Eckhaus-driven dynamics, with more emphasis on the role played by hyperbolicity.

As previously mentioned [90, 96, 105, 106], a phase slip may be defined as a solution of the GL equation whose zeros of the pattern amplitude $|\Omega(x,t)|$ vary as a function of space and time. Let us call t_{slip} and x_{slip}, respectively, the first time instant and the spatial location at which such an event takes place. Due to the impossibility to predict these values theoretically, ad-hoc numerical investigations are performed with the twofold aim of: (i) elucidating how inertial times may affect this phenomenon in the supercritical and subcritical regimes and (ii) establishing strategies to control these quantities independently of each other.

Let us now investigate how the time and the space at which phase slip takes place depend on the model parameters and the initial conditions. In this context it will

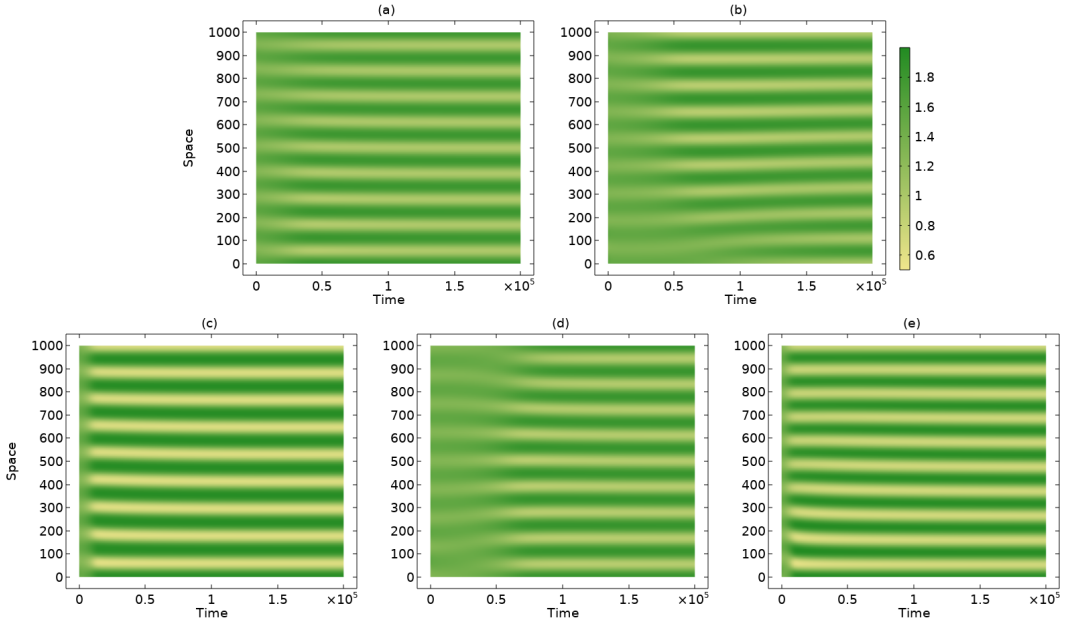

Figure 2.4: Spatio-temporal evolution of subcritical pattern dynamics obtained integrating numerically the hyperbolic Klausmeier model (2.1),(2.2) with the following parameter set: $\mathcal{D} = 10^3$, $A = 0.02$, $d = 10^3$, $\tau^w = 10^{-2}$, $\tau^u = 0.9$. The control parameter B is varied as follows: (a) $B_{E,0} < B < B_0$, (b) $B_1 < B < B_{E,1}$, (c) $B_{E,1} < B < B_2$, (d) $B_2 < B < B_{E,2}$ and (e) $B > B_{E,2}$. The different initial conditions here used are specified in the main text.

be emphasized how inertial times represent, effectively, additional degrees of freedom that may be used to enrich the scenario of transient dynamics. Indeed, in the parabolic version of the Klausmeier model [41, 53, 65, 66], the linearized problem giving rise to Turing threshold is completely determined by all model parameters, i.e. A, B and d, as deduced in (2.5),(2.6). These parameters also specify the stationary amplitude of each branch of quantized periodic state. Consequently, no free parameters are available to characterize the evolution of the system during the transient regime. On the contrary, in the hyperbolic extension it is possible to manage two extra parameters, i.e. τ^u and τ^w, that are the inertial times of the involved species and that are always present in any physical system. As shown in the previous sections, changes applied to inertial times do not yield any variation of existence and stability thresholds, but it is expected that they play a relevant role during transient regime.

To this aim, let us integrate numerically the hyperbolic system by fixing the parameters A, B, d and τ^u, and varying the phenomenological coefficient τ^w. In the first set of investigations, the parameters are chosen in such a way dynamics fall into the supercritical regime. In particular, the plant loss is chosen in the range $B_{e,2} < B < B_{E,2}$ and the initial condition is set as small perturbation of the unstable branch Ω_2, so that the system is expected to undergo an Eckhaus-driven transition towards the stable branch Ω_1 (as depicted in Fig.2.2(d)). Results are shown in Fig.2.5 where τ^w is varied from 10^{-2} to 10. It can be noticed that, as the parameter τ^w increases, the phase slip takes place earlier, leaving its spatial location at the edges of the domain unaltered. Moreover, dynamics reported from (e) to (a) represent progressive deviations from the parabolic limit and allow to appreciate how much longer transient regimes may be experienced by varying a single inertial-related parameter.

To describe in more detail the control of the only time to phase slip, let us characterize its functional dependence. From the numerical standpoint, keeping in mind $(2.7)_2$ and (B.12), a useful way to approximate the occurrence of a zero of pattern amplitude consists of searching where and when the current state $\mathbf{U}(x,t)$ crosses the steady-state $\mathbf{U}_S$. To check the validity of the previous statement, let us depict the trajectory followed by the field variables from the initial state $\mathbf{U}_{\text{in}}$ (taken as small perturbation of the unstable Ω_2 branch) towards the stationary patterned state $\mathbf{U}_{\text{end}}$ (stable patterned branch Ω_0). As illustrative examples, the trajectories corresponding to three different values of $\tau^w = 10^{-2}, 10$ and 50 are shown in Fig.2.6(a) for the supercritical regime, whereas those corresponding to $\tau^w = 10^{-2}, 1$ and 10 for the subcritical one are depicted in Fig.2.7(a). It is found that, independently of the value of τ^w, all the trajectories cross the steady homogeneous state $\mathbf{U}_S$ at the same location: $x_{slip} = 84$ in the supercritical regime and $x_{slip} = 276$ in the subcritical one. Such an intersection occurs at longer times as the phenomenological parameter τ^w is reduced, as denoted by the green squares in Fig.2.6(b) and Fig.2.7(b), and consistently with the meaning of inertial time.

The above observations suggest to correlate the time to phase slip t_{slip} with the linear growth rate $\lambda_n^{(1)}$ (see expressions (2.27) and (2.38)). Indeed, once the growth factor is recasted in the original time variables, say $\overline{\lambda_n^{(1)}}$, one argues that it depends linearly on the parameters ν (in the supercritical regime) or $\overline{\nu}$ (in the subcritical one), which both bring the contribution from inertia. Indeed, by plotting the dependence

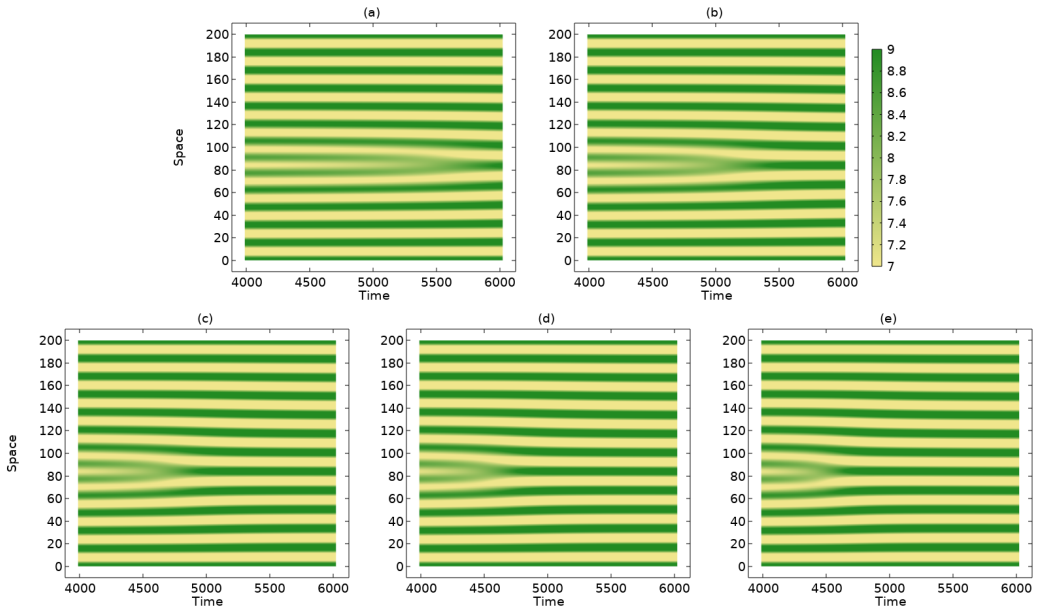

Figure 2.5: Spatio-temporal evolution of patterns deduced from numerical integration of the hyperbolic model. The common parameters are: $\mathcal{D} = 200$, $A = 2.8$, $d = 10^3$, $\tau^u = 10^{-2}$ and $B_{e,2} < B < B_{E,2}$. The parameter τ^w is varied as follows: (a) $\tau^w = 10$, (b) $\tau^w = 7$, (c) $\tau^w = 3$, (d) $\tau^w = 2$ and (e) $\tau^w = 10^{-2}$.

of t_{slip} as a function of $\overline{\lambda_n^{(1)}}$, with $n = 2$, two different linear relationships are retrieved in log-log scale, as depicted in Fig.2.6(c) for the supercritical regime (with adjusted r-squared value $r_a^2 = 0.999$), and in Fig.2.7(c) for the subcritical one ($r_a^2 = 0.995$). These results confirm that the time to phase slip t_{slip}, close to onset, is strictly related to the linear growth rate $\overline{\lambda_n^{(1)}}$ in both dynamical regimes.

Notice that the above analysis is carried out by considering values of inertial times falling either in the ranges $\tau^u < \tau^w$ or $\tau^w < \tau^u$, obtaining the same functional dependence. However, the different signs of the proportionality coefficients deduced in the linear fits indicate that the time to phase slip is negatively correlated with the linear growth rate in the supercritical regime [104], i.e. $t_{slip} \lessapprox \left(\overline{\lambda_2^{(1)}}\right)^{-\frac{1}{2}}$, whereas it is positively correlated in the subcritical one [96], i.e. $t_{slip} \lessapprox \left(\overline{\lambda_2^{(1)}}\right)^{\frac{1}{2}}$.

Results described so far pointed out that the time at which phase slip occurs may be controlled by the linear growth rate, leaving the location unchanged. Let us now inspect whether it is possible to find a strategy to get the opposite scenario, namely the possibility to modulate the location x_{slip} at which wavelength adjustment takes place leaving the time to phase slip unaltered. To this aim, since perfectly-periodic initial conditions may represent an idealization of reality, let us consider an ecologically-realistic scenario where a defect, localized at $x \equiv x_{def}$ with amplitude a, is present in the initial data, as shown schematically in Fig.2.8(a). Let us then build the scatterplots representative of location x_{slip} to phase slip as a function of

defect position x_{def}, obtained for $a = 50$. Results shown in Fig. 2.8(b) reveal that the spatial location of phase slip can be modulated linearly ($r_a^2 = 0.999$) by varying the defect position, leaving the time to phase slip almost unchanged. To confirm the above statements, in Fig.2.9 some examples of spatio-temporal evolution of patterns obtained for three different locations of a large defect are depicted. As it can be noticed, the time to phase slip is kept almost fixed at $t \simeq 350$.

Therefore, the numerical investigations here proposed suggest different strategies to control, separately, the time and the spatial location at which phase slip takes place.

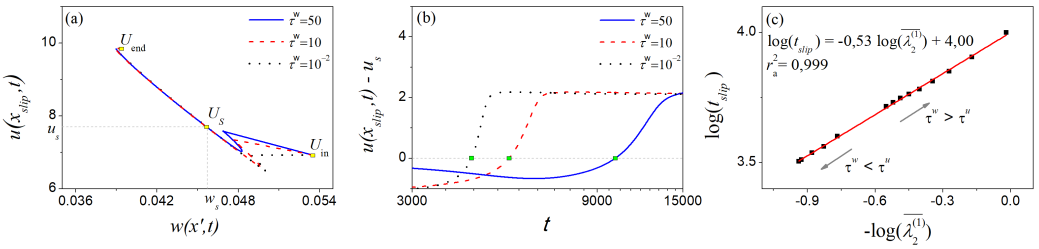

Figure 2.6: (a,b) Numerically-computed trajectories $u(x_{slip}, t)$ corresponding to supercritical dynamics from a small perturbation of the unstable Ω_2 branch ($\mathbf{U}_{\text{in}}$) towards the stable patterned Ω_0 branch ($\mathbf{U}_{\text{end}}$), crossing the homogeneous state $\mathbf{U}_S$. Fixed parameters: $B_{e,2} < B < B_{E,2}$, $d = 10^3$, $A = 2.8$ and $\tau^u = 10^{-2}$. Variables: $\tau^w = 50$ (solid blue line), $\tau^w = 10$ (dashed red line) and $\tau^w = 10^{-2}$ (dotted black line). In (b), green squares represent the time at which phase slip occurs. (c) Plot of $log(\text{t}_{slip})$ as a function of $-log(\overline{\lambda_2^{(1)}})$. Black squares represent results of numerical simulations for different value of τ^w, the solid red line denotes the linear fit.

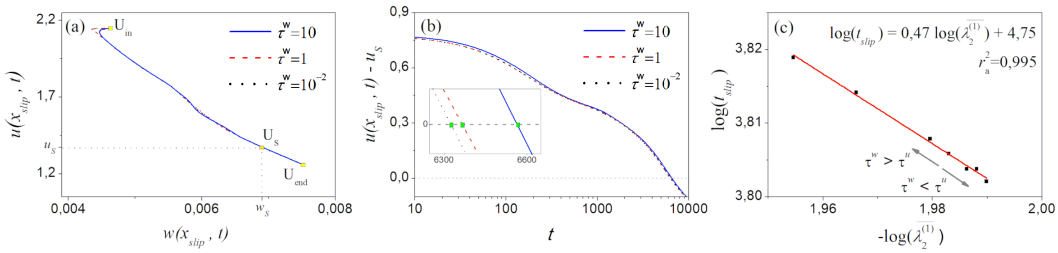

Figure 2.7: Panels, lines and symbols have the same meaning as in Fig.2.6, but dynamics falls into subcritical regime. Fixed parameters: $B_2 < B < B_{E,2}$, $d = 10^3$, $A = 0.02$ and $\tau^u = 0.9$. Variables: $\tau^w = 10$, $\tau^w = 1$ and $\tau^w = 10^{-2}$.

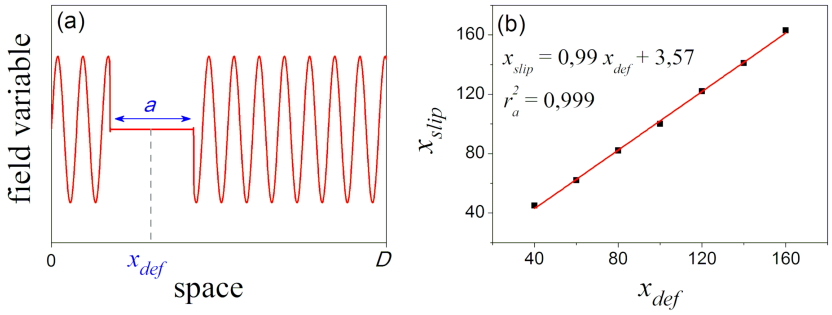

Figure 2.8: The control of the spatial location of phase slip. (a) Schematics of the initial conditions, where x_{def} denotes the location of a defect and a its amplitude. (b) Scatterplot representative of the relationship $x_{slip}\left(x_{def}\right)$, where black square symbols represent results of numerical simulations, and the red solid line is the computed best linear fit. The amplitude of the defect is set to $a = 50$.

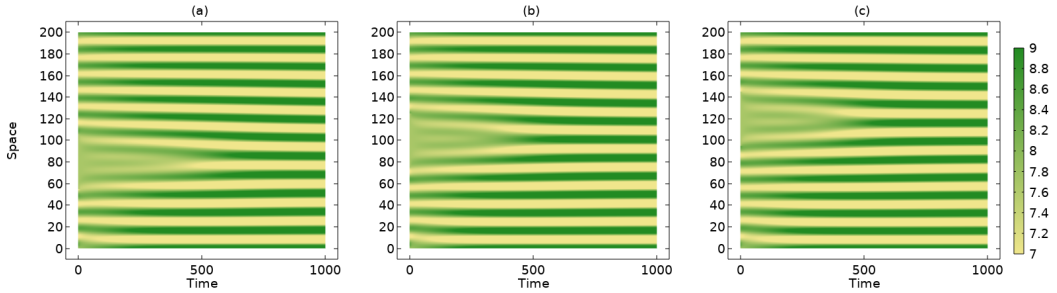

Figure 2.9: Spatiotemporal evolution of patterns with a localized defect in the initial conditions. Parameters are: $\mathcal{D} = 200$, $A = 2.8$, $d = 10^3$, $B_{e,2} < B < B_{E,2}$, $\tau^u = \tau^w = 10^{-2}$, $a = 50$ and (a) $x_{def} = 80$ (b) $x_{def} = 100$ (c) $x_{def} = 120$.

2.4 Concluding remarks

In this chapter, a theoretical study on the EI of stationary patterns in hyperbolic RT systems over large finite domains was addressed in the supercritical and subcritical regimes. To this aim, LSA and WNA were first addressed to deduce the equations governing the pattern amplitude close to criticality. Then, the bifurcation analysis of the EI was carried out to describe existence and stability thresholds of all bifurcating branches. Finally, the above analytical predictions were validated by comparison with results of numerical simulations performed on a model of interest in dryland ecology, the modified Klausmeier model, where stationary vegetation patterns emerge over flat arid terrains. These numerical investigations also allowed to get some insights into the phenomenon of phase-slip.

The main results can be summarized as follows:

(i) It was shown that, while the CRGL equation (2.13) describes satisfactorily well the features associated to primary and secondary branches of periodic solutions in the *supercritical* regime, it is not able to predict the proper range of existence of such

periodic solutions as well as the restabilizing mechanism that n-th order secondary branches, with $n \geq 1$, undergo in the *subcritical* regime. The above restrictions were overcome by pushing WNA up to the fifth order, where the resulting envelope equation takes the form of CQRGL equation (2.16). To achieve this goal, it was necessary to deduce the explicit expressions of the main properties of primary and secondary quantized periodic branches (stationary amplitude Ξ_n, existence $\zeta_{e,n}$ and stability $\zeta_{E,n}$ thresholds, linear growth rate $\overline{\lambda_n^{(1)}}$) characterizing the bifurcation diagram in the subcritical regime in the framework of CQRGL equation. All these quantities were collected in Tables 2.1–2.3. This approach provided the complete description of all ($n \geq 0$) periodic branches appearing in the bifurcation diagram of subcritical modes, as can be noticed from the comparative theoretical-numerical results reported in Tables 2.4 and 2.5.

(ii) From the inspection of numerically-computed bifurcation diagrams (see Figs.2.1, 2.3) and spatio-temporal evolution of patterns (see Figs.2.2, 2.4), it was obtained the twofold goal of: validating the theoretical predictions arising from multiple-scale WNA and elucidating the role played by inertial effects that are always present in any physical system. From the theoretical viewpoint, in particular, it was shown that hyperbolicity affects the expression of the linear growth rate but leaves the other quantities (stationary amplitude, existence and stability thresholds) unchanged. This result suggested that the hyperbolic model provides additional degrees of freedom that may be used to better characterize transient regimes, in particular the transition from an Eckhaus-unstable state towards a more favorable stable configuration through sequences of phase-slips.

(iii) The functional dependence of time and location at which wavelength adjustment takes place is investigated numerically with the main goal of finding strategies to control these quantities independently of each other. Results revealed that the *time to phase slip* may be modulated by varying the inertial times leaving its location unaltered. Moreover, it was shown that t_{slip} strongly depends upon the linear growth rate $\overline{\lambda_n^{(1)}}$, in both dynamical regimes (as depicted in Figs.2.6 and 2.7). In particular, results indicate that t_{slip} and $\overline{\lambda_n^{(1)}}$ are negatively correlated in the supercritical regime but positively in the subcritical one. On the other hand, it was numerically shown that, by considering a localized defect into the initial conditions, it is possible to modulate the location to phase slip leaving the time to phase slip almost unchanged (see Figs.2.8 and 2.9).

Chapter 3

Oscillatory patterns in 1D hyperbolic RT systems

In this chapter, the oscillatory behavior of patterned dynamics in one-dimensional domain is studied by means of hyperbolic RT models.

In the first section, a quite general class of two-compartment 1D hyperbolic RT systems (1.8)-(1.9) where both species undergo self-diffusion and only one undergoes advection ($\psi = 0$) is considered with the main aim of elucidating the role played by inertial effects in oscillatory periodic patterns. To this aim, LSA techniques are used to deduce the conditions under which wave (or oscillatory Turing) instability takes place. Then, WNA is applied to determine the equation which rules the spatio-temporal evolution of pattern amplitude close to criticality.

Then, the focus is moved to the study of an alternative class of two-compartment 1D hyperbolic RT systems (1.8)-(1.9) in which both species undergo advection and only one undergoes self-diffusion ($d = 0$). In this case, LSA is carried out to inspect the dependence of the wave instability locus on the model parameters, with particular emphasis on the role played by the combined effect of inertial time and the advection speeds. Periodic travelling wave solutions are also taken into account to better characterize modulus and direction of the migration speed of oscillatory periodic patterns. Theoretical predictions are corroborated by numerical investigations carried out in hyperbolic extensions of the classical Klausmeier model and ecological implications are also discussed. Finally, it is highlighted how the hyperbolic nature of the model may provide possible interpretations about some ecological controversial field observations.

3.1 Two-compartment systems with two self-diffusion terms and one advection term

The occurrence of travelling patterns in two-compartment 1D hyperbolic RT systems (1.8)-(1.9) where both species undergo diffusion and only one undergoes advection ($\psi = 0$) is here theoretically investigated.

Under the above-mentioned hypotheses, the class of hyperbolic RT systems (1.8)-(1.9) reads:

$$\mathbf{U}_t + \mathrm{M}\mathbf{U}_x = \mathbf{N}(\mathbf{U}, B), \tag{3.1}$$

being:

$$\mathbf{U} = \begin{bmatrix} u \\ w \\ J^u \\ J^w \end{bmatrix}, \quad \mathrm{M} = \begin{bmatrix} 0 & 0 & 1 & 0 \\ 0 & -\nu & 0 & 1 \\ \frac{1}{\tau^u} & 0 & 0 & 0 \\ 0 & \frac{d}{\tau^w} & 0 & 0 \end{bmatrix}, \quad \mathbf{N}(\mathbf{U}, B) = \begin{bmatrix} f(u,w,B) \\ g(u,w,B) \\ -\frac{J^u}{\tau^u} \\ -\frac{J^w}{\tau^w} \end{bmatrix}. \tag{3.2}$$

3.1.1 LSA

Let $\mathbf{U}^* = (u^*, v^*, 0, 0)$ be a positive spatially-homogeneous steady-state satisfying $\mathbf{N}(\mathbf{U}, B) = \mathbf{0}$. By looking for solutions of system (3.1)-(3.2) of the form $\mathbf{U} = \mathbf{U}^* + \widehat{\mathbf{U}} \exp(\omega t + \mathrm{i}\, k\, x)$, the following dispersion relation, which gives the growth factor ω as a function of the wavenumber k, is derived:

$$\begin{aligned} \tau^u\tau^w\omega^4 + \left(\widetilde{A}_3 - ik\nu\tau^u\tau^w\right)\omega^3 + \left(\widehat{A}_2 k^2 + \widetilde{A}_2 + ik\nu\widehat{b}_2\right)\omega^2 + \\ + \left[\widehat{A}_1 k^2 + \widetilde{A}_1 + ik\nu\left(\widehat{b}_1 - \tau^w k^2\right)\right]\omega + \widetilde{A}_0 + ik\nu\widehat{b}_0 = 0 \end{aligned} \tag{3.3}$$

with

$$\begin{aligned} \widetilde{A}_3 &= \tau^u + \tau^w - \left(f_u^* + g_w^*\right)\tau^u\tau^w \\ \widehat{A}_2 &= d\tau^u + \tau^w \\ \widetilde{A}_2 &= 1 - \left(\tau^u + \tau^w\right)\left(f_u^* + g_w^*\right) + \tau^u\tau^w\left(f_u^* g_w^* - f_w^* g_u^*\right) \\ \widehat{b}_2 &= \tau^u\tau^w f_u^* - \tau^u - \tau^w \\ \widehat{A}_1 &= d + 1 - \tau^w g_w^* - d\tau^u f_u^* \\ \widetilde{A}_1 &= \left(\tau^u + \tau^w\right)\left(f_u^* g_w^* - f_w^* g_u^*\right) - \left(f_u^* + g_w^*\right) \\ \widehat{b}_1 &= \left(\tau^u + \tau^w\right) f_u^* - 1 \\ \widetilde{A}_0 &= dk^4 - \left(df_u^* + g_w^*\right)k^2 + f_u^* g_w^* - f_w^* g_u^* \\ \widehat{b}_0 &= f_u^* - k^2 \end{aligned} \tag{3.4}$$

where the asterisk denotes that the function is evaluated at the steady state $\mathbf{U}^*$.

It is straightforward to ascertain that, for the homogeneous perturbation $k = 0$, the equation (3.3) can be easily factorized and its solutions are:

$$\begin{aligned} \omega_1 = -\tfrac{1}{\tau^u} < 0, \quad \omega_2 = -\tfrac{1}{\tau^w} < 0 \\ \omega_{3,4} = \tfrac{1}{2}\left(f_u^* + g_w^* \pm \sqrt{\left(f_u^* + g_w^*\right)^2 - 4\left(f_u^* g_w^* - f_w^* g_u^*\right)}\right). \end{aligned} \tag{3.5}$$

Therefore $\mathbf{U}^*$ is stable with respect homogeneous perturbation iff

$$f_u^* + g_w^* < 0, \quad f_u^* g_w^* - f_w^* g_u^* > 0. \tag{3.6}$$

As far as non-homogeneous perturbations are concerned, it can be noticed that a non-vanishing advection term ($\nu \neq 0$) prevents the occurrence of Turing instability, because it doesn't exist a value $k \neq 0$ that makes the real and imaginary part of the quantity $\widetilde{A}_0 + ik\nu\widehat{b}_0$ simultaneously null. Therefore, the attention is focused on the occurrence of wave instability as a control parameter, say B, is varied. To this aim, let us look for solutions of the characteristic equation (3.3) having null real part for some $k \neq 0$ and require the transition from negative to positive real part to occur via a maximum. More precisely, it is assumed $\omega = -isk$, with $s = s(k) \in \mathbb{R}$, so that any perturbation can be recast in the form of a travelling wave with speed s, i.e. $\widehat{\mathbf{U}} \exp\left[\mathrm{i}\, k\,(x - st)\right]$. Then, by substituting the previous ansatz into the characteristic equation and taking the derivative of this latter with respect to k, the following system is obtained:

$$\begin{cases} k^4 - \delta_2 k^2 + \delta_4 = 0 \\ \delta_1 k^2 - \delta_3 = 0 \\ 2k\left(2k^2 - \delta_2\right) + \left(\frac{\partial \delta_4}{\partial s} - \frac{\partial \delta_2}{\partial s} k^2\right)\frac{\partial s}{\partial k} = 0 \\ (\delta_1\delta_2 - 2\delta_3)\left(\delta_1 \frac{\partial \delta_3}{\partial s} - \delta_3 \frac{\partial \delta_1}{\partial s}\right) - \delta_1^2\left(\delta_1 \frac{\partial \delta_4}{\partial s} - \delta_3 \frac{\partial \delta_2}{\partial s}\right) = 0 \end{cases} \tag{3.7}$$

where

$$\begin{aligned} \delta_1 &= \frac{\nu + \widehat{A}_1 s + \nu\widehat{b}_2 s^2 - \widetilde{A}_3 s^3}{\left(\tau^u s^2 - 1\right)\left(\tau^w s^2 + \nu\tau^w s - d\right)}, \\ \delta_2 &= \frac{\widetilde{A}_2 s^2 - \widehat{b}_1 \nu s + d f_u^* + g_w^*}{\left(\tau^u s^2 - 1\right)\left(\tau^w s^2 + \nu\tau^w s - d\right)}, \\ \delta_3 &= \frac{\nu f_u^* - \widetilde{A}_1 s}{\left(\tau^u s^2 - 1\right)\left(\tau^w s^2 + \nu\tau^w s - d\right)}, \\ \delta_4 &= \frac{\left(f_u^* g_w^* - f_w^* g_u^*\right)}{\left(\tau^u s^2 - 1\right)\left(\tau^w s^2 + \nu\tau^w s - d\right)}. \end{aligned} \tag{3.8}$$

System (3.7) defines implicitly the critical value B_c of the control parameter at which wave instability develops, together with the critical wavenumber k_c, the wave speed s and its derivative with respect to the wavenumber $\partial s/\partial k$. Therefore, the presence of inertia affects not only the instability threshold but also the wavenumber of the emerging pattern. This result differs from what was observed in the case of pure stationary Turing patterns, where hyperbolicity does not affect such quantities but plays an active role during transient regime [76, 77].

For comparison, results of wave instability in the case of parabolic models are discussed in Appendix C.

3.1.2 WNA

As it is well known, LSA is only valid for small times and infinitesimal perturbations. For this reason, the transition to the new spatially nonuniform state is usually investigated by means of WNA which, by using a standard perturbative approach, provides an approximate analytical description of the perturbation dynamics. Here, the multiple scale method is employed to derive the amplitude equation describing the dynamics close to the critical bifurcation parameter B_c at which instability develops [5, 6, 15, 16, 58, 76, 81, 110, 111].

By using

$$\overline{\mathbf{U}} = \mathbf{U} - \mathbf{U}^* \tag{3.9}$$

$$L^* = (\nabla \mathbf{N})^* \tag{3.10}$$

$$\mathbf{N}\mathbf{L}^* = \sum_{k\geq 2} \frac{1}{k!} \left[\left(\overline{\mathbf{U}} \cdot \nabla \right)^{(k)} \mathbf{N} \right]^* \tag{3.11}$$

where ∇ and $(\mathbf{V} \cdot \nabla)^{(j)}$ are defined as in Section 2.1, system (3.1) can be cast in the following form

$$\overline{\mathbf{U}}_t + M\overline{\mathbf{U}}_x = L^*\overline{\mathbf{U}} + \mathbf{N}\mathbf{L}^*. \tag{3.12}$$

The field vector $\overline{\mathbf{U}}$ and the control parameter B are expanded with respect to a small positive parameter $\varepsilon \ll 1$; moreover, two time and spatial scales are introduced as follows:

$$\begin{gathered} \overline{\mathbf{U}} = \varepsilon\overline{\mathbf{U}}_1 + \varepsilon^2\overline{\mathbf{U}}_2 + \varepsilon^3\overline{\mathbf{U}}_3 + O\left(\varepsilon^4\right) \\ B = B_c + \varepsilon^2 B_2 + O\left(\varepsilon^4\right) \\ \frac{\partial}{\partial t} \to \frac{\partial}{\partial t} + \varepsilon^2 \frac{\partial}{\partial T_2} \\ \frac{\partial}{\partial x} \to \frac{\partial}{\partial x} + \varepsilon \frac{\partial}{\partial X} \end{gathered} \tag{3.13}$$

Here, the capital letters denote the slow scale, the lowercase ones represent the fast scale. The use of two spatial scales is justified whenever patterns emerge and propagate over large spatial domains in the form of travelling wavefronts.

Then, substituting all the above expansions into the governing system (3.12) and collecting terms of the same orders of ε, the following set of linear partial differential equations is obtained:

$$\begin{aligned} &\text{at order 1} && \frac{\partial\overline{\mathbf{U}}_1}{\partial t} + \mathrm{M}\frac{\partial\overline{\mathbf{U}}_1}{\partial x} = L_c^*\overline{\mathbf{U}}_1 \\ &\text{at order 2} && \frac{\partial\overline{\mathbf{U}}_2}{\partial t} + \mathrm{M}\frac{\partial\overline{\mathbf{U}}_2}{\partial x} + \mathrm{M}\frac{\partial\overline{\mathbf{U}}_1}{\partial X} = L_c^*\overline{\mathbf{U}}_2 + \tfrac{1}{2}\left(\overline{\mathbf{U}}_1 \cdot \bigtriangledown\right)^{(2)} \mathbf{N}|_c^* \\ &\text{at order 3} && \frac{\partial\overline{\mathbf{U}}_3}{\partial t} + \frac{\partial\overline{\mathbf{U}}_1}{\partial T_2} + \mathrm{M}\frac{\partial\overline{\mathbf{U}}_3}{\partial x} + \mathrm{M}\frac{\partial\overline{\mathbf{U}}_2}{\partial X} = \\ &&& = L_c^*\overline{\mathbf{U}}_3 + B_2 \left.\frac{\mathrm{d}L^*}{\mathrm{d}B}\right|_c \overline{\mathbf{U}}_1 + \left(\overline{\mathbf{U}}_1 \cdot \bigtriangledown\right)\left(\overline{\mathbf{U}}_2 \cdot \bigtriangledown\right)\mathbf{N}|_c^* + \tfrac{1}{6}\left(\overline{\mathbf{U}}_1 \cdot \bigtriangledown\right)^{(3)} \mathbf{N}|_c^* \end{aligned} \tag{3.14}$$

where the subscript "c" denotes that the quantity is evaluated at the critical value of the control parameter. We now look for solutions $\overline{\mathbf{U}}_i = \overline{\mathbf{U}}_i(z)$ with $z = x - st$, so that the system (3.14) can be written as a system of ordinary differential equations:

$$\text{at order 1} \qquad \frac{\mathrm{d}\,\overline{\mathbf{U}}_1}{\mathrm{d}\,z} = K_c^*\overline{\mathbf{U}}_1 \tag{3.15}$$

$$\text{at order 2} \qquad \frac{\mathrm{d}\,\overline{\mathbf{U}}_2}{\mathrm{d}\,z} = K_c^*\overline{\mathbf{U}}_2 + (\mathrm{M} - sI)^{-1}\left\{\frac{1}{2}\left(\overline{\mathbf{U}}_1 \cdot \bigtriangledown\right)^{(2)} \mathbf{N}|_c^* - \mathrm{M}\frac{\partial\overline{\mathbf{U}}_1}{\partial X}\right\} \tag{3.16}$$

$$\begin{aligned} \text{at order 3} \qquad \frac{\mathrm{d}\,\overline{\mathbf{U}}_3}{\mathrm{d}\,z} &= K_c^*\overline{\mathbf{U}}_3 + (\mathrm{M} - sI)^{-1} \times \left\{ B_2\frac{\mathrm{d}L^*}{\mathrm{d}B} + \left|_c\right. \overline{\mathbf{U}}_1 \right. \\ &+ \left(\overline{\mathbf{U}}_1 \cdot \bigtriangledown\right)\left(\overline{\mathbf{U}}_2 \cdot \bigtriangledown\right)\mathbf{N}|_c^* + \frac{1}{6}\left(\overline{\mathbf{U}}_1 \cdot \bigtriangledown\right)^{(3)} \mathbf{N}|_c^* - \frac{\partial\overline{\mathbf{U}}_1}{\partial T_2} - \mathrm{M}\frac{\partial\overline{\mathbf{U}}_2}{\partial X}\Bigg\} \end{aligned} \tag{3.17}$$

where I is the identity matrix and

$$K_c^* = (\mathrm{M} - sI)^{-1} L_c^* \tag{3.18}$$

According to WNA developed in Appendix D, the solutions of systems (3.15) and (3.16), satisfying periodic boundary conditions, can be expressed as:

$$\overline{\mathbf{U}}_1 = \Omega(X, T_2) e^{\mathrm{i}\, k_c z} \mathbf{d}^{(\mathrm{i}\, k_c)} + \overline{\Omega}(X, T_2) e^{-\mathrm{i}\, k_c z} \mathbf{d}^{(-\mathrm{i}\, k_c)} \tag{3.19}$$

$$\overline{\mathbf{U}}_2 = \frac{\partial \Omega}{\partial X} e^{\mathrm{i}\, k_c z} \mathbf{g} + \frac{\partial \overline{\Omega}}{\partial X} e^{-\mathrm{i}\, k_c z} \overline{\mathbf{g}} + \Omega^2 e^{2\,\mathrm{i}\, k_c z} \mathbf{q} + \overline{\Omega}^2 e^{-2\,\mathrm{i}\, k_c z} \overline{\mathbf{q}} + 2\mathbf{q}_0 |\Omega|^2 \tag{3.20}$$

where the complex pattern amplitude $\Omega = \Omega(X, T_2)$ obeys the CCGL equation

$$\frac{\partial \Omega}{\partial T_2} = (\rho_1 + \mathrm{i}\, \rho_2) \frac{\partial^2 \Omega}{\partial X^2} + (\sigma_1 + \mathrm{i}\, \sigma_2)\, \Omega - (L_1 - \mathrm{i}\, L_2)\, \Omega\, |\Omega|^2. \tag{3.21}$$

The coefficients appearing in (3.19)-(3.21) are given in Appendix D.

As known, two different qualitative dynamics of the CCGL equation can be observed: $L_1 > 0$ corresponds to the supercritical bifurcation case while $L_1 < 0$ to the subcritical one. The former exists for above-threshold values of the control parameter only, exhibits a small amplitude close to onset and the wavelength of the excited pattern is close to the critical value $2\pi/k_c$. The latter exists for both below- and above-threshold values, exhibits hysteresis and has a large amplitude at onset such that the WNA may only provide qualitative information on the excited patterns [1, 5, 6].

Remark 1. The CCGL equation (3.21) deduced in the more general framework of hyperbolic systems appears formally unchanged with respect to the classical one deduced in parabolic models [58]. It can be indeed verified that the expressions of the coefficients there appearing may be obtained from the ones appearing in (3.21) by setting the inertial times to zero. Of course, each of these coefficients encloses a dependence on the inertial times which, acting as additional degrees of freedom, offers a richer scenario of spatio-temporal dynamics with respect to the parabolic counterpart, as it will be shown below. □

3.1.2.1 Coherent structure solutions of the CCGL equation

Let us now focus our attention on those solutions of the CCGL equation that are referred to as *coherent structures*, and in particular to the one-parameter family of solutions localized in space characterized by features uniformly translating with a constant velocity v [1, 5, 84, 87, 112–114], i.e:

$$\Omega(X, T_2) = Q(\xi) e^{\mathrm{i}\, \phi(\xi)}, \qquad \xi = X - v T_2 \tag{3.22}$$

Substituting this ansatz into the CCGL equation (3.21) and indicating by $\kappa = \phi_\xi$, we get a system of three ordinary differential equations:

$$\begin{cases} Q_\xi = R \\ \rho_2 Q \kappa_\xi - \rho_1 R_\xi = (v - 2\rho_2 \kappa)\, R + \left(\sigma_1 - \rho_1 \kappa^2\right) Q - L_1 Q^3 \\ \rho_2 R_\xi + \rho_1 Q \kappa_\xi = -2\rho_1 \kappa R + \left(\rho_2 \kappa^2 - \sigma_2 - v\kappa\right) Q - L_2 Q^3 \end{cases} \tag{3.23}$$

The dynamical system (3.23) admits two fixed points in the form $\mathbf{F}^* = (R^*, Q^*, \kappa^*)$ given by: $\mathbf{F}_1^* = (0, 0, \kappa_0)$, with κ_0 an arbitrary constant, and $\mathbf{F}_2^* = \left(0, \widetilde{Q}, \widetilde{\kappa}\right)$, where the constants $\widetilde{Q}$ and $\widetilde{\kappa}$ are defined by:

$$\begin{gathered} \widetilde{Q} = \sqrt{\frac{\sigma_1 - \rho_1 \widetilde{\kappa}^2}{L_1}} \\ (\rho_1 L_2 + \rho_2 L_1)\, \widetilde{\kappa}^2 - v L_1 \widetilde{\kappa} - (\sigma_2 L_1 + \sigma_1 L_2) = 0 \end{gathered} \tag{3.24}$$

The fixed point $\mathbf{F}_1^*$ defines a null-amplitude patterned state $\Omega = 0$ that is representative of the spatially-homogeneous steady state $\mathbf{U}^*$ undergoing the spatially-driven destabilization. On the other hand, the plane-wave solution of the CCGL equation associated to the fixed point $\mathbf{F}_2^*$, i.e.

$$\Omega(X, T_2) = \widetilde{Q} e^{\mathrm{i}\left(\widetilde{\kappa} X + \widetilde{\omega} T_2\right)} \quad \text{with} \quad \widetilde{\omega} = -\widetilde{\kappa} v \tag{3.25}$$

represents a particular case of coherent structure named *phase winding* solution [1, 5, 84, 87, 113] and describes a travelling pattern characterized by a total wavenumber $k_{tot} = k_c + \epsilon \widetilde{\kappa}$ and angular frequency $\omega_{tot} = k_c s - \epsilon^2 \widetilde{\omega}$. If the wave bifurcation is supercritical ($L_1 > 0$), under the assumptions that $\sigma_1 > 0$ and $\rho_1 > 0$, according to $(3.24)_1$, such a solution exists if

$$-\sqrt{\frac{\sigma_1}{\rho_1}} < \widetilde{\kappa} < +\sqrt{\frac{\sigma_1}{\rho_1}} \tag{3.26}$$

so that there is a band of permitted wavenumbers around $\widetilde{\kappa} = 0$ and the second-order correction of the angular frequency takes the form:

$$\widetilde{\omega} = \left[(\sigma_2 L_1 + \sigma_1 L_2) - (\rho_1 L_2 + \rho_2 L_1)\, \widetilde{\kappa}^2\right] / L_1 \tag{3.27}$$

Since we deal with three unknowns ($\widetilde{\kappa}$, $\widetilde{Q}$ and $\widetilde{\omega}$) and two conditions arise from the CCGL equation, one parameter needs to be estimated from numerical simulations. For instance, $\widetilde{\kappa}$ can be deduced by comparing the numerically-computed value of the total wavenumber k_{tot} with the theoretical critical wavenumber k_c, whereas the values of amplitude $\widetilde{Q}$ and angular frequency $\widetilde{\omega}$ can be consequently obtained via $(3.24)_1$ and (3.27), respectively.

To investigate the stability of the phase winding solution, we can proceed, as usual in the literature, by perturbing the amplitude (3.25) as follows:

$$\begin{aligned} \Omega(X, T_2) &= \left[1 + a(X, T_2)\right] \widetilde{Q} e^{\mathrm{i}\left(\widetilde{\kappa} X + \widetilde{\omega} T_2\right)} \\ a(X, T_2) &= \Psi(T_2) e^{\mathrm{i}\, l X} + \overline{\Xi}(T_2) e^{-\mathrm{i}\, l X} \end{aligned} \tag{3.28}$$

where $\overline{\Xi}$ is the complex conjugate of Ξ and l denotes the small perturbation of the wavenumber $\widetilde{\kappa}$, namely we look for long-wave effects. After some algebraic manipulations, we end up with the system:

$$\begin{cases} \Psi_{T_2} = \left[-l\,(l + 2\widetilde{\kappa})\,(\rho_1 + \mathrm{i}\,\rho_2) - \widetilde{Q}^2\,(L_1 - \mathrm{i}\,L_2)\right] \Psi - (L_1 - \mathrm{i}\,L_2)\, \widetilde{Q}^2 \Xi \\ \Xi_{T_2} = \left[-l\,(l - 2\widetilde{\kappa})\,(\rho_1 - \mathrm{i}\,\rho_2) - \widetilde{Q}^2\,(L_1 + \mathrm{i}\,L_2)\right] \Xi - (L_1 + \mathrm{i}\,L_2)\, \widetilde{Q}^2 \Psi \end{cases} \tag{3.29}$$

Then, looking for the usual exponential dependence of Ψ and Ξ on T_2, in the limit of large wavelengths (small l), one retrieves a necessary condition for the stability of plane wave structures, named *Benjamin-Feir-Newell* condition [1, 2, 6, 58, 87], that reads:

$$1 - \frac{\rho_2 L_2}{\rho_1 L_1} > 0. \tag{3.30}$$

Remark 2. It should be finally noticed that all the features characterizing the phase winding solution, i.e. amplitude $\widetilde{Q}$, wavenumber $\widetilde{\kappa}$ and angular frequency $\widetilde{\omega}$, together with its stability, inherit the functional dependence on the inertial times from the coefficients of the CCGL equation (3.21). Therefore, it is expected that hyperbolicity effects may manifest, not only during the transient regime from the homogeneous steady state toward the patterned state (the heteroclinic orbit of (3.23) joining $\mathbf{F}_1^*$ and $\mathbf{F}_2^*$) but also modifying the value of the above-mentioned key features of the phase winding solution and, possibly, its stability. □

3.1.3 An illustrative example: the extended Klausmeier model

Let us take into account the pattern formation process in dryland ecology through the hyperbolic generalization [75–77] of the extended Klausmeier model [46, 58], whose dimensionless 1D version belongs to the class of systems (3.1),(3.2). In this framework, the field variables $u(x,t)$ and $w(x,t)$ and the advection speed ν assume the same meaning of those shown in Section 1.3. In detail, this version of the model accounts for a double mechanism for the motion of surface water. First, the downhill water flow on slopes is accounted by an advection term. Second, dispersal of surface water is mimicked via a diffusion term that aims to capture the movement induced by spatial differences in infiltration rate [46]. The source terms are the same of those depicted in (1.2) and follow the original version provided by Klausmeier [41].

Spatially-homogeneous steady states of model (3.1),(3.2) with Klausmeier kinetics (1.2) and their stability toward spatially-homogeneous perturbations can be achieved as in Section 1.4 and Appendix B, respectively. To prove that the state $\mathbf{U}_S^*$ may be destabilized via non-homogeneous perturbations, and can thus undergo wave instability, we need to solve the system (3.7),(3.8). Unfortunately, owing to its highly nonlinear nature, information on the locus of wave instability, together with the dependence of the critical parameters on the inertial times, cannot be obtained analytically. Therefore, by solving the above system numerically, we found that it admits real solutions representing the values of the control parameter B_c, wavenumber k_c, wave speed s and its derivative with respect to k, at the onset of instability. Results of this investigation are shown in Fig.3.1, where the locus of wave instability depicted in the (B, A) parameter plane (solid lines) is obtained by fixing the parameters $d = 100$ [46, 115] and $\nu = 182.5$ [41] and varying the two inertial times τ^u and τ^w. In the same figure we also represent by circles the locus obtained in the parabolic case, i.e. from the numerical solution of (C.4), which gives real and positive root by taking the plus sign. As it can be noticed, this latter coincides with the locus deduced for very small inertial times (black line), as expected. It is worth noticing that, when the system moves away from the parabolic limit, the locus of wave instability progressively shifts up so enlarging the region where non-stationary patterns may be

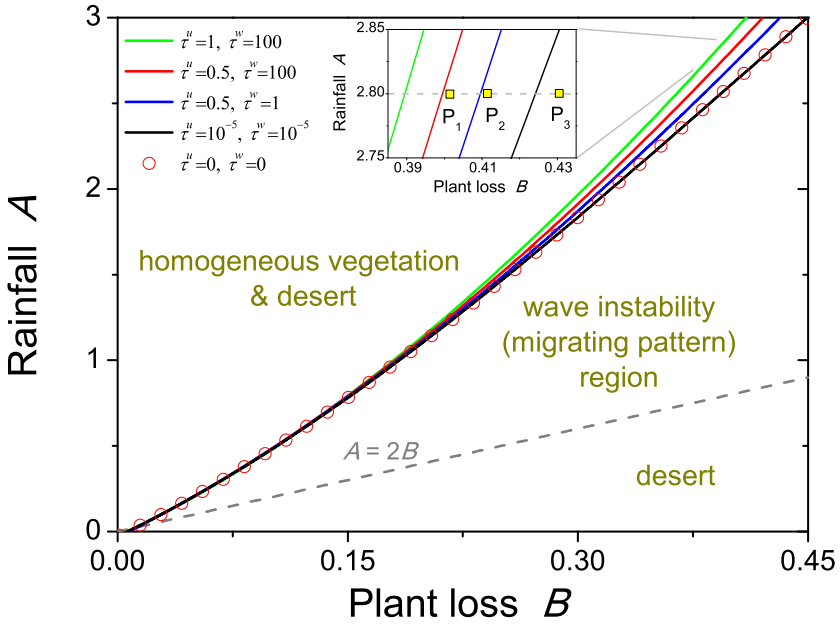

Figure 3.1: Solid lines represent the loci of wave instability in the (B, A) parameter plane obtained by solving numerically the system (3.7),(3.8) for different values of inertial times. Symbols denote the locus obtained in the parabolic case, resulting from integration of equation (C.4). The bottom dashed line defines the condition $A = 2B$, below which the only desert state exists. Fixed parameters: $d = 100$ and $\nu = 182.5$.

observed. This is consistent with previous results obtained for the hyperbolic generalization of the original Klausmeier model, so confirming that the hyperbolicity destabilizes the system and allows to observe oscillatory periodic patterns, i.e. uphill migrating banded vegetation in the context of dryland ecology, over a wider region of the parameter plane [75].

A first check on the validity of these analytical predictions has been carried out by inspecting the wavenumber dependence of the four roots of the characteristic polynomial (3.3) at the three points P_1, P_2 and P_3 indicated in the inset of Fig.3.1, for different couples of inertial times. Results are shown in Fig.3.2 (top row panels (a)-(c) correspond to P_1, middle row panels (d)-(f) to P_2 and bottom row panels (g)-(i) to P_3) for the largest eigenvalue only (being the real part of the other three roots always negative). For brevity, we refer to the couple $(\tau^u, \tau^w) = \left(10^{-5}, 10^{-5}\right)$ (whose corresponding locus is the black curve in Fig.3.1) as setup I; the couple $(0.5, 1)$ as setup II (blue curve in Fig.3.1) and $(0.5, 100)$ as setup III (red curve in Fig.3.1). Setup I is representative of the behavior close to the parabolic limit, while setups II and III mimic dynamics that progressively deviate away from it.

Let us investigate, first, the locus of roots related to P_1. Results related to setups I

and II (panels (a) and (b)) reveal that all roots have negative real part, denoting that the state $\mathbf{U}_S^*$ is also stable with respect to non-homogeneous perturbations. On the contrary, in setup III (panel (c)), there exists a range of wavenumber where one root has positive real part and non-null imaginary part, so pointing out a destabilization of the steady state. These observations are consistent with the predictions reported in Fig.3.1 because, in setups I and II, the investigated point is outside the wave instability region but, in setup III, it is located inside. About the point P_2, in setups II and III (panels (e),(f)) there exists a range of k where the real part of the most unstable root becomes positive. On the contrary, in setup I (panel (d)), the real part of this root keeps negative, consistently with its location with respect to the bifurcation loci. Finally, at point P_3, for each of the chosen setups (panels (g),(h),(i)), there exists a range of k where the real part of the most unstable root becomes positive, consistently with the fact that this point always lies inside the wave instability region.

Another confirmation of the analytical predictions may be achieved by integrating numerically the governing system together with periodic boundary conditions and using small sinusoidal fluctuations about the steady state $\mathbf{U}_S^*$ as initial conditions.

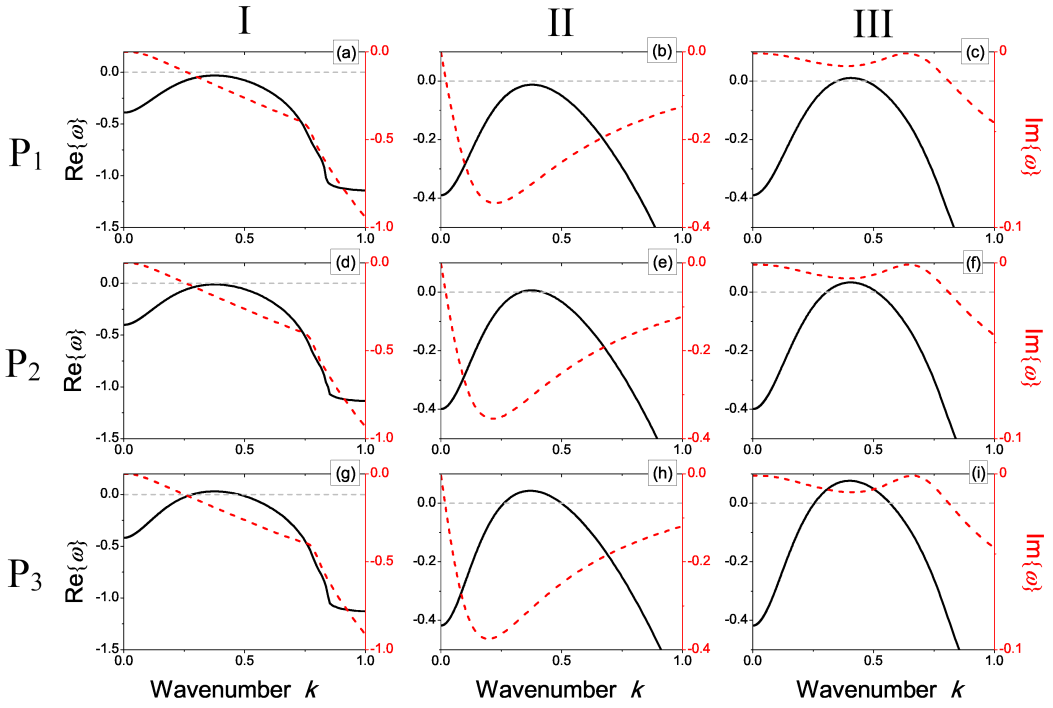

Figure 3.2: Wavenumber dependence of the real (left axes, continuous lines) and imaginary (right axes, discontinuous lines) part of largest root of (3.35) evaluated for $A = 2.8$ at the points P_1 ($B = 0.40$, panels (a)-(c)), P_2 ($B = 0.41$, panels (d)-(f)) and P_3 ($B = 0.43$, panels (g)-(i)) indicated in Fig.3.1, for different couples of inertial times (τ^u, τ^w). In detail, setup I: $(10^{-5}, 10^{-5})$, panels (a),(d),(g); setup II: $(0.5, 1)$, panels (b),(e),(h); setup III: $(0.5, 100)$, panels (c),(f),(i).

Simulations have been performed by means of COMSOL Multiphysics® [108] over a time window $t \in [0, 50]$, considering a spatial domain of length $l_D = 100$ (unless specified differently). Results of this investigation, which make use of the same parameter set as the one used in Fig.3.2, are reported in Fig.3.3. In agreement with the above-mentioned predictions, it is possible to notice that, when all the roots have negative real parts, the initial perturbation dies out and the system converges toward the stable, spatially-uniform, vegetated state $\mathbf{U}_S^*$, see panels (a),(b),(d). On the contrary, if there exists a range of unstable wavenumbers, then the system evolves toward a periodic patterned state that oscillates in time, representative of an uphill migrating vegetation band, see panels (c),(e)-(i).

We can also numerically verify whether the range of unstable wavenumbers depends on inertia. It is known that, if a non-homogeneous perturbation is applied to a state $\mathbf{U}^*$ falling within the wave instability region, the system tends to form a travelling pattern whose wavenumber is close to the one of the most unstable modes, i.e. the mode exhibiting the largest growth rate. The range of unstable wavenumbers that is created when the control parameter is above the critical value B_c degenerates into the single value k_c at onset. To address this point, we track the variations in the (B, k) plane of the root of the characteristic polynomial (3.35) associated to the most unstable mode, for different values of inertial times. Results are shown in Fig.3.4, where the wavenumber of the mode exhibiting the largest growth rate is depicted by dashed lines whereas the range of unstable wavenumbers is delimited by solid lines. When we move away from the parabolic limit (from black to red curves in the figure), the role played by inertia becomes manifold: it decreases the lowest value of the control parameter (plant loss) at which instability may form, it modifies the wavenumber of the most unstable mode and also enlarges significantly the range of unstable wavenumbers.

Furthermore, by solving numerically the system defining theoretically the wave bifurcation locus (3.7),(3.8), we can quantitatively estimate the wave speed s at the onset of instability as a function of inertial times. From the analysis of the results depicted in Fig.3.5, we infer that the values of the inertial times affect directly and indirectly through the variation of B_c the migrating speed at the onset of instability, as it varies from about 0.8 (close to the parabolic limit) to 1.0 (away from it), i.e. hyperbolicity may increase the wave speed up to 30%. It should be noticed that the fuzzier behaviour shown in the top right corner of Fig.3.5 is not easily predictable as the highly nonlinear dependence of migration speed on the inertial times makes it prohibitive. To get a validation of these results, numerical integration on the governing system is again performed over a larger time window $t \in [0, 200]$ and a larger spatial domain $l_D = 200$. We use the parameter set corresponding to the points Q_1 and Q_2 depicted in Fig.3.5 and choose the control parameter B in such a way the distance from the threshold is $\epsilon^2 = 10^{-3}$ in both cases. Then, in order to extract the critical values of angular frequency ω_c and wavenumber k_c, we perform two Fast-Fourier-Transforms (FFTs) on the variable $u(x, t)$, by fixing either space or time. In detail, in the former case, the solution $u(x, t)$ is evaluated at $x = l_D/2$ while, in the latter case, it is set at $t = t_{end}$. According to the results shown in Fig.3.6, each resulting spectrum contains several peaks, the dominant of which gives information on the angular frequency ω_c and the wavenumber k_c of the main mode, respectively.

Finally, the migrating speed value is simply given by the ratio $s = \omega_c/k_c$. Following this procedure, we get: for the point Q_1, $s = 0.301/0.376 = 0.801$, in excellent agreement with the value extracted from system (3.7),(3.8), that is equal to $s = 0.807$; for the point Q_2, the value $s = 0.380/0.410 = 0.926$, in good agreement with the theoretical value $s = 0.923$. These results reinforce our previous conclusion on the non-negligible role played by inertial times: apart from affecting the migrating speed, they also alter both angular frequency and wavenumber of the emerging pattern.

So far, we have validated all the theoretical predictions connected to LSA developed in Section 3.1.1. Let us now focus on those arising from multiple-scale WNA whose general formulation has been given in the previous section. In the specific case of the hyperbolic extension of the Klausmeier model, the explicit expressions of the quantities here involved are reported in Appendix D.

As known, the sign of the real part of the Landau coefficient determines the supercritical (if $L_1 > 0$) or subcritical (if $L_1 < 0$) character of the generated patterns. Here, we aim to inspect how such a character could be altered by a suitable combination of inertial times. In Fig.3.7 we have addressed numerically this investigation, by using the same set of parameters as those used to build Fig.3.5. In the figure, the colored (white) areas denote a supercritical (subcritical) behavior. These results reveal

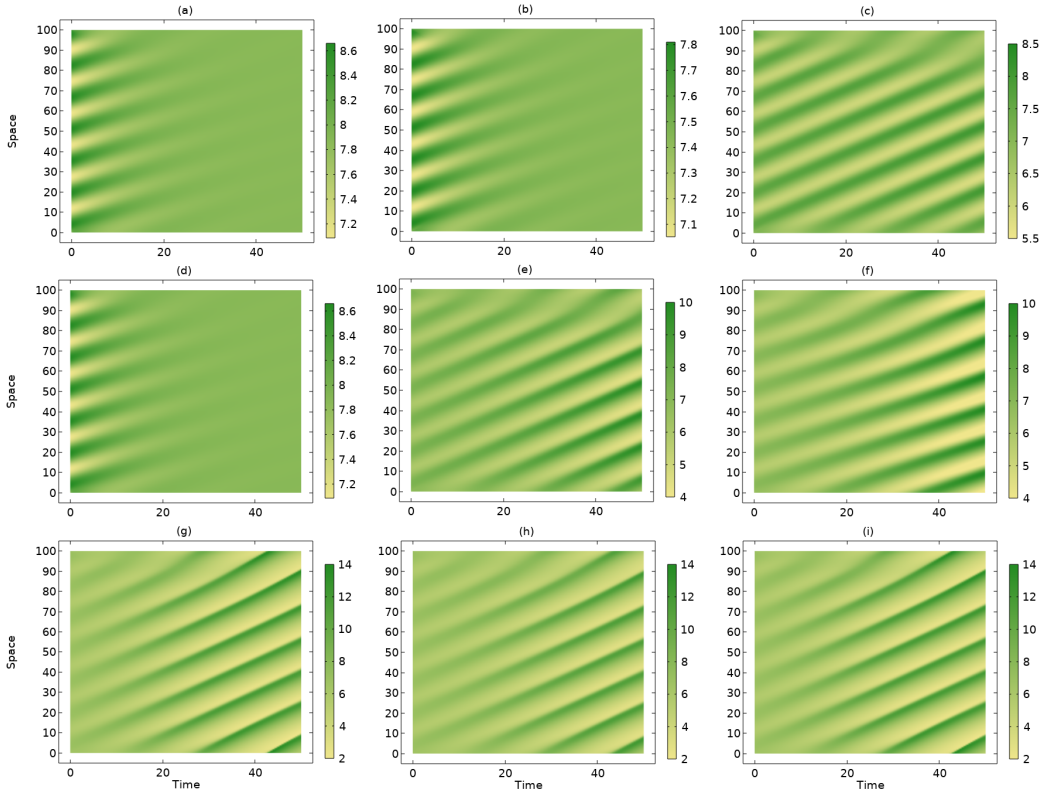

Figure 3.3: Spatio-temporal dynamics of vegetation biomass $u(x,t)$ corresponding to the panels shown in Fig.3.2 obtained via numerical integration of system (3.1),(3.2) with Klausmeier kinetic (1.2).

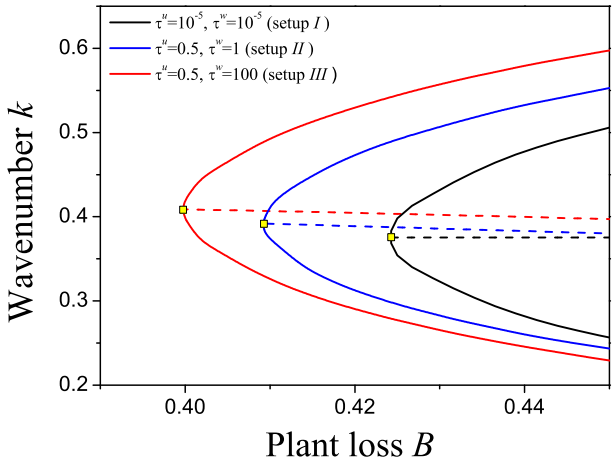

Figure 3.4: (Solid lines) Range of unstable wavenumbers as a function of the plant loss B for different values of inertial times. (Dashed lines) The wavenumber of the perturbation with the larger growth rate. (Squares) The lowest plant loss value B_c at which that steady state $\mathbf{U}_S^*$ undergoes wave instability and that identifies the critical wavenumber k_c.

that, for relatively small values of the inertial times, namely close to the parabolic limit (bottom left corner of the figure), patterns exhibit a supercritical behavior. For increasing values of inertial times, hyperbolicity may give rise to a subcritical instability.

Let us now inspect whether these predictions may be corroborated by numerical simulations. First, the supercritical character associated to the points Q_1 and Q_2 can be extracted from Fig.3.6, where patterns slightly above threshold exhibit small amplitude, do not exist for sub-threshold values of the control parameter and have a wavenumber very close to k_c. Indeed, the numerically-deduced values, i.e. $k_c = 0.376$ in Fig.3.6(c) and $k_c = 0.410$ in Fig.3.6(f), are in close agreement with the theoretical ones deduced from (3.7),(3.8),(D.2), i.e. $k_c = 0.376$ and $k_c = 0.403$, respectively. To test whether a subcritical instability takes place at Q_3, simulations are performed with a initial condition thet is set, at first, as a small sinusoidal perturbation of the steady state and the control parameter is slightly smaller than the critical value. Results indicate that the initial perturbation simply dies out and the system converges towards the stable homogeneously vegetated area, see Fig.3.8(a). Then, we increase the control parameter slightly above threshold and, as expected, large amplitude patterns are generated, see Fig.3.8(b) (notice the larger scale in the color bar in comparison with those of Fig.3.6(a),(d)). Finally, we take the final state of this latter simulation as the initial condition of a new simulation where the control parameter is set to the same below-threshold value as the one used to build Fig.3.8(a). Interestingly, patterns still survive, so denoting the hysteretic behavior typical of a subcritical instability.

Finally, an investigation is performed on the one-parameter family of coherent

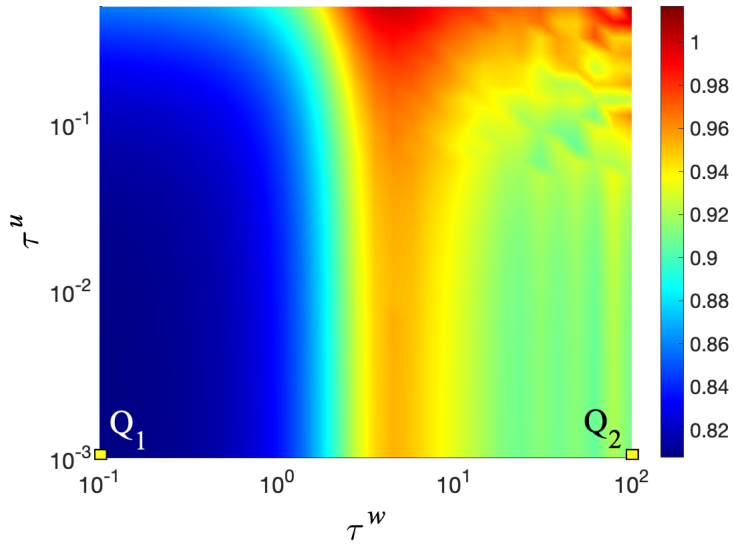

Figure 3.5: Density plot of migrating speed s at onset of instability ($B = B_c$) as a function of the inertial times τ^u and τ^w. Fixed parameters: $\nu = 182.5$, $d = 100$, $A = 2.8$.

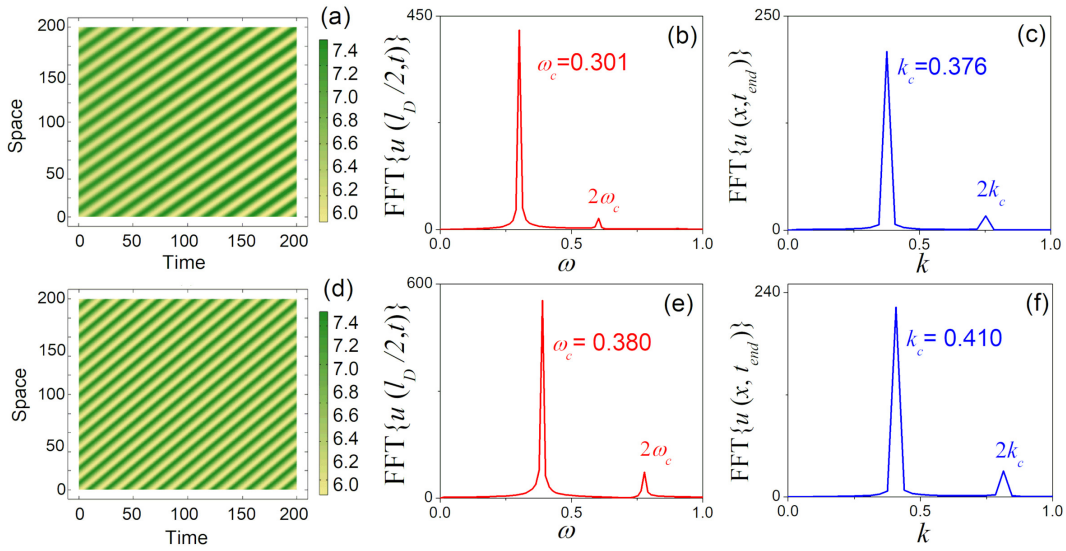

Figure 3.6: (a,d) Snapshots of migrating vegetation patterns. (b,e) FFT of the *time*-dependent solution evaluated at a fixed location within the domain, $u(l_D/2, t)$. (c,f) FFT of the *space*-dependent solution evaluated at the final simulation time, $u(x, t_{end})$. Panels in the top (bottom) row are obtained by using the parameter set corresponding to point Q_1 (Q_2) depicted in Fig.3.5. Note that the arising FFT spectra contain some higher-order harmonics (mainly, the component proportional to $exp(2\,i\,k_c z)$) due to the slow modulation of the pattern close to the onset [112].

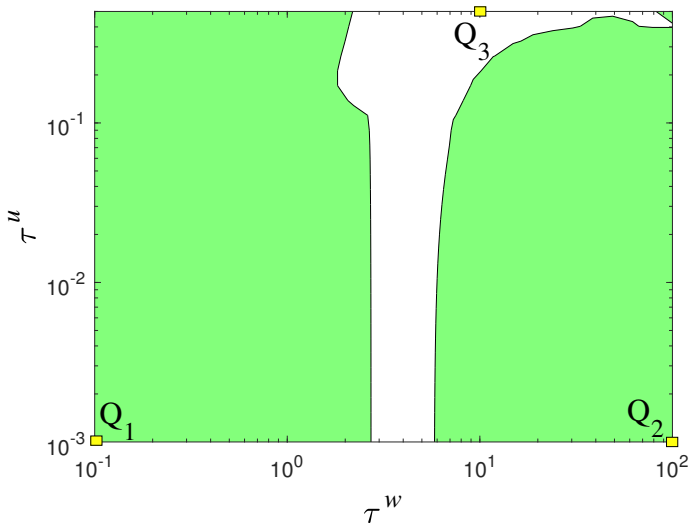

Figure 3.7: Contour plot of L_1 as a function of the inertial times τ^u and τ^w. Colored (white) areas denote positive (negative) values of L_1. The parameter set is the same as the one reported in Fig.3.5.

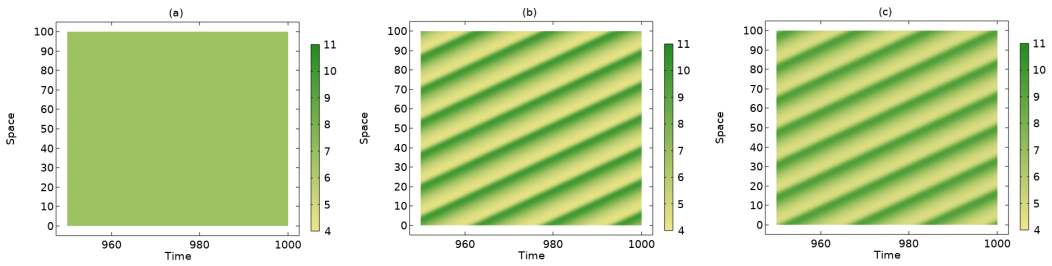

Figure 3.8: Snapshots of spatio-temporal evolution of vegetation biomass corresponding to the point Q_3 shown in Fig.3.7 for (a) $B = 0.403$, (b) $B = 0.405$ and (c) $B = 0.403$. The initial condition in simulations (a) and (b) is taken as a small periodic perturbation of the steady state $\mathbf{U}_S^*$ whereas in (c) it is given by the final state of (b). The critical value of the control parameter is $B_c = 0.404$.

structures, solutions of the CCGL equation, and a comparison between the analytical predictions and numerical simulations is addressed. The discussion is here limited to the supercritical regime by considering those regions of the (τ^w, τ^u) plane where the real part of the Landau coefficient keeps positive (colored areas in Fig.3.7). Then, we study the sign of the necessary condition for stability given by the Benjamin-Feir-Newell criterion (3.30) and report the results in Fig.3.9. Here, the white (orange) color denotes an area where patterns are unstable (may be stable). Our results indicate that, in a wide region enclosing the parabolic limit (point Q_1), i.e. for $\tau^w < 2$ and independently of the value of τ^u, the abovementioned criterion is always satisfied and patterns may be stable. In this region, a slow modulation of travelling patterns is observed, as shown in Fig.3.10(a). Far away from the parabolic limit, there exist

values of inertial times that may lead to destabilization of patterns, as it happens in the subregion of the (τ^w, τ^u) plane depicted in Fig.3.9. Indeed, considering the inertial times corresponding to point Q_4, the wavetrain structure may break up into a sequence of unequal pulses [5], as depicted in Fig.3.10(b).

Then, the role of inertial effects on phase winding solutions, i.e. on the fixed points $\mathbf{F}_1^*$ and $\mathbf{F}_2^*$ of system (3.23), is inspected. In this analysis, the inertial times are set in such a way they correspond to points Q_1 and Q_2 and keep the dimensionless distance from the threshold fixed at $\epsilon^2 = 10^{-2}$. The governing system is integrated over a larger time window $t \in [0, 1000]$ in order to allow transient regime to expire

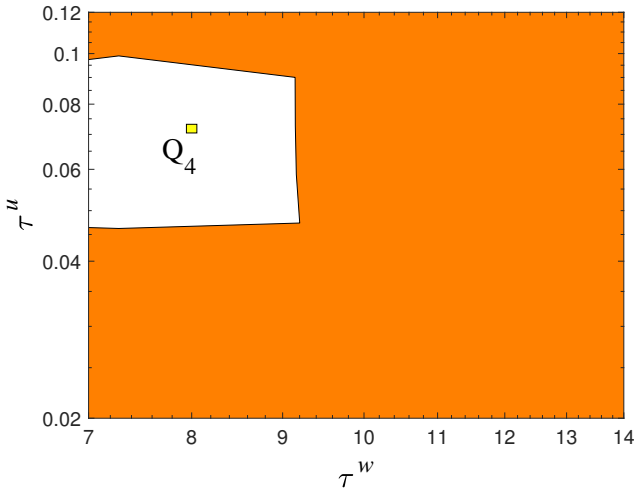

Figure 3.9: Plot of the Benjamin-Feir-Newell necessary condition for stability in the supercritical regime. Colored (white) areas denote regions where the condition (3.30) is (is not) fulfilled.

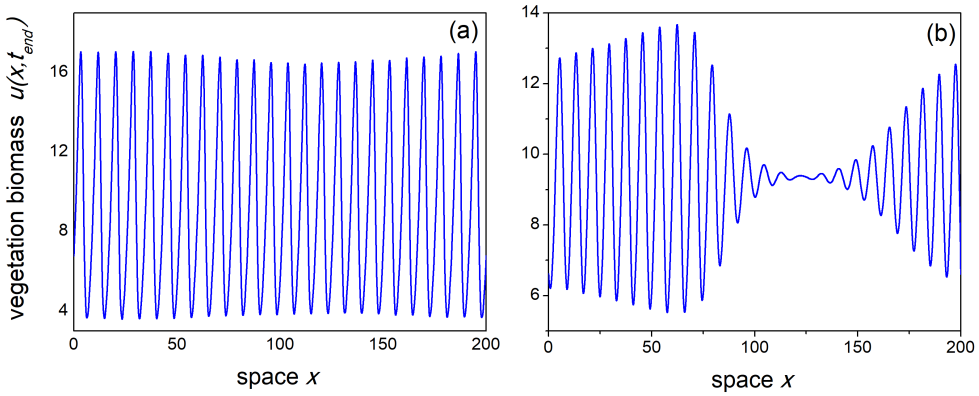

Figure 3.10: Proof of the Benjamin-Feir-Newell instability condition showing the spatial profiles of the patterned configurations obtained at points Q_1 (a) and Q_4 (b) represented in Fig.3.9(a). To improve the visibility of the wavetrain structure breaking, the computational domain has been enlarged to l_D=400.

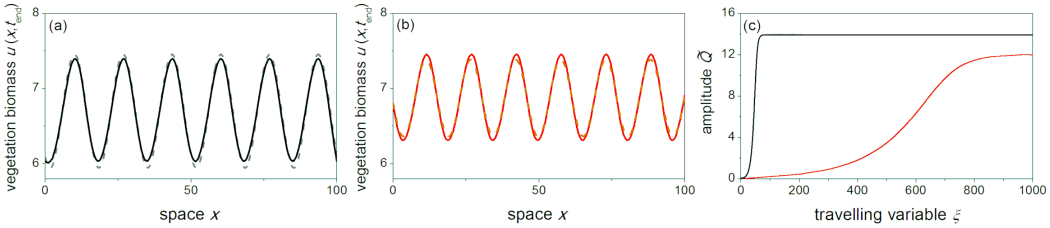

Figure 3.11: (a,b) Comparison between the numerical simulation arising from the integration of the governing system (solid lines) and the analytically-deduced phase winding solution $\overline{\mathbf{U}} = \varepsilon\overline{\mathbf{U}}_1$ together with (3.19),(3.24)-(3.27) (dashed lines). The set of parameters correspond to the points Q_1 (a) and Q_2 (b) with $\epsilon^2 = 10^{-2}$. (c) Results of numerical integration of system (3.23) representative of the heteroclinic orbits joining the fixed points $\mathbf{F}_1^*$ and $\mathbf{F}_2^*$ [black (red) curve stands for dynamics around point Q_1 (Q_2)]. The initial condition is set as a small perturbation of $\mathbf{F}_1^*$.

and the system to reach a steady travelling patterned configuration. These are depicted in Figs.3.11(a),(b) by solid lines. To determine the extra parameter involved in the phase-winding solution $\widetilde{\kappa}$, a comparison between the theoretical critical value k_c and the total wavenumber of the observed pattern k_{tot} is performed. This value is then used in (3.24),(3.27) to compute the amplitude $\widetilde{Q}$ and the second-order correction of the angular frequency $\widetilde{\omega}$, respectively. Then, the corresponding analytical phase winding solutions are built via (3.25). Results are represented in the previously mentioned figures via dashed lines and reveal a satisfying agreement with those arising from numerical simulations. Moreover, system (3.23) is integrated to describe the heteroclinic orbits joining the fixed points $\mathbf{F}_1^*$ (unstable) and $\mathbf{F}_2^*$ (stable) in the two configurations represented by the points Q_1 and Q_2. The initial condition is set as a small perturbation of $\mathbf{F}_1^*$ in both cases. The resulting fronts are depicted in Fig.3.11(c) and confirm that inertial effects take a relevant role, not only in modulating the duration of the transient regime from the homogeneous steady state to the patterned state, but also in modifying the amplitude, the wavenumber and the angular frequency of the travelling patterns.

3.1.4 Concluding remarks

In this section, a class of hyperbolic reaction-advection-diffusion system for two species, one of which undergoes both self-diffusion and advection while the other one has a diffusive character only, is considered. The hyperbolic structure of the model accounts for the biological inertia of both the involved species and allows a better description of transient phenomena characterized by waves evolving in space over a finite time. On this general framework, it is carried out, first, LSA to deduce the conditions under which wave instability, responsible for the occurrence of non-stationary spatial patterns, takes place. Then, by applying multiple-scale WNA the amplitude equation describing the slow modulation in space and time near criticality is determined.

All theoretical findings enclose the parabolic limit as particular case, when the

inertial times tend to zero. In particular, it has been shown that the resulting CCGL equation is formally unchanged with respect to the classical one obtained in parabolic framework, but the coefficients here involved exhibit a strong dependence on inertial times.

Moreover, to better emphasize the role of hyperbolicity, an inspection on coherent structures of the CCGL equation, whose fixed points are in the form of phase winding solutions, is performed. For this class of solutions we have determined the expressions of the key features and established the necessary condition for stability.

The previous theoretical predictions have been tested on an illustrative example, the extended Klausmeier model, describing the formation and the migration of vegetation patterns over a sloping semiarid terrain. Numerical investigations have validated our findings and have allowed to draw several conclusions about the role played by inertia. It has been indeed proven that inertial times:

i) enlarge both the wave instability region in the parameter plane where travelling patterns may be observed and is less selective on the range of unstable wavenumbers. Thus, inertia allows to destabilize the spatially homogeneous steady state over a wider set of model parameters (see Figs.3.1-3.4);

ii) vary the key features associated to migrating patterns, speed, wavelength and angular frequency, leaving all the other model parameters unchanged (see Figs.3.5,3.6);

iii) affect the supercritical or subcritical nature of patterns at onset (see Figs.3.7,3.8);

iv) exert influence on localized coherent structures, and in particular on the fronts connecting the plane-wave state to the unstable spatially-homogeneous steady state. In particular, it has been shown that inertia takes a role, not only during transient regime, but also modifies the amplitude, the wavenumber, the angular frequency and the stability of the phase winding solution associated to the plane wave (see Figs.3.9,3.11).

In the light of the above statements, it has to be emphasized that hyperbolic models provide additional degrees of freedom that can be used to better model experimental observations.

In this framework, it is planned to extend the hyperbolic framework to the case in which both species undergo diffusion and advection, so enabling the possibility of exploring an even richer set of dynamics.

3.2 Two-compartment systems with two advection terms and one self-diffusion term

In this section, the occurrence of oscillatory patterns in two-compartment 1D hyperbolic RT systems (1.8)-(1.9) where both species undergo advection and only one undergoes self-diffusion ($d = 0$) is taken into account.

In the context of dryland ecology, such a model is an attempt to mimic some ecological observations. In particular, regular striped patterns formed along the hillsides of many arid and semi-arid environments are believed to exhibit a non-stationary behavior that manifests itself as an uphill migration of bands. However, a larger availability of field data has brought out some controversial interpretations about the effective motion of these patches [68, 70]. In some previous works [47–52, 54], the origin of the above-mentioned controversy was attributed to the phenomena of mobilization, transport and germination of seeds, which can be gathered under the name of *secondary seed dispersal*. It is indeed known that, in sloped terrains, seeds undergo both a primary dispersal from the plant to the ground followed by a secondary dispersal due to their transport in overland flow. This phenomenon has been included in several parabolic models (to cite a few, [43, 47, 49–51, 67]). In particular, in Ref.[67] secondary dispersal of seeds was included in the framework of the Klausmeier model [41]. The aim of the section is to generalize the results obtained in Ref.[67] and inspect how the dynamics of non-stationary vegetation stripes are affected by the simultaneous action of inertial effects and secondary seed dispersal. Therefore, the analysis here shown will be deducted in the case of the hyperbolic framework of the secondary seed version of the Klausmeier model [41, 67]. In detail, in order to characterize the features of the emerging migrating patterns, LSA has been performed with particular emphasis on the deduction of the threshold condition for wave instability responsible for the onset of oscillatory periodic patterns. Moreover, to gain more insights into the mechanisms underlying the pattern propagation speed, travelling wave solutions have been also taken into account. Analytical predictions have been corroborated by numerical simulations and a qualitative comparison with some ecological field observations is performed. Finally, the focus is moved to analytical approximations in order to extract qualitative information on the behaviour of both migrating and stationary patterns.

3.2.1 Model description

This analysis originates from the classical parabolic version of the Klausmeier model [41]. Here, water diffusion is neglected since the advection contribution is generally dominant on slopes. Later in Ref.[67], this model was extended to include the secondary seed dispersal phenomenon and took the 1D dimensionless form:

$$\begin{bmatrix} u \\ w \end{bmatrix}_t - \begin{bmatrix} 1 & 0 \\ 0 & 0 \end{bmatrix} \begin{bmatrix} u \\ w \end{bmatrix}_{xx} - \begin{bmatrix} \psi & 0 \\ 0 & \nu \end{bmatrix} \begin{bmatrix} u \\ w \end{bmatrix}_x = \begin{bmatrix} f(u,w,B) \\ g(u,w,B) \end{bmatrix} \tag{3.31}$$

where the subscript stands for the partial derivative with respect to the indicated variable, the x-axis points along uphill direction and the advection speeds of plant

and water are denoted by ψ and ν, respectively. Kinetic functions are given as in (1.2).

To account for the presence of biological inertia [18, 24, 27, 71, 72], as well as to provide a better description of pattern propagation, hereafter we consider its hyperbolic generalization obtained by means of ET theory [38]. As can be easily noticed, it is enclosed in the general framework (1.8)-(1.9) proposed in Section 1.3 by neglecting a diffusive term ($d = 0$). The model reads:

$$\mathbf{U}_t + \mathrm{M}\mathbf{U}_x = \mathbf{N}(\mathbf{U}, B), \tag{3.32}$$

with

$$\mathbf{U} = \begin{bmatrix} u \\ w \\ J^u \end{bmatrix}, \quad \mathrm{M} = \begin{bmatrix} -\psi & 0 & 1 \\ 0 & -\nu & 0 \\ \frac{1}{\tau^u} & 0 & 0 \end{bmatrix}, \quad \mathbf{N}(\mathbf{U}, B) = \begin{bmatrix} f(u, w, B) \\ g(u, w, B) \\ -\frac{1}{\tau^u} J^u \end{bmatrix} \tag{3.33}$$

being τ^u and $J^u(x,t)$ the inertial time and the dissipative flux, respectively, associated to plant evolution.

Spatially-homogeneous steady states of model (3.32),(3.33) with Klausmeier kinetic (1.2) can be easily achieved as in Section 1.4. According to literature, since secondary seed dispersal represents a small percentage of water advection speed, it is realistic to assume $\psi \ll \nu$ [67].

3.2.2 Wave bifurcation analysis

In order to investigate the nature of the steady states, a linear stability analysis for the PDE system (3.32),(3.33) is now carried out. Due to its high variability given by natural, human and herbivory effects, the plant loss B is considered as the control parameter. Then, by perturbing the steady state, namely by looking for solutions in the form of $\mathbf{U} = \mathbf{U}^* + \widehat{\mathbf{U}} \exp(\omega t + \mathrm{i}\, k\, x)$, we get

$$\left(\omega I + ik\mathrm{M} - (\nabla \mathbf{N})^*\right) \widehat{\mathbf{U}} = \mathbf{0} \tag{3.34}$$

where $\mathbf{I}$ denotes the identity matrix, $\nabla \equiv \partial/\partial \mathbf{U}$ represents the gradient with respect to the field variables and the asterisk indicates the evaluation at $\mathbf{U}^*$. Searching non-trivial solutions of (3.34) leads to the following characteristic equation:

$$\begin{aligned} &\tau^u \omega^3 + \left[A_1 - ik\tau^u (\nu + \psi)\right] \omega^2 + \left\{A_2 + ik\left[\tau^u (\nu f_u^* + \psi g_w^*) - (\nu + \psi)\right]\right\} \omega + \\ &\quad + A_3 + ik\left[\nu f_u^* + \psi g_w^* - \nu k^2\right] = 0 \end{aligned} \tag{3.35}$$

where

$$\begin{aligned}
A_1 &= 1 - \tau^u \left(f_u^* + g_w^*\right) \\
A_2 &= \widehat{A}_2 k^2 + \widetilde{A}_2 \\
\widehat{A}_2 &= 1 - \tau^u \nu\psi \\
\widetilde{A}_2 &= \tau^u \left(f_u^* g_w^* - g_u^* f_w^*\right) - \left(f_u^* + g_w^*\right) \\
A_3 &= \widehat{A}_3 k^2 + \widetilde{A}_3 \\
\widehat{A}_3 &= -\left(g_w^* + \nu\psi\right) \\
\widetilde{A}_3 &= f_u^* g_w^* - g_u^* f_w^*
\end{aligned} \tag{3.36}$$

Let us now focus on the occurrence of the wave instability. By considering LSA, it can be easily noticed that it conducts to the same results as in Appendix B for the local stability under a homogeneous perturbation ($k = 0$). On the other hand, taking into account non-homogeneous perturbations around the desert state $\mathbf{U}_D^*$, the dispersion relation can be factorized and its solutions are given by:

$$\begin{gathered}
\omega_1 = -1 + i\nu k \\
\omega_{2,3} = \tfrac{1}{2}\left(-B - \tfrac{1}{\tau^u} + i\psi k \pm \sqrt{\left(B - \tfrac{1}{\tau^u}\right)^2 - k^2\left(\tfrac{4}{\tau^u} + \psi\right)^2 + 2i\psi k\left(\tfrac{1}{\tau^u} - B\right)}\right).
\end{gathered} \tag{3.37}$$

Consequently, $\mathbf{U}_D^*$ is always stable under both homogeneous and non-homogeneous perturbations, being the real parts of all eigenvalues negative $\forall k$.

Thus, only the homogeneously-vegetated state configuration that can give rise to oscillatory periodic patterns is $\mathbf{U}_S^*$. In particular, looking for solutions of the dispersion relation (3.35) with $\mathrm{Re}\{\omega\} = 0$ and $\mathrm{Im}\{\omega\} \neq 0$ for some $k \neq 0$, setting to zero the real and imaginary parts and combining the resulting equations, the critical wavenumber at the onset of instability is ruled by:

$$\theta_1 k^6 + \theta_2 k^4 + \theta_3 k^2 + \theta_4 = 0 \tag{3.38}$$

where

$$\begin{aligned}
\theta_1 &= A_1\beta_1^2 + \beta_1\beta_3\left[\tau^u\left(\nu f_u^* + \psi g_w^*\right) - (\nu + \psi)\right] - \beta_3^2\widehat{A}_3, \\
\theta_2 &= 2\beta_1\beta_2 A_1 + \left(\beta_1\beta_4 + \beta_2\beta_3\right)\left[\tau^u\left(\nu f_u^* + \psi g_w^*\right) - (\nu + \psi)\right] - 2\beta_3\beta_4\widehat{A}_3 - \beta_3^2\widetilde{A}_3, \\
\theta_3 &= A_1\beta_2^2 + \beta_2\beta_4\left[\tau^u\left(\nu f_u^* + \psi g_w^*\right) - (\nu + \psi)\right] - \widehat{A}_3\beta_4^2 - 2\widetilde{A}_3\beta_3\beta_4, \\
\theta_4 &= -\beta_4^2\widetilde{A}_3, \\
\beta_1 &= -(\tau^u)^2\widehat{A}_3\left(\nu g_w^* + \psi f_u^*\right) - \nu A_1^2, \\
\beta_2 &= -(\tau^u)^2\widetilde{A}_3\left(\nu g_w^* + \psi f_u^*\right) + A_1^2\left(\nu f_u^* + \psi g_w^*\right), \\
\beta_3 &= A_1\left[\tau^u f_u^* - 1 - (\tau^u)^2\nu\psi\left(f_u^* + g_w^*\right)\right] - (\tau^u)^2\left(f_u^*\psi + g_w^*\nu\right)\left[\tau^u\left(\nu f_u^* + \psi g_w^*\right) - (\nu + \psi)\right], \\
\beta_4 &= \tau^u A_1\widetilde{A}_3 - A_1^2\widetilde{A}_2.
\end{aligned} \tag{3.39}$$

The locus at which wave instability occurs may be obtained by imposing that the cubic equation (3.38) in k^2 admits three real roots, two of which are equal to each other,

positive and representative of the critical squared wavenumber k_c^2. Consequently, the wave instability locus is implicitly defined by:

$$27\theta_4^2\theta_1^2 - \theta_3^2\theta_2^2 + 4\theta_3^3\theta_1 + 4\theta_4\theta_2^3 - 18\theta_4\theta_3\theta_2\theta_1 = 0. \tag{3.40}$$

Note that, the wave instability locus (3.40) here obtained reduces to the one obtained in the parabolic model [67] for $\tau^u \to 0$. Unfortunately, due to the highly nonlinear dependence of (3.40) from the plant loss B, information can be extracted from numerical investigations only.

In Fig.3.12 the loci of wave instability (3.40) are depicted by solid lines in the (B, A) parameter plane for different inertial times $\tau^u \in [1, 100]$, fixing $\nu = 182.5$ and $\psi = 1$. For comparison, in the same figure the parabolic locus is also shown (red circles), pointing out a close agreement with the one obtained in the hyperbolic model for small inertial times $\tau^u \leq 1$.

On the other hand, by moving away from the parabolic limit, the locus of wave instability shifts up so enlarging the region where oscillatory periodic patterns may be observed, in line with our previous results [77, 78, 81]. To confirm this theoretical prediction, let us consider the point $\mathrm{P}_1 = (0.38, 2.8)$ in the parameter plane (see top inset in Fig.3.12) and inspect the wavenumber dependence of real and imaginary parts of the roots of the characteristic equation as the inertial time is varied. Results shown in Fig.3.13(a) reveal that for $\tau^u = 10$, the real part of the largest eigenvalue is always negative so proving that P_1 lies outside the wave instability region. On the other hand, for $\tau^u = 20$ and $\tau^u = 100$, the existence of ranges of unstable wavenumbers confirm the upward shift of the locus of wave instability that has led P_1 to fall within the instability region (see Figs.3.13(b),(c)).

Additional numerical investigations are also performed to better understand the roles of inertial time τ^u and advection speeds ψ and ν on the bifurcation threshold B_c. In particular, results shown in Fig.3.14(a) are obtained for a fixed value of $\psi = 1$ whereas those depicted in Fig.3.14(b) correspond to the case $\nu = 182.5$. In detail, for a fixed value of secondary seed dispersal and independently of the inertial time, the decrease of water advection speed leads to an increase of the critical value of the control parameter which in turn represents a reduction of the instability region (see Fig.3.14(a)). This result agrees with the theoretical expectation that the formation of oscillatory patterns requires a non-null water advection speed. On the other hand, for a fixed value of water advection speed, the behavior of the instability threshold depends on the distance from the parabolic limit. Indeed, as depicted in Fig.3.14(b), for $\tau^u \lesssim 10^{-1}$, the critical value of control parameter is almost unaffected by the strength of secondary seed dispersal. On the contrary, far away from the parabolic limit, the role of seeds advection speed becomes more relevant. In fact, as the parameter ψ decreases, the wave instability region enlarges.

Let us now inspect the properties exhibited by oscillatory patterns by moving along the bifurcation locus. To this aim, let us fix three different points on the locus obtained for $\tau^u = 10$ as shown in the bottom inset of Fig.3.12 and precisely: $\mathrm{P}_2 = (0.244, 1.5)$, $\mathrm{P}_3 = (0.270, 1.7)$ and $\mathrm{P}_4 = (0.293, 1.9)$. For these points, in Fig.3.15 the wavenumber dependence of the most unstable mode at onset, characterized by angular frequency ω_c and critical wavenumber k_c, is tracked. Since the imaginary

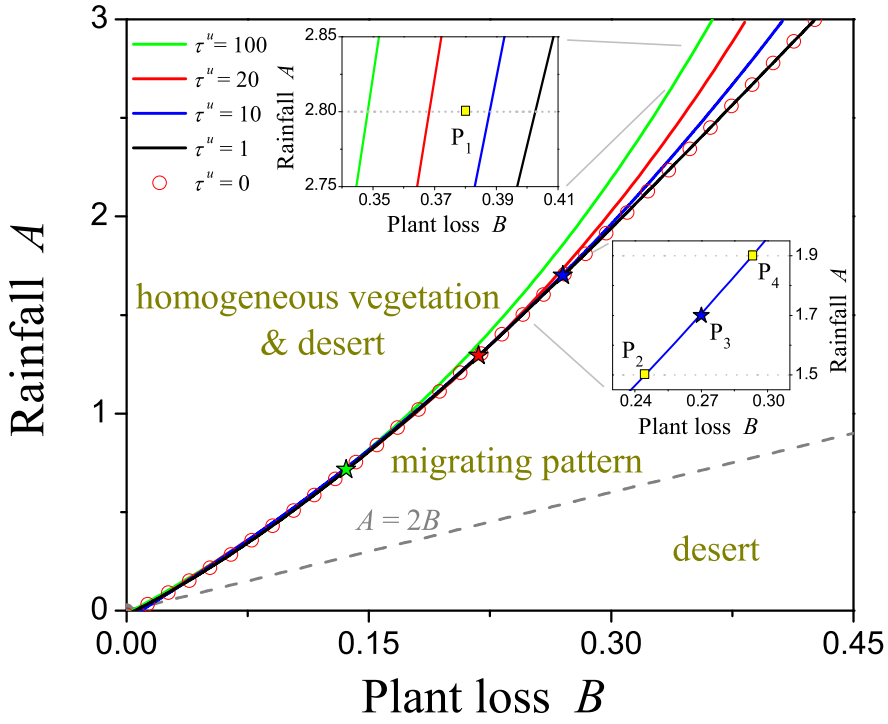

Figure 3.12: Solid lines represent the loci of wave instability in the (B, A) parameter plane for different values of inertial time. Red circles denote the locus obtained in the parabolic case. The bottom dashed line defines the condition $A = 2B$, below which only desert state exists. Insets give zooms over the indicated areas. Points P_i $(i = 1, ..., 4)$ represent different configurations in the (B, A) plane which are used in Figs.3.13-3.16. Stars denote Turing bifurcation points obtained as the inertial time is varied.

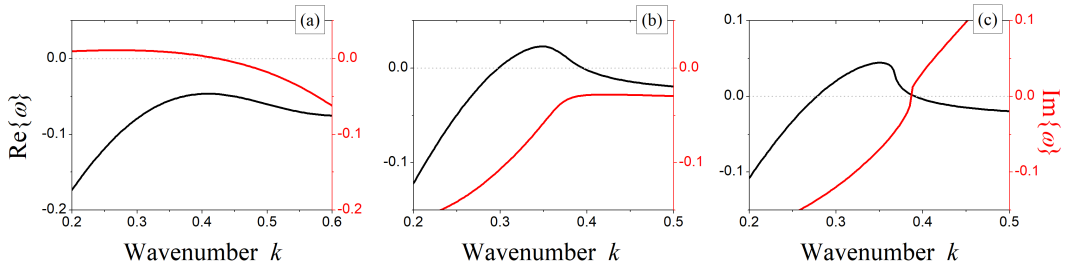

Figure 3.13: Wavenumber dependence of the real (black lines) and imaginary (red lines) part of largest root of (3.35) evaluated at $\mathrm{P}_1 = (0.38, 2.8)$ indicated in the top inset of Fig.3.12, for different inertial times: $(a)\ \tau^u = 10$, $(b)\ \tau^u = 20$ and $(c)\ \tau^u = 100$.

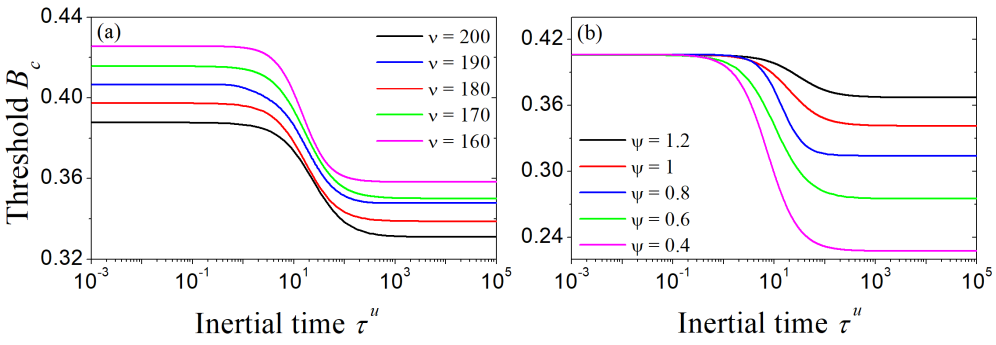

Figure 3.14: Inertial time dependence of the wave instability threshold obtained for $A = 2.8$, (a) $\psi = 1$ and (b) $\nu = 182.5$.

part determines the modulus and direction of pattern speed $s = -\mathrm{Im}\{\omega_c\}/k_c$, uphill (downhill) motion is observed for $\mathrm{Im}\{\omega_c\} < 0$ ($\mathrm{Im}\{\omega_c\} > 0$) whereas stationary patterns originate for $\mathrm{Im}\{\omega_c\} = 0$. Theoretical predictions reveal that downhill motion takes place at the point P_2 (see Fig.3.15(a)), patterns become stationary at P_3 (see Fig.3.15(b)) whereas they move uphill at P_4 (see Fig.3.15(c)). To check the validity of the above results, the governing system (3.1),(3.2) is integrated numerically by means of COMSOL Multiphysics®[108] in the computational domain $x \in [0, 200]$ over the time window $t \in [0, 200]$. Moreover, periodic boundary conditions are used and a small perturbation of the steady state $\mathbf{U}_S^*$ is taken as initial condition, namely patterns originating from degradation of homogeneous vegetation are here considered [67, 116]. Results of numerical simulations confirm our predictions, as shown in Fig.3.16.

The above theoretical results are in line with some body of literature [41, 117], which predicts that vegetation groves move upslope as a result of a larger availability of moisture in the upslope margin of the band. Moreover, the presence of downslope seed transport offers a stabilizing mechanism that reduces the bands' migration speed and can even reverse the direction of propagation [47, 48, 50]. However, it should be mentioned that the occurrence of upslope and downslope migration of bands is still under debate due to some controversial field evidences [47, 68, 70]. In particular, the theoretical observation of downhill movement of bands is sometimes interpreted as a regime in which pattern migration is, instead, precluded [47]. This issue will be investigated in more detail later on.

According to such ecological considerations, let us describe more accurately the occurrence of stationary patterns in a framework enclosing advective terms. To this aim, let us look for solutions of the dispersion relation (3.35) characterized by:

$$\begin{cases} \omega = 0 \\ \frac{\partial \mathrm{Re}\{\omega\}}{\partial k} = 0 \end{cases} \tag{3.41}$$

These constraints lead to the following system that defines a Turing point in the

(B, A)-plane and the critical wavenumber k_c at which such an instability occurs:

$$\begin{cases} k_c = \sqrt{\frac{\nu f_u^* + \psi g_w^*}{\nu}} \\ \nu\left(f_u^* g_w^* - f_w^* g_u^*\right) - \left(\nu f_u^* + \psi g_w^*\right)\left(\nu\psi + g_w^*\right) = 0 \\ \left(g_w^* + \nu\psi\right)\left[\left(1 - \tau^u \nu\psi\right)\left(\nu f_u^* + \psi g_w^*\right) + \tau^u \nu\left(f_u^* g_w^* - f_w^* g_u^*\right) - \nu\left(f_u^* + g_w^*\right)\right] + \\ \quad + \nu\left(\nu f_u^* + \psi g_w^*\right)\left[\tau^u\left(\nu f_u^* + \psi g_w^*\right) - (\nu + \psi)\right] = 0 \end{cases} \tag{3.42}$$

As it can be noticed, the existence of $(3.42)_1$ implies a restriction on the upper limit of seed advection speed

$$\psi \leq \frac{B\nu}{1 + u_S^2} \tag{3.43}$$

Moreover, $(3.42)_3$ denotes the dependence of the Turing point on hyperbolicity. Indeed, by varying the inertial time, the occurrence of stationary patterns takes place at different points in the (B, A)-plane, as represented by the stars in Fig.3.12. In particular, decreasing the inertial time, the Turing point moves upward along the bifurcation locus, so enlarging the range in which downhill motion is observed. Notice that, for $\tau^u = 1$ no star is shown since it is out of the meaningful ecological range. To describe the inertial time dependence of the Turing point B_c^T, we solve system

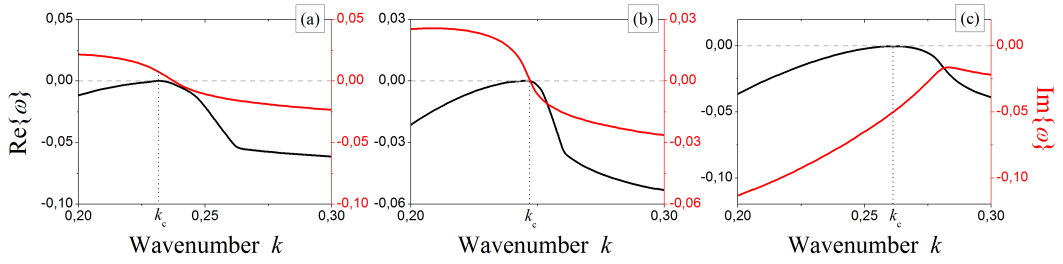

Figure 3.15: Wavenumber dependence of the real (black lines) and imaginary (red lines) part of largest root of (3.35) evaluated at the points P_2 (a), P_3 (b) and P_4 (c) indicated in Fig.3.12 for $\tau^u = 10$.

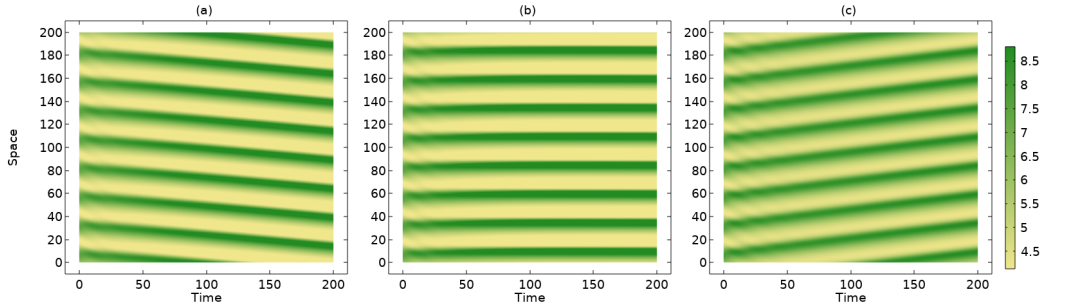

Figure 3.16: Spatio-temporal dynamics of vegetation biomass $u(x, t)$ obtained by integrating numerically the governing system (3.1)-(3.2) by using the parameters associated to the panels reported in Fig.3.15.

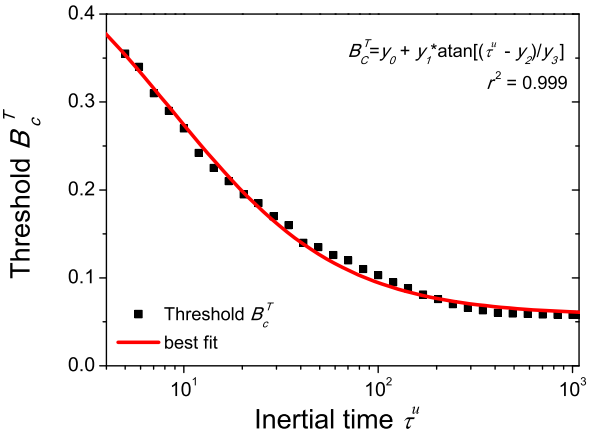

Figure 3.17: Turing threshold B_c^T dependence on the inertial time τ^u. Black squares represent analytical results, whereas red line denotes the best fit. Fixed parameters: $\nu = 182.5$ and $\psi = 1$. Parameters appearing in the best fit function: $y_0 = 25.15$, $y_1 = -15.97$, $y_2 = -8.68$ and $y_3 = 0.25$.

(3.42) for fixed values of ν and ψ. Results are shown in Fig.3.17 where the function that best approximates data is also depicted.

Finally, let us report some quantitative field estimations of migration speeds of vegetation patches extracted from Table 12.2 in [68] and [70], which gather experimental results from several arid regions. Those data pointed out that dynamics in sloped terrains range from the quasi-stationary case, corresponding to almost null migration speed, as observed in Mexico [118], Mali [119], Somalia [120] and Australia [70], to uphill motion with speed up to a 1.5 m/year, as in Mexico [118], Mali [119] and Sudan [121]. To address a direct comparison with such data, let us recast the dimensionless migration speed s and the time t in the original dimensional variables S [m/year] and T [year], respectively. By using the numerical estimates of the ecological parameters provided by Klausmeier in [41], it can be obtained: migration speed $S = 2s$ [m/year] and time $\tilde{T} = t/4$ [year]. Note that, the inertial time τ^u scales with the same law as t, i.e. $T = \tau^u/4$. Then, the dependence of $S(T)$ is reported in Fig.3.18 for different values of ν and ψ. Results in panel (a) reveal that, for a fixed value of ν and for small values of inertial times, pattern speed S changes progressively sign from positive to negative as the seed advection speed ψ increases. On the contrary, for large values of inertial times, migration speed keeps positive and approaches asymptotically the null value far away from the parabolic limit. This behavior holds independently of the value of the water advection speed, as proven in Fig.3.18(b), which is obtained for $\psi = 1$ and variable ν. These intriguing results allow to claim that the hyperbolic model may provide satisfying interpretations of ecological observations both when patterns migrate uphill [68] and when they are believed to be stationary [70]. Indeed, in the former case, the theoretically-predicted maximum speed value, about 1.2 m/year, is in close agreement with the experimental one 1.5 m/year (reported in Sudan, [68, 121]) for $\psi < 1$. This result may suggest

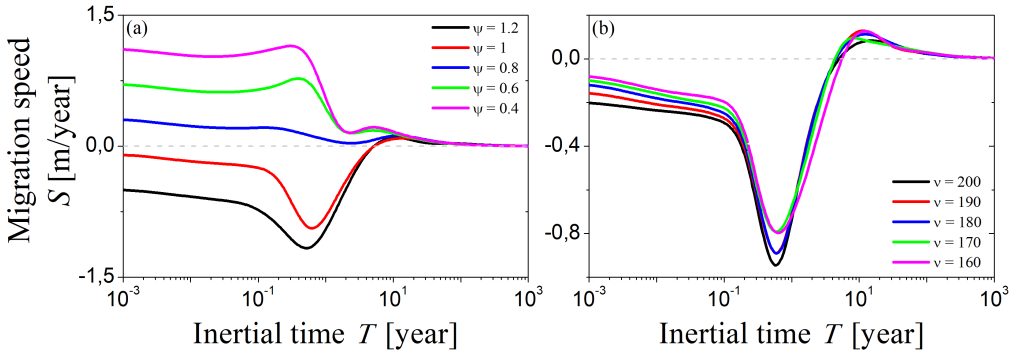

Figure 3.18: Migration speed S at onset of instability ($B = B_c$) as a function of the inertial time T for different values of ψ (a) and ν (b). In (a) the water advection speed is set as $\nu = 182.5$ whereas in (b) the seed advection speed is fixed at $\psi = 1$.

that the uphill migration of patterns has to be associated with a very small percentage of seed advection, an increase of which would lead to the opposite behaviour. In the latter case, the vanishing migration speeds obtained for large values of inertial time yield patterns to behave as they were almost stationary, independently of the strength of secondary seed dispersal. On the other hand, close to the parabolic limit, the agreement with field data would require to set both an upper bound (3.43), to exclude the occurrence of downhill migration [47], and a lower bound, to prevent propagation speed to achieve very large values.

3.2.3 Periodic travelling waves

The analyses carried out in the previous sections have shed some light on the role played by inertial time and advection terms in the mechanism of formation of oscillatory periodic patterns. In this section, let us focus in more detail on the characterization of the pattern speed s in the proposed hyperbolic model (3.32),(3.33). For this reason, we look for solutions of the governing system in the form of periodic travelling waves, namely $\mathbf{U}(x,t) = \mathbf{U}(z)$ with $z = x - st$. This leads to recast the original PDEs system in terms of the following ODEs one:

$$(\mathrm{M} - sI)\,\frac{d\mathbf{U}}{dz} = \mathbf{N}(\mathbf{U}, B) \tag{3.44}$$

It is trivial to notice that (3.44) admits the same three steady states of (3.32),(3.33). Moreover, since we are interested in the occurrence of wave instability, we focus our analysis on the homogeneously vegetated state $\mathbf{U}_S^*$ only. Therefore, searching for solutions in the form of $\mathbf{U} = \mathbf{U}_S^* + \widehat{\mathbf{U}}\exp(\omega z)$, the following cubic characteristic equation with real coefficients is obtained:

$$\omega^3 + D_1\omega^2 + D_2\omega + D_3 = 0 \tag{3.45}$$

where

$$\begin{aligned} D_1 &= \frac{-s^2 A_1 + s\left[\tau^u\left(\nu f_u^* + \psi g_w^*\right) - (\nu+\psi)\right] + \widehat{A}_3}{(\nu+s)\left(\tau^u s^2 + \tau^u \psi s - 1\right)}, \\ D_2 &= \frac{s\widetilde{A}_2 - \left(\nu f_u^* + \psi g_w^*\right)}{(\nu+s)\left(\tau^u s^2 + \tau^u \psi s - 1\right)}, \\ D_3 &= -\frac{\widetilde{A}_3}{(\nu+s)\left(\tau^u s^2 + \tau^u \psi s - 1\right)}. \end{aligned} \tag{3.46}$$

Then, Routh-Hurwitz criterion is applied to determine the local stability of $\mathbf{U}_S^*$, namely:

$$\mathrm{Re}\{\omega\} < 0 \ \forall\omega \iff D_1 > 0 \quad D_3 > 0 \quad D_1 D_2 - D_3 > 0 \tag{3.47}$$

The first two conditions lead to:

$$\begin{aligned} &\text{(i)} && \text{if } \tau^u f_u^* - 1 > 0 \quad \wedge \quad s_4 > s_2 \quad \Rightarrow \quad s_1 < s < \min\{s_2, s_3\} \\ &\text{(ii)} && \text{if } \tau^u f_u^* - 1 > 0 \quad \wedge \quad s_4 < s_2 \quad \Rightarrow \quad s_1 < s < s_3 \vee s_4 < s < s_2 \\ &\text{(iii)} && \text{if } \tau^u f_u^* - 1 < 0 \quad \wedge \quad s_1 > s_3 \quad \Rightarrow \quad \max\{s_1, s_4\} < s < s_2 \\ &\text{(iv)} && \text{if } \tau^u f_u^* - 1 < 0 \quad \wedge \quad s_1 < s_3 \quad \Rightarrow \quad s_1 < s < s_3 \vee s_4 < s < s_2 \end{aligned} \tag{3.48}$$

where

$$\begin{aligned} s_{1,2} &= \tfrac{1}{2}\left(-\psi \mp \sqrt{\psi^2 + 4/\tau^u}\right), \\ s_{3,4} &= \tfrac{1}{2\widehat{A}_1}\left[\tau^u\left(\nu f_u^* + \psi g_w^*\right) - (\nu+\psi) \mp \sqrt{\left[\tau^u\left(\nu f_u^* + \psi g_w^*\right) - (\nu+\psi)\right]^2 + 4A_1\widehat{A}_3}\right]. \end{aligned} \tag{3.49}$$

Note that (3.54) represents the restrictions provided by the hyperbolic nature of the model that, as expected, imposes the speed of propagation to be limited. Indeed, in the parabolic limit $\tau^u \to 0$, the previous conditions reduce to:

$$\begin{cases} s < \tilde{s}_3 \quad \vee \quad s > \tilde{s}_4 \\ \left[s^2 + (\psi+\nu)\, s + \psi\nu + g_w^*\right]\left[\left(g_w^* + f_u^*\right) s + \psi g_w^* + \nu f_u^*\right] - (s+\nu)\left(f_u^* g_w^* - f_w^* g_u^*\right) > 0 \end{cases} \tag{3.50}$$

where

$$\tilde{s}_{3,4} = -\frac{1}{2}\left[\psi + \nu \pm \sqrt{(\psi-\nu)^2 - 4g_w^*}\right] \tag{3.51}$$

which highlight the absence of an upper limit, so allowing the possibility to achieve the paradox of an *infinite* propagation speed.

On the other hand, violation of the last condition in (3.55) defines the locus of Hopf instability:

$$\begin{aligned} &\left\{-s^2 A_1 + s\left[\tau^u\left(\nu f_u^* + \psi g_w^*\right) - (\nu+\psi)\right] + \widehat{A}_3\right\}\left[s\widetilde{A}_2 - \left(\nu f_u^* + \psi g_w^*\right)\right] \\ &\quad + \widetilde{A}_3\,(\nu+\psi)\left(\tau^u s^2 + \tau^u \psi s - 1\right) = 0. \end{aligned} \tag{3.52}$$

As known [64, 122, 123], the occurrence of Hopf bifurcation at $\mathbf{U}_S^*$ to a small amplitude periodic solution of the ODEs system (3.44) corresponds to a travelling wave solution of the PDEs system (3.32)-(3.33).

Unfortunately, due to the highly nonlinear structure of the implicit locus (3.52) on the plant loss B, information can only be extracted numerically. Outcomes of this analysis are shown in Fig.3.19 where the locus of Hopf instability is depicted for different values of the inertial time τ^u, considering $\nu = 182.5$, $\psi = 1$ and $A = 2.8$. This parameter set falls into setup (iii) of (3.54). In the same figure, the horizontal lines represent the constraints $s = s_1$ and $s = s_2$, whereas the condition $s = s_4$ is not depicted as it always lies below the Hopf locus and brings no contribution. Considering the whole restrictions, the stability region varies with the inertial times as shown in Fig.3.20, where all the quantities have been recast in the original dimensional variables (according to [41], the plant mortality $\mathcal{B}$ is related to the dimensionless one by $\mathcal{B} = 4B$). As it can be noticed, despite larger values of inertial times enlarge the region defined by the Hopf locus (as one can argue from Fig.3.19), they progressively restrict the set of allowed speed, according to the stability conditions (3.54)(iii), as depicted by the colored areas in Fig.3.20.

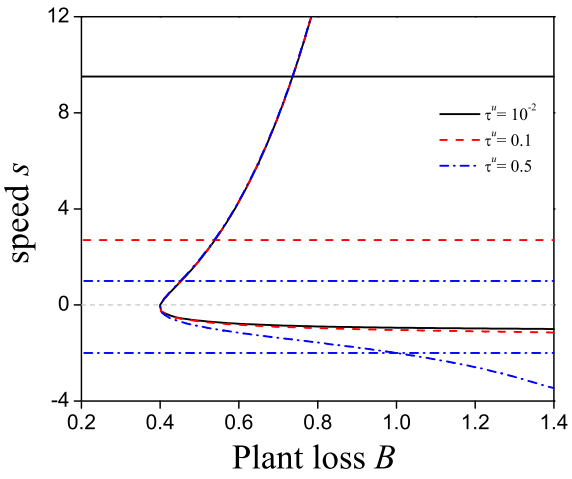

Figure 3.19: Loci of Hopf instability in the (B, s) parameter plane for different values of inertial time τ^u. Horizontal lines denote the constraints arising from eq.(3.54). Fixed parameters: $\nu = 182.5$, $\psi = 1$ and $A = 2.8$.

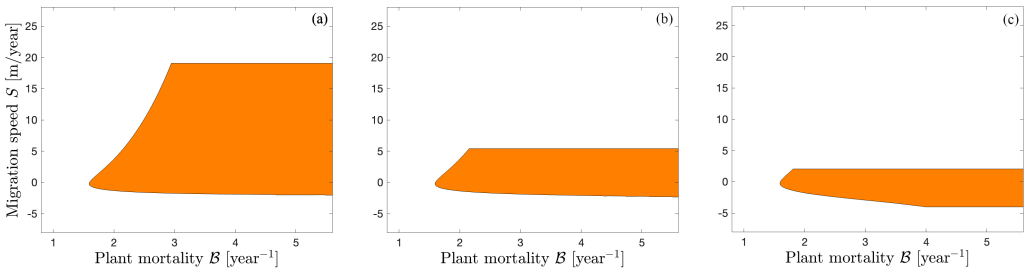

Figure 3.20: Stability regions for travelling waves in the $(\mathcal{B}, S)$ plane as the inertial time is varied: (a) $\tau^u = 10^{-2}$, (b) $\tau^u = 0.1$ and (c) $\tau^u = 0.5$.

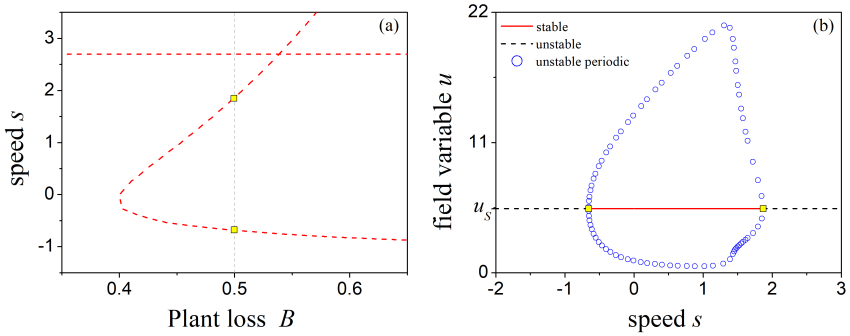

Figure 3.21: (a) Locus of Hopf instability in the (B, s) plane for $\tau^u = 0.1$. (b) The corresponding bifurcation diagram obtained for $B = 0.5$. The parameter set is the same as the one used in Fig.3.19.

Finally, to gain more insights into this phenomenon, we fix the inertial time at $\tau^u = 0.1$ and compare the theoretical predictions (3.54)(iii),(3.52) with the numerical ones extracted from the bifurcation diagram obtained for $B = 0.5$ and built by the XPPAUT tool [124]. Results are shown in Fig.3.21. In both panels of this figure, the yellow squares define the upper and lower bounds of the admitted wave speed within which the limit cycle (represented by blue circles in the right panel) is observed. As it can be noticed, the excellent agreement here obtained provides a further confirmation of the analysis here carried out.

All the above described results fully agree with the ones depicted in Fig.3.18 and point out that, moving far away from the parabolic limit, pattern dynamics becomes almost stationary. Interestingly, by direct comparison with field data, our findings might, in turn, provide a strategy to estimate the order of magnitude of inertial effects taking place in dryland vegetation dynamics.

3.2.4 Approximated loci of migrating and stationary patterns

In this subsection, an insight into the numerical results conducted previously is first presented with the main aim of extracting qualitative information on emerging traveling patterns. Then, an analytical approximation is discussed to better characterize the migrating and stationary patterns behaviours. In all the subsequent analyses, the water advection speed is set to $\nu = 182.5$, in line with literature values [41].

Firstly, let us focus on the dependence of the critical values of control parameter B_c and wavenumber k_c at the onset of wave instability on inertial time τ^u and secondary seed strength ψ, as theoretically predicted by (3.38) and (3.40), respectively. Results depicted in Fig.3.22 for $A = 1.7$ confirm that, close to the parabolic limit, i.e. $\tau^u \lesssim 1$, the critical values do not appreciably vary with τ^u and ψ. On the other hand, as we progressively move away from the parabolic limit, effects due to hyperbolicity and secondary seed dispersal become evident (see also Fig.3.14(b)). Indeed, even a small increase in ψ yields simultaneously a significant decrease of the critical wavenumber, so giving rise to periodic patterns with larger wavelengths, and an increase of the critical control parameter, which implies a reduction of the pattern forming region.

In order to gain a deeper understanding on the phenomenon of wave instability, let us track the wavenumber dependence of the roots of (3.35) for two points in the (τ^u, B_c)-plane, as reported in Fig.3.22(a). In particular, the points P_1 and P_2 are chosen in such a way they may be representative of dynamics occurring close to and far from the parabolic limit, respectively. Results are depicted in Fig.3.23(a)-(d) for $\psi = 0.2$ and in Fig.3.23(e)-(h) for $\psi = 0.8$. In this figure, panels on the left (right) depict the real (imaginary) parts of the roots of the characteristic equation (3.35) evaluated at P_1 [panels (a),(b),(e),(f)] and P_2 [panels (c),(d),(g),(h)]. As it can be noticed, at the configuration P_1, eq.(3.35) admits always roots with negative real part (see Fig.3.23(a,e)), in line with the theoretical prediction reported in Fig.3.22(a) that this point lies outside the wave bifurcation locus, for all considered values of ψ. On the contrary, at P_2, there is at least one root with positive real part, so that this point lies inside the pattern forming region for any considered value of ψ, see Fig.3.23(c,g), consistently with result of Fig.3.22(a).

To further confirm the theoretically predictions here carried out on wave instability, system (3.32),(3.33) is now integrated numerically by means of COMSOL Multiphysics® [108] in a domain $x \in [0, 200]$ over a time window $t \in [0, 200]$. A small perturbation around the state $\mathbf{U}_S^*$ is taken as initial condition and periodic boundary conditions are considered. Results are depicted in Fig.3.24 and validate our previous findings. Indeed, at point P_1 (panels on the left), the perturbation is absorbed and the system relaxes towards the homogeneous steady state, whereas at point P_2 (panels on the right) the spatial perturbation destabilizes the state and generates a traveling pattern. This observation highlights the role of inertia in modifying the wave bifurcation threshold. At the same time, the comparison between Fig.3.24(b) and (d) allows to elucidate the role of secondary seed dispersal. In fact, as its strength is increased, the migration speed is reduced (notice the smaller slope of bands in (d) with respect to (b)), as a consequence of a larger amount of seeds transported downhill by the overland flow.

Let us now address some investigations to extract additional information from the

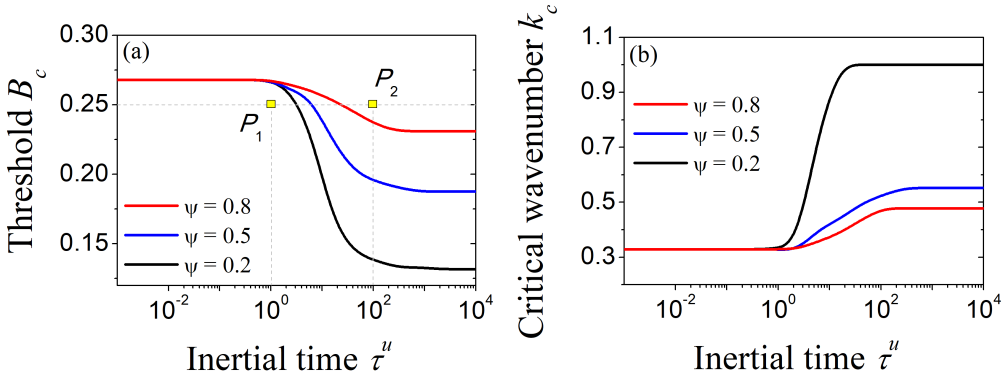

Figure 3.22: Inertial-time dependence of (a) the critical value of control parameter at the onset of wave instability B_c and (b) its associated wavenumber k_c, for different values of seed advection speed ψ. Fixed parameter: $A = 1.7$.

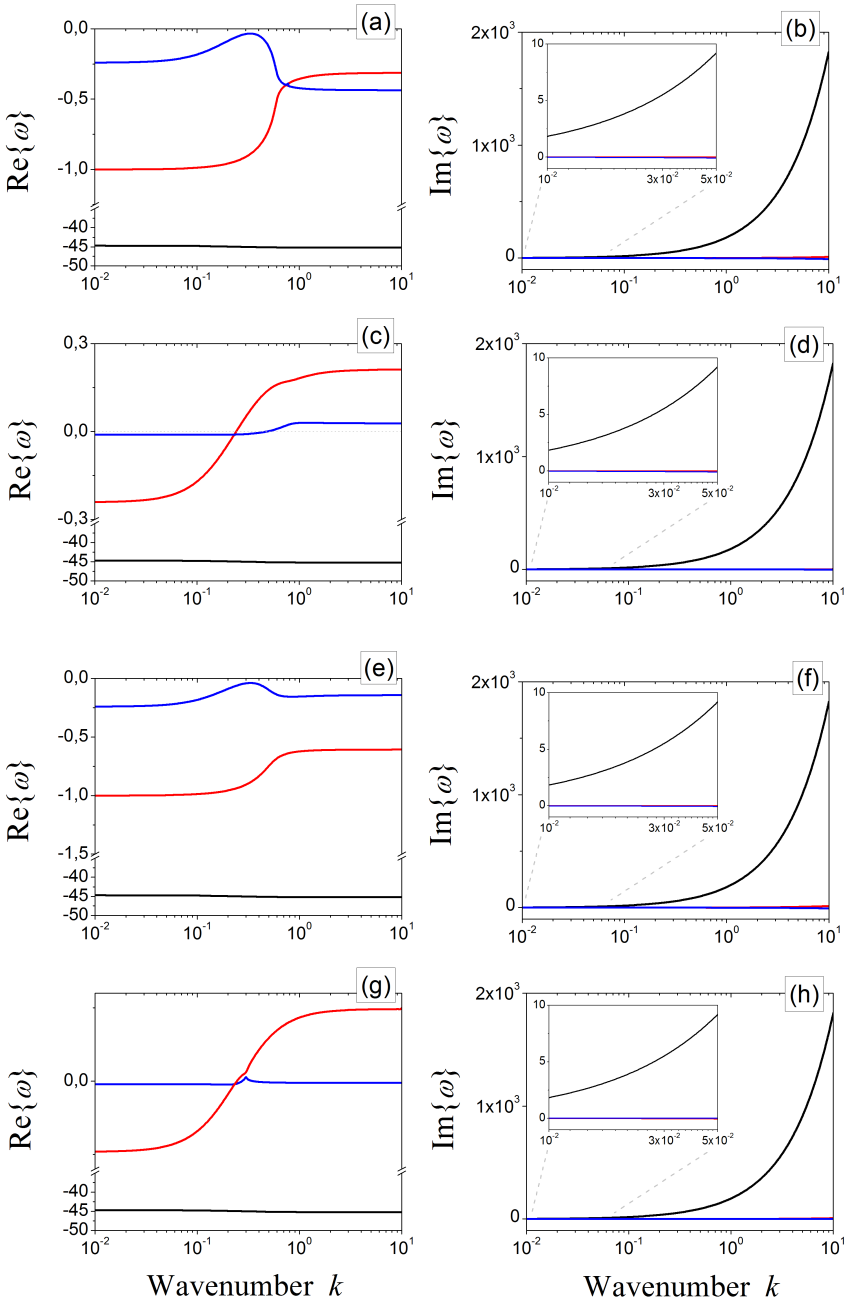

Figure 3.23: Real (left panels) and imaginary (right panels) parts of the roots $\omega_{1,2,3}$ of the characteristic polynomial (3.35) as a function of the wavenumber, obtained for $\psi = 0.2$ [panels (a)-(d)] and $\psi = 0.8$ [panels (e)-(h)]. Panels (a),(b),(e),(f) correspond to the point P_1, whereas (c),(d),(g),(h) to P_2. Blue, red and black lines are representative of ω_1, ω_2 and ω_3, respectively. Fixed parameters: $A = 1.7$ and $B = 0.25$.

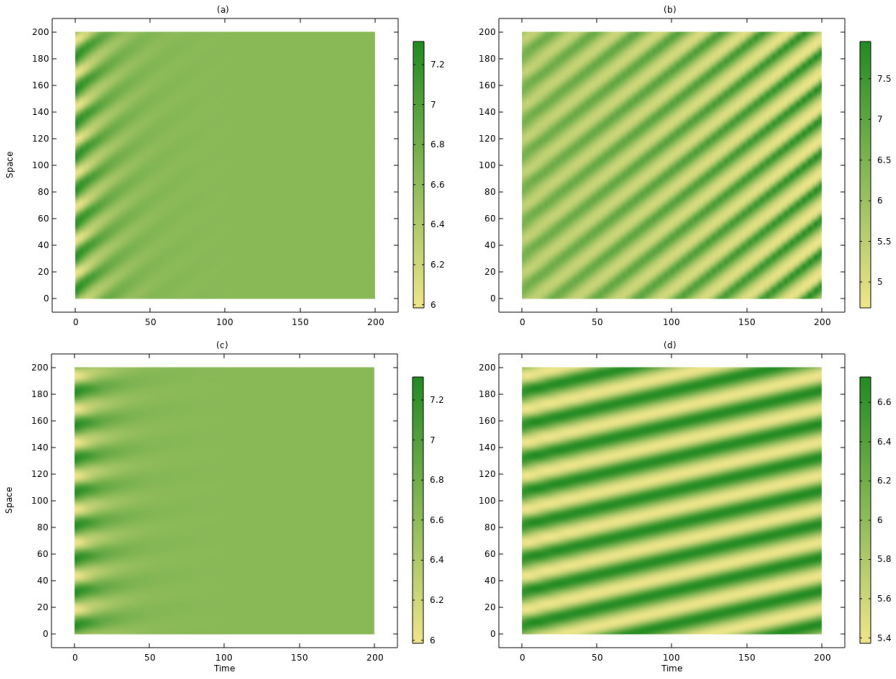

Figure 3.24: Spatio-temporal evolution obtained by numerical integration of the governing system in the configurations P_1 (left panels) and P_2 (right panels). Results in the top row are obtained for $\psi = 0.2$ whereas those in the bottom row for $\psi = 0.8$. Other parameters as in Fig.3.23.

characteristic equation. In particular, let us track the behavior of the three complex roots of the eq.(3.35) with the aim of identifying and determining at least an approximate expression of the functional dependence of the root responsible for the stability character of the steady state. Let us denote the roots as

$$\omega_1 = \alpha + i\beta, \qquad \omega_2 = \gamma + i\delta, \qquad \omega_3 = \theta + i\zeta, \tag{3.53}$$

where α, β, γ, δ, θ, $\zeta \in \mathbb{R}$. Then, by substituting (3.53) into (3.35), the following system in six unknowns (α, β, γ, δ, θ, ζ) is obtained:

$$\begin{cases} \alpha + \gamma + \theta = 1 + u_S^2 - B - \frac{1}{\tau^u} \\ \beta + \delta + \zeta = k\left(\nu + \psi\right) \\ \theta\left(\alpha + \gamma\right) - \zeta\left(\beta + \delta\right) + \alpha\gamma - \beta\delta = \left[\tau^u B\left(u_S^2 - 1\right) + 1 + u_S^2 - B + \left(\tau^u \nu\psi - 1\right) k^2\right] / \tau^u \\ \zeta\left(\alpha + \gamma\right) + \theta\left(\beta + \delta\right) + \alpha\delta + \beta\gamma = k\left[\nu B - \psi\left(1 + u_S^2\right) - \left(\nu + \psi\right) / \tau^u\right] \\ \theta\left(\beta\delta - \alpha\gamma\right) + \zeta\left(\alpha\delta + \beta\gamma\right) = \left[B\left(u_S^2 - 1\right) + \left(1 + u_S^2 - \nu\psi\right) k^2\right] / \tau^u \\ \zeta\left(\beta\delta - \alpha\gamma\right) - \theta\left(\alpha\delta + \beta\gamma\right) = k\left[\nu B - \psi\left(1 + u_S^2\right) - \nu k^2\right] / \tau^u \end{cases} \tag{3.54}$$

Owing to the nontrivial structure of the above system, some simplifying assumptions are needed. One of them has an ecological foundation, i.e. $\psi \ll \nu$, as the rate at which seeds are passively transported downhill by the overland flow is quite small in comparison with the water advection speed [41, 45, 64]. Some others can be deduced mathematically from the inspection of the qualitative behaviour of the roots reported in Fig.3.23. In particular, noticing that the real and imaginary parts of ω_3 are different orders of magnitude larger than those of the other roots, it is reasonable to assume that $\zeta \gg |\delta|, |\beta|$ and $|\theta| \gg |\alpha|, |\gamma|$. Consequently, according to $(3.54)_1$ and $(3.54)_2$, the real and the imaginary part of ω_3 can be safely approximated by $\mathrm{Re}(\omega_3) \approx f_u^* + g_w^* - \frac{1}{\tau^u}$ and $\mathrm{Im}(\omega_3) \approx k\nu$, respectively. Note that, according to (B.3), $\mathrm{Re}(\omega_3)$ is thus always negative and indeed such a root does not determine the stability character of $\mathbf{U}_S^*$.

By considering all the previous assumptions, the system (3.54) can be approximated as

$$\begin{cases} \left(1+u_S^2-B-\frac{1}{\tau^u}\right)(\alpha+\gamma)-k\nu\,(\beta+\delta)+\alpha\gamma-\beta\delta=\left[\tau^u B\left(u_S^2-1\right)+1+u_S^2-B+\left(\tau^u\nu\psi-1\right)k^2\right]/\tau^u \\ k\nu\,(\alpha+\gamma)+\left(1+u_S^2-B-\frac{1}{\tau^u}\right)(\beta+\delta)+\alpha\delta+\beta\gamma=k\left[\nu B-\psi\left(1+u_S^2\right)-(\nu+\psi)/\tau^u\right] \\ \left(1+u_S^2-B-\frac{1}{\tau^u}\right)(\beta\delta-\alpha\gamma)+k\nu\,(\alpha\delta+\beta\gamma)=\left[B\left(u_S^2-1\right)+\left(1+u_S^2-\nu\psi\right)k^2\right]/\tau^u \\ k\nu\,(\beta\delta-\alpha\gamma)-\left(1+u_S^2-B-\frac{1}{\tau^u}\right)(\alpha\delta+\beta\gamma)=k\left[\nu B-\psi\left(1+u_S^2\right)-\nu k^2\right]/\tau^u \end{cases} \tag{3.55}$$

so that the approximate expression for the first two roots is:

$$\begin{aligned} \omega_1 &\approx \eta-\gamma+i\left(\tfrac{\theta\gamma-\chi}{\eta-2\gamma}+\theta\right), \\ \omega_2 &\approx \gamma+i\tfrac{\chi-\theta\gamma}{\eta-2\gamma}, \end{aligned} \tag{3.56}$$

where γ is implicitly defined by

$$4\gamma^4-8\eta\gamma^3+\left(5\eta^2+\theta^2-4\mu\right)\gamma^2-\eta\left(\eta^2+\theta^2-4\mu\right)\gamma+\eta\theta\chi-\chi^2-\eta^2\mu=0 \tag{3.57}$$

and

$$\begin{aligned} \eta &= \frac{\left\{1-\tau^u\left[B-\left(1+u_S^2\right)\right]\right\}\left[B-\left(1+u_s^2\right)-\tau^u B\left(u_s^2-1\right)\right]+\tau^u\nu^2k^2(B-1)-k^2-\tau^u\left[B\left(u_S^2-1-k^2\right)+2k^2\left(1+u_S^2\right)\right]}{\left\{1+\tau^u\left[1+u_S^2-B\right]\right\}^2+(\tau^u)^2k^2\nu^2}+ \\ &\quad+\frac{2(\tau^u)^2\nu k^2\left[\nu k^2+\psi\left(1+u_S^2\right)-\nu B\right]\left[1+\tau^u\left(1+u_S^2-B\right)\right]}{\left\{\left[1+\tau^u\left(1+u_S^2-B\right)\right]^2+(\tau^u)^2k^2\nu^2\right\}^2}, \\ \theta &= -\tfrac{1}{k\nu}\left\{\left(\tfrac{1}{\tau^u}+1+u_S^2-B\right)\eta+\left(\tfrac{1}{\tau^u}-\nu\psi\right)k^2+B\left(u_S^2-1\right)+\tfrac{1}{\tau^u}\left(1+u_S^2-B\right)+\right. \\ &\quad\left.+\frac{\left(B-2-u_S^2\right)\left[B\left(u_S^2-1\right)+\left(1+u_S^2+\nu\psi\right)k^2\right]+\tau^u\nu k^2\left[\nu B-\nu k^2-\psi\left(u_S^2+1\right)\right]}{\left\{1+\tau^u\left[1+u_S^2-B\right]\right\}^2+(\tau^u)^2k^2\nu^2}\right\}, \\ \chi &= k\frac{\left\{1-\tau^u\left[B-\left(1+u_S^2\right)\right]\right\}\left[\nu B-\left(1+u_s^2\right)\psi\right]-\nu k^2+\tau^u\nu\left[B\left(u_S^2-1\right)+(B-\nu\psi)k^2\right]}{\left\{1+\tau^u\left[1+u_S^2-B\right]\right\}^2+(\tau^u)^2k^2\nu^2}, \\ \mu &= -\frac{\left\{1-\tau^u\left[B-\left(1+u_S^2\right)\right]\right\}\left[B\left(u_s^2-1\right)+\left(1+u_S^2\right)k^2\right]-\nu\psi k^2+\tau^u\nu^2k^2\left[k^2-B\right]}{\left\{1-\tau^u\left[1+u_S^2-B\right]\right\}^2+(\tau^u)^2k^2\nu^2}. \end{aligned} \tag{3.58}$$

To check the validity of the approximated formulation carried out so far, in Fig.3.25 we present the comparison between numerically-computed (solid lines) and approximated (symbols) values of the complex roots of characteristic equation (3.35). Without loss of generality, let us evaluate these roots at the points P_1 and P_2 previously introduced. Based on the satisfying agreement achieved in all cases, with particular focus on the range of wavenumber where the real part of the roots crosses the zero, it is possible to inspect in more detail the functional dependencies of ω_1 and ω_2.

Results shown in Fig.3.25 suggest also that ω_1 cannot produce any spatial instability through Turing or wave instabilities. Indeed, its real part does not cross the real axis through a maximum. Instead, it may give rise to a different kind of instability as it originates an infinite range of unstable wavenumbers. Therefore, the only root that might be responsible for oscillatory or stationary patterns is ω_2, whose real part exhibits the required behavior [see Fig.3.25(b),(e)]. For an oscillatory instability to take place, we thus need to impose the following conditions (to hold for $k \neq 0$):

$$\begin{cases} \mathrm{Re}(\omega_2) = 0 \\ \frac{\partial \mathrm{Re}(\omega_2)}{\partial k} = 0 \end{cases} \tag{3.59}$$

that, by virtue of (3.56),(3.57), reduce to:

$$\begin{cases} \eta\theta\chi - \chi^2 - \eta^2\mu = 0 \\ \frac{\partial}{\partial k}\left[\eta\theta\chi - \chi^2 - \eta^2\mu\right] = 0 \end{cases} \tag{3.60}$$

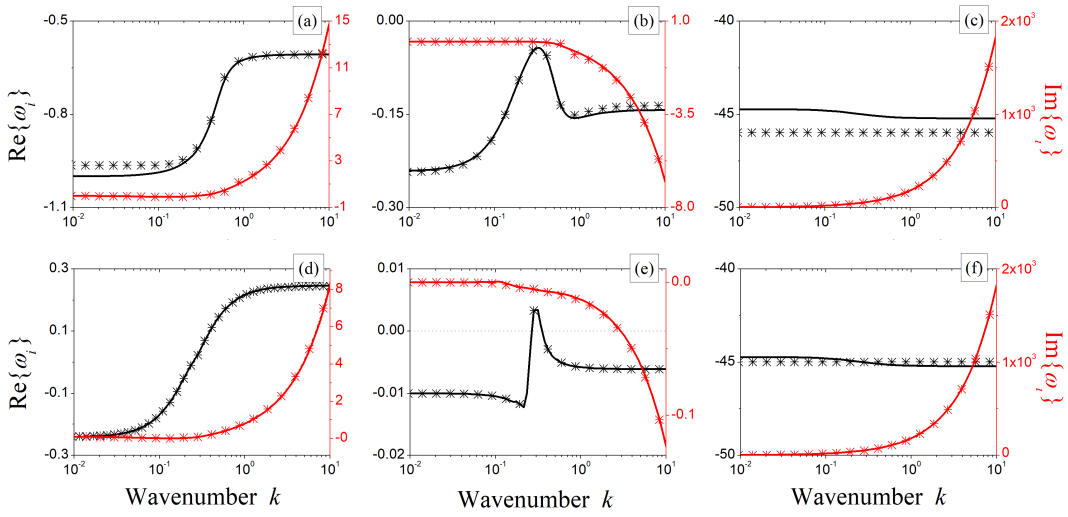

Figure 3.25: Comparison between numerically computed (solid lines) and theoretically estimated (symbols) roots of the complex characteristic equation (3.35) evaluated at the points P_1 [panels (a),(b),(c)] and P_2 [panels (d),(e),(f)]. Real parts are depicted in black, whereas the imaginary ones in red. Root ω_1 is represented in panels (a),(d); ω_2 is depicted in (b),(e) whereas ω_3 in (c),(f). Fixed parameters: $\psi = 0.8$, $A = 1.7$ and $B = 0.25$.

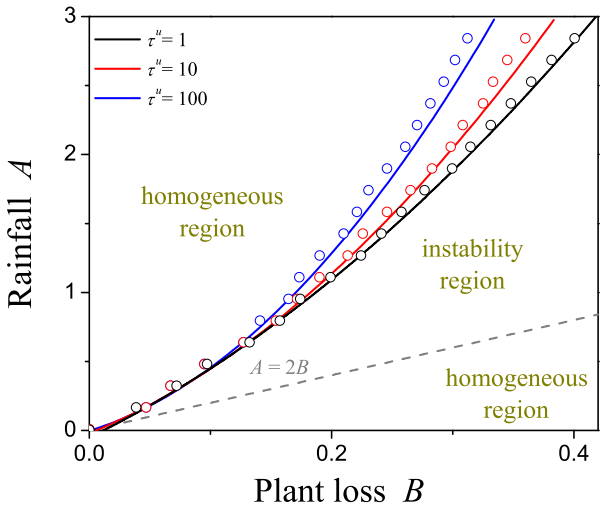

Figure 3.26: The locus at which spatial bifurcations occur for different values of inertial time τ^u. Solid lines represent the numerically computed loci, whereas symbols denote the theoretically approximated predicted ones. Fixed parameters: $\psi = 0.8$.

Note that, equations (3.60) implicitly define the approximated critical wavenumber and the locus at which wave bifurcation occurs, respectively. Again, to check the validity of the approximated bifurcation locus, a comparison with numerical results arising from the exact expression defined in (3.40) is addressed. Results shown in Fig.3.26 confirm a satisfactory agreement, for all the considered values of inertial times, revealing that eq.(3.60) may be safely used as an approximate description of key features associated to oscillatory patterns near criticality.

With this in mind, the migration speed of the oscillatory pattern at onset, under the hypothesis that the only excited mode is the one characterizerd by the largest growth rate, is proportional to $\mathrm{Im}(\omega_2) = \delta$. In particular, positive (negative) values of δ correspond to patterns migrating downhill (uphill) whereas null values are representative of stationary patterns. Therefore, taking into account (3.53) and (3.56), the approximated locus of stationary patterns is implicitly defined by:

$$\theta\gamma - \chi = 0. \tag{3.61}$$

It should be noticed that such a locus exhibits a dependence on inertial time through the coefficients θ, γ, and χ. Moreover, due to the implicit definition of γ, it is necessary to still rely on numerical investigations. However, the approximate expression (3.61) enables the possibility of evaluating the occurrence of stationary patterns in the whole parameter plane, being conscious that its validity has to be restricted to close-to-threshold values. To this aim, numerical investigations are carried out and the results are depicted in Fig.3.27 for different values of inertial time τ^u. First of all, let us focus on the behaviour of stationary patterns at the onset of criticality, which corresponds to the intersection in the (B, A)-plane between the locus

of null-migration patterns (red curve) and the wave instability one (black one). As it can be noticed, for $\tau^u \leq 1$ (panels (a)-(d)), hyperbolicity yields a negligible effect on such an intersection point, in reasonable agreement with our previous results (see Fig.3.34), so confirming that $\tau^u \simeq 1$ can be considered a good approximation of the parabolic limit. When inertial effects become more relevant, the onset of stationary patterns takes place for progressively smaller values of the main control parameter (notice the different scales of the axes in panels (e)-(f)), so enlarging the region characterized by uphill migration of bands. Then, moving away from wave instability threshold, the behavior of the theoretically-predicted locus of stationary patterns is non-monotonous with respect to variations of inertial time. Indeed, the region of uphill migration shrinks from panel (a) to (c) whereas it enlarges from (d) to (f). All these results are in line with previous theoretical findings [80].

Finally, as illustrative example of out-of-equilibrium dynamics, let us integrate the governing system (3.32),(3.33) over $x \in [0, 200]$ in a time window $t \in [0, 100]$ by fixing the inertial time at $\tau^u = 1$ and considering the configurations in the (B, A) plane depicted in Fig.3.28(a). In particular, points $Q_1 = (0.2, 1)$, $Q_2 = (0.23, 1.3)$ and $Q_3 = (0.25, 1.5)$ correspond to near criticality conditions whereas $Q_4 = (0.5, 0.18)$ and $Q_5 = (0.5, 0.23)$ to far-from-threshold ones. Overall results are shown in Fig.3.28(b)-(f).

In detail, the theoretically-predicted downhill, stationary or uphill motion of bands observed near criticality at the configurations Q_1, Q_2 and Q_3, respectively, is confirmed by numerical simulations, see panels (b)-(d). On the contrary, in far-from-threshold conditions, numerical results confirm the downhill motion occurring at Q_4 (see panel (e)) but contradict the predictions on the uphill motion at Q_5, where patterns still migrate downhill (see panel (f)). These observations provide a rough estimation of the range of validity of the approximated stationary locus. At the same

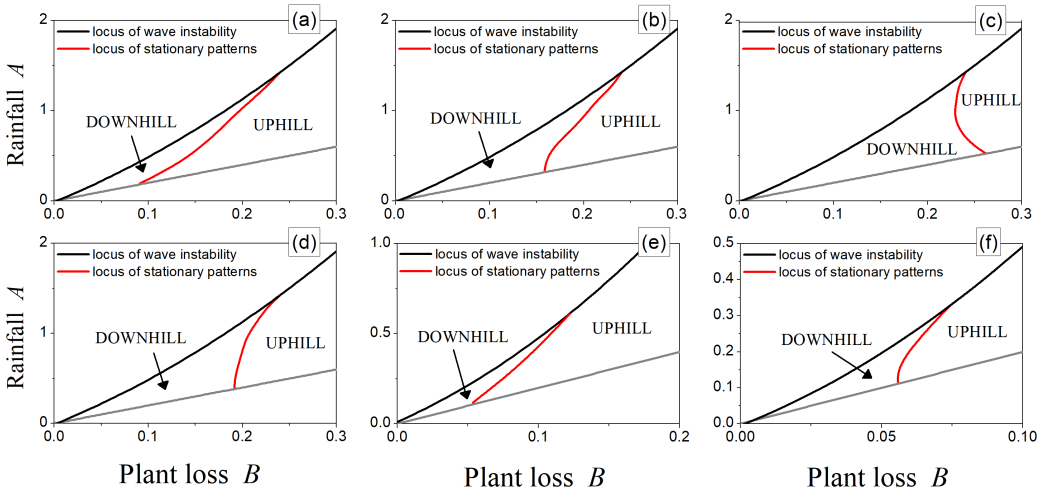

Figure 3.27: Loci of wave instability (black lines) and null-migration patterns (red lines) for (a) $\tau^u = 10^{-5}$, (b) $\tau^u = 10^{-3}$, (c) $\tau^u = 10^{-2}$, (d) $\tau^u = 1$, (e) $\tau^u = 10$, (f) $\tau^u = 10^2$. Fixed parameter $\psi = 0.8$.

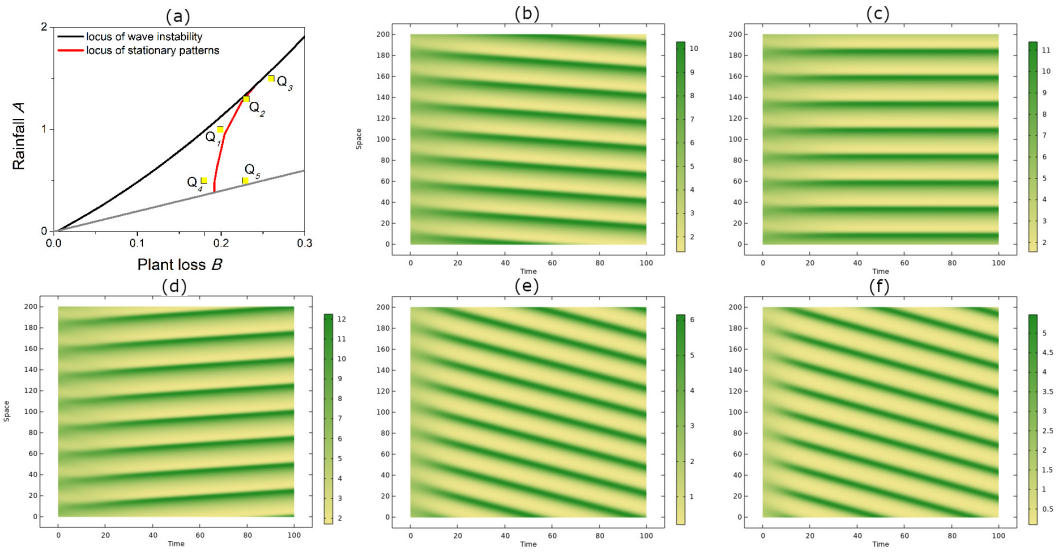

Figure 3.28: (a) Detail of Fig.3.27(d) and configurations Q_i (i=1,...,5) in which numerical simulations of system (3.32),(3.33) are performed. Panels (b)-(f) denote the spatio-temporal evolutions obtained in: (b) Q_1, (c) Q_2, (d) Q_3, (e) Q_4 and (f) Q_5. Fixed parameter: $\psi = 0.8$.

time, such simulations suggest that the downhill motion of bands is the predominant behavior occurring in out-of-equilibrium conditions.

3.2.5 Concluding remarks

In this section we propose a twofold generalization of the Klausmeier model. Compared to the original parabolic model [41], the one here discussed also accounts for: (i) secondary dispersal of seeds, through an additional advection term and (ii) inertial effects on the vegetation component, which lead to build up an hyperbolic framework. Patterned vegetation dynamics are analyzed by means of LSA in order to deduce and characterize the locus of wave instability as a function of all the model parameters. Moreover, additional information on the pattern speed are extracted by means of periodic travelling waves. To inspect the behaviour of stationary and migrating patterns, analytical approximations for the wave instability locus such as for the pattern speed, the locus of null-migrating patterns, and the excited wavenumber are provided. Theoretical predictions, which are complemented by numerical simulations, allow to draw several conclusions.

First, the pattern-forming region enlarges (reduces) as the inertial time (seed advection speed) increases, as depicted in Fig.3.12 and Fig.3.14. Therefore, the presence of inertia does not only affect transient dynamics, as expected, but also plays an active role in allowing pattern dynamics to be observed over a wider range of model parameters.

Then, the proposed hyperbolic generalization of the Klausmeier model may provide a satisfying description of experimental data for both migrating and stationary patterns. Indeed, close to the parabolic limit, the model allows to reproduce both

directions of pattern propagation as a function of seed advection speed, as shown in Figs.3.15-3.18. On the contrary, far from the parabolic limit and independently of secondary seed dispersal, the theoretically-predicted migration speed approaches the zero value so mimicking the regime of quasi-stationary patterns. The constraints on the allowed wave speed arising from the hyperbolic nature of the model are particularly tangible in Figs.3.19,3.20, where the stability region of travelling waves progressively shrinks as the inertial time is increased.

Finally, the analytical approximation analysis here conducted shows results which agree well with the numerically ones, see Figs.3.25-3.26. On one hand, near the parabolic limit, the dynamics of stationary patterns at the onset of criticality are unaffected by hyperbolicity whereas, on the other hand, far from it inertial effects favor the presence of uphill patterns, see Figs.3.27-3.28.

Results here obtained might shed some light on the current debate on the mechanisms responsible for the effective migration on vegetation bands along slopes of arid terrains. At the same time, despite the huge difficulties encountered in addressing such long-term experimental field observations, a larger and more accurate availability of field data might provide an indirect estimation of the order of magnitude of plant inertia.

Chapter 4

Stationary patterns in 2D hyperbolic RT systems

In the literature of hyperbolic bio-mathematical models not based on the ET theory, the occurrence of stationary and non-stationary Turing patterns in the bi-dimensional framework has been mostly investigated by means of LSA tools and numerical simulations [15, 16, 32–35]. However, no efforts have been there made to address nonlinear stability analyses aimed to the characterization of these structured solutions. The investigations carried out here constitute an attempt to fill this gap. In detail, two widely used patterned planform geometries will be taken into account: rhombs and hexagons.

In line with the previous chapters, the present study also aims to elucidate the role played by inertia in the formation of bidimensional stationary patterns. This analysis is stimulated by the dynamics observed in the context of dryland ecology, where the interaction-competition between water and vegetation biomass gives rise to several fascinating patterns with different geometries [7, 41, 53, 58, 60–62, 65, 66].

In this chapter the formation of rhombic and hexagonal Turing patterns in bidimensional hyperbolic RT systems (1.5)-(1.7) is addressed in the case where only a diffusive character is taken into account ($\psi = \nu = 0$). In order to keep the thesis at a reasonable length, all the analyses are performed in the context of dryland ecology. Results can be however generalized by considering generic kinetic terms.

This chapter is organized as follows. In Section 4.1, LSA is performed on the steady states, with the main aim of determining the conditions under which Turing instability takes place. This analysis is useful to establish the critical values of the wavenumber and of the control parameter (here assumed the plant loss), around which the subsequent analyses originate. In Section 4.2, multiple-scale WNA is addressed for both rhombic and hexagonal planform geometries, with the aim of deducing the equations ruling the pattern evolution close to onset and to highlight the role played by inertia in this context. Finally, numerical simulations are also discussed to corroborate the theoretical predictions as well as to provide additional insights into the inertial-dependence of the transient dynamics between an uniform state towards a patterned state. Concluding remarks are given in the last section.

4.1 LSA

Under the hypothesis that the two species undergo isotropic diffusive transport only, the 2D hyperbolic reaction-transport model (1.5)-(1.7) reads:

$$\mathbf{U}_t + \mathrm{M}^{(1)}(\mathbf{U})\mathbf{U}_x + \mathrm{M}^{(2)}(\mathbf{U})\mathbf{U}_y = \mathbf{N}(\mathbf{U}, B) \tag{4.1}$$

where the 6×6 matrices $\mathrm{M}^{(1)}$ and $\mathrm{M}^{(2)}$ are expressed as

$$\mathrm{M}^{(1)} = \begin{bmatrix} 0 & 0 & 1 & 0 & 0 & 0 \\ 0 & 0 & 0 & 0 & 1 & 0 \\ \frac{1}{\tau^u} & 0 & 0 & 0 & 0 & 0 \\ 0 & 0 & 0 & 0 & 0 & 0 \\ 0 & \frac{d}{\tau^w} & 0 & 0 & 0 & 0 \\ 0 & 0 & 0 & 0 & 0 & 0 \end{bmatrix}, \quad \mathrm{M}^{(2)} = \begin{bmatrix} 0 & 0 & 0 & 1 & 0 & 0 \\ 0 & 0 & 0 & 0 & 0 & 1 \\ 0 & 0 & 0 & 0 & 0 & 0 \\ \frac{1}{\tau^u} & 0 & 0 & 0 & 0 & 0 \\ 0 & 0 & 0 & 0 & 0 & 0 \\ 0 & \frac{d}{\tau^w} & 0 & 0 & 0 & 0 \end{bmatrix} \tag{4.2}$$

and the vectors of field variables and kinetic terms are given by

$$\begin{aligned} \mathbf{U} &= \left[u\,, w\,, J_1^u, J_2^u, J_1^w, J_2^w\right]^T \\ \mathbf{N}\left(\mathbf{U}, B\right) &= \left[f(u,w,B),\, g(u,w,B),\, -J_1^u/\tau^u, -J_2^u/\tau^u,\, -J_1^w/\tau^w,\, -J_2^w/\tau^w\right]^T. \end{aligned} \tag{4.3}$$

Its spatially-homogeneous steady states $\mathbf{U}^* \equiv [u^*, w^*, \mathbf{J}^{u^*}, \mathbf{J}^{w^*}]^T$ are the same as those achieved in Section 1.4.

Let us now analyze in detail the local stability character of these steady states with the goal of establishing the possibility to observe Turing patterns. To this aim, let us linearize the governing system through

$$\mathbf{U} = \mathbf{U}^* + \widetilde{\mathbf{U}} \exp\left(\omega t + \mathrm{i}\, k_1 x + \mathrm{i}\, k_2 y\right) \tag{4.4}$$

which leads to

$$\left[\omega \mathrm{I} + \mathrm{i}\left(k_1 \mathrm{M}^{(1)} + k_2 \mathrm{M}^{(2)}\right) - \left(\nabla_{\mathbf{U}} \mathbf{N}\right)\right]^* \widetilde{\mathbf{U}} = \mathbf{0} \tag{4.5}$$

where the asterisk denotes that the functions are evaluated at $\mathbf{U}^*$, $\mathbf{I}$ is 6×6 identity matrix, while ω and $\mathbf{k} = (k_1, k_2)$ represent the growth factor and the wavevector, respectively. The growth factor ω satisfies the following characteristic equation

$$\left(\omega + \frac{1}{\tau^u}\right)\left(\omega + \frac{1}{\tau^w}\right)\left(\omega^4 + A_1\omega^3 + A_2\omega^2 + A_3\omega + A_4\right) = 0 \tag{4.6}$$

where

$$\begin{aligned} A_1 &= \tfrac{1}{\tau^u} + \tfrac{1}{\tau^w} - \left(f_u^* + g_w^*\right), \\ A_2 &= \left(\tfrac{1}{\tau^u} + \tfrac{d}{\tau^w}\right) k^2 + \tau^u\tau^w - \left(f_u^* + g_w^*\right)\left(\tfrac{1}{\tau^u} + \tfrac{1}{\tau^w}\right) + f_u^* g_w^* - f_w^* g_u^*, \\ A_3 &= \left[\left(d+1\right)\tau^u\tau^w - f_u^*\tfrac{d}{\tau^w} - g_w^*\tfrac{1}{\tau^u}\right] k^2 + \left(f_u^* g_w^* - f_w^* g_u^*\right)\left(\tfrac{1}{\tau^u} + \tfrac{1}{\tau^w}\right) - \left(f_u^* + g_w^*\right)\tau^u\tau^w, \\ A_4 &= \tfrac{d}{\tau^u\tau^w}\left[k^4 - \left(f_u^* + \tfrac{g_w^*}{d}\right) k^2 + \tfrac{f_u^* g_w^* - f_w^* g_u^*}{d}\right], \end{aligned}$$

and $k = |\mathbf{k}|$. We note that, since $\omega_1 = -\frac{1}{\tau^u}$ and $\omega_2 = -\frac{1}{\tau^w}$ are always real and negative, the stability character of the steady state $\mathbf{U}^*$ depends on the sign of the quartic equation

$$\omega^4 + A_1\omega^3 + A_2\omega^2 + A_3\omega + A_4 = 0 \tag{4.7}$$

which formally coincides with the one found in the 1D case [76] except k represents the modulus of the 2D wavevector. In the absence of diffusion ($\mathbf{k} = \mathbf{0}$), equation (4.7) can be factorized as

$$\left(\omega + \frac{1}{\tau^u}\right)\left(\omega + \frac{1}{\tau^w}\right)\left[\omega^2 - (f_u^* + g_w^*)\omega + (f_u^* g_w^* - f_w^* g_u^*)\right] = 0 \tag{4.8}$$

so that the steady state $\mathbf{U}^*$ is asymptotically linearly stable iff

$$f_u^* + g_w^* < 0, \qquad f_u^* g_w^* - f_w^* g_u^* > 0. \tag{4.9}$$

Therefore, considering Klausmeier kinetics as in (1.2), as it can be easily noticed, the desert state $\mathbf{U}_D^*$ and the vegetated state $\mathbf{U}_S^*$ are stable whereas $\mathbf{U}_L^*$ is always unstable.

In the case of non-homogeneous perturbations, the equation (4.7) evaluated at $\mathbf{U}_D^*$ admits the following explicit solutions

$$\omega_{3,4} = -\frac{1}{2}\left(1 + \frac{1}{\tau^w} \pm \sqrt{\left(1 - \frac{1}{\tau^w}\right)^2 - 4\frac{d}{\tau^w}k^2}\right) \tag{4.10}$$

$$\omega_{5,6} = -\frac{1}{2}\left(B + \frac{1}{\tau^u} \pm \sqrt{\left(B - \frac{1}{\tau^u}\right)^2 - 4\frac{1}{\tau^u}k^2}\right), \tag{4.11}$$

so that we can conclude that $\mathbf{U}_D^*$ is stable also under non-homogeneous perturbations provided that

$$k^2 \leq \min\left\{\frac{\tau^w}{4d}\left(1 - \frac{1}{\tau^w}\right)^2, \frac{\tau^u}{4}\left(B - \frac{1}{\tau^u}\right)^2\right\}. \tag{4.12}$$

These restrictions on the allowed wavenumbers have an ecological foundation since damped temporal oscillations about the desert state cannot occur. Consequently, the only steady configuration that can give rise to periodic patterns is the uniformly-vegetated state $\mathbf{U}_S^*$. Its stability character can be investigated by means of the Routh-Hurwitz criterion, which reads

$$\operatorname{Re}\omega < 0 \quad \forall\,\omega \Leftrightarrow A_1 > 0, \quad A_3 > 0, \quad A_4 > 0, \quad A_1A_2A_3 > A_3^2 + A_1^2A_4 \quad \forall\,\mathbf{k}. \tag{4.13}$$

Therefore, under assumptions (4.9), A_1 and A_2 are positive for all $\mathbf{k}$ and, in turn, the condition $A_3 > 0$ is redundant. Consequently, the previous conditions reduce to

$$\operatorname{Re}\omega < 0 \quad \forall\,\omega \Leftrightarrow A_4 > 0, \quad A_1A_2A_3 - A_3^2 - A_1^2A_4 > 0 \quad \forall\,\mathbf{k} \tag{4.14}$$

that can be expressed as

$$\begin{aligned} A_4 > 0 \quad &\text{for} \quad df_u^* + g_w^* < 0 \ \text{ or } \ (df_u^* + g_w^*)^2 - 4d\,(f_u^* g_w^* - f_w^* g_u^*) < 0 \\ A_1A_2A_3 - A_3^2 - A_1^2A_4 > 0 \quad &\text{for} \quad f_u^* < \tfrac{1}{\tau^u} \end{aligned} \tag{4.15}$$

Thus, in the case of Klausmeier kinetics (1.2), the necessary conditions for diffusion-driven instabilities yielding Turing patterns are given by

$$\begin{cases} B-1-u_S^2<0 \\ B\left(u_S^2-1\right)>0 \\ dB-\left(1+u_S^2\right)>0 \\ \left(dB-1-u_S^2\right)^2-4dB\left(u_S^2-1\right)>0 \\ B<\frac{1}{\tau^u} \end{cases} \tag{4.16}$$

As known, the onset of Turing bifurcation corresponds to the presence of a null root of the characteristic equation (4.6) for a value of $\mathbf{k}\neq\mathbf{0}$ which is tantamount to requiring $A_4(k^2)=0$. Therefore, by assuming B as the main control parameter, its critical value B_c at the bifurcation threshold is given by

$$B_c=\frac{3u_{S_c}^2-1+2u_{S_c}\sqrt{2\left(u_{S_c}^2-1\right)}}{d} \tag{4.17}$$

being $u_{S_c}=\frac{A+\sqrt{A^2-4B_c^2}}{2B_c}$. Consequently, the critical value of the modulus of wavevector k_c can be defined as

$$k_c^2=\sqrt{\frac{B_c\left(u_{S_c}^2-1\right)}{d}}. \tag{4.18}$$

As can be noticed, hyperbolicity does not affect the instability threshold and the critical wavenumber of the emerging stationary patterns [75–77, 79]. Moreover, notice that the results here obtained coincide with the ones obtained in the 1D case (2.5)-(2.6), where the scalar wavenumber is here replaced by its modulus.

4.2 WNA

Let us now perform a weakly nonlinear stability analysis on the uniform steady state $\mathbf{U}_S^*$ about the critical value of the control parameter B_c determining Turing instability. Note that, a similar analysis was already performed for two-dimensional parabolic models [125–132].

To this aim, let us consider the following expansions for the main control parameter B, the field variables $\mathbf{U}$ and the time t as:

$$\begin{aligned} B&=B_c+\epsilon B_1+\epsilon^2B_2+\epsilon^3B_3+O\left(\epsilon^4\right) \\ \mathbf{U}&=\mathbf{U}_S^*+\epsilon\mathbf{U}_1+\epsilon^2\mathbf{U}_2+\epsilon^3\mathbf{U}_3+O\left(\epsilon^4\right) \\ \frac{\partial}{\partial t}&=\epsilon\frac{\partial}{\partial T_1}+\epsilon^2\frac{\partial}{\partial T_2}+\epsilon^3\frac{\partial}{\partial T_3}+O\left(\epsilon^4\right) \end{aligned} \tag{4.19}$$

Substituting (4.19) into the governing system (4.1)-(4.3), taking into account the Klausmeier kinetic (1.2), and collecting terms of the same orders of ϵ, the following

set of linear partial differential equations is obtained

$$\begin{aligned}
&\text{at order } \epsilon \quad \mathrm{M}^{(1)}\tfrac{\partial \mathbf{U}_1}{\partial x}+\mathrm{M}^{(2)}\tfrac{\partial \mathbf{U}_1}{\partial y}=L_c^*\mathbf{U}_1\\
&\text{at order } \epsilon^2 \quad \mathrm{M}^{(1)}\tfrac{\partial \mathbf{U}_2}{\partial x}+\mathrm{M}^{(2)}\tfrac{\partial \mathbf{U}_2}{\partial y}=L_c^*\mathbf{U}_2+B_1\left[(\mathbf{U}_1\cdot\nabla_U)\,\tfrac{\partial \mathbf{N}}{\partial B}\right]_C^*+\\
&\qquad\qquad +\tfrac{1}{2}\left[(\mathbf{U}_1\cdot\nabla_U)^{(2)}\,\mathbf{N}\right]_C^*-\tfrac{\partial \mathbf{U}_1}{\partial T_1}\\
&\text{at order } \epsilon^3 \quad \mathrm{M}^{(1)}\tfrac{\partial \mathbf{U}_3}{\partial x}+\mathrm{M}^{(2)}\tfrac{\partial \mathbf{U}_3}{\partial y}=L_c^*\mathbf{U}_3+B_1\left[(\mathbf{U}_2\cdot\nabla_U)\,\tfrac{\partial \mathbf{N}}{\partial B}\right]_C^*-\tfrac{\partial \mathbf{U}_2}{\partial T_1}-\tfrac{\partial \mathbf{U}_1}{\partial T_2}+\\
&\qquad\qquad +B_2\left[(\mathbf{U}_1\cdot\nabla_U)\,\tfrac{\partial \mathbf{N}}{\partial B}\right]_C^*+\tfrac{1}{2}B_1^2\left[(\mathbf{U}_1\cdot\nabla_U)\,\tfrac{\partial^2 \mathbf{N}}{\partial B^2}\right]_C^*+\\
&\qquad\qquad +\tfrac{1}{2}B_1\left[(\mathbf{U}_1\cdot\nabla_U)^{(2)}\,\tfrac{\partial \mathbf{N}}{\partial B}\right]_C^*+\tfrac{1}{6}\left[(\mathbf{U}_1\cdot\nabla_U)^{(3)}\,\mathbf{N}\right]_C^*+\\
&\qquad\qquad +\left[(\mathbf{U}_1\cdot\nabla_U)\,(\mathbf{U}_2\cdot\nabla_U)\,\mathbf{N}\right]_C^*
\end{aligned} \tag{4.20}$$

where $L_c^*=(\nabla_{\mathbf{U}}\mathbf{N})_c^*$ and, for a generic vector $\mathbf{V}$, the expression $(\mathbf{V}\cdot\nabla_{\mathbf{U}})^{(j)}$ works as in Section 2.1.

In the following sections let us investigate rhombic and hexagonal planform solutions of the governing hyperbolic system. Similar analysis has been done in Refs. [125–128] for parabolic models.

4.2.1 Rhombic planform analysis

Let us search for solutions of (4.20) at the lowest perturbative order in the form

$$\mathbf{U}_1(x,z,T_1,T_2)=\mathbf{X}(x,T_1,T_2)+\mathbf{Z}(z,T_1,T_2) \tag{4.21}$$

where

$$z=x\cos\phi+y\sin\phi \tag{4.22}$$

and $\phi\in(0,\pi)$. Then, by requiring the secular terms to vanish, the solution (4.21) satisfying zero-flux boundary conditions reads

$$\mathbf{U}_1=\Omega_1\begin{bmatrix} r_1\cos(k_cx)\\ r_2\cos(k_cx)\\ k_cr_1\sin(k_cx)\\ 0\\ k_cdr_2\sin(k_cx)\\ 0\end{bmatrix}+\Omega_2\begin{bmatrix} r_1\cos(k_cz)\\ r_2\cos(k_cz)\\ k_cr_1\cos\phi\sin(k_cz)\\ k_cr_1\sin\phi\sin(k_cz)\\ k_cdr_2\cos\phi\sin(k_cz)\\ k_cdr_2\sin\phi\sin(k_cz)\end{bmatrix} \tag{4.23}$$

where $\Omega_1(T_1,T_2)$ and $\Omega_2(T_1,T_2)$ are the pattern amplitudes along x and z direction, respectively.

Now inserting (4.23) into the nonhomogeous linear system (4.20) at the second perturbative order, the requirement that resonant terms vanish leads to

$$B_1=\frac{\partial\Omega_1}{\partial T_1}=\frac{\partial\Omega_2}{\partial T_1}=0. \tag{4.24}$$

Thus, the solution reads

$$\mathbf{U}_2(x,z,T_2)=\Omega_1^2\mathbf{U}_{20}+\Omega_2^2\mathbf{U}_{02}+\Omega_1\Omega_2\left(\frac{1}{(1+2\cos\phi)^2}\mathbf{U}_{12}+\frac{1}{(1-2\cos\phi)^2}\mathbf{U}_{21}\right) \tag{4.25}$$

where the vectors $\mathbf{U}_{20}(x)$, $\mathbf{U}_{02}(z)$, $\mathbf{U}_{12}(x+z)$ and $\mathbf{U}_{21}(x-z)$ are given in Appendix E. Finally, substituting (4.23),(4.25) into $(4.20)_3$, the elimination of secular terms leads to the following two cubic SL equations for the pattern amplitudes:

$$\begin{aligned}\frac{\partial\Omega_1}{\partial T_2}&=B_2\sigma\Omega_1-\Omega_1\left(L_1\Omega_1^2+L_2\Omega_2^2\right)\\ \frac{\partial\Omega_2}{\partial T_2}&=B_2\sigma\Omega_2-\Omega_2\left(L_1\Omega_2^2+L_2\Omega_1^2\right)\end{aligned} \tag{4.26}$$

with

$$\begin{aligned}\sigma&=\frac{B_c r_1(2r_1+r_2d)\left(1-u_{S_c}^2\right)+2u_{S_c}^2 r_2(r_1+r_2d)\left(1+u_{S_c}^2\right)}{B_c\left(1-u_{S_c}^2\right)r_1r_2\left[d-1+dk_c^2(\tau^w-\tau^u)\right]},\\ L_1&=-\frac{(r_1+r_2d)a_1}{r_1r_2\left[d-1+dk_c^2(\tau^w-\tau^u)\right]},\\ L_2&=-\frac{(r_1+r_2d)a_2}{r_1r_2\left[d-1+dk_c^2(\tau^w-\tau^u)\right]},\end{aligned} \tag{4.27}$$

where the coefficients a_1 and a_2 are given in Appendix E. Note that, the expressions of the coefficients σ and L_1 are the same as those deduced in the one-dimensional case [76].

Recalling that $\sigma>0$, system (4.26) admits, apart from the trivial equilibrium (which is always unstable), the following fixed points (Ω_1^*,Ω_2^*):

$$\begin{aligned}&\text{for } L_1>0\Rightarrow\mathbf{P}_{1,2}^*=\left(\pm\sqrt{\tfrac{B_2\sigma}{L_1}},0\right),\mathbf{P}_{3,4}^*=\left(0,\pm\sqrt{\tfrac{B_2\sigma}{L_1}}\right),\text{which are stable for } L_2>L_1\\ &\text{for } L_1+L_2>0\Rightarrow\mathbf{Q}_{1,2,3,4}^*=\left(\pm\sqrt{\tfrac{B_2\sigma}{L_1+L_2}},\pm\sqrt{\tfrac{B_2\sigma}{L_1+L_2}}\right),\text{which are stable for } L_1>L_2\end{aligned} \tag{4.28}$$

It should be noticed that these fixed points are representative of different patterned configurations. In detail, while $\mathbf{P}_{1,2}^*$ and $\mathbf{P}_{3,4}^*$ denote stripes that are perpendicular to the x-axis and z-axis, respectively, the points $\mathbf{Q}_{1,2,3,4}^*$ correspond to rhombic planform patterns.

Owing to the common structure of the denominators of the coefficients appearing in (4.27), the stationary value of the pattern amplitude and their existence and stability character (4.28) are independent of inertial times. However, according to (4.26), the time evolution of the pattern amplitude is strictly ruled by inertia, so that hyperbolicity plays an active role in determining the transient regime from an uniform state toward a patterned state and between different patterned states.

To get insight into the properties of the emerging patterns and their dependence on inertial effects, let us address a numerical investigation on the quantities here deduced. Firstly, existence and stability conditions of the fixed points defined in (4.28) are plotted in Fig.(4.1). In detail, Fig.4.1(a) shows the existence condition for $\mathbf{P}_{1,2,3,4}^*$, which is expressed by the positiveness of the coefficient L_1 as a function of B_c. It reveals that such patterns exist over a wide range of the critical control

parameter, i.e. $B > B^*$ (see the square symbol in the figure). The stability character of these configurations, depicted in the plane $(\phi, \frac{L_2}{L_1})$ in Fig.4.1(b), is associated to the condition $\frac{L_2}{L_1} > 1$, so that stripe patterns can be only observed within given ranges of ϕ. The same figure is also useful to show the existence and stability conditions for $\mathbf{Q}^*_{1,2,3,4}$ that can be easily gathered under the only constraint $-1 < \frac{L_2}{L_1} < 1$.

In order to confirm the previous theoretical predictions as well as to extract information on the steady configurations corresponding to the abovementioned fixed points, the governing system is now integrated numerically by means of COMSOL Multiphysics$^{(R)}$ [108]. The computational domain is a square with sides of length 100 and zero-flux boundary conditions are imposed at each boundary. Results shown in Fig.4.2 reveal that different stripe patterns can be obtained by considering different small perturbations of the spatially-homogeneous steady states $\mathbf{U}^*_S$ as initial data. For instance, Fig.4.2(a) corresponds to the fixed points $\mathbf{P}^*_{1,2}$, whereas panels (b) and (c) are representative of $\mathbf{P}^*_{3,4}$ with $\phi = \frac{\pi}{2}$ and $\phi = \frac{\pi}{8}$, respectively. It should be noticed that, the theoretically-predicted amplitude pattern $\left(\Omega_{theo} = \epsilon\sqrt{\frac{\sigma}{L_1}} = 2.9\right)$ is in a good agreement with the numerical one ($\Omega_{num} = 3.0$), despite the control parameter is taken at a relatively large distance from the threshold ($\epsilon = 10^{-1}$).

To elucidate the role played by inertial effects on vegetation pattern dynamics, the SL system (4.26) is integrated over a time window $T_2 \in (0, 200)$. The resulting evolution of the pattern amplitudes in the transient regime is depicted in Fig.4.3 for different inertial times and initial conditions. In particular, Figs.4.3(a,b) show the behavior of stripes that are perpendicular to x-axis (denoted by $\mathbf{P}^*_{1,2}$), as the Ω_2-component approaches zero. Figs.4.3(c,d) correspond to stripes perpendicular to z-axis (denoted by $\mathbf{P}^*_{3,4}$), as the Ω_1-component vanishes once the transient is expired. Finally, Figs.4.3(e,f) show the configuration in which both steady amplitudes are non-null (referred to as $\mathbf{Q}^*_{1,2,3,4}$). These latter solutions are named rhombic planform patterns, as their geometry differs from stripes. The above results allow to address a twofold conclusion. On the one hand, the numerically-computed fixed points are

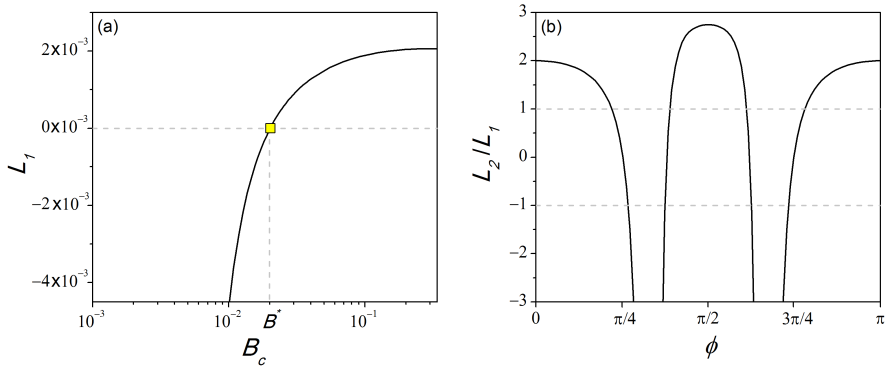

Figure 4.1: Panels (a) and (b) depict, respectively, the existence and stability conditions for $\mathbf{P}^*_{1,2,3,4}$. Panel (b) encloses both conditions for $\mathbf{Q}^*_{1,2,3,4}$. The used parameters are: $d = 500$, $\tau^u = 10^{-5}$ and $\tau^w = 5 \times 10^{-3}$. In (b) $A = 2.8$.

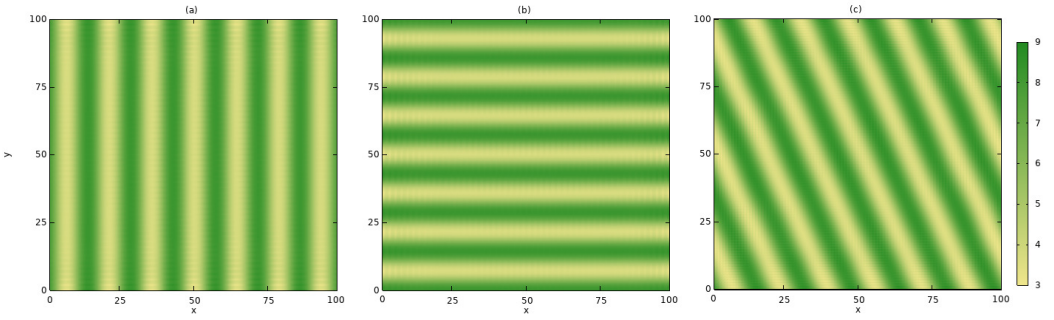

Figure 4.2: Snapshots of the steady pattern configurations obtained by integrating numerically the governing system. Panel (a) corresponds to the $\mathbf{P}^*_{1,2}$, whereas panels (b) and (c) denote $\mathbf{P}^*_{3,4}$ with $\phi = \frac{\pi}{2}$ and $\phi = \frac{\pi}{8}$, respectively. The used parameters are: $d = 500$, $\tau^u = 10^{-5}$, $\tau^w = 5 \times 10^{-3}$, $A = 2.8$ and $B = 0.455$.

in excellent agreement with the theoretically-predicted ones (4.28). On the other hand, the presence of inertia modulates the duration of the transient regime from the uniformly-vegetation area toward the patterned state, independently of the geometry characterizing the steady configuration. Indeed, by leaving the parameter τ^u fixed and reducing the inertial time τ^w, the transient regime progressively shortens.

Let us now further inspect the role of hyperbolicity through numerical integration of the governing system where the initial data are fixed (and set to a small perturbation of the homogeneously-vegetated area) and the inertial times are varied. Results are depicted in Fig.4.4(a,b,c) for $\tau^w = 5 \times 10^{-3}$, that represents a configuration very close to the parabolic limit, and in Fig.4.4(d,e,f) for $\tau^w = 50$, that is far from it. To better appreciate the dynamics occurring during the transient regime, snapshots of the vegetation biomass distribution $u(x, y)$ are reported at different times: $t = 200$ in panels (a,d), $t = 500$ in panels (b,e) and $t = 1000$ in panels (c,f). As can be noticed from Figs.4.4(b,c), in the parabolic regime, at $t = 500$ the system has already completed the transition from the uniform state to the rhombic patterned configuration. On the other hand, as reported in Figs.4.4(e)-(f), far from the parabolic limit, the transition at $t = 1000$ is still in progress even though it converges towards the same steady vegetated rhombic configuration. Finally, it is interesting to address a direct comparison between the numerical solution obtained by integrating system, shown in Fig.4.4(c,f), and the rhombic planform patterned solution obtained analytically from (4.19),(4.23), depicted in Fig.4.5. The resulting satisfying agreement allows to definitively prove the correctness of the proposed theoretical approach and to address further investigations on the properties exhibited by the hyperbolic model during transient regime.

One interesting feature involves the possibility of nullifying hyperbolicity effects when the inertial times associated to the two species fully compensate each other, i.e. $\tau^u = \tau^w$. According to (4.26),(4.27), inertial effects are related to the difference $\tau^u - \tau^w$, so that it is expected that, under this constraint, the time evolution of the pattern amplitudes becomes independent of inertial times, independently of their values [76]. Numerical results carried out close to the parabolic limit ($\tau^u = 10^{-5}$ and

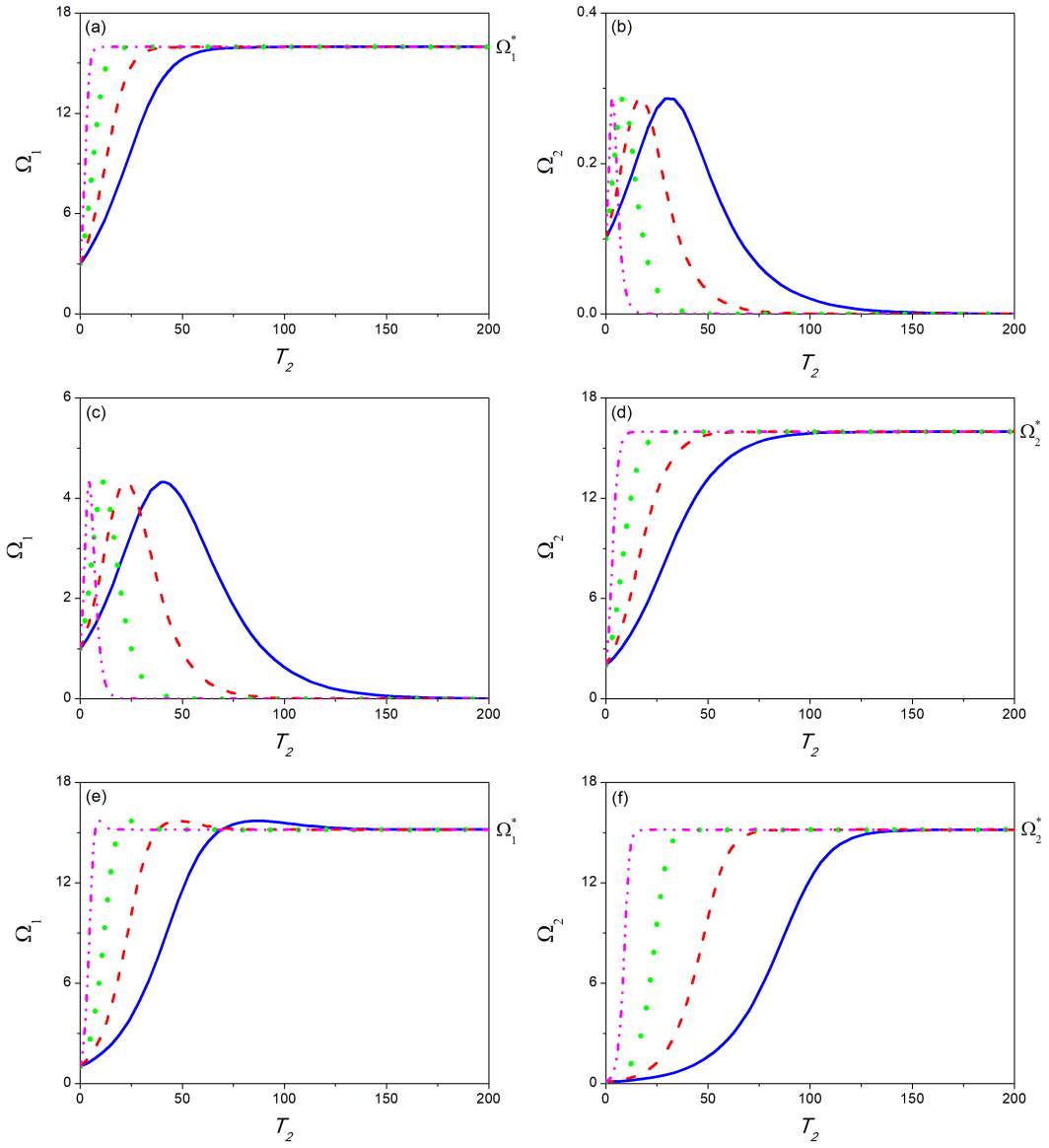

Figure 4.3: Time evolution of pattern amplitudes arising from the integration of Stuart-Landau system (4.26), for different τ^w and initial data. Dynamics illustrated in panels (a),(b) converge towards the fixed points $\mathbf{P}^*_{1,2}$, whereas those in (c),(d) and (e),(f) towards $\mathbf{P}^*_{3,4}$ and $\mathbf{Q}^*_{1,2,3,4}$, respectively. Fixed parameters are: $d = 500$, $\tau^u = 10^{-5}$ and $A = 2.8$. For all panels, the different lines correspond to: $\tau^w = 50$ (solid blue), $\tau^w = 25$ (dashed red), $\tau^w = 10$ (dotted green) and $\tau^w = 0.5$ (dash-dotted magenta).

$\tau^w = 5 \times 10^{-3}$) and far from it ($\tau^u = \tau^w = 1$) confirm our prediction, as depicted in Fig.4.6.

4.2.2 Hexagonal planform analysis

Let us now analyze the case of hexagonal patterns by looking for solutions of system (4.20) at the first perturbative order in the form

$$\mathbf{U}_1 = \mathbf{X}(x) + \mathbf{Z}(\zeta) + \mathbf{\Xi}(\xi) \tag{4.29}$$

where $\zeta = \frac{1}{2}x + \frac{\sqrt{3}}{2}y$ and $\xi = \frac{1}{2}x - \frac{\sqrt{3}}{2}y$. Note that these variables can be deduced from (4.22) for $\phi = \pi/3$ and $\phi = -\pi/3$, respectively. Then, by using the same strategy adopted in the previous section, the solution can be expressed as

$$\mathbf{U}_1 = \Omega_1 \begin{bmatrix} r_1\cos(k_c x) \\ r_2\cos(k_c x) \\ k_c r_1 \sin(k_c x) \\ 0 \\ k_c d r_2 \sin(k_c x) \\ 0 \end{bmatrix} + \frac{\Omega_2}{2} \begin{bmatrix} r_1\Big(\cos(k_c\zeta) + \cos(k_c\xi)\Big) \\ r_2\Big(\cos(k_c\zeta) + \cos(k_c\xi)\Big) \\ \frac{1}{2}k_c r_1\Big(\sin(k_c\zeta) + \sin(k_c\xi)\Big) \\ \frac{\sqrt{3}}{2}k_c r_1\Big(\sin(k_c\zeta) - \sin(k_c\xi)\Big) \\ \frac{1}{2}k_c d r_2\Big(\sin(k_c\zeta) + \sin(k_c\xi)\Big) \\ \frac{\sqrt{3}}{2}k_c d r_2\Big(\sin(k_c\zeta) - \sin(k_c\xi)\Big) \end{bmatrix} \tag{4.30}$$

Inserting (4.30) into the nonhomogeneous linear system (4.20) at the second perturbative order, the requirement that resonant terms vanish leads to

$$\begin{cases} \frac{\partial\Omega_1}{\partial T_1} = B_1\sigma\Omega_1 - \frac{L}{4}\Omega_2^2 \\ \frac{\partial\Omega_2}{\partial T_1} = B_1\sigma\Omega_2 - L\Omega_1\Omega_2 \end{cases} \tag{4.31}$$

being

$$L = -\frac{(r_1+dr_2)\left(B_c r_1 + 2r_2 u_{S_c}^2\right)}{r_2 u_{S_c}\left[d-1+dk_c^2(\tau^w-\tau^u)\right]} \tag{4.32}$$

and the solution reads

$$\mathbf{U}_2(x,\zeta,\xi,T_1,T_2) = \Omega_1\widetilde{\mathbf{U}}_{10} + \Omega_2\widetilde{\mathbf{U}}_{01} + \Omega_1\Omega_2\widetilde{\mathbf{U}}_{11} + \Omega_1^2\widetilde{\mathbf{U}}_{20} + \Omega_2^2\widetilde{\mathbf{U}}_{02} \tag{4.33}$$

where the vectors $\widetilde{\mathbf{U}}_{10}(x)$, $\widetilde{\mathbf{U}}_{01}(\zeta,\xi)$, $\widetilde{\mathbf{U}}_{11}(x,\zeta,\xi)$, $\widetilde{\mathbf{U}}_{20}(x)$ and $\widetilde{\mathbf{U}}_{02}(x,\zeta,\xi)$ are defined in Appendix F.

Note that, system (4.31) does not admit stable equilibria, so that WNA has to be pushed to the next perturbative order. Therefore, substituting (4.30),(4.33) into (4.20) at the third perturbative order, the elimination of secular terms leads to the following cubic SL equations for the amplitudes:

$$\begin{cases} \frac{\partial\Omega_1}{\partial T_2} = \tilde{\sigma}\Omega_1 + \psi\Omega_2^2 - L_1\Omega_1^3 + \tilde{L}\Omega_1\Omega_2^2 \\ \frac{\partial\Omega_2}{\partial T_2} = \tilde{\sigma}\Omega_2 + \frac{1}{4}\left(2\tilde{L} - L_1\right)\Omega_2^3 + 4\psi\Omega_1\Omega_2 + 2\tilde{L}\Omega_1^2\Omega_2 \end{cases} \tag{4.34}$$

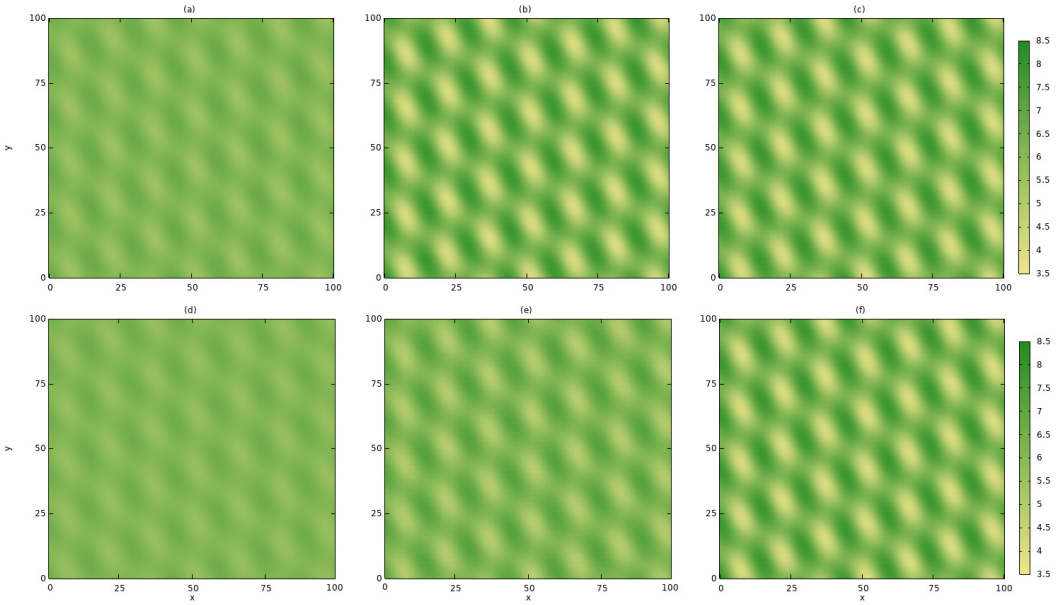

Figure 4.4: Snapshots of vegetation dynamics obtained by integrating numerically the governing system by using the same initial condition and considering different inertial times: (a)-(c) $\tau^w = 5 \times 10^{-3}$, (d)-(f) $\tau^w = 50$. The different time evolutions can be appreciated by comparing vertically the panels: (a),(d) $t = 200$, (b),(e) $t = 500$ and (c),(f) $t = 1000$. The common parameters are: $d = 500$, $\tau^u = 10^{-5}$, $A = 2.8$ and $B = 0.445$.

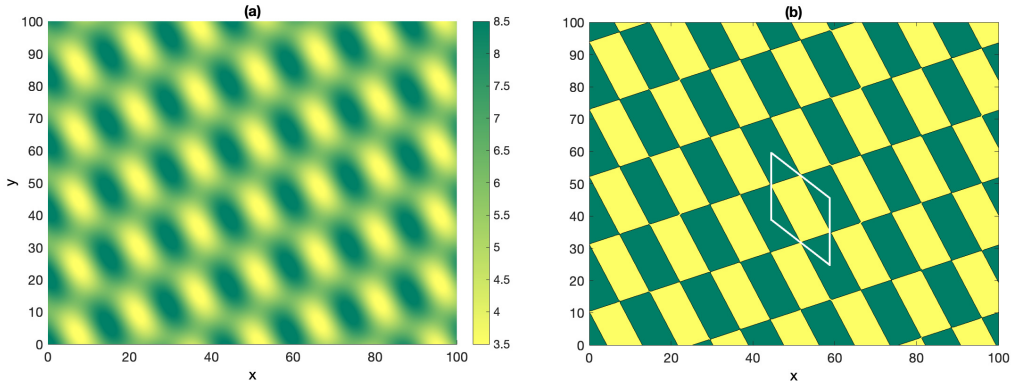

Figure 4.5: (a) Rhombic planform patterned solution obtained analytically from (4.19),(4.23) and (b) its contour plot. Parameters as in Fig.4.4.

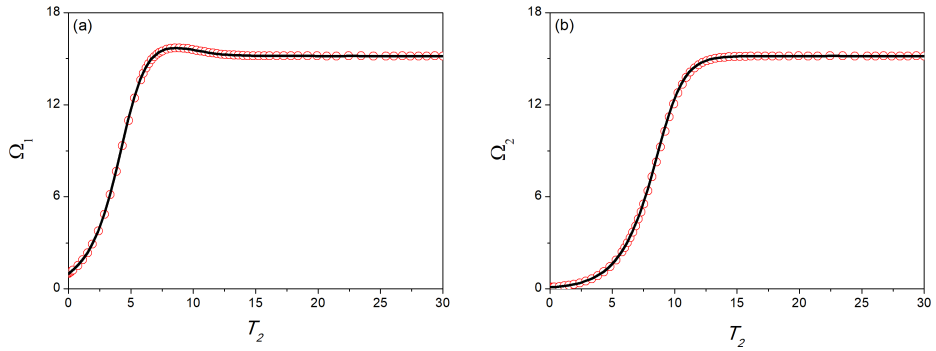

Figure 4.6: Time evolution of pattern amplitudes arising from the integration of Stuart-Landau system (4.26) when the inertial times are equal to each other, i.e. $\tau^u = \tau^w$. Symbols denote the theoretical amplitudes in the parabolic limit ($\tau^u = 10^{-5}$ and $\tau^w = 5 \times 10^{-3}$), whereas lines show the behaviour far from it ($\tau^u = \tau^w = 1$). Other common parameters: $d = 500$ and $A = 2.8$.

where

$$\tilde{\sigma} = \tilde{a}_0 \sigma B_1^2 + \tilde{a}_1, \qquad \psi = B_1 \frac{\tilde{a}_3 + 2\tilde{a}_4\sigma - \tilde{a}_0 L}{4}, \qquad \tilde{L} = \frac{\tilde{a}_2 - \tilde{a}_4 L}{2}$$

and the coefficients $\tilde{a}_i$ $(i = 0, ..., 4)$ are defined in Appendix F.

Finally, by adding (4.31) to (4.34), the system that rules the pattern amplitudes reads:

$$\begin{cases} \frac{\partial \Omega_1}{\partial T} = \bar{\sigma}\Omega_1 + \bar{\psi}\Omega_2^2 - \bar{L}_1\Omega_1^3 + \bar{L}\Omega_1\Omega_2^2 \\ \frac{\partial \Omega_2}{\partial T} = \bar{\sigma}\Omega_2 + \frac{1}{4}\left(2\bar{L} - \bar{L}_1\right)\Omega_2^3 + 4\bar{\psi}\Omega_1\Omega_2 + 2\bar{L}\Omega_1^2\Omega_2 \end{cases} \tag{4.35}$$

where

$$\frac{\partial}{\partial T} = \frac{\partial}{\partial T_1} + \epsilon\frac{\partial}{\partial T_2} \qquad \bar{\sigma} = B_1\sigma + \epsilon\tilde{\sigma}, \qquad \bar{\psi} = -\frac{L}{4} + \epsilon\psi, \qquad \bar{L}_1 = \epsilon L_1, \qquad \bar{L} = \epsilon\tilde{L}.$$

System (4.35) admits, apart from the trivial equilibrium $\mathcal{P}_0^* = (0, 0)$, the following fixed points (Ω_1^*, Ω_2^*):

$$\begin{aligned} \mathcal{P}_{1,2}^* &= \left(\pm\sqrt{\tfrac{\bar{\sigma}}{\bar{L}_1}}, 0\right) \\ \mathcal{Q}_{1,2}^* &= \left(-\tfrac{4\bar{\psi}}{2\bar{L}+\bar{L}_1}, \pm\tfrac{2}{\left|2\bar{L}+\bar{L}_1\right|}\sqrt{\tfrac{\bar{\sigma}\left(2\bar{L}+\bar{L}_1\right)^2 - 16\bar{\psi}^2\bar{L}_1}{\bar{L}_1 - 2\bar{L}}}\right) \\ \mathcal{Q}_{3,4}^* &= \left(\tfrac{2\bar{\psi}+\sqrt{4\bar{\psi}^2+\left(\bar{L}_1-4\bar{L}\right)\bar{\sigma}}}{\bar{L}_1-4\bar{L}}, \pm\tfrac{2\left[2\bar{\psi}+\sqrt{4\bar{\psi}^2+\left(\bar{L}_1-4\bar{L}\right)\bar{\sigma}}\right]}{\bar{L}_1-4\bar{L}}\right) \\ \mathcal{Q}_{5,6}^* &= \left(\tfrac{2\bar{\psi}-\sqrt{4\bar{\psi}^2+\left(\bar{L}_1-4\bar{L}\right)\bar{\sigma}}}{\bar{L}_1-4\bar{L}}, \pm\tfrac{2\left[2\bar{\psi}-\sqrt{4\bar{\psi}^2+\left(\bar{L}_1-4\bar{L}\right)\bar{\sigma}}\right]}{\bar{L}_1-4\bar{L}}\right) \end{aligned} \tag{4.36}$$

	Existence condition	**Stability condition**
$\mathcal{P}_0^*$	always	never
$\mathcal{P}_{1,2}^*$	$\bar{L}_1 > 0$	$\bar{\sigma} \pm 4\bar{\psi}\sqrt{\frac{\bar{\sigma}}{\bar{L}_1}} + 2\frac{\bar{L}\bar{\sigma}}{\bar{L}_1} < 0$
$\mathcal{Q}_{1,2}^*$	$\frac{\bar{\sigma}\left(2\bar{L}+\bar{L}_1\right)^2 - 16\bar{\psi}^2\bar{L}_1}{\left(\bar{L}_1-2\bar{L}\right)} \geq 0$	$\begin{cases} \frac{\bar{\sigma}\left(\bar{L}_1+2\bar{L}\right)\left(6\bar{L}-\bar{L}_1\right)-16\bar{\psi}^2\bar{L}_1}{\left(\bar{L}_1-2\bar{L}\right)\left(\bar{L}_1+2\bar{L}\right)} < 0 \\ \bar{\sigma}\left(\bar{L}_1+2\bar{L}\right)^3 + 32\bar{\psi}^2\left(2\bar{L}^2 - \bar{L}\bar{L}_1 - \bar{L}_1^2\right) < 0 \end{cases}$
$\mathcal{Q}_{3,4,5,6}^*$	$4\bar{\psi}^2 + \left(\bar{L}_1 - 4\bar{L}\right)\bar{\sigma} \geq 0$	$\begin{cases} \bar{\sigma} + \left(8\bar{L} - 5\bar{L}_1\right)\Omega_1^{*^2} < 0 \\ 3\left(2\bar{L} - \bar{L}_1\right)\left(4\bar{L} - \bar{L}_1\right)\Omega_1^{*^2} + \left(10\bar{L} - \bar{L}_1\right)\bar{\sigma} - 16\bar{\psi}^2 > 0 \end{cases}$

Table 4.1: Existence and stability conditions for the fixed points (4.36) of the Stuart-Landau system (4.35).

whose existence and stability conditions are schematically reported in Table 4.1.

In Table 4.1 it has been taken into account that $\bar{\sigma} > 0$ being $B_1 > 0$, $\sigma > 0$ and $\epsilon\tilde{\sigma}$ is a first order correction. The nontrivial fixed points are representative of different patterned configurations. In detail, $\mathcal{P}_{1,2}^*$ denote stripes that are perpendicular to the x-axis, whereas the points $\mathcal{Q}_{1,..,6}^*$ correspond to hexagonal planform patterns.

Due to the nonlinear and nontrivial dependence of the coefficients appearing in (4.35) on inertial times, numerical investigations are carried out to elucidate how inertia affects the existence and the stability conditions as well as pattern transient dynamics.

The behavior of stripes $\mathcal{P}_{1,2}^*$ will be here not discussed, as it has been addressed in the previous section. The existence condition associated to the hexagonal patterns $\mathcal{Q}_{1,2}^*$ and $\mathcal{Q}_{3,..,6}^*$ is depicted in Figs.4.7 in panels (a) and (b), respectively. The analysis is here carried out by considering the following setup: $d = 500$, $\tau^u = 10^{-5}$ and different values of τ^w. The control parameter is swept in the range of values generally assumed for plant loss $B_c \in (0.04, 0.46)$, whereas the rainfall parameter is varied at the bifurcation threshold (4.17) accordingly, keeping it in the range $A \in (0, 3)$. Our inspection reveals that, in such a setup, the existence condition for $\mathcal{Q}_{1,2}^*$ is never met, while the one for $\mathcal{Q}_{3,..,6}^*$ is always fulfilled. Therefore, let us focus on the stability of these latter, which is depicted in panels (c,d) for $\mathcal{Q}_{3,4}^*$ and in (e,f) for $\mathcal{Q}_{5,6}^*$. Results suggest that the former are unstable (both conditions violated) whereas the latter are stable (both conditions satisfied). As a consequence of that, the only hexagonal patterns that may be observed, using the above set of parameters, correspond to $\mathcal{Q}_{5,6}^*$. The subsequent investigations will be thus focused on these states with particular emphasis on the time evolution of the pattern amplitudes Ω_1 and Ω_2 that arise from the integration of SL system (4.35) for different values of τ^w. Results depicted in Fig.4.8 provide a twofold information. First, inertial effects dictate the time scale along which transient regime takes place and, indeed, the larger the τ^w the shorter the transition from the uniform state toward the patterned state. Second, the theoretically-predicted values of stationary amplitudes depend on inertial times. This apparent contradiction has to be treated as an artifact of the weakly nonlinear expansion, as such inertial dependencies of stationary solutions are not expected to take place. Notice that an analogous result was obtained in our previous work

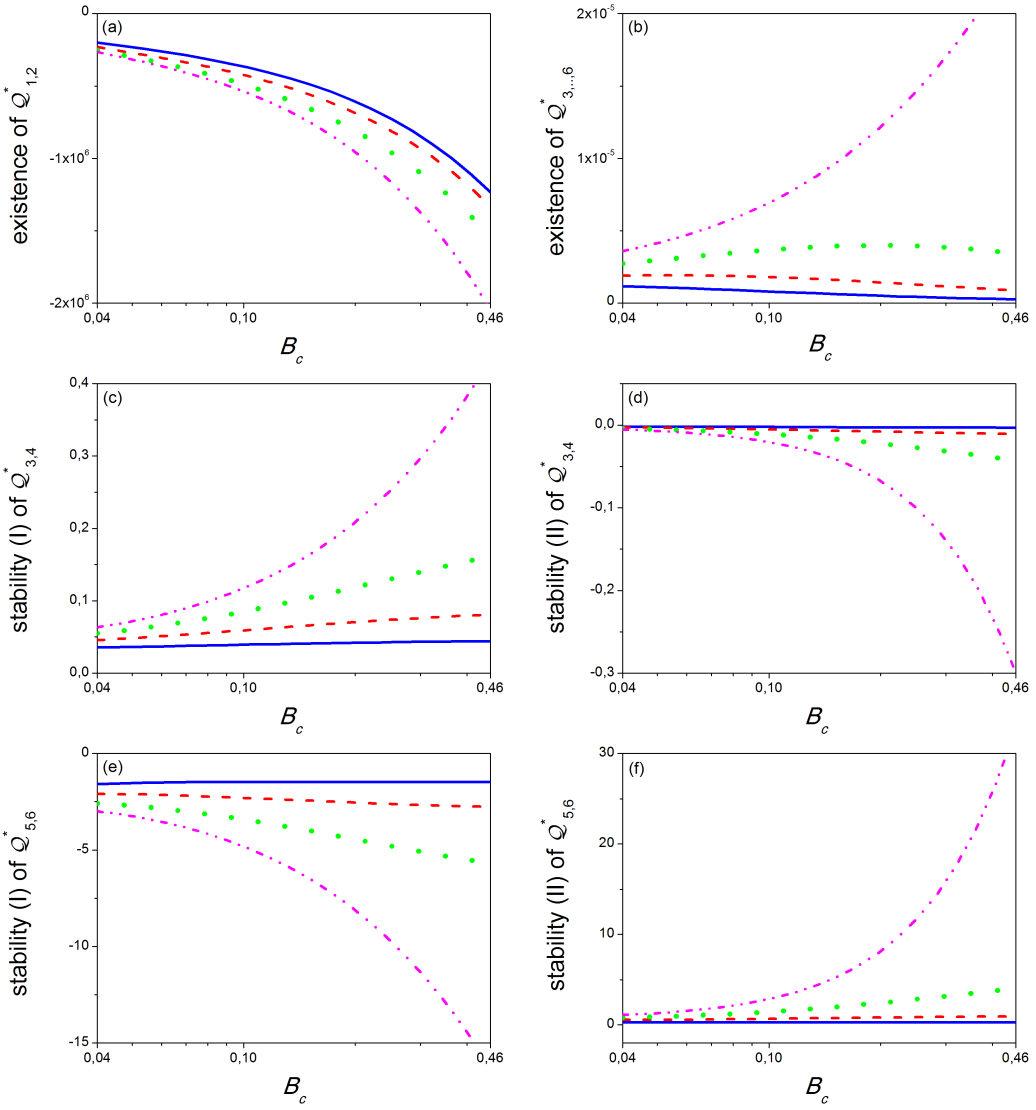

Figure 4.7: Panels (a) and (b) depict the existence conditions (namely, the quantities at left-hand side reported in the second column of Table 4.1) for $\mathcal{Q}^*_{1,2}$ and $\mathcal{Q}^*_{3,4,5,6}$, respectively. Panels (c) and (d) enclose the stability conditions (third column of Table 4.1) for $\mathcal{Q}^*_{3,4}$, whereas panels (e) and (f) those for $\mathcal{Q}^*_{5,6}$. The used parameters are: $d = 500$, $\tau^u = 10^{-5}$. For all panels, the different lines correspond to: $\tau^w = 50$ (solid blue), $\tau^w = 25$ (dashed red), $\tau^w = 10$ (dotted green) and $\tau^w = 0.5$ (dash-dotted magenta).

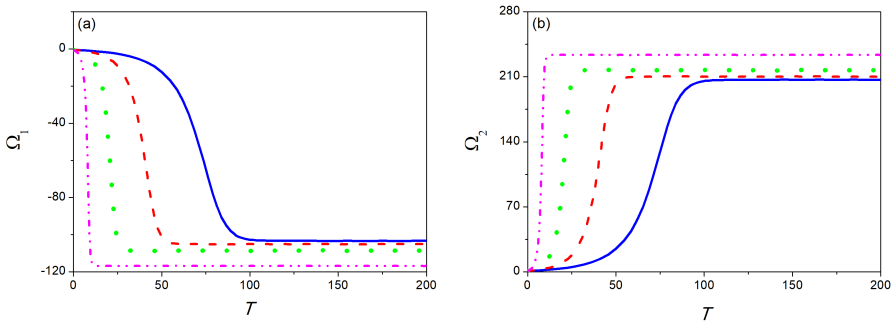

Figure 4.8: Time evolution of pattern amplitudes arising from the integration of Stuart-Landau system (4.35), for different values of τ^w (lines as in Fig.4.7). Fixed parameters are: $d = 500$, $\tau^u = 10^{-5}$ and $A = 2.8$.

about the stationary pattern amplitude in the subcritical regime [76]. To investigate this issue in more detail, let us integrate numerically the governing system for two different inertial times, $\tau^w = 5 \times 10^{-3}$ and $\tau^w = 50$, and by using, in both cases, the same small perturbation of the steady state $\mathbf{U}_S^*$ as initial condition. The sequences of snapshots represented in shown in Fig.4.9 provide a confirmation of our previous statements. In fact, panels (a)-(c), representing the solution obtained at different time instants for $\tau^w = 5 \times 10^{-3}$, describe a much faster transition from the uniform state toward the hexagonal patterned state than the one depicted in panels (d)-(f), that is associated to $\tau^w = 50$, i.e. a system with larger inertia. However, as it can be appreciated from the scale appearing in the colorbar on the right of the panels, the final state is the same for both configurations, so confirming that the stationary amplitudes do not depend on inertia.

Then, to further prove the validity of the theoretical approach, let us build in Fig.4.10 the hexagonal solution obtained by substituting the pattern amplitudes Ω_1 and Ω_2 into (4.30) and (4.19). By comparing the final states obtained numerically (Fig.4.9) and analytically (Fig.4.10), a more than satisfying agreement is achieved as no appreciable differences arise between them (note, once again, the same scale on the colorbar).

Finally, let us address wether the possibility of nullifying hyperbolicity effects via compensation of the inertial times takes also place for the hexagonal geometry. As it can be noticed from (4.35),(4.36),(F.8),(F.10), the quantities here involved don't exhibit the simple dependence $(\tau^u - \tau^w)$ on the inertial times. By checking it numerically, it is found that the equality between inertial times away from the parabolic limit allows the system to follow the same transient dynamics observed close to it, see Fig.4.11. The above mentioned nontrivial dependence on inertial times only leads to a slightly difference in the stationary amplitudes, in line with what observed in Fig.4.8.

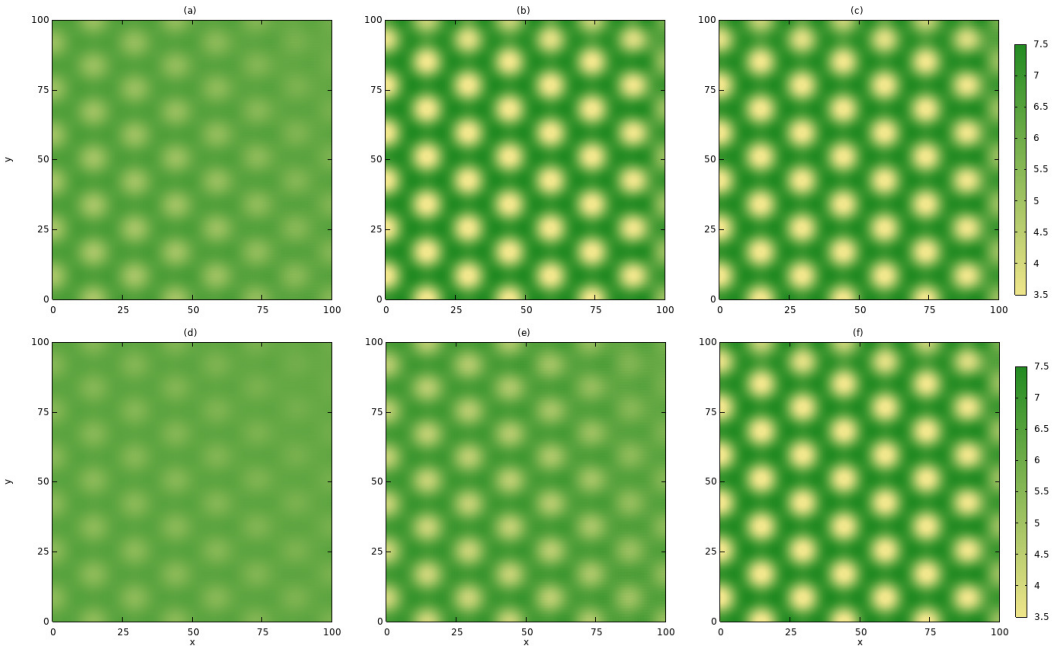

Figure 4.9: Snapshots of vegetation dynamics obtained by integrating numerically the governing system by using the same initial condition and considering different inertial times: (a)-(c) $\tau^w = 5 \times 10^{-3}$, (d)-(f) $\tau^w = 50$. The different time evolutions can be appreciated by comparing vertically the panels: (a),(d) $t = 600$, (b),(e) $t = 800$ and (c),(f) $t = 1000$. The common parameters are: $d = 500$, $\tau^u = 10^{-5}$, $A = 2.8$ and $B = 0.445$.

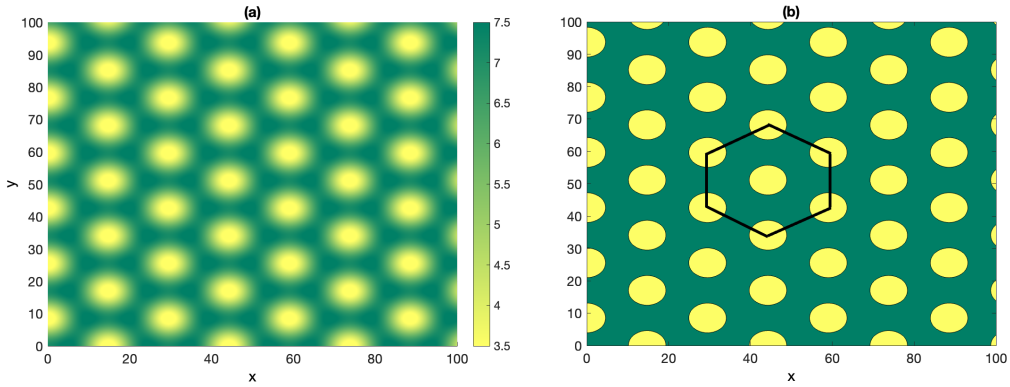

Figure 4.10: (a) Hexagonals planform patterned solution obtained analytically from (4.19),(4.30) and (b) its contour plot. Parameters as in Fig.4.9.

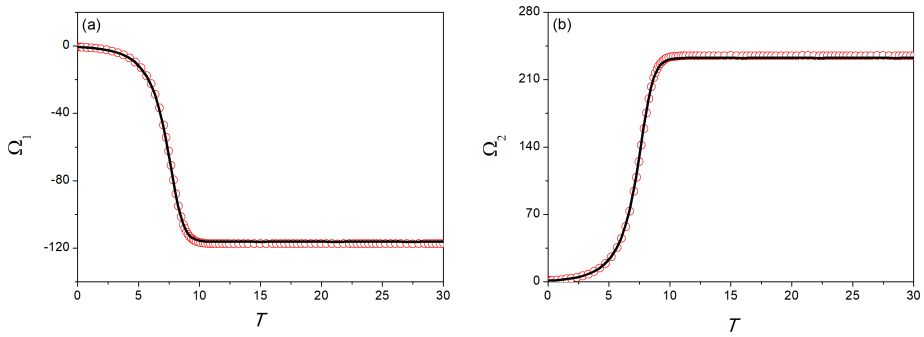

Figure 4.11: Time evolution of pattern amplitudes arising from the integration of Stuart-Landau system (4.35) when the inertial times are equal to each other, i.e. $\tau^u = \tau^w$. Symbols denote the theoretical amplitudes in the parabolic limit ($\tau^u = 10^{-5}$ and $\tau^w = 5 \times 10^{-3}$), whereas lines show the behaviour far from it ($\tau^u = \tau^w = 1$). Other common parameters: $d = 500$, $B = 0.445$ and $A = 2.8$.

4.3 Concluding remarks

This chapter describes how the formation of bidimensional vegetation patterns in dryland areas may be tackled through a hyperbolic RT system. The proposed framework encloses the inertial effects that any physical system possesses, so allowing a more suitable description of transient dynamics, as the ones involved in the transitions between a spatially-homogeneous steady state (representative of a uniformly vegetated area) towards a patterned configuration (such as stripes, spots, holes and other geometries).

To achieve this goal, exploiting the guidelines of the ET theory, a 2D version of the two-species hyperbolic RT model is deduced. Then, linear stability analysis on the uniform steady states is addressed to deduce the conditions for the occurrence of Turing instability. It reveals that hyperbolicity does not affect the bifurcation threshold and the wavenumber of the stationary patterns, but introduces an upper bound to the range of the inertial time associated to vegetation. Next, a multiple-scale WNA is performed to determine the SL equations ruling the time evolution of the pattern amplitudes close to onset. In particular, this analysis characterizes two specific planform geometries: rhombs and hexagons. The satisfying agreement achieved, for both geometries, between theoretically-predicted and numerically-computed solutions is also insightful to clarify the role of inertial times in dictating the timescales involved during transient regimes. Indeed, it is found that hyperbolicity does not affect the stationary amplitude of the emerging patterns, as confirmed by numerical simulations. Nevertheless, hexagonal analysis reveals a dependence of the stationary amplitude on inertial times, which has to be thus attributed to an artifact arising from the weakly nonlinear expansion.

Once the robustness of the proposed theoretical framework has been proved, an interesting property appearing in transient dynamics is here highlighted. It is indeed found that hyperbolicity may be nullified if the inertial times associated to the two species fully compensate each other. Under this constraint, the system evolves

through the same transient states as in parabolic models. This property is observed to hold for both rhombic and hexagonal geometries.

From the ecological viewpoint, some intriguing issues need still to be addressed. One of the most striking one is the possibility to describe how inertial effects in the vegetation response (in particular for the woody component) affect the transitions between different patterned states. Experimental evidences of such a phenomenon were already given in the literature [27] and will constitute the starting point of future theoretical investigations.

Conclusions

In this thesis, the pattern formation and stability mechanisms were studied in several hyperbolic reaction-transport frameworks which constitute subsets of the general class presented in (1.5)-(1.7). In particular, in each considered model, emphasis was given to the role played by inertial effects in patterned dynamics.

In Chapter 2, the focus was given to the stationary periodic pattern arising from the Turing instability process. In detail, the presence of EI over a large finite domain was addressed theoretically in both supercritical and subcritical regimes. WNA was addressed to deduce the CRGL and CQRGL equations and, then, the bifurcation analysis was carried out to describe the existence and stability thresholds of all bifurcating branches. It was shown that, while the CRGL equation describes satisfactorily well the features associated with the supercritical regime, to properly describe the subcritical dynamics it is necessary to push WNA up to the fifth order and to work with the CQRGL equation. In particular, it was proved that hyperbolicity affects the expression of the linear growth rate but leaves the other quantities unchanged. This result suggested that the hyperbolic model provides additional degrees of freedom that may be used to better characterize transient regimes. Moreover, through numerical investigations, it was found that the time to phase slip can be modulated by varying the inertial times, whereas the location to phase slip can be controlled through a local defect in the initial data.

In Chapter 3, the presence of oscillatory periodic patterns was taken into account in two different frameworks. First, the occurrence of non-stationary patterned dynamics was investigated in two-compartment hyperbolic RT systems (1.8)-(1.9) where both species undergo self-diffusion and only one is also ruled by an advection term ($\psi = 0$). Here, LSA and WNA showed that the presence of inertia plays a manifold role: (i) it allows to destabilize the spatially homogeneous steady state over a wider set of model parameters by enlarging the wave instability region; (ii) it varies the key features associated with migrating patterns, such as speed, wavelength, and angular frequency; (iii) it affects the supercritical or subcritical nature of patterns at onset; (iv) it takes a role not only during transient regimes but also modifies the amplitude, the wavenumber, the angular frequency, and the stability of patterns. Then, the focus was moved to two-compartment hyperbolic systems RT (1.8)-(1.9) where both species undergo advection and only one was also ruled by self-diffusion ($d = 0$). Patterned dynamics were here studied through the LSA tool to depict the locus at which the instability occurs. Insights into the migration speed of the oscillatory patterns were extracted by means of periodic travelling waves analysis. Numerical simula-

tions performed in the context of dryland ecology through the original kinetics of the Klausmeier model provided a satisfying description of experimental data. Moreover, close to the parabolic limit, the model allowed the reproduction of both uphill and downhill patterns as a function of seed advection speed, whereas, far from it, the migration speed approached the zero value so mimicking quasi-stationary behaviours. Analytical approximations suggested us that, from one hand, near the parabolic limit the dynamics of stationary patterns at the onset of criticality are unaffected by hyperbolicity whereas, on the other hand, far from it hyperbolicity favors the presence of uphill or quasi-stationary patterns.

In Chapter 4, the study of stationary periodic patterns in bi-dimensional hyperbolic RT systems (1.5)-(1.7) was addressed in the presence of diffusive character only ($\psi = \nu = 0$). To this aim, LSA was addressed to deduce the region in which Turing instability can be observed and WNA was performed to determine the SL equations ruling the evolution of the pattern amplitudes close to the criticality. The above analyses revealed that hyperbolicity does not affect the bifurcation threshold and the wavenumber of the stationary patterns, but introduces an upper bound to the range of the inertial times. WNA was developed to characterize rhombic and hexagons geometries and the agreement achieved between theoretically-predicted and numerically-computed solutions showed that inertia doesn't affect the stationary amplitude of the emerging patterns

Future investigations are planned as follows: (i) by studying the connections between periodic patterns near criticality and far-from-equilibrium patterns by means of Busse balloon theory; (ii) by considering extensions of the previous frameworks, such as the addition of cross-diffusion terms and/or the presence of oscillatory periodic patterns in bi-dimensional hyperbolic systems; (iii) by introducing the study of the above-mentioned dynamics far from the bifurcation threshold by means of geometrical singular perturbation technique.

Appendices

A Derivation of 2D hyperbolic RT systems

Let us consider two interacting species, whose densities are denoted by u and w, that interact and diffuse in an environment belonging to the (x, y) plane. The spatio-temporal evolution of such densities is generally ruled by:

$$\begin{aligned} &\frac{\partial u}{\partial t} + \nabla \cdot \mathbf{J}^u - \psi u_x = f(u, w, B), \\ &\frac{\partial w}{\partial t} + \nabla \cdot \mathbf{J}^w - \nu w_x = g(u, w, B), \end{aligned} \tag{A.1}$$

being $\mathbf{J}^u$ and $\mathbf{J}^w$ the corresponding diffusive fluxes and $f(u, w)$ and $g(u, w)$ the functions describing the kinetic interactions. As known, if the fluxes obey a gradient-based constitutive equation, such as Fick's law, the system takes the form of a classical *parabolic* system, as in (1.3). On the other hand, if the dissipative fluxes are considered as additional field variables, as suggested by ET theory [38], the system can be cast in the form of a *hyperbolic* model. In this framework, the dissipative fluxes have to satisfy the following balance equations

$$\begin{aligned} &\frac{\partial \mathbf{J}^u}{\partial t} + \nabla \cdot \mathbf{T}^u = \mathbf{G}^u, \\ &\frac{\partial \mathbf{J}^w}{\partial t} + \nabla \cdot \mathbf{T}^w = \mathbf{G}^w, \end{aligned} \tag{A.2}$$

where the constitutive functions $\mathbf{T}$ and $\mathbf{G}$ must be determined in terms of the whole set of the independent variables $\mathbf{U} = [u\,, w\,, \mathbf{J}^u\,, \mathbf{J}^w]^T$. At this step the system is not closed because the constitutive functions $\mathbf{T}$ and $\mathbf{G}$ appearing in (A.2) are not known. The constitutive theory established in ET allows to determine those functions or, at least, to reduce their generality. To restrict these arbitrary functional forms, we hypothesize firstly a linear dependence of $\mathbf{T}$ and $\mathbf{G}$ on the fluxes. Such a constraint is equivalent to consider processes not far from the thermodynamical equilibrium, characterized by vanishing fluxes.

Then, by assuming that the balance equations (A.2) reduce to Fick laws in the stationary case, it can be deduced

$$\begin{aligned} &\mathbf{T}^u = \gamma\,(u)\,\mathbf{I}, \quad \mathbf{G}^u = -\gamma_u \mathbf{J}^u, \\ &\mathbf{T}^w = \mu\,(w)\,\mathbf{I}, \quad \mathbf{G}^w = -\tfrac{\mu_w}{d}\mathbf{J}^w, \end{aligned} \tag{A.3}$$

being $\mathbf{I}$ the 2×2 identity matrix.

A further restriction on the constitutive functions (A.3) arises from the compatibility of system (1.5)-(1.7) with the well-known entropy balance law

$$\eta_t + \nabla \cdot \phi \geq 0 \tag{A.4}$$

where the concave entropy density η and the entropy flux ϕ have to be considered as constitutive functions of whole set of the field variables.

By using the so-called Lagrange multipliers Λ, Γ, $\mathbf{\Pi}$, $\mathbf{\Xi}$ [38, 133], the searched compatibility is ensured if

$$\begin{aligned}
&\eta = \widehat{\eta}\,(u,w) + \tfrac{\Lambda_0}{2}\mathbf{J}^u \cdot \mathbf{J}^u + \tfrac{\Gamma_0}{2}\mathbf{J}^w \cdot \mathbf{J}^w,\\
&\phi = \Lambda\,(u)\,J^u + \Gamma\,(w)\,J^w,\\
&\Lambda = \Lambda_0\gamma(u) + \widetilde{\Lambda}_0,\\
&\Gamma = \Gamma_0\mu(w) + \widetilde{\Gamma}_0,\\
&\mathbf{\Pi} = \Lambda_0\mathbf{J}^u,\\
&\mathbf{\Xi} = \Gamma_0\mathbf{J}^w,
\end{aligned} \tag{A.5}$$

with

$$\frac{\partial\widehat{\eta}}{\partial u} = \Lambda, \quad \frac{\partial\widehat{\eta}}{\partial w} = \Gamma. \tag{A.6}$$

Finally, the concavity condition for η with respect to the field variables yields the further restrictions

$$\Lambda_0 < 0, \quad \Gamma_0 < 0, \quad \gamma_u > 0, \quad \mu_w > 0 \tag{A.7}$$

which provide the positiveness of the relaxation times $\tau^u = 1/\gamma_u$ and $\tau^w = d/\mu_w$, as expected. Notice that, if the phenomenological functions $\gamma(u)$ and $\mu(w)$ depend linearly on their arguments, the inertial times are constant.

Taking into account (A.2)-(A.7), the system of balance laws (A.2) becomes:

$$\begin{aligned}
&\tfrac{\partial\mathbf{J}^u}{\partial t} + \tfrac{1}{\tau^u}\nabla u = -\tfrac{1}{\tau^u}\mathbf{J}^u,\\
&\tfrac{\partial\mathbf{J}^w}{\partial t} + \tfrac{d}{\tau^w}\nabla w = -\tfrac{1}{\tau^w}\mathbf{J}^w.
\end{aligned} \tag{A.8}$$

Therefore, the two-species hyperbolic reaction-diffusion system in two spatial coordinates is given by (A.1),(A.8).

We remark that the concavity condition for η with respect to the field variables (A.6) guarantees the governing system (A.1),(A.8) to be symmetric–hyperbolic in the sense of Friedrichs–Lax [134] when the Lagrange multipliers are chosen as field variables. The advantage of having symmetric hyperbolic systems lies in the fact that the Cauchy problem is well-posed for suitable smooth data, i.e. existence, uniqueness, and continuous dependence of the solutions on the data is guaranteed [135]. We also notice that, in the limit case $\tau^u \to 0$ and $\tau^w \to 0$, the hyperbolic model (A.1),(A.8) reduces to the corresponding parabolic one.

B LSA and WNA for stationary pattern in 1D hyperbolic RT systems

In this Appendix the expressions of the quantities involved in LSA and WNA are provided for the specific case of the hyperbolic modified Klausmeier model (2.1),(2.2) with kinetic terms specified in (1.2). As already mentioned, the plant mortality B is taken as the main control parameter and the spatially-homogeneous steady states are reported in Section (1.4).

In the model under investigation, the characteristic equation reads

$$\omega^4 + A_1\omega^3 + A_2\omega^2 + A_3\omega + A_4 = 0 \tag{B.1}$$

where

$$\begin{aligned}
A_1 &= \tfrac{1}{\tau^u} + \tfrac{1}{\tau^w} - \left(f_u^* + g_w^*\right), \\
A_2 &= \left(\tfrac{1}{\tau^u} + \tfrac{d}{\tau^w}\right) k^2 + \tau^u\tau^w - \left(f_u^* + g_w^*\right)\left(\tfrac{1}{\tau^u} + \tfrac{1}{\tau^w}\right) + f_u^* g_w^* - f_w^* g_u^*, \\
A_3 &= \left[\left(d+1\right)\tau^u\tau^w - f_u^*\tfrac{d}{\tau^w} - g_w^*\tfrac{1}{\tau^u}\right] k^2 + \left(f_u^* g_w^* - f_w^* g_u^*\right)\left(\tfrac{1}{\tau^u} + \tfrac{1}{\tau^w}\right) - \left(f_u^* + g_w^*\right)\tau^u\tau^w, \\
A_4 &= \tfrac{d}{\tau^u\tau^w}\left[k^4 - \left(f_u^* + \tfrac{g_w^*}{d}\right) k^2 + \tfrac{f_u^* g_w^* - f_w^* g_u^*}{d}\right],
\end{aligned}$$

and the only non-zero partial derivatives of kinetic terms take the form:

$$\begin{aligned}
&f_u^* = B, \quad f_w^* = u_S^2, \quad g_u^* = -2B, \quad g_w^* = -\left(1 + u_S^2\right), \quad f_{uu}^* = 2B/u_S, \\
&f_{uw}^* = 2u_S, \quad g_{uu}^* = -2B/u_S, \quad g_{uw}^* = -2u_S, \quad f_{uuw}^* = 2, \quad g_{uuw}^* = -2.
\end{aligned} \tag{B.2}$$

LSA reveals that the states $\mathbf{U}_D^*$ and $\mathbf{U}_L^*$ are always stable and unstable, respectively. Thus, this latter one cannot gives rise to pattern formation and it will not be further considered in our analysis. On the other hand, the state $\mathbf{U}_S^*$ is found to be stable against spatially-uniform perturbations if:

$$\begin{cases}
B - 1 - u_S^2 < 0, \\
B\left(u_S^2 - 1\right) > 0,
\end{cases} \tag{B.3}$$

that are always fulfilled since realistic values of plant loss B are in the range $(0, 2)$ [64] and $u_S > 1$. By looking for the stability against non-homogeneous perturbations, the state $\mathbf{U}_D^*$ is always stable, so preventing the possibility to giving rise to Turing type patterns, whereas $\mathbf{U}_S^*$ is stable iff:

$$\begin{cases}
dB - \left(1 + u_S^2\right) < 0 \\
\left(dB - 1 - u_S^2\right)^2 - 4dB\left(u_S^2 - 1\right) < 0
\end{cases} \tag{B.4}$$

When conditions (B.4) are violated, Turing patterns may originate as a consequence of destabilization of the state $\mathbf{U}_S^*$. From (2.5),(2.6), the critical values of control

parameter B_c and wavenumber k_c at the onset of Turing instability read:

$$B_c = \frac{3u_{S_c}^2 - 1 + 2u_{S_c}\sqrt{2\left(u_{S_c}^2 - 1\right)}}{d}, \tag{B.5}$$

$$k_c^2 = \sqrt{\frac{B_c\left(u_{S_c}^2 - 1\right)}{d}}, \tag{B.6}$$

being $u_{S_c} = \left(A + \sqrt{A^2 - 4B_c^2}\right) / (2B_c)$.

Let us now focus on the results of WNA. Applying expansions

$$\begin{aligned} B &= B_c + \epsilon^2 B_2 + \epsilon^4 B_4 + O(\epsilon^6), \\ \overline{\mathbf{U}} &= \epsilon\overline{\mathbf{U}}_1 + \epsilon^2\overline{\mathbf{U}}_2 + \epsilon^3\overline{\mathbf{U}}_3 + \epsilon^4\overline{\mathbf{U}}_4 + \epsilon^5\overline{\mathbf{U}}_5 + O(\epsilon^6), \end{aligned} \tag{B.7}$$

in the governing system (2.1)-(2.2) and collecting the terms of the same orders of ϵ, the set of linear equation (2.9) is obtained. It reads:

$$\begin{aligned} &\text{at order 1} && \tfrac{\partial\overline{\mathbf{U}}_1}{\partial x} - K_c^*\overline{\mathbf{U}}_1 = \mathbf{0} \\ &\text{at order 2} && \tfrac{\partial\overline{\mathbf{U}}_2}{\partial x} - K_c^*\overline{\mathbf{U}}_2 = \mathrm{M}^{-1}\,\widetilde{\mathbf{F}}_2 \\ &\text{at order 3} && \tfrac{\partial\overline{\mathbf{U}}_3}{\partial x} - K_c^*\overline{\mathbf{U}}_3 = \mathrm{M}^{-1}\,\widetilde{\mathbf{F}}_3 \\ &\text{at order 4} && \tfrac{\partial\overline{\mathbf{U}}_4}{\partial x} - K_c^*\overline{\mathbf{U}}_4 = \mathrm{M}^{-1}\,\widetilde{\mathbf{F}}_4 \\ &\text{at order 5} && \tfrac{\partial\overline{\mathbf{U}}_5}{\partial x} - K_c^*\overline{\mathbf{U}}_5 = \mathrm{M}^{-1}\,\widetilde{\mathbf{F}}_5 \end{aligned} \tag{B.8}$$

where the vectors $\widetilde{\mathbf{F}}_j$ $(j = 2, ..., 5)$ and the matrix K_c^* are defined as in (2.10) and (2.11), respectively.

Taking into account (B.2),(B.5),(B.6), the matrix K_c^*, defined in (2.11), admits two complex eigenvalues $\mp ik_c$ with algebraic and geometric multiplicity given by 2 and 1, respectively. By introducing the invertible transform matrix P and the Jordan canonical form Υ of K_c^*, the general solution of $(\mathrm{B.8})_1$ can be expressed as:

$$\overline{\mathbf{U}}_1 = Pe^{\Upsilon x}P^{-1}\mathbf{C}_1, \tag{B.9}$$

being:

$$P = \begin{bmatrix} iY_1 & r_1 & -iY_1 & r_1 \\ iY_2 & r_2 & -iY_2 & r_2 \\ Y_3 & ir_3 & Y_3 & -ir_3 \\ Y_4 & ir_4 & Y_4 & -ir_4 \end{bmatrix}, \qquad \Upsilon = \begin{bmatrix} ik_c & 0 & 0 & 0 \\ 1 & ik_c & 0 & 0 \\ 0 & 0 & -ik_c & 0 \\ 0 & 0 & 1 & -ik_c \end{bmatrix}, \tag{B.10}$$

where the vector $\mathbf{C}_1(X, T_2, T_4)$ is determined by boundary conditions and removal of secular terms, whereas r_i and Y_i $(i = 1, ..., 4)$ are the components of simple and generalized right eigenvectors of K_c^*, given by:

$$\begin{aligned} r_1 = 1, \quad r_2 = r_1\left(k_c^2 - B_c\right)/u_{S_c}^2, \quad r_3 = -k_c r_1, \quad r_4 = -dk_c r_2, \\ Y_1 = \tfrac{2k_c r_1}{k_c^2 - B_c}, \quad Y_2 = 0, \quad Y_3 = k_c Y_1 - r_1, \quad Y_4 = -dr_2. \end{aligned} \tag{B.11}$$

The solution at the first perturbative order, satisfying zero-flux boundary conditions, reads

$$\overline{\mathbf{U}}_1 = \mathrm{Re}\{\Omega\,\mathbf{r}\,e^{ik_c\,x}\}, \tag{B.12}$$

being $\mathbf{r} = [r_1, r_2, ir_3, ir_4]^T$.

On the other hand, the general solution of nonhomogeneous equations $(B.8)_2$-$(B.8)_5$ can be expressed as

$$\overline{\mathbf{U}}_j = Pe^{\Upsilon x}P^{-1}\mathbf{C}_j + Pe^{\Upsilon x}\int e^{-\Upsilon x}\,(\mathrm{M}P)^{-1}\,\widetilde{\mathbf{F}}_j dx \qquad j = 2, ..., 5, \tag{B.13}$$

being $\mathbf{C}_j$ the vector of arbitrary constants.

From the removal of secular terms at the third perturbative order, we get the CRGL equation

$$\frac{\partial\Omega}{\partial T_2} = \sigma\Omega - L|\Omega|^2\Omega + \nu\frac{\partial^2\Omega}{\partial X^2}, \tag{B.14}$$

where the real coefficients σ, L and ν are given by:

$$\begin{aligned}
\sigma &= \frac{B_2[2u_{S_c}^2(1+u_{S_c}^2)r(1+dr)+B_c(1-u_{S_c}^2)(2+dr)]}{B_c r(1-u_{S_c}^2)\big[d-1+k_c^2 d(\tau^w-\tau^u)\big]},\\
L &= -\frac{(6r+8\alpha+4\beta)(1+dr)}{8r\big[d-1+k_c^2 d(\tau^w-\tau^u)\big]},\\
\nu &= \frac{4dk_c^2}{\big(B_c-k_c^2\big)\big[d-1+k_c^2 d(\tau^w-\tau^u)\big]},
\end{aligned} \tag{B.15}$$

with

$$\begin{aligned}
r &= \frac{k_c^2 - B_c}{u_{S_c}^2}, \quad \alpha = \frac{\Big(B_c + 2ru_{S_c}^2\Big)\Big[ru_{S_c}^2 + B_c\Big(1-u_{S_c}^2\Big)\Big]}{B_c u_{S_C}^2\Big(u_{S_c}^2-1\Big)},\\
\beta &= \frac{\Big(B_c + 2u_{S_c}^2 r\Big)\Big[B_c(1+4dk_c^2) + u_{S_c}^2\Big(r - B_c - 4k_c^2(1-dr)\Big)\Big]}{9B_c u_{S_c}^2\Big(u_{S_c}^2-1\Big)}.
\end{aligned} \tag{B.16}$$

After that, removing secular terms at $O(\epsilon^4)$, the following compatibility equation is obtained:

$$k_1\Omega_{XXX} + k_2|\Omega|^2\Omega_X + k_3\Omega_X = 0, \tag{B.17}$$

where

$$\begin{aligned}
k_1 &= 4dk_c\nu(\gamma_u l_4 r_1 - l_3\mu_w r_2) - 4d\gamma_u\mu_w\left[k_c(\omega_{12}r_2 - \omega_{22}r_1) + r_2(\omega_{32} + l_1\nu)\right] + 4\gamma_u\mu_w r_1(\omega_{42} + l_2\nu),\\
k_2 &= \gamma_u\mu_w d[r_1r_2(2l_1r_2 + l_2r_1) + 4r_2u_{S_c}(\omega_{14}r_2 + \omega_{24}r_1 - l_1m_2 - l_2m_1 + 2l_1n_2 + 2l_2n_1) +\\
&\quad + 12r_2(Ll_1 - \omega_{31}) + 12k_c(\omega_{21}r_1 - \omega_{11}r_2) + 4r_2w_{S_c}(\omega_{14}r_1 - l_1m_1 + 2l_1n_1)] +\\
&\quad + \gamma_u\mu_w[12r_1(\omega_{41} - Ll_2) + 4r_1u_{S_c}(2l_2n_1 + 2l_1n_2 - l_2m_1 - l_1m_2 + \omega_{14}r_2 + \omega_{24}r_1) +\\
&\quad + 4r_1w_{S_c}(2l_1n_1 - l_1m_1 + r_1\omega_{14}) + r_1^2(l_2r_1 + 2l_1r_2)] + 12Lk_cd(l_3r_2\mu_w - l_4r_1\gamma_u),\\
k_3 &= 4\gamma_u\mu_w\{\sigma(l_2r_1 - dl_1r_2) + r_1(\omega_{40} + dk_c\omega_{20}) + B_2\left[r_1(2l_1 + 2u_{S_c}\delta_1 l_2) + dr_2(l_1 + 2u_{S_c}\delta_1 l_2)\right] +\\
&\quad - dr_2(\omega_{30} + k_c\omega_{10})\} + 4dk_c\sigma(\gamma_u l_4 r_1 - l_3\mu_w r_2),
\end{aligned} \tag{B.18}$$

being $\gamma_u = 1/\tau^u$, $\mu_w = d/\tau^w$, $w_{S_C} = B_c/u_{S_c}$, $\delta_1 = u_{S_c}\left(1+u_{S_c}^2\right)/[B_c\left(1-u_{S_c}^2\right)]$ and

$$\omega_{10} = \frac{B_2\Big\{E_1\big(r_1+2r_2u_{S_c}\delta_1\big)+r_1^2\big[2r_1k_c(\mu_w-\gamma_u d)+\mu_w Y_1\big(k_c^2+\gamma_u\big)\big]\Big\}}{4k_c^2r_2Y_1\big[\gamma_u\mu_w(d-1)+dk_c^2(\gamma_u d-\mu_w)\big]},$$

$$\omega_{20} = \frac{B_2\big(r_1+2r_2u_{S_c}\delta_1\big)\Big\{r_1E_1+2k_cY_1^2\big[\gamma_u\mu_w(r_1+r_2)-k_c^2\big(\gamma_u d^2r_2+\mu_w r_1\big)\big]\Big\}}{4k_c^2r_1^2Y_1\big[\gamma_u\mu_w(d-1)+dk_c^2(\gamma_u d-\mu_w)\big]}+$$
$$+\frac{B_2\big\{2r_1^2k_c(\mu_w-\gamma_u d)+r_1\mu_wY_1\big(k_c^2+\gamma_u\big)+2k_c\mu_wY_1^2\big(\gamma_u-k_c^2\big)\big\}}{4k_c^2Y_1\big[\gamma_u\mu_w(d-1)+dk_c^2(\gamma_u d-\mu_w)\big]},$$

$$\omega_{30} = \frac{B_2\Big\{\big(r_1+2r_2u_{S_c}\delta_1\big)\big[E_1-4k_c^2\mu_wY_1(r_1+dr_2)\big]+r_1^2\big[2r_1k_c(\mu_w-\gamma_u d)+\mu_wY_1\big(\gamma_u-3k_c^2\big)\big]\Big\}}{4k_cr_2Y_1\big[\gamma_u\mu_w(d-1)+dk_c^2(\gamma_u d-\mu_w)\big]},$$

$$\omega_{40} = \frac{dB_2\big(r_1+2r_2u_{S_c}\delta_1\big)\Big\{r_1E_1+2k_cY_1^2\big[\gamma_u\mu_w(r_1+r_2)-k_c^2\big(\gamma_u d^2r_2+\mu_wr_1\big)\big]-4dk_c^2\gamma_ur_1Y_1(r_1+dr_2)\Big\}}{4k_cr_1^2Y_1\big[\gamma_u\mu_w(d-1)+dk_c^2(\gamma_u d-\mu_w)\big]}+$$
$$+\frac{dB_2\Big\{r_1^2\big[2k_c\mu_wY_1^2\big(\gamma_u-k_c^2\big)+r_1\mu_wY_1\big(k_c^2+\gamma_u\big)+r_1^2k_c(\mu_w-\gamma_u d)\big]-4dk_c^2\gamma_ur_1Y_1\big(r_1^2+r_1+dr_2\big)\Big\}}{4k_cr_1^2Y_1\big[\gamma_u\mu_w(d-1)+dk_c^2(\gamma_u d-\mu_w)\big]},$$

$$\omega_{11} = \frac{\big(6r_1^2r_2+8q_1+4s_1\big)E_1}{32k_c^2r_2Y_1\big[\gamma_u\mu_w(d-1)+dk_c^2(\gamma_u d-\mu_w)\big]}+\frac{r_1}{r_2}c_3,$$

$$\omega_{21} = \frac{\big(6r_1^2r_2+8q_1+4s_1\big)\Big\{r_1E_1+2k_cY_1^2\big[\gamma_u\mu_w(r_1+r_2)-k_c^2\big(\mu_wr_1+d^2\gamma_ur_2\big)\big]\Big\}}{32Y_1k_c^2r_1^2\big[\gamma_u\mu_w(d-1)+dk_c^2(\gamma_u d-\mu_w)\big]}+c_3,$$

$$\omega_{31} = \frac{\big(6r_1^2r_2+8q_1+4s_1\big)\big[E_1-4k_c^2\mu_wY_1(r_1+dr_2)\big]}{32Y_1k_cr_2\big[\gamma_u\mu_w(d-1)+dk_c^2(\gamma_u d-\mu_w)\big]}+\frac{k_cr_1}{r_2}c_3,$$

$$\omega_{41} = \frac{d\big(6r_1^2r_2+8q_1+4s_1\big)\Big\{r_1E_1-4dk_c^2r_1\gamma_uY_1(r_1+dr_2)+2k_cY_1^2\big[\gamma_u\mu_w(r_1+r_2)-k_c^2\big(\mu_wr_1+d^2\gamma_ur_2\big)\big]\Big\}}{32Y_1k_cr_1^2\big[\gamma_u\mu_w(d-1)+dk_c^2(\gamma_u d-\mu_w)\big]}+dk_cc_3,$$

$$\omega_{12} = -\frac{2r_1^2(\mu_w+d\gamma_u)p_{42}+Y_1dk_c\big(k_c^2p_{12}-\gamma_up_{42}\big)(2k_cY_1+r_1)+\mu_wY_1(k_cp_{22}-\gamma_up_{32})(Y1-r_1)}{4Y_1k_c^2r_1r_2\big[\gamma_u\mu_w(d-1)+dk_c^2(\gamma_u d-\mu_w)\big]}+$$
$$-\frac{2\gamma_ur_1^2(Y_1k_c-r_1)(dk_cl_4-l_2\mu_w)+2\mu_wr_2dr_1(\gamma_ul_1-l_3k_c)}{4Y_1k_c^2r_1r_2\big[\gamma_u\mu_w(d-1)+dk_c^2(\gamma_u d-\mu_w)\big]},$$

$$\omega_{22} = -\frac{(2r_1-Y_1k_c)(\gamma_udp_{42}+\mu_wp_{22})-\mu_wY_1(k_cr_1p_{22}-\gamma_up_{32})+2\gamma_ur_1(Y_1k_c-r_1)(dk_cl_4-l_2\mu_w)}{4Y_1k_c^2r_1\big[\gamma_u\mu_w(d-1)+dk_c^2(\gamma_u d-\mu_w)\big]}+$$
$$-\frac{2\mu_wr_2dr_1(\gamma_ul_1-l_3k_c)+Y_1dk_c^3(r_1-1)p_{12}}{4Y_1k_c^2r_1\big[\gamma_u\mu_w(d-1)+dk_c^2(\gamma_u d-\mu_w)\big]},$$

$$\omega_{32} = -\frac{Y_1dk_c^3(2k_cY_1-3r_1)p_{12}+\mu_w\big[Y_1k_c(Y_1-r_1)+10r_1^2\big]p_{22}-\gamma_u\mu_wY_1(Y_1-5r_1)p_{32}+10\mu_wr_2dr_1(\gamma_ul_1-l_3k_c)}{4Y_1k_cr_1r_2\big[\gamma_u\mu_w(d-1)+dk_c^2(\gamma_u d-\mu_w)\big]}+$$
$$-\frac{10\gamma_ur_1(Y_1k_c-r_1)(dk_cl_4-l_2\mu_w)-\gamma_ud\big[Y_1^2k_c-5r_1(2r_1-Y_1k_c)\big]p_{42}+4\mu_wr_2Y_1dk_cr_1(l_3k_c-\gamma_ul_1)}{4Y_1k_cr_1r_2\big[\gamma_u\mu_w(d-1)+dk_c^2(\gamma_u d-\mu_w)\big]},$$

$$\omega_{42} = -\frac{d\gamma_u(3Y_1k_c+2r_1)p_{42}-3Y_1dk_c^3p_{12}-2\gamma_u(Y_1k_c+r_1)(dp_{22}+p_{12})+\mu_w(Y_1\gamma_u+2dr_1k_c)p_{32}-\mu_w\big[Y_1k_c+2r_1(d-1)\big]p_{22}}{4Y_1k_cr_1\big[\gamma_u\mu_w(d-1)+dk_c^2(\gamma_u d-\mu_w)\big]},$$

$$\omega_{13} = -\frac{\big(6r_1^2r_2+12s_1\big)\big[dr_2(r_1-4Y_1k_c)+r_1^2\big]}{768dk_c^3r_2Y_1},$$

$$\omega_{23} = -\frac{\big(6r_1^2r_2+12s_1\big)[dr_2+4Y_1k_c+r_1]}{768dk_c^3Y_1},$$

$$\omega_{33} = 3k_c\omega_{13},$$

$$\omega_{43} = 3dk_c\omega_{23},$$

$$\omega_{14} = -\frac{2r_1\big[p_{14}(r_1+dr_2)-2dr_2p_{24}+2r_1p_{34}\big]-3Y_1dk_cr_2(p_{14}-2p_{24})}{9Y_1dk_c^3r_2},$$

$$\omega_{24} = -\frac{2\left[p_{14}(r_1+dr_2)-2dr_2p_{24}+2r_1p_{34}\right]+3Y_1k_c(p_{14}+2p_{34})}{9Y_1dk_c^3},$$
$$\omega_{34} = -2\left(k_c\omega_{14}+m_1\right),$$
$$\omega_{44} = -2d\left(k_c\omega_{24}+m_2\right),$$
$$\omega_{35} = -2n_1,$$
$$\omega_{45} = -2dn_2,$$
$$E_1 = 2k_cr_1\left(\mu_w-\gamma_ud\right)\left(r_1+dr_2\right)+Y_1\left[\gamma_u\mu_w\left(r_1+r_2\right)+\mu_wk_c^2\left(r_1+dr_2\right)+dk_c^2r_2\left(\mu_w-\gamma_ud\right)\right],$$
$$q_1 = \frac{r_1\left(B_cr_1+2u_{S_c}^2r_2\right)\left[r_2u_{S_c}^2+B_cr_1\left(1-u_{S_c}^2\right)\right]}{B_cu_{S_c}^2\left(u_{S_c}^2-1\right)},$$
$$s_1 = \frac{r_1\left(B_cr_1+2u_{S_c}^2r_2\right)\left[B_cr_1\left(1+4dk_c^2\right)+u_{S_c}^2\left(r_2-B_cr_1-4k_c^2(r_1-dr_2)\right)\right]}{9B_cu_{S_c}^2\left(u_{S_c}^2-1\right)},$$
$$p_{12} = \gamma_ul_1r_2d-\mu_wl_2r_1,$$
$$p_{22} = l_4k_cr_1-\gamma_ul_1r_2,$$
$$p_{32} = l_4r_1-l_3r_2,$$
$$p_{42} = l_3r_2dk_c-l_2\mu_wr_1,$$
$$p_{14} = l_1r_2u_{S_c}+r_1\left(l_2u_{S_c}+l_1w_{S_c}\right),$$
$$p_{24} = m_3+2m_1k_c,$$
$$p_{34} = m_4+2m_2dk_c.$$

with

$$n_1 = \frac{r_1\left(B_cr_1+2u_{S_c}^2r_2\right)}{2B_cu_{S_c}\left(u_{S_c}^2-1\right)}, \qquad n_2 = -B_cn_1, \qquad m_1 = \frac{1+4dk_c^2}{9}n_1,$$
$$m_2 = -\frac{B_c+4k_c^2}{9}n_1, \qquad m_3 = 2k_cm_1, \qquad m_4 = 2dk_cm_2,$$
$$l_1 = -\frac{l_3+r_1}{k_c}, \qquad l_2 = -\frac{r_2(r_1-Y_1k_c+l_3)}{k_cr_1}, \quad l_4 = \frac{dr_2(l_3-Y_1k_c)}{r_1}.$$

Finally, l_3 and c_3 are implicitly given by

$$\begin{aligned}
&8h_1\left(3Lk_1+\nu k_2\right)+\gamma_u\mu_wk_1h_0\{4w_{S_c}\left[l_1\omega_{14}+r_1\rho_{12}+2r_1\rho_{10}\right]+l_1\left(l_1r_2+2l_2r_1\right)+\\
&\quad+4u_{S_c}\left[l_1\omega_{24}+l_2\omega_{14}+r_2\rho_{12}+r_1\rho_{22}+2\left(r_1\rho_{20}+r_2\rho_{10}\right)\right]\}+\\
&\quad+8\gamma_u\mu_wk_1\left[dk_c\left(\psi_{11}r_2-\psi_{21}r_1\right)+\psi_{41}r_1-d\psi_{31}r_2\right]=0,\\
&(4k_2\nu+12Lk_1)h_1-4\gamma_u\mu_wk_1[d\psi_{31}r_2-\psi_{41}r_1+dk_c(\psi_{21}r_1-\psi_{11}r_2)]+\\
&\quad-12k_1\nu([\gamma_u\mu_w(d\omega_{11}r_2-\omega_{21}r_1)+dk_c(\gamma_u\omega_{41}r_1-\mu_w\omega_{31}r_2)]+\\
&\quad+\gamma_u\mu_wk_1h_0\{3r_1(2\omega_{12}r_2+\omega_{22}r_1)+4r_1w_{S_c}(\tau_{12}+2\tau_{10})+4u_{S_c}[r_1(\tau_{22}+2\tau_{20})+\\
&\quad r_2(\tau_{12}+2\tau_{10})]+\ +4\omega_{12}u_{S_c}(m_2+2n_2)+4(m_1+2n_1)(\omega_{22}u_{S_c}+\omega_{12}w_{S_c})\}=0,
\end{aligned} \tag{B.19}$$

where $h_0 = dr_2+r_1$ and $h_1 = \gamma_u\mu_w\left(d\omega_{12}r_2-\omega_{22}r_1\right)+dk_c\left(\gamma_u\omega_{42}r_1-\mu_wr_2\omega_{32}\right)$.

Then, pushing WNA up to the fifth perturbative order, the removal of secular terms leads to the real CQRGL equation:

$$\frac{\partial\Omega}{\partial T} = \overline{\sigma}\Omega - \overline{L}|\Omega|^2\Omega + \overline{R}|\Omega|^4\Omega + \overline{\nu}\frac{\partial^2\Omega}{\partial X^2}, \tag{B.20}$$

where $\overline{\sigma} = \sigma + \epsilon^2\widetilde{\sigma}$, $\overline{L} = L + \epsilon^2\widetilde{L}$, $\overline{\nu} = \nu + \epsilon^2\widetilde{\nu}$ and $\overline{R} = \epsilon^2\widetilde{R}$, being the second-order corrections given by

$$\widetilde{\sigma} = \gamma_u\mu_w\frac{h_0\left[4u_{S_c}\delta_1(B_4r_2+B_2\omega_{20})+B_2^2\delta_3r_2\right]+2(h_0+r_1)(\omega_{10}B_2+r_1B_4)}{2r_1r_2\left[\gamma_u\mu_w(d-1)+dk_c^2(d\gamma_u-\mu_w)\right]}+$$
$$+\sigma\frac{\gamma_u\mu_w(d\omega_{10}r_2-\omega_{20}r_1)+dk_c(\gamma_u\omega_{40}r_1-\mu_w\omega_{30}r_2)}{r_1r_2\left[\gamma_u\mu_w(d-1)+dk_c^2(d\gamma_u-\mu_w)\right]},$$

$$\widetilde{L} = \gamma_u\mu_w\left\{\frac{12\sigma(\omega_{21}r_1-d\omega_{11}r_2)+(r_1+dr_2)\left[4(2\zeta_{10}+\zeta_{12})(r_2u_{S_c}+r_1w_{S_c})+4B_2[2u_{S_c}\delta_1\omega_{21}+\delta_1r_1(m_2+2n_2)]\right.}{4r_1r_2\left[\gamma_u\mu_w(d-1)+dk_c^2(d\gamma_u-\mu_w)\right]}+\right.$$
$$+\frac{4[\omega_{10}w_{S_c}+B_2(\delta_1r_2+\delta_2r_1)](m_1+2n_1)+4u_{S_c}(m_2\omega_{10}+m_1\omega_{20})+8u_{S_c}(n_2\omega_{10}+n_1\omega_{20})+3r_1(2\omega_{10}r_2+\omega_{20}r_1)}{4r_1r_2\left[\gamma_u\mu_w(d-1)+dk_c^2(d\gamma_u-\mu_w)\right]}+$$
$$\left.+\frac{\left.4r_1u_{S_c}(2\zeta_{20}+\zeta_{22})\right]+4B_2\omega_{11}(2r_1+dr_2)-4L(\omega_{20}r_1-d\omega_{10}r_2)}{4r_1r_2\left[\gamma_u\mu_w(d-1)+dk_c^2(d\gamma_u-\mu_w)\right]}\right\}+$$
$$+\frac{Ldk_c(\gamma_u\omega_{40}r_1-\mu_w\omega_{30}r_2)-3dk_c\sigma(\gamma_u\omega_{41}r_1-\mu_w\omega_{31}r_2)}{r_1r_2\left[\gamma_u\mu_w(d-1)+dk_c^2(d\gamma_u-\mu_w)\right]},$$

$$\widetilde{R} = \frac{12Ldk_c(\omega_{31}r_2\mu_w-\omega_{41}r_1\gamma_u)-\gamma_u\mu_w\left\{12L(d\omega_{11}r_2-\omega_{21}r_1)+4r_1^2[n_2(2n_1+m_1)+m_2(m_1+n_1)]+4r_1r_2m_1n_1+\right.}{4r_1r_2\left[\gamma_u\mu_w(d-1)+dk_c^2(d\gamma_u-\mu_w)\right]}+$$
$$+\frac{h_0\left[r_1^2(\omega_{23}+3\omega_{21})+4r_1u_{S_c}(\eta_{22}+2\eta_{20})+2r_2(m_1^2+2n_1^2)+4m_2u_{S_c}(\omega_{13}+\omega_{11})+2r_1r_2(\omega_{13}+3\omega_{11})\right.}{4r_1r_2\left[\gamma_u\mu_w(d-1)+dk_c^2(d\gamma_u-\mu_w)\right]}+$$
$$+\frac{4m_1u_{S_c}(\omega_{21}+\omega_{23})+8u_{S_c}(n_2\omega_{11}+n_1\omega_{21})+4(\eta_{12}+2\eta_{10})(r_2u_{S_c}+r_1w_{S_c})+4w_{S_c}[m_1(\omega_{11}+\omega_{13})+2n_1\omega_{11}]\right.}{4r_1r_2\left[\gamma_u\mu_w(d-1)+dk_c^2(d\gamma_u-\mu_w)\right]}+$$
$$\left.\left.+\frac{4d\left.\left[m_1r_2(n_1r_2+m_2r_1)+r_1r_2(m_1n_2+m_2n_1+2n_1n_2)\right]\right\}}{4r_1r_2\left[\gamma_u\mu_w(d-1)+dk_c^2(d\gamma_u-\mu_w)\right]},\right.$$

$$\widetilde{\nu} = \frac{B_2\gamma_u\mu_wk_1\left[\omega_{12}(h_0+r_1)+2u_{S_c}\delta_1\omega_{22}h_0\right]-h_1(k_1\sigma-k_3\nu)}{k_1r_1r_2\left[\gamma_u\mu_w(d-1)+dk_c^2(d\gamma_u-\mu_w)\right]}+$$
$$-\frac{k_1\left\{\nu dk_c[\gamma_u\omega_{40}r_1-\mu_w\omega_{30}r_2]+\mu_w\gamma_u\left[dk_c(r_1\rho_{21}-r_2\rho_{11})+\nu(d\omega_{10}r_2-\omega_{20}r_1)+dr_2\rho_{31}-r_1\rho_{41}\right]\right\}}{k_1r_1r_2\left[\gamma_u\mu_w(d-1)+dk_c^2(d\gamma_u-\mu_w)\right]},$$

where the coefficients here appearing are given implicitly by

$$\omega_{14}+\rho_{32}-2k_c\rho_{12}=0,$$
$$k_1l_3+\gamma_uk_1\omega_{10}-\gamma_uk_3\omega_{12}+\gamma_uk_1\rho_{31}+\gamma_uk_1k_c\rho_{11}=0,$$
$$3k_1\omega_{11}-9k_1\omega_{13}-k_2\omega_{12}+k_1\psi_{31}-3k_1\psi_{33}+k_1k_c\psi_{11}-9k_1k_c\psi_{13}=0,$$
$$3\omega_{13}+\psi_{33}+3k_c\psi_{13}=0,$$
$$\eta_{34}-4\eta_{14}k_c=0,$$
$$2m_3\sigma+\gamma_u\zeta_{32}-2\gamma_uk_c\zeta_{12}=0,$$
$$\gamma_u\omega_{14}+\gamma_u\tau_{32}+2m_3\nu-2\gamma_uk_c\tau_{12}=0,$$
$$\eta_{32}\gamma_u-2Lm_3-2\eta_{34}\gamma_u-2\eta_{12}\gamma_uk_c+8\eta_{14}\gamma_uk_c=0,$$
$$\rho_{42}+d\omega_{24}-2dk_c\rho_{22}=0,$$
$$dk_1l_4+k_1\mu_w\rho_{41}+dk_1\mu_w\omega_{20}-dk_3\mu_w\omega_{22}+dk_1k_c\mu_w\rho_{21}=0,$$
$$k_1\psi_{41}-3k_1\psi_{43}+3dk_1\omega_{21}-9dk_1\omega_{23}-dk_2\omega_{22}+dk_1k_c\psi_{21}-9dk_1k_c\psi_{23}=0,$$
$$\psi_{43}+3d\omega_{23}+3dk_c\psi_{23}=0,$$
$$\eta_{42}\mu_w-2\eta_{44}\mu_w-2Ldm_4-2d\eta_{22}k_c\mu_w+8d\eta_{24}k_c\mu_w=0,$$
$$\eta_{44}-4d\eta_{24}k_c=0,$$
$$\mu_w\zeta_{42}+2dm_4\sigma-2dk_c\mu_w\zeta_{22}=0,$$
$$\mu_w\tau_{42}+2dm_4\nu+d\mu_w\omega_{24}-2dk_c\mu_w\tau_{22}=0,$$
$$2\omega_{34}u_{S_c}+B_cl_1^2-2\rho_{22}u_{S_c}^3+2l_1l_2u_{S_c}^2-2B_c\rho_{12}u_{S_c}+4k_c\rho_{32}u_{S_c}=0,$$
$$\omega_{35}u_{S_c}-\omega_{34}u_{S_c}-B_cl_1^2-\rho_{20}u_{S_c}^3+\rho_{22}u_{S_c}^3-2l_1l_2u_{S_c}^2-B_c\rho_{10}u_{S_c}+B_c\rho_{12}u_{S_c}-2k_c\rho_{32}u_{S_c}=0,$$
$$-k_1\rho_{21}u_{S_c}^2+k_1l_1+k_1\omega_{30}-k_3\omega_{32}-B_2k_1l_1-B_ck_1\rho_{11}-k_1k_c\rho_{31}-B_22u_{S_c}\delta_1k_1l_2=0,$$
$$\begin{aligned}&k_1\psi_{23}u_{S_c}^3-k_1\psi_{21}u_{S_c}^3+3k_1\omega_{31}u_{S_c}-3k_1\omega_{33}u_{S_c}-k_2\omega_{32}u_{S_c}-k_1k_c\psi_{31}u_{S_c}+3k_1k_c\psi_{33}u_{S_c}+\\&+2k_1l_1m_2u_{S_c}^2+2k_1l_2m_1u_{S_c}^2-2k_1l_1n_2u_{S_c}^2-2k_1l_2n_1u_{S_c}^2+2B_ck_1l_1m_1-2B_ck_1l_1n_1+\\&-B_ck_1\psi_{11}u_{S_c}+B_ck_1\psi_{13}u_{S_c}=0,\end{aligned}$$
$$\begin{aligned}&12\omega_{33}u_{S_c}-4\psi_{23}u_{S_c}^3-4l_1m_2u_{S_c}^2-4l_2m_1u_{S_c}^2-l_2r_1^2u_{S_c}-4\omega_{14}r_2u_{S_c}^2-4\omega_{24}r_1u_{S_c}^2-4B_cl_1m_1+\\&-4B_c\omega_{14}r_1-4B_c\psi_{13}u_{S_c}-12k_c\psi_{33}u_{S_c}-2l_1r_1r_2u_{S_c}=0,\end{aligned}$$
$$\begin{aligned}&16\eta_{34}k_cu_{S_c}-4\eta_{24}u_{S_c}^3-4m_1m_2u_{S_c}^2-m_2r_1^2u_{S_c}-4\omega_{13}r_2u_{S_c}^2-4\omega_{23}r_1u_{S_c}^2-4B_c\eta_{14}u_{S_c}+\\&-4B_c\omega_{13}r_1-2B_cm_1^2-2m_1r_1r_2u_{S_c}=0,\end{aligned}$$
$$\begin{aligned}&4B_cm_1^2-2\eta_{22}u_{S_c}^3+8\eta_{24}u_{S_c}^3+8m_1m_2u_{S_c}^2-4m_1n_2u_{S_c}^2-4m_2n_1u_{S_c}^2+m_2r_1^2u_{S_c}-n_2r_1^2u_{S_c}+\\&-2\omega_{11}r_2u_{S_c}^2+6\omega_{13}r_2u_{S_c}^2-2\omega_{21}r_1u_{S_c}^2+6\omega_{23}r_1u_{S_c}^2-2B_c\eta_{12}u_{S_c}+8B_c\eta_{14}u_{S_c}-4B_cm_1n_1+\\&-2B_c\omega_{11}r_1+6B_c\omega_{13}r_1-4Lm_1u_{S_c}+4\eta_{32}k_cu_{S_c}-32\eta_{34}k_cu_{S_c}+2m_1r_1r_2u_{S_c}-2n_1r_1r_2u_{S_c}=0,\end{aligned}$$
$$\begin{aligned}&\eta_{22}u_{S_c}^3-B_cn_1^2-\eta_{20}u_{S_c}^3-B_cm_1^2-\eta_{24}u_{S_c}^3-2m_1m_2u_{S_c}^2+2m_1n_2u_{S_c}^2+2m_2n_1u_{S_c}^2-2n_1n_2u_{S_c}^2+\\&-B_c\eta_{10}u_{S_c}+B_c\eta_{12}u_{S_c}-B_c\eta_{14}u_{S_c}+2B_cm_1n_1+2Lm_1u_{S_c}-2Ln_1u_{S_c}-2\eta_{32}k_cu_{S_c}+4\eta_{34}k_cu_{S_c}=0,\end{aligned}$$
$$\begin{aligned}&4m_1\sigma u_{S_c}-2\omega_{10}r_2u_{S_c}^2-2\omega_{20}r_1u_{S_c}^2-2B_c\omega_{10}r_1-2B_2m_1u_{S_c}-2B_cu_{S_c}\zeta_{12}-2u_{S_c}^3\zeta_{22}+4k_cu_{S_c}\zeta_{32}+\\&-B_2\delta_2r_1^2u_{S_c}-2B_22u_{S_c}\delta_1m_2u_{S_c}-2B_2\delta_1r_1r_2u_{S_c}=0,\end{aligned}$$
$$\begin{aligned}&B_2m_1-B_2n_1-B_c\zeta_{10}+B_c\zeta_{12}-2m_1\sigma+2n_1\sigma-2k_c\zeta_{32}-u_{S_c}^2\zeta_{20}+u_{S_c}^2\zeta_{22}+\\&+B_22u_{S_c}\delta_1m_2-B_22u_{S_c}\delta_1n_2=0,\end{aligned}$$
$$\omega_{34}u_{S_c}-\tau_{22}u_{S_c}^3-\omega_{12}r_2u_{S_c}^2-\omega_{22}r_1u_{S_c}^2-B_c\omega_{12}r_1-B_c\tau_{12}u_{S_c}+2m_1\nu u_{S_c}+2k_c\tau_{32}u_{S_c}=0,$$
$$\omega_{35}-\omega_{34}-B_c\tau_{10}+B_c\tau_{12}-2m_1\nu+2n_1\nu-2k_c\tau_{32}-\tau_{20}u_{S_c}^2+\tau_{22}u_{S_c}^2=0,$$

$$2\omega_{44}u_{S_c} + 2\rho_{22}u_{S_c} - B_c l_1^2 + 2\rho_{22}u_{S_c}^3 - 2l_1 l_2 u_{S_c}^2 + 4B_c\rho_{12}u_{S_c} + 4k_c\rho_{42}u_{S_c} = 0,$$
$$\omega_{45}u_{S_c} - \omega_{44}u_{S_c} + \rho_{20}u_{S_c} - \rho_{22}u_{S_c} + B_c l_1^2 + \rho_{20}u_{S_c}^3 - \rho_{22}u_{S_c}^3 + 2l_1 l_2 u_{S_c}^2 + 2B_c\rho_{10}u_{S_c} +$$
$$-2B_c\rho_{12}u_{S_c} - 2k_c\rho_{42}u_{S_c} = 0,$$
$$k_1\rho_{21}u_{S_c}^2 + k_1 l_2 + k_1\omega_{40} - k_3\omega_{42} + k_1\rho_{21} + 2B_2 k_1 l_1 + 2B_c k_1\rho_{11} - k_1 k_c\rho_{41} + B_2 2u_{S_c}\delta_1 k_1 l_2 = 0,$$
$$k_1\psi_{21}u_{S_c}^3 - k_1\psi_{23}u_{S_c}^3 + 3k_1\omega_{41}u_{S_c} - 3k_1\omega_{43}u_{S_c} - k_2\omega_{42}u_{S_c} + k_1\psi_{21}u_{S_c} - k_1\psi_{23}u_{S_c} - k_1 k_c\psi_{41}u_{S_c} +$$
$$+3k_1 k_c\psi_{43}u_{S_c} - 2k_1 l_1 m_2 u_{S_c}^2 - 2k_1 l_2 m_1 u_{S_c}^2 + 2k_1 l_1 n_2 u_{S_c}^2 + 2k_1 l_2 n_1 u_{S_c}^2 - 2B_c k_1 l_1 m_1 + 2B_c k_1 l_1 n_1 +$$
$$+2B_c k_1\psi_{11}u_{S_c} - 2B_c k_1\psi_{13}u_{S_c} = 0,$$
$$12\omega_{43}u_{S_c} + 4\psi_{23}u_{S_c} + 4\psi_{23}u_{S_c}^3 + 4l_1 m_2 u_{S_c}^2 + 4l_2 m_1 u_{S_c}^2 + l_2 r_1^2 u_{S_c} + 4\omega_{14}r_2 u_{S_c}^2 + 4\omega_{24}r_1 u_{S_c}^2 +$$
$$+4B_c l_1 m_1 + 4B_c\omega_{14}r_1 + 8B_c\psi_{13}u_{S_c} - 12k_c\psi_{43}u_{S_c} + 2l_1 r_1 r_2 u_{S_c} = 0,$$
$$4\eta_{24}u_{S_c} + 2B_c m_1^2 + 4\eta_{24}u_{S_c}^3 + 4m_1 m_2 u_{S_c}^2 + m_2 r_1^2 u_{S_c} + 4\omega_{13}r_2 u_{S_c}^2 + 4\omega_{23}r_1 u_{S_c}^2 + 8B_c\eta_{14}u_{S_c} +$$
$$+4B_c\omega_{13}r_1 + 16\eta_{44}k_c u_{S_c} + 2m_1 r_1 r_2 u_{S_c} = 0,$$
$$2\eta_{22}u_{S_c} - 8\eta_{24}u_{S_c} - 4B_c m_1^2 + 2\eta_{22}u_{S_c}^3 - 8\eta_{24}u_{S_c}^3 - 8m_1 m_2 u_{S_c}^2 + 4m_1 n_2 u_{S_c}^2 + 4m_2 n_1 u_{S_c}^2 +$$
$$-m_2 r_1^2 u_{S_c} + n_2 r_1^2 u_{S_c} + 2\omega_{11}r_2 u_{S_c}^2 - 6\omega_{13}r_2 u_{S_c}^2 + 2\omega_{21}r_1 u_{S_c}^2 - 6\omega_{23}r_1 u_{S_c}^2 + 4B_c\eta_{12}u_{S_c} +$$
$$-16B_c\eta_{14}u_{S_c} + 4B_c m_1 n_1 + 2B_c\omega_{11}r_1 - 6B_c\omega_{13}r_1 - 4Lm_2 u_{S_c} + 4\eta_{42}k_c u_{S_c} - 32\eta_{44}k_c u_{S_c} +$$
$$-2m_1 r_1 r_2 u_{S_c} + 2n_1 r_1 r_2 u_{S_c} = 0,$$
$$\eta_{20}u_{S_c} - \eta_{22}u_{S_c} + \eta_{24}u_{S_c} + B_c m_1^2 + B_c n_1^2 + \eta_{20}u_{S_c}^3 - \eta_{22}u_{S_c}^3 + \eta_{24}u_{S_c}^3 + 2m_1 m_2 u_{S_c}^2 - 2m_1 n_2 u_{S_c}^2 +$$
$$-2m_2 n_1 u_{S_c}^2 + 2n_1 n_2 u_{S_c}^2 + 2B_c\eta_{10}u_{S_c} - 2B_c\eta_{12}u_{S_c} + 2B_c\eta_{14}u_{S_c} - 2B_c m_1 n_1 + 2Lm_2 u_{S_c} +$$
$$-2Ln_2 u_{S_c} - 2\eta_{42}k_c u_{S_c} + 4\eta_{44}k_c u_{S_c} = 0,$$
$$2u_{S_c}\zeta_{22} + 2u_{S_c}^3\zeta_{22} + 2\omega_{10}r_2 u_{S_c}^2 + 2\omega_{20}r_1 u_{S_c}^2 + 2B_c\omega_{10}r_1 + 4B_2 m_1 u_{S_c} + 4B_c u_{S_c}\zeta_{12} + 4m_2\sigma u_{S_c} +$$
$$+4k_c u_{S_c}\zeta_{42} + B_2\delta_2 r_1^2 u_{S_c} + 2B_2 2u_{S_c}\delta_1 m_2 u_{S_c} + 2B_2\delta_1 r_1 r_2 u_{S_c} = 0,$$
$$\zeta_{20} - \zeta_{22} - 2B_2 m_1 + 2B_2 n_1 + 2B_c\zeta_{10} - 2B_c\zeta_{12} - 2m_2\sigma + 2n_2\sigma - 2k_c\zeta_{42} + u_{S_c}^2\zeta_{20} - u_{S_c}^2\zeta_{22} +$$
$$-B_2 2u_{S_c}\delta_1 m_2 + B_2 2u_{S_c}\delta_1 n_2 = 0,$$
$$\omega_{44}u_{S_c} + \tau_{22}u_{S_c} + \tau_{22}u_{S_c}^3 + \omega_{12}r_2 u_{S_c}^2 + \omega_{22}r_1 u_{S_c}^2 + B_c\omega_{12}r_1 + 2B_c\tau_{12}u_{S_c} + 2m_2\nu u_{S_c} + 2k_c\tau_{42}u_{S_c} = 0,$$
$$\omega_{45} - \omega_{44} + \tau_{20} - \tau_{22} + 2B_c\tau_{10} - 2B_c\tau_{12} - 2m_2\nu + 2n_2\nu - 2k_c\tau_{42} + \tau_{20}u_{S_c}^2 - \tau_{22}u_{S_c}^2 = 0$$

and $\delta_2 = -2u_{S_c}/\left(1 - u_{S_c}^2\right)$.

C Wave instability in parabolic RAD systems

In this Appendix some details on the occurrence of wave instability in *parabolic* RAD models are given. In this framework, where diffusion occurs through Fick's laws, i.e. $J^u = -u_x$ and $J^w = -dw_x$, the governing system is cast as:

$$\widetilde{\mathbf{U}}_t + \widetilde{\mathrm{M}}\widetilde{\mathbf{U}}_x + D\widetilde{\mathbf{U}}_{xx} = \widetilde{\mathbf{N}}(\widetilde{\mathbf{U}}, B), \tag{C.1}$$

with:

$$\widetilde{\mathbf{U}} = \begin{bmatrix} u \\ w \end{bmatrix}, \quad \widetilde{\mathrm{M}} = \begin{bmatrix} 0 & 0 \\ 0 & -\nu \end{bmatrix}, \quad D = \begin{bmatrix} -1 & 0 \\ 0 & -d \end{bmatrix}, \quad \widetilde{\mathbf{N}}\left(\widetilde{\mathbf{U}}, B\right) = \begin{bmatrix} f(u,w,B) \\ g(u,w,B) \end{bmatrix}. \tag{C.2}$$

The resulting spatially-homogeneous steady-states are denoted by $\widetilde{\mathbf{U}}^* = (u^*, v^*)$ and the dispersion relation reduces to a quadratic equation:

$$\omega^2 + \left[k^2\,(d+1) - (f_u^* + g_w^*) - ik\nu\right]\omega + \widetilde{A}_0 + ik\nu\widehat{b}_0 = 0 \tag{C.3}$$

with $\widetilde{A}_0$ and $\widehat{b}_0$ given in (3.4). Conditions (3.6) for the stability of $\widetilde{\mathbf{U}}^*$ against homogeneous perturbations hold for both hyperbolic and parabolic models.

By applying the same procedure as the one discussed in the hyperbolic framework, but exploiting the lower complexity of the characteristic equation (C.3) with respect to (3.3), the locus of wave instability can be defined implicitly via the following equation:

$$(4\chi_2^3 + 2\chi_0\chi_2 + \chi_1)(4\chi_2^3 + 2\chi_0\chi_2 - \chi_1) = 0 \tag{C.4}$$

whereas the critical wavenumber is given by:

$$k_c^2 = -\frac{\chi_3}{\chi_4} \pm \chi_2 \tag{C.5}$$

and the wave speed obeys:

$$s = \nu\left(f_u^* - k_c^2\right) / \left[k_c^2(d+1) - f_u^* - g_w^*\right]. \tag{C.6}$$

The expressions of the coefficients χ_i $(i = 0, \ldots, 4)$ appearing in (C.4),(C.5) are given by:

$$\begin{gathered} \chi_0 = \tfrac{8\chi_4\chi_8 - 3\chi_3^2}{8\chi_4^2}, \quad \chi_1 = \tfrac{8\chi_4^2\chi_9 - 4\chi_4\chi_3\chi_8 + \chi_3^3}{8\chi_4^3}, \quad \chi_2 = \tfrac{1}{2}\sqrt{-\tfrac{2}{3}\chi_0 + \tfrac{1}{3\chi_4}\left(\chi_5 + \tfrac{\chi_6}{\chi_5}\right)}, \\ \chi_3 = d\nu^2 - (d+1)^2\,(g_w^* + df_u^*) - 2d\,(d+1)\,(f_u^* + g_w^*), \quad \chi_4 = d\,(d+1)^2 \end{gathered} \tag{C.7}$$

where

$$\chi_5 = \sqrt[3]{\frac{\chi_7+\sqrt{\chi_7^2-4\chi_6^3}}{2}}, \quad \chi_6 = 12\chi_4\chi_{10} - 3\chi_3\chi_9 + \chi_8^2,$$
$$\chi_7 = 27\chi_4\chi_9^2 - 72\chi_4\chi_8\chi_{10} + 27\chi_3^2\chi_{10} - 9\chi_3\chi_8\chi_9 + 2\chi_8^3,$$
$$\chi_8 = d\left(f_u^* + g_w^*\right)^2 + 2\left(d+1\right)\left(f_u^* + g_w^* - \nu^2\right)\left(g_w^* + df_u^*\right) + \left(d+1\right)^2\left(f_u^* g_w^* + f_w^* g_u^*\right),$$
$$\chi_9 = \nu^2 f_u^* g_w^* - \left(g_w^* + df_u^*\right)\left(f_u^* + g_w^*\right)^2 - 2\left(d+1\right)\left(f_u^* + g_w^*\right)\left(f_u^* g_w^* + f_w^* g_u^*\right),$$
$$\chi_{10} = \left(f_u^* + g_w^*\right)^2\left(f_u^* g_w^* + f_w^* g_u^*\right). \tag{C.8}$$

Note that, in the parabolic case, the critical value of the control parameter B_c is defined implicitly by the sole highly nonlinear equation (C.4), which results to be decoupled from the others. Moreover, the sign in (C.5) has to be chosen in such a way it gives real and positive values for B_c and k_c.

D WNA for oscillatory pattern in 1D hyperbolic RT systems

In this Appendix the fully the procedure to deduce the CCGL equation (3.21) for the hyperbolic reaction-advection-diffusion model (3.1)-(3.2) is described.

First of all, substituting the expansion (3.13) into the governing system (3.12) and looking for solution $\overline{\mathbf{U}}_i = \overline{\mathbf{U}}_i(z)$ with $z = x - st$, the set of ordinary differential equations (3.15)-(3.17), to be solved sequentially, is obtained. At the first perturbative order, the system reads:

$$\frac{\mathrm{d}\,\overline{\mathbf{U}}_1}{\mathrm{d}\,z} = K_c^* \overline{\mathbf{U}}_1 \tag{D.1}$$

where the matrix K_c^*, defined in (3.18), admits four complex eigenvalues given by

$$\lambda_{1,2} = \mp i k_c \quad \text{with} \quad k_c^2 = \left.\frac{\delta_3}{\delta_1}\right|_c \tag{D.2}$$

and

$$\lambda_{3,4} = \alpha \mp i\beta \quad \text{with} \quad \alpha = -\left.\frac{\delta_1}{2}\right|_c \quad \text{and} \quad \beta = \left.\sqrt{\left(\frac{\delta_1\delta_4}{\delta_3} - \frac{\delta_1^2}{4}\right)}\right|_c \tag{D.3}$$

to which there correspond the following right eigenvectors

$$\mathbf{d}^{(\pm\,\mathrm{i}\,k_c)} = \begin{bmatrix} r_1 \pm \mathrm{i}\,\widehat{r}_1 \\ r_2 \pm \mathrm{i}\,\widehat{r}_2 \\ r_3 \pm \mathrm{i}\,\widehat{r}_3 \\ r_4 \pm \mathrm{i}\,\widehat{r}_4 \end{bmatrix}, \qquad \mathbf{d}^{(\alpha\pm\mathrm{i}\,\beta)} = \begin{bmatrix} y_1 \pm \mathrm{i}\,\widehat{y}_1 \\ y_2 \pm \mathrm{i}\,\widehat{y}_2 \\ y_3 \pm \mathrm{i}\,\widehat{y}_3 \\ y_4 \pm \mathrm{i}\,\widehat{y}_4 \end{bmatrix}. \tag{D.4}$$

The general solution of the homogeneous linear system (D.1) can be expressed as:

$$\mathbf{U}_1 = P e^{Qz} P^{-1} \mathbf{C}(T_2) \tag{D.5}$$

where the vector $\mathbf{C}(T_2)$ is determined by boundary conditions, whereas P and Q are, respectively, the eigenvectors and eigenvalues matrices of K_c^* given by

$$\begin{aligned} P &= \begin{bmatrix} r_1 + \mathrm{i}\,\widehat{r}_1 & r_1 - \mathrm{i}\,\widehat{r}_1 & y_1 + \mathrm{i}\,\widehat{y}_1 & y_1 - \mathrm{i}\,\widehat{y}_1 \\ r_2 + \mathrm{i}\,\widehat{r}_2 & r_2 - \mathrm{i}\,\widehat{r}_2 & y_2 + \mathrm{i}\,\widehat{y}_2 & y_2 - \mathrm{i}\,\widehat{y}_2 \\ r_3 + \mathrm{i}\,\widehat{r}_3 & r_3 - \mathrm{i}\,\widehat{r}_3 & y_3 + \mathrm{i}\,\widehat{y}_3 & y_3 - \mathrm{i}\,\widehat{y}_3 \\ r_4 + \mathrm{i}\,\widehat{r}_4 & r_4 - \mathrm{i}\,\widehat{r}_4 & y_4 + \mathrm{i}\,\widehat{y}_4 & y_4 - \mathrm{i}\,\widehat{y}_4 \end{bmatrix}, \\ Q &= \begin{bmatrix} \mathrm{i}\,k_c & 0 & 0 & 0 \\ 0 & -\mathrm{i}\,k_c & 0 & 0 \\ 0 & 0 & \alpha + \mathrm{i}\,\beta & 0 \\ 0 & 0 & 0 & \alpha - \mathrm{i}\,\beta \end{bmatrix}. \end{aligned} \tag{D.6}$$

Then, solution of (D.1) reads:

$$\overline{\mathbf{U}}_1 = \Omega(X, T_2) e^{\mathrm{i}\,k_c z} \mathbf{d}^{(\mathrm{i}\,k_c)} + \overline{\Omega}(X, T_2) e^{-\mathrm{i}\,k_c z} \mathbf{d}^{(-\,\mathrm{i}\,k_c)} \tag{D.7}$$

where the complex pattern amplitude Ω remains undetermined at this stage and $\overline{\Omega}$ denotes its complex conjugate.

At the second order, the governing system is the following:

$$\frac{\mathrm{d}\,\overline{\mathbf{U}}_2}{\mathrm{d}\,z} - K_c^*\overline{\mathbf{U}}_2 = (\mathrm{M} - sI)^{-1}\left\{\frac{1}{2}\left(\overline{\mathbf{U}}_1\cdot\bigtriangledown\right)^{(2)}\mathbf{N}|_c^* - M\frac{\partial\overline{\mathbf{U}}_1}{\partial X}\right\} \tag{D.8}$$

whose general solution is given by

$$\mathbf{U}_2 = Pe^{Qz}P^{-1}\mathbf{C}(T_2) + Pe^{Qz}\int e^{-Qz}(MP)^{-1}\mathbf{F}dz \tag{D.9}$$

where $\mathbf{F}$ is the non-homogeneous term at the right-hand side of (D.8).

Now, taking into account (D.9) and inserting (D.7) into the non-homogeneous linear system (D.8), the solution at the second perturbative order satisfying periodic boundary conditions reads:

$$\overline{\mathbf{U}}_2 = \frac{\partial\Omega}{\partial X}e^{\mathrm{i}\,k_c z}\mathbf{g} + \frac{\partial\overline{\Omega}}{\partial X}e^{-\mathrm{i}\,k_c z}\overline{\mathbf{g}} + \Omega^2 e^{2\,\mathrm{i}\,k_c z}\mathbf{q} + \overline{\Omega}^2 e^{-2\,\mathrm{i}\,k_c z}\overline{\mathbf{q}} + 2\mathbf{q}_0|\Omega|^2 \tag{D.10}$$

where the vectors:

$$\mathbf{g} = \begin{bmatrix} g_1 + \mathrm{i}\,\widehat{g}_1 \\ g_2 + \mathrm{i}\,\widehat{g}_2 \\ g_3 + \mathrm{i}\,\widehat{g}_3 \\ g_4 + \mathrm{i}\,\widehat{g}_4 \end{bmatrix}, \quad \mathbf{q} = \begin{bmatrix} q_1 + \mathrm{i}\,\widehat{q}_1 \\ q_2 + \mathrm{i}\,\widehat{q}_2 \\ q_3 + \mathrm{i}\,\widehat{q}_3 \\ q_4 + \mathrm{i}\,\widehat{q}_4 \end{bmatrix}, \quad \mathbf{q}_0 = \begin{bmatrix} q_{01} \\ q_{02} \\ 0 \\ 0 \end{bmatrix} \tag{D.11}$$

fulfill the linear systems:

$$\begin{aligned} &\left[L_c^* - \mathrm{i}\,k_c(\mathrm{M} - sI)\right]\mathbf{g} = M\mathbf{d}^{(\mathrm{i}\,k_c)} \\ &\left[L_c^* - 2\,\mathrm{i}\,k_c(\mathrm{M} - sI)\right]\mathbf{q} = -\frac{1}{2}\left(\mathbf{d}^{(\mathrm{i}\,k_c)}\cdot\nabla\right)^{(2)}\mathbf{N}\Big|_c^* \\ &L_c^*\mathbf{q}_0 = -\frac{1}{2}\left(\mathbf{d}^{(\mathrm{i}\,k_c)}\cdot\nabla\right)\left(\mathbf{d}^{(-\,\mathrm{i}\,k_c)}\cdot\nabla\right)\mathbf{N}\Big|_c^* \end{aligned} \tag{D.12}$$

with

$$\begin{aligned} &\mathbf{l}\mathrm{M}\mathbf{d}^{(\mathrm{i}\,k_c)} = \mathbf{0}, \\ &\mathbf{l}\left[L_c^* - \mathrm{i}\,k_c(\mathrm{M} - sI)\right] = \mathbf{0}, \end{aligned} \tag{D.13}$$

being $\mathbf{l}$ the left eigenvectors whereas $\overline{\mathbf{g}}$ and $\overline{\mathbf{q}}$ are the complex conjugate of $\mathbf{g}$ and $\mathbf{q}$, respectively.

Finally, by substituting (D.7) and (D.10) into (3.17), from the removal of secular terms, we deduce that the pattern amplitude $\Omega(X, T_2)$ satisfies the CCGL equation:

$$\frac{\partial\Omega}{\partial T_2} = (\rho_1 + \mathrm{i}\,\rho_2)\frac{\partial^2\Omega}{\partial X^2} + (\sigma_1 + \mathrm{i}\,\sigma_2)\,\Omega - (L_1 - \mathrm{i}\,L_2)\,\Omega\,|\Omega|^2 \tag{D.14}$$

where:

$$\begin{aligned} \rho_1 + \mathrm{i}\,\rho_2 &= \left[(n_1e_1 + n_2e_2) + \mathrm{i}\,(n_2e_1 - n_1e_2)\right] / \left(e_1^2 + e_2^2\right) \\ \sigma_1 + \mathrm{i}\,\sigma_2 &= B_2\left[(m_1e_1 + m_2e_2) + \mathrm{i}\,(m_2e_1 - m_1e_2)\right] / \left(e_1^2 + e_2^2\right) \\ L_1 - \mathrm{i}\,L_2 &= (p_1 - \mathrm{i}\,p_2) / \left(e_1^2 + e_2^2\right) \end{aligned} \tag{D.15}$$

with:

$$
\begin{aligned}
n_1 = \quad & \left[(g_4-\nu g_2)f_u^* - g_3 g_u^*\right] E_{1r} + \left[(g_4-\nu g_2)f_w^* - g_3 g_w^*\right] E_{2r} + \\
& + (f_u^* g_w^* - f_w^* g_u^*)(d g_2 E_{4r} - g_1 E_{3r}), \\
n_2 = \quad & \left[(g_4-\nu g_2)f_u^* - g_3 g_u^*\right] E_{1i} + \left[(g_4-\nu g_2)f_w^* - g_3 g_w^*\right] E_{2i} + \\
& + (f_u^* g_w^* - f_w^* g_u^*)(d g_2 E_{4i} - g_1 E_{3i}), \\
m_1 = \quad & -(s_1 r_1 + s_2 r_2)\left(E_{1r} f_u^* + E_{2r} f_w^*\right) + (s_1 \widehat{r}_1 + s_2 \widehat{r}_2)\left(E_{1i} f_u^* + E_{2i} f_w^*\right) + \\
& + (h_1 r_1 + h_2 r_2)\left(E_{1r} g_u^* + E_{2r} g_w^*\right) - (h_1 \widehat{r}_1 + h_2 \widehat{r}_2)\left(E_{1i} g_u^* + E_{2i} g_w^*\right), \\
m_2 = \quad & -(s_1 r_1 + s_2 r_2)\left(E_{1i} f_u^* + E_{2i} f_w^*\right) - (s_1 \widehat{r}_1 + s_2 \widehat{r}_2)\left(E_{1r} f_u^* + E_{2r} f_w^*\right) + \\
& + (h_1 r_1 + h_2 r_2)\left(E_{1i} g_u^* + E_{2i} g_w^*\right) + (h_1 \widehat{r}_1 + h_2 \widehat{r}_2)\left(E_{1r} g_u^* + E_{2r} g_w^*\right), \\
p_1 = \quad & (b_1 f_u^* - a_1 g_u^*)\left(E_{1r} e_1 + E_{1i} e_2\right) - (b_2 f_u^* - a_2 g_u^*)\left(E_{1i} e_1 - E_{1r} e_2\right) + \\
& + (b_1 f_w^* - a_1 g_w^*)\left(E_{2r} e_1 + E_{2i} e_2\right) - (b_2 f_w^* - a_2 g_w^*)\left(E_{2i} e_1 - E_{2r} e_2\right), \\
p_2 = \quad & (b_1 f_u^* - a_1 g_u^*)\left(E_{1i} e_1 - E_{1r} e_2\right) - (b_2 f_u^* - a_2 g_u^*)\left(E_{1r} e_1 + E_{1i} e_2\right) + \\
& + (b_1 f_w^* - a_1 g_w^*)\left(E_{2i} e_1 - E_{2r} e_2\right) - (b_2 f_w^* - a_2 g_w^*)\left(E_{2r} e_1 + E_{2i} e_2\right), \\
e_1 = \quad & (r_1 g_u^* - r_2 f_u^*) E_{1r} - (\widehat{r}_1 g_u^* - \widehat{r}_2 f_u^*) E_{1i} + (r_1 g_w^* - r_2 f_w^*) E_{2r} - (\widehat{r}_1 g_w^* - \widehat{r}_2 f_w^*) E_{2i} + \\
& (f_u^* g_w^* - f_w^* g_u^*)\left(\tau^u r_3 E_{3r} - \tau^w r_4 E_{4r} - \tau^u \widehat{r}_3 E_{3i} + \tau^w \widehat{r}_4 E_{4i}\right), \\
e_2 = \quad & (r_1 g_u^* - r_2 f_u^*) E_{1i} + (\widehat{r}_1 g_u^* - \widehat{r}_2 f_u^*) E_{1r} + (r_1 g_w^* - r_2 f_w^*) E_{2i} + (\widehat{r}_1 g_w^* - \widehat{r}_2 f_w^*) E_{2r} + \\
& (f_u^* g_w^* - f_w^* g_u^*)\left(\tau^u r_3 E_{3i} - \tau^w r_4 E_{4i} + \tau^u \widehat{r}_3 E_{3r} - \tau^w \widehat{r}_4 E_{4r}\right), \\
E_{1r} + \mathrm{i}\, E_{1i} = \quad & \widehat{r}_4(y_1\widehat{y}_3 - y_3\widehat{y}_1) + \widehat{r}_3(y_4\widehat{y}_1 - y_1\widehat{y}_4) + \widehat{r}_1(y_3\widehat{y}_4 - y_4\widehat{y}_3) + \\
& \mathrm{i}\left[r_4(y_1\widehat{y}_3 - y_3\widehat{y}_1) + r_3(y_4\widehat{y}_1 - y_1\widehat{y}_4) + r_1(y_3\widehat{y}_4 - y_4\widehat{y}_3)\right], \\
E_{2r} + \mathrm{i}\, E_{2i} = \quad & \widehat{r}_4(y_2\widehat{y}_3 - y_3\widehat{y}_2) + \widehat{r}_3(y_4\widehat{y}_2 - y_2\widehat{y}_4) + \widehat{r}_2(y_3\widehat{y}_4 - y_4\widehat{y}_3) + \\
& \mathrm{i}\left[r_4(y_2\widehat{y}_3 - y_3\widehat{y}_2) + r_3(y_4\widehat{y}_2 - y_2\widehat{y}_4) + r_2(y_3\widehat{y}_4 - y_4\widehat{y}_3)\right], \\
E_{3r} + \mathrm{i}\, E_{3i} = \quad & \widehat{r}_4(y_2\widehat{y}_1 - y_1\widehat{y}_2) + \widehat{r}_2(y_1\widehat{y}_4 - y_4\widehat{y}_1) + \widehat{r}_1(y_4\widehat{y}_2 - y_2\widehat{y}_4) + \\
& \mathrm{i}\left[r_4(y_2\widehat{y}_1 - y_1\widehat{y}_2) + r_2(y_1\widehat{y}_4 - y_4\widehat{y}_1) + r_1(y_4\widehat{y}_2 - y_2\widehat{y}_4)\right], \\
E_{4r} + \mathrm{i}\, E_{4i} = \quad & \widehat{r}_3(y_2\widehat{y}_1 - y_1\widehat{y}_2) + \widehat{r}_2(y_1\widehat{y}_3 - y_3\widehat{y}_1) + \widehat{r}_1(y_3\widehat{y}_2 - y_2\widehat{y}_3) + \\
& \mathrm{i}\left[r_3(y_2\widehat{y}_1 - y_1\widehat{y}_2) + r_2(y_1\widehat{y}_3 - y_3\widehat{y}_1) + r_1(y_3\widehat{y}_2 - y_2\widehat{y}_3)\right],
\end{aligned}
\tag{D.16}
$$

and

$$
\begin{aligned}
& h_1 = \tfrac{\mathrm{d}f_u}{\mathrm{d}B}|_c^*, \quad h_2 = \tfrac{\mathrm{d}f_w}{\mathrm{d}B}|_c^*, \quad s_1 = \tfrac{\mathrm{d}g_u}{\mathrm{d}B}|_c^*, \quad s_2 = \tfrac{\mathrm{d}g_w}{\mathrm{d}B}|_c^* \\
a_1 + \mathrm{i}\, a_2 = \; & f_{uu}|_c^* \left\{ r_1(2q_{01}+q_1) + \widehat{r}_1\widehat{q}_1 + \mathrm{i}\left[\widehat{r}_1(2q_{01}-q_1) + r_1\widehat{q}_1\right]\right\} + \\
& f_{uw}|_c^* \left\{ r_1(2q_{02}+q_2) + \widehat{r}_1\widehat{q}_2 + r_2(2q_{01}+q_1) + \widehat{r}_2\widehat{q}_1 + \right. \\
& \left. \mathrm{i}\left[\widehat{r}_1(2q_{02}-q_2) + r_1\widehat{q}_2 + \widehat{r}_2(2q_{01}-q_1) + r_2\widehat{q}_1\right]\right\} + \\
& f_{ww}|_c^* \left\{ r_2(2q_{02}+q_2) + \widehat{r}_2\widehat{q}_2 + \mathrm{i}\left[\widehat{r}_2(2q_{02}-q_2) + r_2\widehat{q}_2\right]\right\} + \\
& \tfrac{1}{2} f_{uuu}|_c^* (r_1^2 + \widehat{r}_1^2)(r_1 + \mathrm{i}\,\widehat{r}_1) + \tfrac{1}{2} f_{www}|_c^* (r_2^2 + \widehat{r}_2^2)(r_2 + \mathrm{i}\,\widehat{r}_2) + \\
& \tfrac{1}{2} f_{uuw}|_c^* \left\{ 2r_1\widehat{r}_1\widehat{r}_2 + r_2(3r_1^2 + \widehat{r}_1^2) + \mathrm{i}\left[2r_1\widehat{r}_1 r_2 + \widehat{r}_2(r_1^2 + 3\widehat{r}_1^2)\right]\right\} + \\
& \tfrac{1}{2} f_{uww}|_c^* \left\{ 2r_2\widehat{r}_1\widehat{r}_2 + r_1(3r_2^2 + \widehat{r}_2^2) + \mathrm{i}\left[2r_1\widehat{r}_1 r_2 + \widehat{r}_1(r_2^2 + 3\widehat{r}_2^2)\right]\right\}, \\
b_1 + \mathrm{i}\, b_2 = \; & g_{uu}|_c^* \left\{ r_1(2q_{01}+q_1) + \widehat{r}_1\widehat{q}_1 + \mathrm{i}\left[\widehat{r}_1(2q_{01}-q_1) + r_1\widehat{q}_1\right]\right\} + \\
& g_{uw}|_c^* \left\{ r_1(2q_{02}+q_2) + \widehat{r}_1\widehat{q}_2 + r_2(2q_{01}+q_1) + \widehat{r}_2\widehat{q}_1 + \right. \\
& \left. \mathrm{i}\left[\widehat{r}_1(2q_{02}-q_2) + r_1\widehat{q}_2 + \widehat{r}_2(2q_{01}-q_1) + r_2\widehat{q}_1\right]\right\} + \\
& g_{ww}|_c^* \left\{ r_2(2q_{02}+q_2) + \widehat{r}_2\widehat{q}_2 + \mathrm{i}\left[\widehat{r}_2(2q_{02}-q_2) + r_2\widehat{q}_2\right]\right\} + \\
& \tfrac{1}{2} g_{uuu}|_c^* (r_1^2 + \widehat{r}_1^2)(r_1 + \mathrm{i}\,\widehat{r}_1) + \tfrac{1}{2} (g_{www})|_c^* (r_2^2 + \widehat{r}_2^2)(r_2 + \mathrm{i}\,\widehat{r}_2) + \\
& \tfrac{1}{2} g_{uuw}|_c^* \left\{ 2r_1\widehat{r}_1\widehat{r}_2 + r_2(3r_1^2 + \widehat{r}_1^2) + \mathrm{i}\left[2r_1\widehat{r}_1 r_2 + \widehat{r}_2(r_1^2 + 3\widehat{r}_1^2)\right]\right\} + \\
& \tfrac{1}{2} g_{uww}|_c^* \left\{ 2r_2\widehat{r}_1\widehat{r}_2 + r_1(3r_2^2 + \widehat{r}_2^2) + \mathrm{i}\left[2r_1\widehat{r}_1 r_2 + \widehat{r}_1(r_2^2 + 3\widehat{r}_2^2)\right]\right\}.
\end{aligned}
\tag{D.17}
$$

In the particular case of the hyperbolic extension of the Klausmeier model, taking into account

$$
\begin{aligned}
& f_u^* = B, \quad f_w^* = u_S^2, \quad g_u^* = -2B, \quad g_w^* = -\left(1 + u_S^2\right), \\
& f_{uu}^* = 2B/u_S, \quad f_{uw}^* = 2u_S, \quad f_{ww}^* = 0, \\
& g_{uu}^* = -2B/u_S, \quad g_{uw}^* = -2u_S, \quad g_{ww}^* = 0, \\
& f_{uuu}^* = f_{uww}^* = f_{www}^* = 0, \quad f_{uuw}^* = 2, \\
& g_{uuu}^* = g_{uww}^* = g_{www}^* = 0, \quad g_{uuw}^* = -2,
\end{aligned}
\tag{D.18}
$$

the components of the right eigenvectors $\mathbf{d}^{(\pm\,\mathrm{i}\,k_c)}$ and $\mathbf{d}^{(\alpha\pm\mathrm{i}\,\beta)}$ reported in (D.4) become:

$$
\begin{aligned}
r_1 &= 1, & \widehat{r}_1 &= 0,\\
r_2 &= \tfrac{k_c^2 - B_c - (\tau^u)^2 k_c^2 s^2 B_c}{u_{S_c}^2\left[k_c^2 s^2 (\tau^u)^2 + 1\right]}, & \widehat{r}_2 &= -\tfrac{k_c s\left[1 + k_c^2 \tau^u\left(\tau^u s^2 - 1\right)\right]}{u_{S_c}^2\left[k_c^2 s^2 (\tau^u)^2 + 1\right]},\\
r_3 &= \tfrac{k_c^2 s \tau^u}{k_c^2 s^2 (\tau^u)^2 + 1}, & \widehat{r}_3 &= -\tfrac{k_c}{k_c^2 s^2 (\tau^u)^2 + 1},\\
r_4 &= \tfrac{k_c d\left(\widehat{r}_2 + k_c s r_2 \tau^w\right)}{1 + (\tau^w)^2 k_c^2 s^2}, & \widehat{r}_4 &= \tfrac{k_c d\left(-r_2 + k_c s \widehat{r_2} \tau^w\right)}{1 + (\tau^w)^2 k_c^2 s^2},\\
y_1 &= 1, & \widehat{y}_1 &= 0,\\
y_2 &= \tfrac{(\alpha s \tau^u - 1) l_1 + \beta s \tau^u l_2}{u_{S_c}^2\left[(\alpha s \tau^u - 1)^2 + \beta^2 s^2 (\tau^u)^2\right]}, & \widehat{y}_2 &= \tfrac{(\alpha s \tau^u - 1) l_2 - \beta s \tau^u l_1}{u_{S_c}^2\left[(\alpha s \tau^u - 1)^2 + \beta^2 s^2 (\tau^u)^2\right]},\\
y_3 &= \tfrac{\alpha(\alpha s \tau^u - 1) + \beta^2 s \tau^u}{(\alpha s \tau^u - 1)^2 + \beta^2 s^2 (\tau^u)^2}, & \widehat{y}_3 &= -\tfrac{\beta}{(\alpha s \tau^u - 1)^2 + \beta^2 s^2 (\tau^u)^2},\\
y_4 &= \tfrac{d\left[\left(\alpha y_2 - \beta \widehat{y_2}\right)(\alpha s \tau^w - 1) + \beta s \tau^w\left(\beta y_2 + \alpha \widehat{y_2}\right)\right]}{(\tau^w \alpha s - 1)^2 + \beta^2 s^2 (\tau^w)^2}, & \widehat{y}_4 &= \tfrac{d\left[\left(\beta y_2 + \alpha \widehat{y_2}\right)(\alpha s \tau^w - 1) + \beta s \tau^w\left(\beta \widehat{y_2} - \alpha y_2\right)\right]}{(\tau^w \alpha s - 1)^2 + \beta^2 s^2 (\tau^w)^2},
\end{aligned}
\tag{D.19}
$$

where

$$
\begin{aligned}
l_1 &= \left(\alpha^2 - \beta^2\right)\left(1 - s^2 \tau^u\right) + \alpha s\left(1 - B_c \tau^u\right) + Bc,\\
l_2 &= 2\alpha\beta\left(1 - s^2 \tau^u\right) + \beta s\left(1 - \tau^u B_c\right).
\end{aligned}
\tag{D.20}
$$

Moreover, the coefficients occurring in (D.17) reduce to:

$$
\begin{aligned}
a_1 + \mathrm{i}\, a_2 = \;& 2B_c/u_{S_c}\left[r_1(2q_{01} + q_1) + \widehat{r}_1 \widehat{q}_1\right] + 2r_1 \widehat{r}_1 \widehat{r}_2 + r_2(3r_1^2 + \widehat{r}_1^2) +\\
& + 2u_{S_c}\left[r_1(2q_{02} + q_2) + \widehat{r}_1 \widehat{q}_2 + r_2(2q_{01} + q_1) + \widehat{r}_2 \widehat{q}_1\right] +\\
& + \mathrm{i}\left\{2B_c/u_{S_c}\left[\widehat{r}_1(2q_{01} - q_1) + r_1 \widehat{q}_1\right] + 2r_1 \widehat{r}_1 r_2 + \widehat{r}_2(r_1^2 + 3\widehat{r}_1^2) +\right.\\
& \left. + 2u_{S_c}\left[\widehat{r}_1(2q_{02} - q_2) + r_1 \widehat{q}_2 + \widehat{r}_2(2q_{01} - q_1) + r_2 \widehat{q}_1\right]\right\},\\
b_1 + \mathrm{i}\, b_2 = \;& -\left(a_1 + \mathrm{i}\, a_2\right).
\end{aligned}
\tag{D.21}
$$

E Details on rhombic planform analysis in 2D hyperbolic RT systems.

In this Appendix, some details on the derivation of the SL equations (4.26), obtained by performing the WNA for rhombic geometry, are given. Substituting the expansions (4.19) into the governing system, the set of linear partial differential equations (4.20) are obtained.

Specifically, by looking for the solution at the lowest order in the form

$$\mathbf{U}_1(x,z,T_1,T_2) = \mathbf{X}(x,T_1,T_2) + \mathbf{Z}(z,T_1,T_2), \tag{E.1}$$

where $z = x\cos\phi + y\sin\phi$ from $(4.20)_1$, the following compatibility conditions hold:

$$\begin{gathered} \mathrm{M}^{(1)}\frac{\partial \mathbf{X}}{\partial x} = L_c^*\mathbf{X}, \\ \left(\mathrm{M}^{(1)}\cos\phi + \mathrm{M}^{(2)}\sin\phi\right)\frac{\partial \mathbf{Z}}{\partial z} = L_c^*\mathbf{Z}. \end{gathered} \tag{E.2}$$

As far as the system $(\mathrm{E}.2)_1$ is concerned, two components of $\mathbf{X}$ vanish, namely $\mathbf{X} = (X_1, X_2, X_3, 0, X_5, 0)^T$. Therefore, it is possible to analyze the reduced system

$$\frac{\partial \tilde{\mathbf{X}}}{\partial x} = K_c^*\tilde{\mathbf{X}} \tag{E.3}$$

with

$$\tilde{\mathbf{X}} = \begin{bmatrix} X_1 \\ X_2 \\ X_3 \\ X_5 \end{bmatrix} \quad K_c^* = \begin{bmatrix} 0 & 0 & 1 & 0 \\ 0 & 0 & 0 & 1 \\ \frac{1}{\tau^u} & 0 & 0 & 0 \\ 0 & \frac{d}{\tau^w} & 0 & 0 \end{bmatrix}^{-1} \begin{bmatrix} f_u^* & f_w^* & 0 & 0 \\ g_u^* & g_w^* & 0 & 0 \\ 0 & 0 & -\frac{1}{\tau^u} & 0 \\ 0 & 0 & 0 & -\frac{1}{\tau^w} \end{bmatrix} \tag{E.4}$$

Since the matrix K_c^* admits two complex eigenvalues $\lambda_{1,2} = \pm ik_c$ with algebraic and geometric multiplicity given by 2 and 1, respectively, the general solution of the homogeneous linear system (E.3) is given by

$$\tilde{\mathbf{X}} = Pe^{Jx}P^{-1}\mathbf{C}(T_i) \tag{E.5}$$

being P the invertible transform matrix with columns consisting of the eigenvectors of K_c^* whereas J denotes the Jordan canonical form of K_c^*

$$P = \begin{bmatrix} iY_1 & r_1 & -iY_1 & r_1 \\ 0 & r_2 & 0 & r_2 \\ Y_3 & -ik_c r_1 & Y_3 & ik_c r_1 \\ Y_4 & -ik_c d r_2 & Y_4 & ik_c d r_2 \end{bmatrix}, \quad J = \begin{bmatrix} ik_c & 0 & 0 & 0 \\ 1 & ik_c & 0 & 0 \\ 0 & 0 & -ik_c & 0 \\ 0 & 0 & 1 & -ik_c \end{bmatrix} \tag{E.6}$$

with

$$\begin{gathered} \left(B_c - k_c^2\right) r_1 + u_S^2 r_2 = 0 \\ 2B_c r_1 + \left(u_S^2 + 1 + dk_c^2\right) r_2 = 0 \\ Y_1 = \frac{2k_c r_1}{k_c^2 - B_c} \\ Y_3 = k_c Y_1 - r_1 \\ Y_4 = -dr_2 \end{gathered} \tag{E.7}$$

Then the solution $(\text{E.2})_1$ satisfying zero flux boundary conditions becomes

$$\mathbf{X} = \Omega_1 (T_1, T_2) \begin{bmatrix} r_1 \cos(k_c x) \\ r_2 \cos(k_c x) \\ k_c r_1 \sin(k_c x) \\ 0 \\ k_c d r_2 \sin(k_c x) \\ 0 \end{bmatrix} \tag{E.8}$$

About the solution of the system $(\text{E.2})_2$, it can be noticed that

$$\mathbf{Z} = (Z_1, Z_2, \cot\phi Z_{4,} Z_4, \cot\phi Z_{6,}, Z_6)^T, \tag{E.9}$$

so that the reduced system is obtained

$$\frac{\partial \tilde{\mathbf{Z}}}{\partial z} = \tilde{K}_c^* \tilde{\mathbf{Z}}, \tag{E.10}$$

where

$$\tilde{\mathbf{Z}} = \begin{bmatrix} Z_1 \\ Z_2 \\ Z_4 \\ Z_6 \end{bmatrix} \quad \tilde{K}_c^* = \begin{bmatrix} 0 & 0 & 1 & 0 \\ 0 & 0 & 0 & 1 \\ \frac{1}{\tau^u} & 0 & 0 & 0 \\ 0 & \frac{d}{\tau^w} & 0 & 0 \end{bmatrix}^{-1} \begin{bmatrix} \sin\phi f_u^* & \sin\phi f_w^* & 0 & 0 \\ \sin\phi g_u^* & \sin\phi g_w^* & 0 & 0 \\ 0 & 0 & -\frac{1}{\tau^u \sin\phi} & 0 \\ 0 & 0 & 0 & -\frac{1}{\tau^w \sin\phi} \end{bmatrix} \tag{E.11}$$

Since the matrix $\tilde{K}_c^*$ admits the same two complex eigenvalues $\lambda_{1,2} = \pm i k_c$ of K_c^* with algebraic and geometric multiplicity given by 2 and 1, respectively, the general solution of the homogeneous linear system (E.10) is given by

$$\tilde{\mathbf{Z}} = \tilde{P} e^{Jx} \tilde{P}^{-1} \mathbf{C}(T_i) \tag{E.12}$$

with

$$\tilde{P} = \begin{bmatrix} iY_1 & r_1 & -iY_1 & r_1 \\ 0 & r_2 & 0 & r_2 \\ \sin\phi Y_3 & -ik_c \sin\phi r_1 & \sin\phi Y_3 & ik_c \sin\phi r_1 \\ \sin\phi Y_4 & -ik_c d \sin\phi r_2 & \sin\phi Y_4 & ik_c d \sin\phi r_2 \end{bmatrix} \tag{E.13}$$

Then the solution $(\text{E.2})_2$ satisfying zero flux boundary conditions becomes

$$\mathbf{Z} = \Omega_2 (T_1, T_2) \begin{bmatrix} r_1 \cos(k_c z) \\ r_2 \cos(k_c z) \\ k_c \cos\phi r_1 \sin(k_c z) \\ k_c \sin\phi r_1 \sin(k_c z) \\ k_c \cos\phi d r_2 \sin(k_c z) \\ k_c \sin\phi d r_2 \sin(k_c z) \end{bmatrix} \tag{E.14}$$

Finally, the rhombic solution (E.1) of $(4.20)_1$ reads

$$\mathbf{U}_1 = \Omega_1\left(T_1, T_2\right)\begin{bmatrix} r_1\cos\left(k_c x\right) \\ r_2\cos\left(k_c x\right) \\ k_c r_1\sin\left(k_c x\right) \\ 0 \\ k_c d r_2\sin\left(k_c x\right) \\ 0 \end{bmatrix} + \Omega_2\left(T_1, T_2\right)\begin{bmatrix} r_1\cos\left(k_c z\right) \\ r_2\cos\left(k_c z\right) \\ k_c\cos\phi\, r_1\sin\left(k_c z\right) \\ k_c\sin\phi\, r_1\sin\left(k_c z\right) \\ k_c\cos\phi\, d r_2\sin\left(k_c z\right) \\ k_c\sin\phi\, d r_2\sin\left(k_c z\right) \end{bmatrix} \tag{E.15}$$

where Ω_1 and Ω_2 are the pattern amplitudes, which are still arbitrary at this stage.

Now, substituting (E.15) into the nonhomogeous linear system $(4.20)_2$, and requiring to eliminate resonant terms, the conditions $B_1 = \frac{\partial\Omega_1}{\partial T_1} = \frac{\partial\Omega_2}{\partial T_1} = 0$ hold. Then, by using the same procedure outlined above, the solution at the second perturbative order $\mathbf{U}_2$ reads:

$$\mathbf{U}_2(x, z, T_2) = \Omega_1^2\mathbf{U}_{20} + \Omega_2^2\mathbf{U}_{02} + \Omega_1\Omega_2\left(\frac{1}{\left(1+2\cos\phi\right)^2}\mathbf{U}_{12} + \frac{1}{\left(1-2\cos\phi\right)^2}\mathbf{U}_{21}\right) \tag{E.16}$$

where the vectors $\mathbf{U}_{20}(x)$, $\mathbf{U}_{02}\left(z\right)$, $\mathbf{U}_{12}(x+z)$ and $\mathbf{U}_{21}(x-z)$ are given by

$$\mathbf{U}_{20} = n_1\begin{bmatrix} 1+\frac{1+4dk_c^2}{9}\cos\left(2k_c x\right) \\ -B_c - \frac{B_c+4k_c^2}{9}\cos\left(2k_c x\right) \\ \frac{2k_c\left(1+4dk_c^2\right)}{9}\sin\left(2k_c x\right) \\ 0 \\ -\frac{2k_c d\left(B_c+4k_c^2\right)}{9}\sin\left(2k_c x\right) \\ 0 \end{bmatrix}, \quad \mathbf{U}_{02} = n_1\begin{bmatrix} 1+\frac{1+4dk_c^2}{9}\cos\left(2k_c z\right) \\ -B_c - \frac{B_c+4k_c^2}{9}\cos\left(2k_c z\right) \\ \frac{2k_c\left(1+4dk_c^2\right)}{9}\cos\phi\sin\left(2k_c z\right) \\ \frac{2k_c\left(1+4dk_c^2\right)}{9}\sin\phi\sin\left(2k_c z\right) \\ -\frac{2k_c d\left(B_c+4k_c^2\right)}{9}\cos\phi\sin\left(2k_c z\right) \\ -\frac{2k_c d\left(B_c+4k_c^2\right)}{9}\sin\phi\sin\left(2k_c z\right) \end{bmatrix},$$

$$\mathbf{U}_{12} = 2n_1\begin{bmatrix} \left(1+2dk_c^2+\frac{2B_c\left(u_{S_c}^2-1\right)}{k_c^2}\cos\phi\right)\cos\left[k_c\left(x+z\right)\right] \\ -\left(B_c+2k_c^2+\frac{2B_c\left(u_{S_c}^2-1\right)}{dk_c^2}\cos\phi\right)\cos\left[k_c\left(x+z\right)\right] \\ \left(1+\cos\phi\right)\left(k_c\left(1+2dk_c^2\right)+\frac{2B_c\left(u_{S_c}^2-1\right)}{k_c}\cos\phi\right)\sin\left[k_c\left(x+z\right)\right] \\ \sin\phi\left(k_c\left(1+2dk_c^2\right)+\frac{2B_c\left(u_{S_c}^2-1\right)}{k_c}\cos\phi\right)\sin\left[k_c\left(x+z\right)\right] \\ -\left(1+\cos\phi\right)\left(dk_c\left(B_c+2k_c^2\right)+\frac{2B_c\left(u_{S_c}^2-1\right)}{k_c}\cos\phi\right)\sin\left[k_c\left(x+z\right)\right] \\ \sin\phi\left(dk_c\left(B_c+2k_c^2\right)+\frac{2B_c\left(u_{S_c}^2-1\right)}{k_c}\cos\phi\right)\sin\left[k_c\left(x+z\right)\right] \end{bmatrix},$$

$$\mathbf{U}_{21} = 2n_1 \begin{bmatrix} \left(1 + 2dk_c^2 - \frac{2B_c\left(u_{S_c}^2 - 1\right)}{k_c^2}\cos\phi\right)\cos\left[k_c\left(x-z\right)\right] \\ -\left(B_c + 2k_c^2 - \frac{2B_c\left(u_{S_c}^2 - 1\right)}{dk_c^2}\cos\phi\right)\cos\left[k_c\left(x-z\right)\right] \\ \left(1-\cos\phi\right)\left(k_c\left(1+2dk_c^2\right) - \frac{2B_c\left(u_{S_c}^2-1\right)}{k_c}\cos\phi\right)\sin\left[k_c\left(x-z\right)\right] \\ -\sin\phi\left(k_c\left(1+2dk_c^2\right) - \frac{2B_c\left(u_{S_c}^2-1\right)}{k_c}\cos\phi\right)\sin\left[k_c\left(x-z\right)\right] \\ -\left(1-\cos\phi\right)\left(dk_c\left(B_c+2k_c^2\right) - \frac{2B_c\left(u_{S_c}^2-1\right)}{k_c}\cos\phi\right)\sin\left[k_c\left(x-z\right)\right] \\ -\sin\phi\left(dk_c\left(B_c+2k_c^2\right) - \frac{2B_c\left(u_{S_c}^2-1\right)}{k_c}\cos\phi\right)\sin\left[k_c\left(x-z\right)\right] \end{bmatrix}$$

with $n_1 = \frac{r_1\left(B_c r_1 + 2u_{S_c}^2 r_2\right)}{2B_c u_{S_c}\left(u_{S_c}^2-1\right)}$.

Finally, taking into account (E.15) and (E.16), the elimination of secular terms of the system $(4.20)_3$ leads to the following two cubic SL equations for the amplitudes:

$$\begin{aligned} \tfrac{\partial\Omega_1}{\partial T_2} &= \sigma\Omega_1 - \Omega_1\left(L_1\Omega_1^2 + L_2\Omega_2^2\right) \\ \tfrac{\partial\Omega_2}{\partial T_2} &= \sigma\Omega_2 - \Omega_2\left(L_1\Omega_2^2 + L_2\Omega_1^2\right) \end{aligned} \tag{E.17}$$

where the growth rate σ and the Landau coefficients L_1,L_2 are given by

$$\begin{aligned} \sigma &= B_2\frac{B_c r_1(2r_1+r_2 d)\left(1-u_{S_c}^2\right)+2u_{S_c}^2 r_2(r_1+r_2 d)\left(1+u_{S_c}^2\right)}{B_c\left(1-u_{S_c}^2\right)r_1 r_2\left[d-1+dk_c^2(\tau^w-\tau^u)\right]} \\ L_1 &= -\frac{(r_1+r_2 d)a_1}{r_1 r_2\left[d-1+dk_c^2(\tau^w-\tau^u)\right]} \\ L_2 &= -\frac{(r_1+r_2 d)a_2}{r_1 r_2\left[d-1+dk_c^2(\tau^w-\tau^u)\right]} \end{aligned} \tag{E.18}$$

with

$$a_1 = \tfrac{3}{4}r_1^2 r_2 + \left[\frac{\left(B_c r_1 + u_{S_c}^2 r_2\right)}{9u_{S_c}}\left(19 + 4dk_c^2\right) - \frac{u_{S_c} r_1}{9}\left(19B_c + 4k_c^2\right)\right] n_1,$$

$$a_2 = \tfrac{3}{2}r_1^2 r_2 + 2\tfrac{n_1}{u_{S_c}}\left\{B_c r_1 + u_{S_c}^2 r_2 - B_c r_1 u_{S_c}^2 + \frac{2\left(1+4\cos^2\phi\right)}{\left(1-4\cos^2\phi\right)^2}\left[\left(B_c r_1 + u_{S_c}^2 r_2\right)\left(1+2dk_c^2\right) + \right.\right.$$
$$\left.\left. -r_1 u_{S_c}^2\left(B_c + 2k_c^2\right)\right] - \frac{16B_c\left(u_{S_c}^2-1\right)\cos^2\phi}{k_c^2\left(1-4\cos^2\phi\right)^2}\left[B_c r_1 + u_{S_c}^2 r_2 - \tfrac{r_1}{d}u_{S_c}^2\right]\right\}.$$

F Details on hexagonal planform analysis in 2D hyperbolic RT systems

In this Appendix, some details on the derivation of the SL equations (4.35), obtained by performing the WNA for hexagonal geometry, are given. Substituting the expansions (4.19) into the governing system the set of linear partial differential equations (4.20) are obtained. In this case, the solution at the lowest perturbative order appear in the form

$$\mathbf{U}_1(x,\zeta,\xi,T_1,T_2)=\mathbf{X}(x,T_1,T_2)+\mathbf{Z}(\zeta,T_1,T_2)+\mathbf{\Xi}(\xi,T_1,T_2), \tag{F.1}$$

where $\zeta=\frac{1}{2}x+\frac{\sqrt{3}}{2}y$ and $\xi=\frac{1}{2}x-\frac{\sqrt{3}}{2}y$, and the following compatibility conditions hold

$$\begin{aligned}
\mathrm{M}^{(1)}\frac{\partial\mathbf{X}}{\partial x}&=L_c^*\mathbf{X}\\
\Big(\tfrac{1}{2}\mathrm{M}^{(1)}+\tfrac{\sqrt{3}}{2}\mathrm{M}^{(2)}\Big)\frac{\partial\mathbf{Z}}{\partial\zeta}&=L_c^*\mathbf{Z}\\
\Big(\tfrac{1}{2}\mathrm{M}^{(1)}-\tfrac{\sqrt{3}}{2}\mathrm{M}^{(2)}\Big)\frac{\partial\mathbf{\Xi}}{\partial\xi}&=L_c^*\mathbf{\Xi}
\end{aligned} \tag{F.2}$$

It is easy to see that the system $(\mathrm{F}.2)_1$ is the same as $(\mathrm{E}.2)_1$ whereas $(\mathrm{F}.2)_{2,3}$ can be obtained from $(\mathrm{E}.2)_2$ for $\phi=\pm\frac{\pi}{3}$. Then, by using the same strategy outlined in the Appendix E, the solution at first perturbative order is obtained

$$\mathbf{U}_1=\Omega_1\begin{bmatrix} r_1\cos(k_cx)\\ r_2\cos(k_cx)\\ k_cr_1\sin(k_cx)\\ 0\\ k_cdr_2\sin(k_cx)\\ 0\end{bmatrix}+\frac{\Omega_2}{2}\begin{bmatrix} r_1\Big(\cos(k_c\zeta)+\cos(k_c\xi)\Big)\\ r_2\Big(\cos(k_c\zeta)+\cos(k_c\xi)\Big)\\ \frac{1}{2}k_cr_1\Big(\sin(k_c\zeta)+\sin(k_c\xi)\Big)\\ \frac{\sqrt{3}}{2}k_cr_1\Big(\sin(k_c\zeta)-\sin(k_c\xi)\Big)\\ \frac{1}{2}k_cdr_2\Big(\sin(k_c\zeta)+\sin(k_c\xi)\Big)\\ \frac{\sqrt{3}}{2}k_cdr_2\Big(\sin(k_c\zeta)-\sin(k_c\xi)\Big)\end{bmatrix}. \tag{F.3}$$

Now, substituting (F.3) into the nonhomogeous linear system $(4.20)_2$ and requiring to eliminate resonant terms, the following system is obtained

$$\begin{cases}\frac{\partial\Omega_1}{\partial T_1}=B_1\sigma\Omega_1-\frac{L}{4}\Omega_2^2\\ \frac{\partial\Omega_2}{\partial T_1}=B_1\sigma\Omega_2-L\Omega_1\Omega_2\end{cases} \tag{F.4}$$

where

$$L=-\frac{2B_c\Big(u_{S_c}^2-1\Big)(r_1+dr_2)n_1}{r_1r_2\big[d-1+dk_c^2(\tau^w-\tau^u)\big]}. \tag{F.5}$$

Note that, system (F.4) does not admit stable equilibria, so that WNA has to be pushed to the next perturbative order. Therefore, taking into account (4.19),(F.4), the solution at the second perturbative order reads

$$\mathbf{U}_2(x,\zeta,\xi,T_1,T_2)=\Omega_1\widetilde{\mathbf{U}}_{10}+\Omega_2\widetilde{\mathbf{U}}_{01}+\Omega_1\Omega_2\widetilde{\mathbf{U}}_{11}+\Omega_1^2\widetilde{\mathbf{U}}_{20}+\Omega_2^2\widetilde{\mathbf{U}}_{02} \tag{F.6}$$

where the vectors $\widetilde{\mathbf{U}}_{10}(x)$, $\widetilde{\mathbf{U}}_{01}(\zeta,\xi)$, $\widetilde{\mathbf{U}}_{11}(x,\zeta,\xi)$, $\widetilde{\mathbf{U}}_{20}(x)$ and $\widetilde{\mathbf{U}}_{02}(x,\zeta,\xi)$ are given by

$$\widetilde{\mathbf{U}}_{10} = B_1 \begin{bmatrix} p_1\cos(k_c x) \\ p_2\cos(k_c x) \\ p_3\sin(k_c x) \\ 0 \\ p_4\sin(k_c x) \\ 0 \end{bmatrix}, \quad \widetilde{\mathbf{U}}_{01} = \tfrac{B_1}{2} \begin{bmatrix} p_1\Big(\cos(k_c\zeta)+\cos(k_c\xi)\Big) \\ p_2\Big(\cos(k_c\zeta)+\cos(k_c\xi)\Big) \\ \frac{1}{2}p_3\Big(\sin(k_c\zeta)+\sin(k_c\xi)\Big) \\ \frac{\sqrt{3}}{2}p_3\Big(\sin(k_c\zeta)-\sin(k_c\xi)\Big) \\ \frac{1}{2}p_4\Big(\sin(k_c\zeta)+\sin(k_c\xi)\Big) \\ \frac{\sqrt{3}}{2}p_4\Big(\sin(k_c\zeta)-\sin(k_c\xi)\Big) \end{bmatrix},$$

$$\widetilde{\mathbf{U}}_{20} = n_1 \begin{bmatrix} 1+\frac{1+4dk_c^2}{9}\cos(2k_c x) \\ -B_c-\frac{B_c+4k_c^2}{9}\cos(2k_c x) \\ \frac{2k_c\left(1+4d_c k_c^2\right)}{9}\sin(2k_c x) \\ 0 \\ -\frac{2k_c d\left(B_c+4k_c^2\right)}{9}\sin(2k_c x) \\ 0 \end{bmatrix},$$

$$\widetilde{\mathbf{U}}_{02} = \tfrac{1}{4} \begin{bmatrix} q_1\cos(k_c x)+\tilde{q}_1\cos(k_c(\zeta-\xi))+n_1\left(1+\frac{1+4dk_c^2}{9}\right)\Big(\cos(2k_c\zeta)+\cos(2k_c\xi)\Big) \\ q_2\cos(k_c x)+\tilde{q}_2\cos(k_c(\zeta-\xi))-n_1\left(B_c+\frac{B_c+4k_c^2}{9}\right)\Big(\cos(2k_c\zeta)+\cos(2k_c\xi)\Big) \\ q_3\sin(k_c x)+n_1\frac{k_c\left(1+4d_c k_c^2\right)}{9}\Big(\sin(2k_c\zeta)+\sin(2k_c\xi)\Big) \\ \sqrt{3}k_c\tilde{q}_1\sin(k_c(\zeta-\xi))+n_1\frac{\sqrt{3}k_c\left(1+4d_c k_c^2\right)}{9}\Big(\sin(2k_c\zeta)-\sin(2k_c\xi)\Big) \\ q_4\sin(k_c x)-n_1\frac{k_c d\left(B_c+4k_c^2\right)}{9}\Big(\sin(2k_c\zeta)+\sin(2k_c\xi)\Big) \\ \sqrt{3}dk_c\tilde{q}_2\sin(k_c(\zeta-\xi))+n_1\frac{\sqrt{3}k_c d\left(B_c+4k_c^2\right)}{9}\Big(\sin(2k_c\zeta)-\sin(2k_c\xi)\Big) \end{bmatrix},$$

$$\widetilde{\mathbf{U}}_{11} = \tfrac{1}{2} \begin{bmatrix} q_1\Big(\cos(k_c\zeta)+\cos(k_c\xi)\Big)+\tilde{q}_1\Big[\cos(k_c(x+\zeta))+\cos(k_c(x+\xi))\Big] \\ q_2\Big(\cos(k_c\zeta)+\cos(k_c\xi)\Big)+\tilde{q}_2\Big[\cos(k_c(x+\zeta))+\cos(k_c(x+\xi))\Big] \\ \frac{1}{2}q_3\Big(\sin(k_c\zeta)+\sin(k_c\xi)\Big)+\frac{3}{2}k_c\tilde{q}_1\Big[\sin(k_c(x+\zeta))+\sin(k_c(x+\xi))\Big] \\ \frac{\sqrt{3}}{2}q_3\Big(\sin(k_c\zeta)-\sin(k_c\xi)\Big)+\frac{\sqrt{3}}{2}k_c\tilde{q}_1\Big[\sin(k_c(x+\zeta))-\sin(k_c(x+\xi))\Big] \\ \frac{1}{2}q_4\Big(\sin(k_c\zeta)+\sin(k_c\xi)\Big)+\frac{3}{2}dk_c\tilde{q}_2\Big[\sin(k_c(x+\zeta))+\sin(k_c(x+\xi))\Big] \\ \frac{\sqrt{3}}{2}q_4\Big(\sin(k_c\zeta)-\sin(k_c\xi)\Big)+\frac{\sqrt{3}}{2}dk_c\tilde{q}_2\Big[\sin(k_c(x+\zeta))-\sin(k_c(x+\xi))\Big] \end{bmatrix}, \tag{F.7}$$

with

$$
\begin{aligned}
p_1 &= \tfrac{r_1\sigma}{4k_c^2}\left[\tfrac{k_c^2-B_c}{\gamma_u}+\tfrac{d\left(k_c^2+B_c\right)}{\mu_w}\right]+\tfrac{\left(3k_c^2+B_c\right)}{4r_2k_c^2\left(k_c^2-B_c\right)\left[d-1+dk_c^2\left(\frac{d}{\mu_w}-\frac{1}{\gamma_u}\right)\right]}\times .\\
&\times\left\{r_1\left[2r_1\left(\tfrac{k_c^2}{\gamma_u}-1\right)+r_2\left(\tfrac{d^2k_c^2}{\mu_w}-1\right)\right]+\tfrac{2u_{S_c}^2\left(1+u_{S_c}^2\right)r_2}{B_c\left(1-u_{S_c}^2\right)}\left[r_1\left(\tfrac{k_c^2}{\gamma_u}-1\right)+r_2\left(\tfrac{d^2k_c^2}{\mu_w}-1\right)\right]\right\},\\
p_2 &= \tfrac{r_2}{r_1}p_1+\tfrac{1}{r_1\left(k_c^2-B_c\right)\left[d-1+dk_c^2\left(\frac{d}{\mu_w}-\frac{1}{\gamma_u}\right)\right]}\left\{r_1\left[2r_1\left(\tfrac{k_c^2}{\gamma_u}-1\right)+r_2\left(\tfrac{d^2k_c^2}{\mu_w}-1\right)\right]\right.\\
&\left.+\tfrac{2u_{S_c}^2\left(1+u_{S_c}^2\right)r_2}{B_c\left(1-u_{S_c}^2\right)}\left[r_1\left(\tfrac{k_c^2}{\gamma_u}-1\right)+r_2\left(\tfrac{d^2k_c^2}{\mu_w}-1\right)\right]\right\},\\
p_3 &= k_cp_1-\tfrac{r_1k_c}{\gamma_u}\sigma\\
p_4 &= dk_cp_2-\tfrac{d^2r_2k_c}{\mu_w}\sigma\\
q_1 &= \frac{B_c\left(u_{S_c}^2-1\right)n_1\left\{(r_1+r_2d)\left(k_c^2-B_c\right)\left[\frac{k_c^2-B_c}{\gamma_u}+\frac{d\left(k_c^2+B_c\right)}{\mu_w}\right]+\left(3k_c^2+B_c\right)\left[r_1\left(\frac{k_c^2}{\gamma_u}-1\right)+r_2\left(\frac{d^2k_c^2}{\mu_w}-1\right)\right]\right\}}{2r_2k_c^2\left(k_c^2-B_c\right)\left[d-1+dk_c^2\left(\frac{d}{\mu_w}-\frac{1}{\gamma_u}\right)\right]}\\
q_2 &= \tfrac{r_2}{r_1}q_1+\frac{2B_c\left(u_{S_c}^2-1\right)n_1\left[r_2\left(1-\frac{d^2k_c^2}{\mu_w}\right)+r_1\left(1-\frac{k_c^2}{\gamma_u}\right)\right]}{r_1\left(k_c^2-B_c\right)\left[d-1+dk_c^2\left(\frac{d}{\mu_w}-\frac{1}{\gamma_u}\right)\right]}\\
q_3 &= k_cq_1+\tfrac{r_1k_c}{\gamma_u}L\\
q_4 &= dk_cq_2+\tfrac{d^2r_2k_c}{\mu_w}L\\
\tilde{q}_1 &= \tfrac{\left[r_1\left(B_c-k_c^2\right)+dr_2\left(B_c+k_c^2\right)\right]n_1}{2r_2}\\
\tilde{q}_2 &= \tfrac{\left[r_1\left(B_c-3k_c^2\right)+dr_2\left(B_c-k_c^2\right)\right]n_1}{2r_1}
\end{aligned}
\tag{F.8}
$$

where $\gamma_u = 1/\tau^u$ and $\mu_w = d/\tau^w$.

Then, taking into account expressions (F.3) and (F.6), elimination of the secular terms into $(4.20)_3$ leads to the following system

$$
\begin{cases}
\frac{\partial\Omega_1}{\partial T_2} = \tilde{a}_0B_1\frac{\partial\Omega_1}{\partial T_1}-L_1\Omega_1^3+\tilde{a}_1\Omega_1+\frac{\tilde{a}_2}{2}\Omega_1\Omega_2^2+\frac{\tilde{a}_3}{4}B_1\Omega_2^2+\frac{\tilde{a}_4}{2}\Omega_2\frac{\partial\Omega_2}{\partial T_1}\\
\frac{\partial\Omega_2}{\partial T_2} = \tilde{a}_0B_1\frac{\partial\Omega_2}{\partial T_1}-\frac{L_1}{4}\Omega_2^3+\tilde{a}_1\Omega_2+\tilde{a}_2\Omega_2\left\{\Omega_1^2+\frac{1}{4}\Omega_2^2\right\}+\tilde{a}_3B_1\Omega_1\Omega_2+\tilde{a}_4\left(\frac{\partial\Omega_1}{\partial T_1}\Omega_2+\frac{\partial\Omega_2}{\partial T_1}\Omega_1\right)
\end{cases}
\tag{F.9}
$$

where

$$\tilde{a}_0 = \frac{dr_2p_1\left(\frac{k_c^2}{\gamma_u}-1\right)+r_1p_2\left[1-\frac{d^2k_c^2}{\mu_w}\right]+dk_c^2r_1r_2\sigma\frac{\left(d^2\gamma_u^2-\mu_0^2\right)}{\gamma_u^2\mu_w^2}}{r_1r_2\left[d-1+dk_c^2\left(\frac{d}{\mu_w}-\frac{1}{\gamma_u}\right)\right]},$$

$$\tilde{a}_1 = \frac{\left(p_1B_1^2+r_1B_2\right)(2r_1+dr_2)}{r_1r_2\left[d-1+dk_c^2\left(\frac{d}{\mu_w}-\frac{1}{\gamma_u}\right)\right]}+\frac{(r_1+dr_2)u_{S_c}^2\left(1+u_{S_c}^2\right)}{B_c\left(1-u_{S_c}^2\right)r_1r_2\left[d-1+dk_c^2\left(\frac{d}{\mu_w}-\frac{1}{\gamma_u}\right)\right]}\left[2\left(p_2B_1^2+r_2B_2\right)+\frac{r_2B_1^2\left(1+6u_{S_c}^2-3u_{S_c}^4\right)}{B_c\left(1-u_{S_c}^2\right)^2}\right],$$

$$\tilde{a}_2 = \frac{(r_1+dr_2)}{2r_1r_2u_{S_c}\left[d-1+dk_c^2\left(\frac{d}{\mu_w}-\frac{1}{\gamma_u}\right)\right]}\left[2\left(r_1B_c+r_2u_{S_c}^2\right)(2n_1+q_1+\tilde{q}_1)+2r_1u_{S_c}^2\left(2n_2+q_2+\tilde{q}_2\right)+3r_1^2r_2u_{S_c}\right],$$

$$\tilde{a}_3 = \frac{2(r_1+dr_2)}{r_1r_2\left[d-1+dk_c^2\left(\frac{d}{\mu_w}-\frac{1}{\gamma_u}\right)\right]}\left[\frac{r_1p_1B_c}{u_{S_c}}+\left(r_1p_2+r_2p_1\right)u_{S_c}+\frac{u_{S_c}\left(1+u_{S_c}^2\right)}{B_c\left(1-u_{S_c}^2\right)}\left(u_{S_c}q_2+r_1r_2\right)+\frac{r_1^2u_{S_c}}{\left(1-u_{S_c}^2\right)}\right]+$$
$$+\frac{(2r_1+dr_2)q_1}{r_1r_2\left[d-1+dk_c^2\left(\frac{d}{\mu_w}-\frac{1}{\gamma_u}\right)\right]},$$

$$\tilde{a}_4 = -\frac{dr_2q_1\left[1-\frac{k_c^2}{\gamma_u}\right]-r_1q_2\left[1-\frac{d^2k_c^2}{\mu_w}\right]+dk_c^2r_1r_2L\frac{\mu_w^2-d^2\gamma_u^2}{\gamma_0^2\mu_w^2}}{r_1r_2\left[d-1+dk_c^2\left(\frac{d}{\mu_w}-\frac{1}{\gamma_u}\right)\right]}. \tag{F.10}$$

By taking into account expressions (F.4) and (F.7), system (F.9) can be recast as

$$\begin{cases}\frac{\partial\Omega_1}{\partial T_2} = \tilde{\sigma}\Omega_1+\psi\Omega_2^2-L_1\Omega_1^3+\tilde{L}\Omega_1\Omega_2^2\\ \frac{\partial\Omega_2}{\partial T_2} = \tilde{\sigma}\Omega_2+\frac{1}{4}\left(2\tilde{L}-L_1\right)\Omega_2^3+4\psi\Omega_1\Omega_2+2\tilde{L}\Omega_1^2\Omega_2\end{cases} \tag{F.11}$$

Finally, by adding (F.4) to (F.11), pattern amplitudes are ruled by

$$\begin{cases}\frac{\partial\Omega_1}{\partial T} = \bar{\sigma}\Omega_1+\bar{\psi}\Omega_2^2-\bar{L}_1\Omega_1^3+\bar{L}\Omega_1\Omega_2^2\\ \frac{\partial\Omega_2}{\partial T} = \bar{\sigma}\Omega_2+\frac{1}{4}\left(2\bar{L}-\bar{L}_1\right)\Omega_2^3+4\bar{\psi}\Omega_1\Omega_2+2\bar{L}\Omega_1^2\Omega_2\end{cases} \tag{F.12}$$

where

$$\frac{\partial}{\partial T} = \frac{\partial}{\partial T_1}+\epsilon\frac{\partial}{\partial T_2} \qquad \bar{\sigma} = B_1\sigma+\epsilon\tilde{\sigma}, \qquad \bar{\psi} = -\frac{L}{4}+\epsilon\psi, \qquad \bar{L}_1 = \epsilon L_1, \qquad \bar{L} = \epsilon\tilde{L}.$$

Bibliography

[1] M.C. Cross and P.C. Hohenberg. Pattern formation outside of equilibrium. *Review of Modern Physics*, 65(7):851–1112, 1993. doi: 10.1103/RevModPhys.65.851.

[2] D. Walgraef. *Spatio-Temporal Pattern Formation*. Springer-Verlag, New York, first edition, 1997. doi: 10.1007/978-1-4612-1850-0.

[3] J.D. Murray. *Mathematical Biology: I. An introduction*. Springer-Verlag, New York, third edition, 2002. doi: 10.1007/b98868.

[4] J.D. Murray. *Mathematical Biology II: Spatial Models and Biomedical Applications*. Springer, Berlin, third edition, 2003. doi: 10.1007/b98869.

[5] R. Hoyle. *Pattern formation. An introduction to methods*. Cambridge University Press, New York, first edition, 2007. doi: 10.1017/CBO9780511616051.

[6] M. Cross and H. Greenside. *Pattern Formation and Dynamics in Nonequilibrium Systems*. Cambridge University Press, Cambridge, first edition, 2009. doi: 10.1017/CBO9780511627200.

[7] E. Meron. *Nonlinear Physics of Ecosystems*. CRC Press, Boca Raton, first edition, 2015. doi: 10.1201/b18360.

[8] G. Tesauro. Pattern formation in models of convection. In D. Walgraef, editor, *Patterns, Defects and Microstructures in Nonequilibrium Systems*, pages 23–45. NATO ASI Series, Dordrecht, 1987.

[9] B.P. Belousov. A periodic reaction and its mechanism. *Sbornik Referatov po Radiatsionnoĵ Meditsine za 1958 god*, page 145, 1958.

[10] A.M. Turing. The chemical basis of morphogenesis. *Philosophical Transactions of the Royal Society B*, 237:37–72, 1952. doi: 10.1098/rstb.1952.0012.

[11] A. Doelman. Pattern formation in reaction-diffusion systems – an explicit approach. In M.A Peletier and E. Steur, editors, *Complexity Science. An introduction.*, chapter 4, pages 129–182. World Scientific, 2019. doi: 10.1142/9789813239609_0004.

[12] C.K.R.T. Jones. Geometric singular perturbation theory. In R. Johnson, editor, *Lecture Notes in Mathematics*. Springer: Berlin, Heidelberg, 1995.

[13] G. Hek. Geometric singular perturbation theory in biological practice. *Journal of Mathematical Biology*, 60:347–386, 2010. doi: 10.1007/s00285-009-0266-7.

[14] V. Mendez, S. Fedotov, and W. Horsthemke. *Reaction-Transport Systems*. Springer-Verlag, Berlin Heidelberg, first edition, 2010. doi: 10.1007/978-3-642-11443-4.

[15] M. Al-Ghoul and B.C. Eu. Hyperbolic reaction-diffusion equations and irreversible thermodynamics: Cubic reversible reaction model. *Physica D*, 90(1–2): 119–153, 1996. doi: 10.1016/0167-2789(95)00231-6.

[16] M. Al-Ghoul and B.C. Eu. Hyperbolic reaction-diffusion equations and irreversible thermodynamics: Ii. two dimen- sional patterns and dissipation of energy and matter. *Physica D*, 97(4):531–562, 1996. doi: 10.1016/0167-2789(96)00008-5.

[17] U.I. Cho and B.C. Eu. Hyperbolic reaction-diffusion equations and chemical oscillations in the Brusselator. *Physica D*, 68(3–4):351–363, 1993. doi: 10.1016/0167-2789(93)90130-S.

[18] D.G. Milchunas and W.K. Lauenroth. Inertia in plant community structure: state changes after cessation of nutrient-enrichment stress. *Ecological Applications*, 5(2):452–458, 1995. doi: 10.2307/1942035.

[19] V. Mendez and J.E. Llebot. Hyperbolic reaction-diffusion equations for a forest fire model. *Physical Review E*, 56:6557–6563, 1997. doi: 10.1103/PhysRevE.56.6557.

[20] C. Valentin and J.M. d'Herbes. Niger tiger bush as a natural water harvesting system. *Catena*, 37(1–2):231–256, 1999. doi: 10.1016/S0341-8162(98)00061-7.

[21] K.P. Hadeler. Reaction transport systems in biological modelling. In V. Capasso, editor, *Mathematics Inspired by Biology*, chapter 3, pages 95—-150. Springer, 1999. doi: 10.1007/BFb0092376.

[22] T. Hillen and Hadeler K.P. Hyperbolic systems and transport equations in mathematical biology. In G. Warnecke, editor, *Analysis and Numerics for Conservation Laws*, chapter 11, pages 257—-279. Springer, 2005. doi: 10.1007/3-540-27907-5_11.

[23] J. Fort and V. Mendez. Wavefronts in time-delayed reaction-diffusion system. theory and comparison to experiments. *Reports on Progress in Physics*, 65(6): 895–954, 2002. doi: 10.1088/0034-4885/65/6/201.

[24] P. Garcia-Fayos and M. Gasque. Consequences of a severe drought on spatial patterns of woody plants in a two-phase mosaic steppe of Stipa tenacissima L. *Journal of Arid Environments*, 52(2):199–208, 2002. doi: 10.1006/jare.2002.0987.

[25] B. Straughan. *Heat Waves*. Springer, New York, first edition, 2011. doi: 10.1007/978-1-4614-0493-4.

[26] V. Deblauwe, P. Couteron, O. Lejeune, J. Bogaert, and N. Barbier. Environmental modulation of self-organized periodic vegetation patterns in Sudan. *Ecography*, 34(6):990–1001, 2011. doi: 10.1111/j.1600-0587.2010.06694.x.

[27] V. Deblauwe, P. Couteron, J. Bogaert, and N. Barbier. Determinants and dynamics of banded vegetation pattern migration in arid climates. *Ecological Monograph*, 82(1):3–21, 2012. doi: 10.1890/11-0362.1.

[28] W. Horsthemke. Spatial instabilities in reaction random walks with direction-independent kinetics. *Physical Review E*, 60:2651–2663, 1999. doi: 10.1103/physreve.60.2651.

[29] V. Mendez, D. Campos, and W. Horsthemke. Growth and dispersal with inertia: Hyperbolic reaction-transport systems. *Physical Review E*, 90(4):042114, 2014. doi: 10.1103/PhysRevE.90.042114.

[30] P.L. Buono and R. Eftimie. Symmetries and pattern formation in hyperbolic versus parabolic models of self-organised aggregation. *Journal of Mathematical Biology*, 71(4):847–881, 2015. doi: 10.1007/s00285-014-0842-3.

[31] E. Barbera, C. Curró, and G. Valenti. On discontinuous travelling wave solutions for a class of hyperbolic reaction-diffusion models. *Physica D*, 308: 116–126, 2015. doi: 10.1016/j.physd.2015.06.011.

[32] E.P. Zemskov and W. Horsthemke. Diffusive instabilities in hyperbolic reaction-diffusion equations. *Physical Review E*, 93:032211, 2016. doi: 10.1103/PhysRevE.93.032211.

[33] J.E. Macias-Diaz and A.S. Hendy. Numerical simulation of turing patterns in a fractional hyperbolic reaction-diffusion model with grunwald differences. *The European Physical Journal Plus*, 134:324, 2019. doi: 10.1140/epjp/i2019-12703-2.

[34] S. Ghorai, S. Poria, and N. Bairagi. Diffusive instability in hyperbolic reaction-diffusion equation with different inertia. *Chaos*, 32:013101, 2022. doi: 10.1063/5.0071959.

[35] J.S. Ritchie, A.L. Krauseb, and R.A. Van Gordera. Turing and wave instabilities in hyperbolic reaction-diffusion systems: The role of second-order time derivatives and cross-diffusion terms on pattern formation. *Annals of Physics*, 444:169033, 2022. doi: 10.1016/j.aop.2022.169033.

[36] B. Straughan. Thermal convection in a brinkman-darcy-kelvin-voigt fluid with a generalized maxwell-cattaneo law. *Annali dell'Universitá di Ferrara*, 2022. doi: 10.1007/s11565-022-00448-z.

[37] E. Barbera and A. Pollino. An extended thermodynamics model for blood flow. *Mathematics*, 10:2977, 2022. doi: 10.3390/math10162977.

[38] T. Ruggeri and M. Sugiyama. *Classical and Relativistic Rational Extended Thermodynamics of Gases*. Springer, Cham, first edition, 2021. doi: 10.1007/978-3-030-59144-1.

[39] National Aeronautics and Space Administration in NASA global climate change. `https://climate.nasa.gov/`, 2022.

[40] World Methereological Organization. Climate change and desertification. `https://library.wmo.int/index.php?lvl=notice_display&id=5066#.Y3NABezMI-Q`, 2007.

[41] C.A. Klausmeier. Regular and irregular patterns in semiarid vegetation. *Science*, 284(5421):1826–1828, 1999. doi: 10.1126/science.284.5421.1826.

[42] M. Rietkerk, P. Ketner, J. Burger, B. Hoorens, and H. Olff. Multiscale soil and vegetation patchiness along a gradient of herbivore impact in a semi-arid grazing system in west Africa. *Plant Ecology*, 148:207–224, 2000. doi: 10.1023/A:1009828432690.

[43] R. HilleRisLambers, M. Rietkerk, F. van de Bosch, H.H.T. Prins, and H. de Kroon. Vegetation pattern formation in semi-arid grazing systems. *Ecology*, 82(1):50, 2001. doi: 10.1890/0012-9658(2001)082[0050:VPFISA]2.0.CO;2.

[44] J. von Hardenberg, E. Meron, M. Shachak, and Y. Zarmi. Diversity of vegetation patterns and desertification. *Physical Review Letters*, 87:198101, 2001. doi: 10.1103/PhysRevLett.87.198101.

[45] J.A. Sherratt. An analysis of vegetation stripe formation in semi-arid landscapes. *Journal of Mathematical Biology*, 51:183–197, 2005. doi: 10.1007/s00285-005-0319-5.

[46] K. Siteur, E. Siero, M.B. Eppinga, J.D.M. Rademacher, A. Doelman, and M. Rietkerk. Beyond turing: The response of patterned ecosystems to environmental change. *Ecological Complexity*, 20:81–96, 2014. doi: 10.1016/j.ecocom.2014.09.002.

[47] S. Thompson, G. Katul, and S.M. McMahon. Role of biomass spread in vegetation pattern formation within arid ecosystems. *Water Resource Research*, 44 (10):W10421, 2008. doi: 10.1029/2008WR006916.

[48] S. Thompson, S. Assouline, L. Chen, A. Trahktenbrot, T. Svoray, and G. Katul. Secondary dispersal driven by overland flow in drylands: Review and mechanistic model development. *Movement Ecology*, 2:7, 2014. doi: 10.1186/2051-3933-2-7.

[49] S. Thompson and G. Katul. Secondary seed dispersal and its role in landscape organization. *Geophysical Research Letters*, 36(2):L02402, 2009. doi: 10.1029/2008GL036044.

[50] P.M. Saco, G.R. Willgoose, and G.R. Hancock. Eco-geomorphology of banded vegetation patterns in arid and semi-arid regions. *Hydrology and Earth System Sciences*, 11:1717–1730, 2007. doi: 10.1029/2008GL036044.

[51] M. Pueyo, J. Mateu, A. Rigol, M. Vidal, J.F. López-Sánchez, and G. Rauret. Use of the modified bcr three-step sequential extraction procedure for the study of trace element dynamics in contaminated soils. *Environmental Pollution*, 152 (2):330–341, 2008. doi: 10.1016/j.envpol.2007.06.020.

[52] N. Ursino and M.C. Rulli. Combined effect of fire and water scarcity on vegetation patterns in arid lands. *Ecological Modelling*, 221(19):2353–2362, 2010. doi: 10.1016/j.ecolmodel.2010.06.018.

[53] Y. Zelnik, S. Kinast, H. Yizhaq, G. Bel, and E. Meron. Regime shifts in models of dryland vegetation. *Philosophical Transactions of the Royal Society A*, 371 (2004):20120358, 2013. doi: 10.1098/rsta.2012.0358.

[54] F. van Langevelde, Z.K. Tessema, W.F. de Boer, and H.H.T. Prinsa. Soil seed bank dynamics under the influence of grazing as alternative explanation for herbaceous vegetation transitions in semi-arid rangelands. *Ecological Modelling*, 337:253–261, 2016. doi: 10.1016/j.ecolmodel.2016.07.013.

[55] F. Borgogno, P. D'Odorico, F. Laio, and L. Ridolfi. Mathematical models of vegetation pattern formation in ecohydrology. *Review of Geophisics*, 47(1): RG1005, 2009. doi: 10.1029/2007RG000256.

[56] J.A. Sherratt and A.D. Synodinos. Vegetation patterns and desertification waves in semi-arid environments: mathematical models based on local facilitation in plants. *Discrete Cont. Dyn. Syst. Ser. B*, 17(8):2815–2827, 2012. doi: 10.3934/dcdsb.2012.17.2815.

[57] J.A. Sherratt. Pattern solutions of the Klausmeier model for banded vegetation in semi-arid environments III: The transition between homoclinic solutions. *Physica D*, 242(1):30–41, 2013. doi: 10.1016/j.physd.2012.08.014.

[58] S. van der Stelt, A. Doelman, G. Hek, and J.D.M. Rademacher. Rise and fall of periodic patterns for a generalized Klausmeier-Gray-Scott model. *Journal of Nonlinear Science*, 23(7):39–95, 2013. doi: 10.1007/s00332-012-9139-0.

[59] L. Eigentler and J.A. Sherratt. An integrodifference model for vegetation patterns in semi-arid environments with seasonality. *Journal of Mathematical Biology*, 81:875–904, 2020. doi: 10.1007/s00285-020-01530-w.

[60] A. Marasco, A. Iuorio, F. Cartení, G. Bonanomi, D.M. Tartakovsky, S. Mazzoleni, and F. Giannino. Vegetation pattern formation due to interactions between water availability and toxicity in plant-soil feedback. *Bulletin of Mathematical Biology*, 76(11):2866–2883, 2014. doi: 10.1007/s11538-014-0036-6.

[61] P. Gandhi, L. Werner, S. Iams, K. Gowda, and M. Silber. A topographic mechanism for arcing of dryland vegetation bands. *Journal of Royal Society Interface*, 15(147):20180508, 2018. doi: 10.1098/rsif.2018.0508.

[62] R. Bastiaansen, P. Carter, and A. Doelman. Stable planar vegetation stripe patterns on sloped terrain in dryland ecosystems. *Nonlinearity*, 32(8):2759, 2019. doi: 10.1088/1361-6544/ab1767.

[63] Y.R. Zelnik, H. Uecker, U. Feudel, and E. Meron. Desertification by front propagation? *Journal of Theoretical Biology*, 418:27–35, 2017. doi: 10.1016/j.jtbi.2017.01.029.

[64] J.A. Sherratt. Pattern solutions of the Klausmeier model for banded vegetation in semi-arid environments I. *Nonlinearity*, 23(8):2657–2675, 2010. doi: 10.1088/0951-7715/23/10/016.

[65] B.J. Kealy and D.J. Wollkind. A nonlinear stability analysis of vegetative turing pattern formation for an interaction-diffusion plant-surface water model system in an arid flat environment. *Bulletin of Mathematical Biology*, 74(4): 803–833, 2012. doi: 10.1007/s11538-011-9688-7.

[66] G.Q. Sun, L. Li, and Z.K. Zhang. Spatial dynamics of a vegetation model in an arid flat environment. *Nonlinear Dynamics*, 73(5):2207–2219, 2013. doi: 10.1007/s11071-013-0935-3.

[67] G. Consolo and G. Valenti. Secondary seed dispersal in the Klausmeier model of vegetation for sloped semi-arid environments. *Ecological Modelling*, 402: 66–75, 2019. doi: 10.1016/j.ecolmodel.2019.02.009.

[68] D.J. Tongway. *Banded Vegetation Patterning in Arid and Semiarid Environments*. Springer, New York, first edition, 2001. doi: 10.1007/978-1-4613-0207-0.

[69] K. Gowda, S. Iams, and M. Silber. Signatures of human impact on self-organized vegetation in the horn of Africa. *Scientific Reports*, 8:3622, 2018. doi: 10.1038/s41598-018-22075-5.

[70] D. Dunkerley. Banded vegetation in some australian semi-arid landscapes: 20 years of field observations to support the development and evaluation of numerical models of vegetation pattern evolution. *Desert*, 23(2):165–187, 2018.

[71] B. Von Holle, H.R. Delcourt, and D. Simberloff. The importance of biological inertia in plant community resistance to invasion. *Journal of Vegetation Science*, 14(3):425–432, 2003. doi: 10.1111/j.1654-1103.2003.tb02168.x.

[72] J. Brown, T. Whitham, E. Morgan, and C. Gehring. Complex species interactions and the dynamics of ecological systems: Long-term experiments. *Science*, 293(5530):643–650, 2001. doi: 10.1126/science.293.5530.643.

[73] A. Hastings. Transients: the key to long-term ecological understanding? *Trends in Ecology and Evolution*, 19(1):39–45, 2004. doi: 10.1016/j.tree.2003.09.007.

[74] A. Hastings, K.C. Abbott, K. Cuddington, T. Francis, G. Gellner, Y.C. Lai, A. Morozov, S. Petrovskii, K. Scranton, and M.L. Zeeman. Transient phenomena in ecology. *Science*, 361(6406):eaat6412, 2018. doi: 10.1126/science.aat6412.

[75] G. Consolo, C. Curró, and G. Valenti. Pattern formation and modulation in a hyperbolic vegetation model for semiarid environments. *Applied Mathematical Modelling*, 43(3):372–392, 2017. doi: 10.1016/j.apm.2016.11.031.

[76] G. Consolo, C. Curró, and G. Valenti. Supercritical and subcritical Turing pattern formation in a hyperbolic vegetation model for flat arid environments. *Physica D*, 398(11):141–163, 2019. doi: 10.1016/j.physd.2019.03.006.

[77] G. Consolo, C. Curró, and G. Valenti. Turing vegetation patterns in a generalized hyperbolic Klausmeier model. *Mathematical Methods in the Applied Science*, 43(18):10474, 2020. doi: 10.1002/mma.6518.

[78] G. Consolo, C. Curró, G. Grifó, and G. Valenti. Oscillatory periodic pattern dynamics in hyperbolic reaction-advection-diffusion models. *Physical Review E*, 105:034206, 2022. doi: 10.1103/PhysRevE.105.034206.

[79] G. Consolo and G. Grifó. Eckhaus instability of stationary patterns in hyperbolic reaction-diffusion models on large finite domains. *Partial Differential Equations and Applications*, 3:57, 2022. doi: 10.1007/s42985-022-00193-0.

[80] G. Consolo, G. Grifó, and G. Valenti. Dryland vegetation pattern dynamics driven by inertial effects and secondary seed dispersal. *Ecological Modelling*, 474:110171, 2022. doi: 10.1016/j.ecolmodel.2022.110171.

[81] C. Curró and G. Valenti. Pattern formation in hyperbolic models with cross-diffusion: theory and applications. *Physica D*, 418(4):132846, 2021. doi: 10.1016/j.physd.2021.132846.

[82] A. Mvogo, J.E. Macias-Diaz, and T.C. Kofané. Diffusive instabilities in a hyperbolic activator-inhibitor system with superdiffusion. *Physical Review E*, 97:032129, 2018. doi: 10.1103/PhysRevE.97.032129.

[83] E.P. Zemskov, M.A. Tsyganov, and W. Horsthemke. Wavy fronts in a hyperbolic Fitzhugh-Nagumo system and the effects of cross diffusion. *Physical Review E*, 91:062917, 2015. doi: 10.1103/PhysRevE.91.062917.

[84] W. Van Saarloos and P.C. Hohenberg. Fronts, pulses, sources and sinks in generalized complex Ginzburg-Landau equations. *Physica D*, 56(4):303–367, 1992. doi: 10.1016/0167-2789(92)90175-M.

[85] A. Mielke and G. Schneider. Derivation and justification of the complex Ginzburg-Landau equation as a modulation equation. In P. Deift, C.D. Levermore, and C.E. Wayne, editors, *Lecture in Applied Mathematics*, chapter 3, pages 191–216. American Mathematical Society, 1994.

[86] A. Mielke. The Ginzburg-Landau equation in its role as a modulation equation. In B. Fiedler, editor, *Handbook of dynamical systems*, chapter 15, pages 759–834. Elsevier, 2002. doi: 10.1016/S1874-575X(02)80036-4.

[87] I.S. Aranson and L. Kramer. The world of the complex Ginzburg-Landau equation. *Reviews of modern Physics*, 74(2):99–143, 2002. doi: 10.1103/RevModPhys.74.99.

[88] W. Eckhaus and G. Iooss. Strong selection or rejection of spatially periodic patterns in degenerate bifurcations. *Physica D*, 39(1):124–146, 1989. doi: 10.1016/0167-2789(89)90043-2.

[89] L.S. Tuckerman and D. Barkley. Bifurcation analysis of the Eckhaus instability. *Physica D*, 46(1):57–86, 1990. doi: 10.1016/0167-2789(90)90113-4.

[90] J.P. Eckmann, T. Gallay, and C.E. Wayne. Phase slips and the Eckhaus instability. *Nonlinearity*, 8(6):943–961, 1995. doi: 10.1088/0951-7715/8/6/004.

[91] E. Knobloch and R. Krechetnikov. Stability on time-dependent domains. *Journal of Nonlinear Science*, 24(3):493–523, 2014. doi: 10.1007/s00332-014-9197-6.

[92] A. Doelman. Pattern formation in reaction-diffusion systems - an explicit approach. In M.A. Peletier, R.A. van Santen, and E. Siteur, editors, *Complexity Science, an Introduction*, chapter 4, pages 129–182. World Scientific, 2018. doi: 10.1142/9789813239609_0004.

[93] A. Doelman and W. Eckhaus. Periodic and quasi-periodic solutions of degenerate modulation equations. *Physica D*, 53(2–4):249–266, 1991. doi: 10.1016/0167-2789(91)90065-H.

[94] H.R. Brand and R.J. Deissler. Eckhaus and Benjamin-Feir instabilities near a weakly inverted bifurcation. *Physical Review A*, 45:3732–3736, 1992. doi: 10.1103/PhysRevA.45.3732.

[95] J.H.P. Dawes. Modulated and localized states in a finite domain. *SIAM Journal on Applied Dynamical Systems*, 8(3):909–930, 2009. doi: 10.1137/080724344.

[96] H.C. Kao and E. Knobloch. Weakly subcritical stationary patterns: Eckhaus instability and homoclinic snaking. *Physical Review E*, 85:026211, 2012. doi: 10.1103/PhysRevE.85.026211.

[97] D. Morgan and J.H.P. Dawes. The Swift-Hohenberg equation with a nonlocal nonlinearity. *Physica D*, 270(1):60–80, 2014. doi: 10.1016/j.physd.2013.11.018.

[98] H.C. Kao and E. Knobloch. Instabilities and dynamics of weakly subcritical patterns. *Mathematical Modelling of Nature Phenomena*, 8(5):131–154, 2013. doi: 0.1051/mmnp/20138509.

[99] E. Barbera, G. Consolo, and G. Valenti. Spread of infectious diseases in a hyperbolic reaction-diffusion susceptible-infected-removed model. *Physical Review E*, 88:052719, 2013. doi: 10.1103/PhysRevE.88.052719.

[100] E. Barbera, C. Curró, and G. Valenti. A hyperbolic model for the effects of urbanization on air pollution. *Appl. Math. Modell.*, 34(8):2192–2202, 2010. doi: 10.1016/j.apm.2009.10.030.

[101] G. Gambino, M.C. Lombardo, S. Lupo, and M. Sammartino. Super-critical and sub-critical bifurcations in a reaction-diffusion Schnakenberg model with linear cross-diffusion. *Ricerche di Matematica*, 65(5):449–467, 2016. doi: 10.1007/s11587-016-0267-y.

[102] Y. Rameshwar, V. Anuradha, L.M. Srinivas, G.and Perez, D. Laroze, and H. Pleiner. Nonlinear convection of binary liquids in a porous medium. *Chaos*, 28(7):075512, 2018. doi: 10.1063/1.5027468.

[103] W.W. Mohammed. Modulation equation for the stochastic Swift-Hohenberg equation with cubic and quintic nonlinearities on the real line. *Mathematics*, 7(12):1217, 2019. doi: 10.3390/math7121217.

[104] E. Bilotta, F. Gargano, V. Giunta, M.C. Lombardo, P. Pantano, and M. Sammartino. Eckhaus and zigzag instability in a chemotaxis model of multiple sclerosis. *Atti dell'Accademia Peloritana dei Pericolanti*, 93(S3):A9, 2018. doi: 10.1478/AAPP.96S3A9.

[105] M. Stich and A.S. Mikhailov. Complex pacemakers and wave sinks in heterogeneous oscillatory chemical systems. *Zeitschrift für Physikalische Chemie*, 216 (4):521–533, 2002. doi: 10.1524/zpch.2002.216.4.521.

[106] R. Krechetnikov and E. Knobloch. Stability on time-dependent domains: convective and dilution effects. *Physica D*, 342(3):16–23, 2017. doi: 10.1016/j.physd.2016.10.003.

[107] G.D. Granzow and H. Riecke. Double phase slips and spatiotemporal chaos in a model for parametrically excited standing waves. *SIAM Journal on Applied Mathematics*, 59(3):900–919, 1999. doi: 10.1137/S0036139996313861.

[108] COMSOL Multiphysics ®. Vser 6.0 COMSOL AB, Stockholm, Sweden. URL `https://www.comsol.com/`.

[109] H. Uecker, D. Wetzel, and J. Rademacher. pde2path - a Matlab package for continuation and bifurcation in 2D elliptic systems. *Numerical Mathematics: Theory, Methods and Applications*, 7(1):58–106, 2014. doi: 10.1017/S1004897900000295.

[110] G. Gambino, S. Lupo, M. Sammartino, D. Lacitignola, I. Sgura, and B. Bozzini. Weakly nonlinear analysis of Turing patterns in a morphochemical model for metal growth. *Computational Mathematics with Applications*, 70(8):1948–1969, 2015. doi: 10.1016/j.camwa.2015.08.019.

[111] V. Giunta, M.C. Lombardo, and M. Sammartino. Pattern formation and transition to chaos in a chemotaxis model of acute inflammation. *SIAM Journal on Applied Dynamical Systems*, 20(4):1844–1881, 2021. doi: 10.1137/20M1358104.

[112] W. van Saarloos and P.C. Hohenberg. Pulses and fronts in the complex Ginzburg-Landau equation near a subcritical bifurcation. *Physical Review Letters*, 64:749–752, 1990. doi: 10.1103/PhysRevLett.64.749.

[113] W. Van Saarloos. The complex Ginzburg-Landau equation for beginners. In P.E. Cladis and P. Palffy-Muhoray, editors, *Proceedings of the Santa Fe Workshop on "Spatio-Temporal Patterns in Nonequilibrium Complex Systems"*. Addison-Wesley, Chicago, 1994.

[114] L. Brusch, A. Torcini, M. Van Hecke, M.G. Zimmermann, and M. Bar. Modulated amplitude waves and defect formation in the one-dimensional complex Ginzburg-Landau equation. *Physica D*, 160(3–4):127–148, 2001. doi: 10.1016/S0167-2789(01)00355-4.

[115] Y.R. Zelnik, P. Gandhi, E. Knobloch, and E. Meron. Implications of tristability in pattern-forming ecosystems. *Chaos*, 28(3):033609, 2018. doi: 10.1063/1.5018925.

[116] J.A. Sherratt. Using wavelength and slope to infer the historical origin of semiarid vegetation bands. *Proceedings of the National Academy of Sciences*, 112(14):4202, 2015. doi: 10.1073/pnas.1420171112.

[117] J. Esteban and V. Fairén. Self-organized formation of banded vegetation patterns in semi-arid regions: A model. *Ecological Complexity*, 3(2):109–118, 2006. doi: 10.1016/j.ecocom.2005.10.001.

[118] C. Montana. The colonisation of bare areas two-phase mosaics of an arid ecosystem. *Journal of Ecology*, 80:315–327, 1992. doi: 10.2307/2261014.

[119] J.C. Leprun. Etude de quelques brousses tigrés sahéliennes: structure, dynamique, écologie. In E. Le Floch, M. Grouzis, A. Cornet, and J.C. Bille, editors, *L'aridité, une contrainte au développement*, pages 221–224. Editions de l'ORSTOM, Paris, 1992.

[120] S.B. Boaler and C.A.H. Hodge. Observations on vegetation arcs in the northern region. *Journal of Ecology*, 52(3):511–544, 1964. doi: 10.2307/2257847.

[121] G.A. Worral. The Butanna grass pattern. *European Journal of Soil Science*, 10(1):34–53, 1959. doi: 10.1111/j.1365-2389.1959.tb00664.x.

[122] J.A. Sherratt and G.J. Lord. Nonlinear dynamics and pattern bifurcations in a model for vegetation stripes in semi-arid environments. *Theoretical Population Biology*, 71(1):1–11, 2007. doi: 10.1016/j.tpb.2006.07.009.

[123] J.A. Sherratt. Pattern solutions of the Klausmeier model for banded vegetation in semi-arid environments II: patterns with the largest possible propagation speeds. *Proceeding of the Royal Society A*, 467(2135):3272–3294, 2011. doi: 10.1098/rspa.2011.0194.

[124] B. Ermentrout. *Simulating, Analyzing, and Animating Dynamical Systems*. SIAM, first edition, 2002. doi: 10.1137/1.9780898718195.

[125] G.C. Cruywagen, P.K. Maini, and J.D. Murray. Biological pattern formation on two- dimensional spatial domains: A nonlinear bifurcation analysis. *SIAM Journal of Applied Mathematics*, 57:1485–1509, 1997. doi: 10.1137/S0036139996297900.

[126] P.K. Maini and J.D. Murray. A nonlinear analysis of a mechanical model for biological pattern formation. *SIAM Journal of Applied Mathematics*, 48: 1064–1072, 1998. doi: 10.1137/0148062.

[127] D. Wollkind and L. Stephenson. Chemical turing pattern formation analyses: comparison of theory with experiment. *SIAM Journal of Applied Mathematics*, 61:387–431, 2000. doi: 10.1137/S0036139997326211.

[128] N. Boonkorkuea, Y. Lenbury, F. J. Alvarado, and D. J. Wollkind. Nonlinear stability analyses of vegetative pattern formation in an arid environment. *Journal of Biological Dynamics*, 4:346–380, 2010. doi: 10.1080/17513750903301954.

[129] G. Gambino, M. C. Lombardo, M. Sammartino, and V. Sciacca. Turing pattern formation in the brusselator system with nonlinear diffusion. *Physical Review E*, 88:042925, 2013. doi: 10.1103/PhysRevE.88.042925.

[130] G. Gambino, M. C. Lombardo, and M. Sammartino. Pattern formation driven by cross-diffusion in a 2d domain. *Nonlinear Analysis: Real World Applications*, 14(3):1755–1779, 2013. doi: 10.1016/j.nonrwa.2012.11.009.

[131] B. Bozzini, G. Gambino, D. Lacitignola, S. Lupo, M. Sammartino, and I. Sgurad. Weakly nonlinear analysis of turing patterns in a morphochemical model for metal growth. *Computers and Mathematics with Applications*, 70(8):1948–1969, 2015. doi: 10.1016/j.camwa.2015.08.019.

[132] G. Gambino, M. C. Lombardo, and M. Sammartino. Cross-diffusion-induced subharmonic spatial resonances in a predator-prey system. *Physical Review E*, 97:012220, 2018. doi: 10.1103/PhysRevE.97.012220.

[133] I.S. Liu. Method of lagrange multipliers for exploitation of the entropy principle. *Archive for Rational Mechanics and Analysis*, 46:131–148, 1972. doi: 10.1007/BF00250688.

[134] K.O. Friedrichs and P.D. Lax. System of conservation equation with a convex extension. *Proceedings of the National Academy of Sciences*, 68(8):1686–1688, 1971. doi: 10.1073/pnas.68.8.1686.

[135] A.E. Fischer and J.E. Marsden. The einstein evolution equations as a first-order quasi-linear symmetric hyperbolic system. *Communications in Mathematical Physics*, 28:1–38, 1972. doi: 10.1007/BF02099369.

List of publications

This thesis represents the collection of different works and subjects of study. In the following the reader can find the references to the author's related papers.

1. G. Consolo, C. Currò, G. Grifó, G. Valenti: *Oscillatory periodic pattern dynamics in hyperbolic reaction-advection-diffusion models*, Physical Review E, 105, 2022. https://doi.org/10.1103/PhysRevE.105.034206

2. G. Consolo and G. Grifó: *Eckhaus instability of stationary patterns in hyperbolic reaction-diffusion models on finite domains*, Partial Differential Equations and Applications, 3, 57, 2022. https://doi.org/10.1007/s42985-022-00193-0

3. G. Consolo, G. Grifó, G. Valenti: *Dryland vegetation pattern dynamics driven by inertial effects and secondary seed dispersal*, Ecological Modelling, 474, 110171, 2022. https://doi.org/10.1016/j.ecolmodel.2022.110171

4. G. Grifó, G. Consolo, C. Currò, G. Valenti: *Rhombic and hexagonal pattern formation in 2D hyperbolic reaction-transport systems in the context of dryland ecology*, submitted.

5. G. Grifó: *Vegetation patterns in the hyperbolic Klausmeier model with secondary seed dispersal*, submitted.

In the following, there is a list of references to other published papers dealing with other topics (mostly related to collaborations with marine biologists, ecologists and industrial engineers):

1. C. Currò, G. Grifó, N. Manganaro: *Solutions via double wave ansatz to the 1D non-homogenous gas-dynamics equations*, International Journal of Non-Linear Mechanics, 123, 2020. https://doi.org/10.1016/j.ijnonlinmec.2020.103492

2. S. Savoca, G. Grifó, G. Panarello, M. Albano, S. Giacobbe, G. Capillo, N. Spanó, G. Consolo: *Modeling prey-predator interactions in Messina beachrock pools*, Ecological Modelling, 434, 2020. https://doi.org/10.1016/j.ecolmodel.2020.109206

3. J.M. Abbate, G. Grifó, F. Capparucci, F. Arfuso, S. Savoca, L. Cicero, G. Consolo, G. Lanteri: *Postmortem electrical conductivity changes of Dicentrarchus labrax skeletal muscle: Root Mean square (RMS) parameter in estimating time since death*, Animals, 12, 1062, 2022. https://doi.org/10.3390/ani12091062

4. E. Piperopoulos, G. Grifó, G. Scionti, M. Atria, L. Calabrese, G. Consolo, E. Proverbio: *Study of intumescent coatings growth for fire retardant systems in naval applications: experimental test and mathematical model*, Coatings, 12(8), 1180, 2022. https://doi.org/10.3390/coatings12081180